SLAC-235
UC-34
(E)

A STUDY OF LEADING STRANGE MESON RESONANCES AND SPIN-ORBIT SPLITTINGS IN $K^- p \to K^- \pi^+ n$ AT 11 GeV/c*

Alan Kern Honma

Stanford Linear Accelerator Center
Stanford University
Stanford, California 94305

November 1980

Prepared for the Department of Energy

under contract number DE-AC03-76SF00515

Printed in the United States of America. Available from the National Technical Information Service, U.S. Department of Commerce, 5285 Port Royal Road, Springfield, VA 22161. Price: Printed Copy A12; Microfiche A01.

---

* Ph.D. dissertation.

ABSTRACT

The results from a high statistics study of $K\pi$ elastic scattering in the reaction $K^-p \to K^-\pi^+n$ are presented. The data for this analysis is taken from an 11 GeV/c K^-p experiment performed on the Large Aperture Solenoidal Spectrometer (LASS) facility at the Stanford Linear Accelerator Center (SLAC). By selecting the very forward produced $K^-\pi^+$ events, a sample consisting of data for the $K\pi \to K\pi$ elastic scattering reaction was extracted. The angular distribution for this meson-meson scattering is studied by using both a spherical harmonic moments analysis and a partial wave analysis (PWA). The previously established leading natural spin-parity strange meson resonances (the $J^P=1^-$ K*(895), the 2^+ K*(1430), and the 3^- K*(1780)) are observed in the results from both the moments analysis and the PWA. In addition, evidence for a new spin 4 K* resonance with a mass of 2080 MeV and a width of about 225 MeV is presented. The results from the PWA confirm the existence of a 0^+ κ(1490) and propose the existence of a second scalar meson resonance, the 0^+ κ'(1900). Structure in the P wave amplitude indicates resonance behavior in the mass region near 1700 MeV. In two of the four ambiguous solutions for the mass region above 1800 MeV, there is strong evidence for another P wave resonant structure near 2100 MeV. The observed strange meson resonances are found to have a natural interpretation in terms of states predicted by the quark model. In particular, the mass splittings of the leading trajectory natural spin-parity strange meson states and the mass splittings between the spin-orbit triplet states are discussed.

ACKNOWLEDGEMENTS

There are a number of people that I would like to thank for their help during the running of this experiment and the data analysis that led up to this thesis.

I greatly appreciate the following SLAC Group B staff members for their expert assistance with the technical and programming aspects of this experiment: M. Gravina, H. Hanerfeld, F. Holst, A. Kilert, D. McShurley, G. Oxoby, and W. Walsh. Special thanks to R. Bierce for his skillful handling of the data collected in this experiment.

I would like to thank the following physicists who were an integral part of the experiment and the data analysis: R. Carnegie, S. Durkin, P. Estabrooks, T. Fieguth, R. Hemingway, D. Hutchinson, W. Johnson, P. Kunz, T. Lasinski, D.W.G.S. Leith, R. McKee, W. Meyer, G. Oakham, B. Ratcliff, S. Shapiro, S. Suzuki, and J. Va'vra.

I am grateful to the members of my thesis reading and oral exam committees: Profs. D.W.G.S. Leith, R. Blankenbecler, A. Litke, and R. Hollebeek.

I would like to thank Dr. Blair Ratcliff for many enlightening discussions and for his assistance in the physics analysis. I am also very grateful to my advisor, Prof. David Leith, for the guidance, assistance, and encouragement he provided throughout my years as a graduate student at Stanford. Finally, I am indebted to my friend and colleague, Stan Durkin, who shared equally in the hard work that went into the greater part of this physics analysis.

TABLE OF CONTENTS

LIST OF TABLES

LIST OF FIGURES

Chapter I

INTRODUCTION

Over the past ten years, experimental results, especially those involving the charmonium spectrum, have clearly demonstrated the success of the quark model in explaining the basic structure of meson spectroscopy. However, only in the last few years has substantial progress been made in observing the expected strange meson states (see [1] for reviews of this subject). One of the primary goals of this experiment was to study the meson systems containing one or more strange quarks (or antiquarks). This would hopefully lead to the discovery of more of the states that are expected in the quark model meson spectra. In addition to identification of expected quark model states, accurate mass measurements would enable the calculation of mass splittings between radial states, between orbital states, and between states split by spin-orbit interactions. These mass splittings contain much information about quark forces; in fact the splittings would provide a rigorous test of potential theoretical models of mesons.

The usual SU(3) model of the light quark mesons (the heavier charmed and bottom quark mesons will not be discussed here) involves the $3 \otimes \bar{3} = 8 \oplus 1$ representation, i.e., a nonet of $q\bar{q}$ states composed of an octet and a singlet. A common way of classifying the states in this nonet is by the isospin quantum number. In this nonet there are three I=1 states ($u\bar{d}$, $\bar{u}d$, $[u\bar{u}-d\bar{d}]/\sqrt{2}$), two I=0 states (the $[u\bar{u}+d\bar{d}-2s\bar{s}]/\sqrt{6}$ octet

member and the $[u\bar{u}+d\bar{d}+s\bar{s}]/\sqrt{3}$ singlet member), and four I=1/2 states ($s\bar{u}$, $s\bar{d}$, $\bar{s}u$, $\bar{s}d$). Due to the near degeneracy of u and d quark masses, the four meson states with I=1/2 are nearly identical in mass and are therefore often considered to be one state in terms of mass (the same is true for the three I=0 states). A typical schematic of the $q\bar{q}$ model is given in fig. 1 along with the quantum numbers expected for such a system.

A convenient way to represent the expected states for the $q\bar{q}$ system, loosely based on a simple harmonic oscillator potential, is shown in fig. 2. The states are categorized by I, J^{PC}, L (total $q\bar{q}$ system angular momentum), and n (radial quantum number) and are plotted as a function of mass squared, M^2. The eight boxes in the n=0, L=0 group represent the S=0 and S=1 $q\bar{q}$ system total spin states which give rise to the four pseudoscalar ($J^P=0^-$) and four vector ($J^P=1^-$) meson states. For L>0, spin-orbit (L·S) splittings allow a triplet of J^P states for S=1 and thus with the singlet for S=0 there are a total of four sets of four states. Results from the charmonium spectrum imply the existence of radially excited states and recent results have confirmed the existence of such states for the light quark mesons. The series of boxes to the right of the primary series represent the first radially excited states (n=2).

In fig. 2 the light quark meson states observed prior to this analysis are denoted by the labelled boxes. These include well established states as well as those needing confirmation. Clearly the upper row of boxes in each group are the best established states. These states are known as the leading natural spin-parity resonances (leading

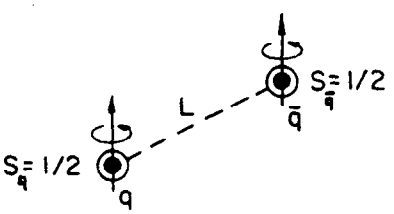

$$J = L + S$$
$$P = (-1)^{L+1}$$
$$C = (-1)^{L+S}$$
$$G = (-1)^{L+S-I}$$

10-80
3942A57

Figure 1 -- The $q\bar{q}$ meson system and its quantum numbers. Parity (P), charge conjugation (C), and G parity are determined by the angular momentum (L), total spin (S), and total isospin (I) of the $q\bar{q}$ system.

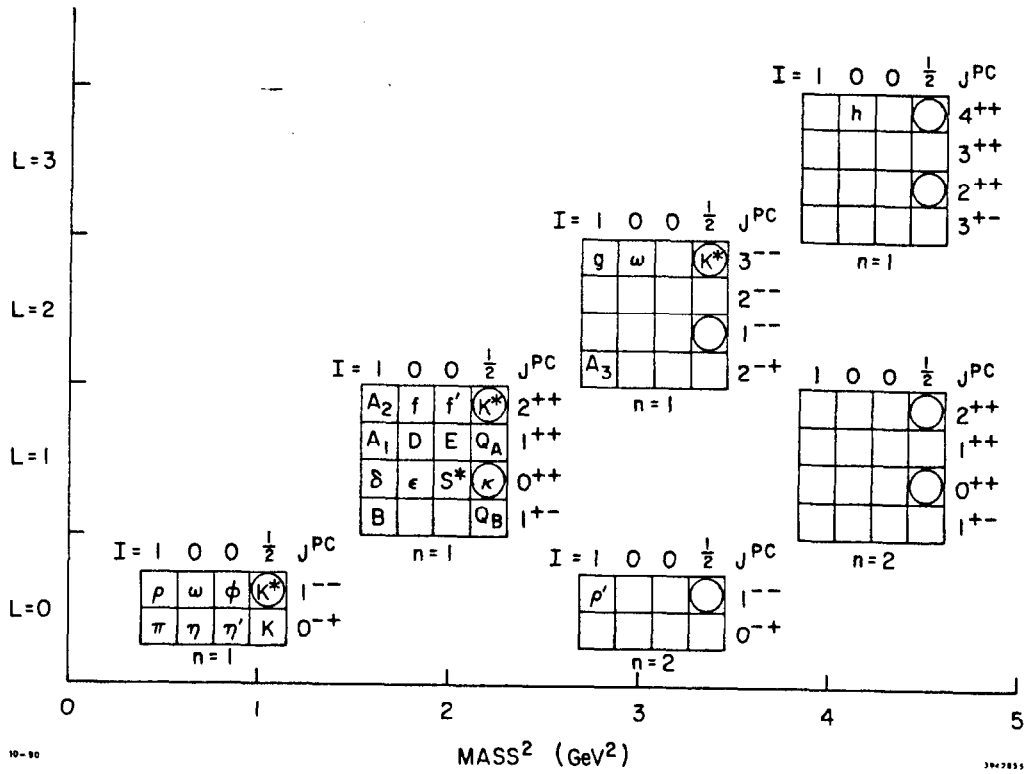

Figure 2 -- Light quark meson spectrum prior to this analysis. Circled states are those accessible to this analysis.

means the lowest mass for a given J^P assignment, natural means $P=(-1)^J$; unnatural is therefore $P=(-1)^{J+1}$). Although the status of the light quark meson spectrum is much improved from what existed even five years ago, there are still many states that need to be observed or confirmed.

The analysis to be presented in this paper concerns the specific reaction $K^-p\rightarrow K^-\pi^+n$. In particular, the $K^-\pi^+$ elastic scattering angular distribution is studied yielding the resonance structure of the $K^-\pi^+$ system. The $K^-\pi^+$ system has $I=1/2$ and the 2 body decay of the system imposes a restriction on the allowed J^P of the resonant state due to parity conservation. This restriction implies only natural spin-parity states are allowed, i.e., 0^+, 1^-, 2^+, etc. The quark content of the $(K^-\pi^+)$ state is $s\bar{d}$. Thus, the results from this analysis can only lead to information for the $q\bar{q}$ states inscribed by circles in fig. 2.

In order to obtain the spin-parity as well as the mass, width, and other parameters of resonant structures, it is necessary to have adequate decay angular distribution information for the $K\pi$ state. In general, this requires a large amount of data taken in a wide kinematical region. In the past, it was often the case that experiments were able to obtain large data samples with limited acceptance (e.g. forward spectrometers) or small data samples with good overall acceptance (e.g. bubble chambers). Recently, a new series of spectrometers have been built that combine good acceptance with high statistics data taking capability (e.g., MPS, OMEGA, LASS [3]) and thus have opened the door to the more difficult to measure resonances. From November 1977 to June 1978, an experiment was run on one of these new spectrometers, the LASS spectrometer at the Stanford Linear Accelerator

Center (SLAC). The data obtained in this experiment was the basis for the physics analysis to be presented. What follows is a brief overview of the process which produced the physics results from the raw experimental data.

The experiment was a collaborative effort of Experimental Group B at SLAC and Carleton University of Canada [4]. The eight months of data taking resulted in approximately 42 million K^-p inelastic events written to magnetic tapes. The data obtained in this experiment contained a large variety of final states. During the time that the multi-particle event analysis programs were being developed and tuned up, the decision was made to proceed with the $K\pi$ two body physics analysis. To this end a software filter (off-line trigger) was developed which effectively selected low multiplicity events. The processing of this selected sample was performed separately from the processing of the complete (unfiltered) event sample. The data processing chain consisted of the off-line selection of the low multiplicity sample, event reconstruction, topology selection, and kinematic selection. The end result was a $K^-\pi^+n$ data sample that was uncorrected for spectrometer acceptance.

Since meson resonances were the goal of this physics analysis, the study of the production of strange meson resonant states decaying into $K^-\pi^+$ was of primary interest. In order to unravel the complicated effects of numerous resonances with differing spins, a systematic study of the $K^-\pi^+$ decay angular distribution was necessary. However, because the acceptance of the spectrometer was not perfectly uniform, it was necessary to understand the spectrometer acceptance in detail, so that the produced $K^-\pi^+$ angular distribution could be extracted from the

experimentally observed angular distribution. Determination of the spectrometer acceptance involved the creation of an elaborate Monte Carlo event simulation program. This program was used to generate a high statistics sample of Monte Carlo events that was then used to properly correct the data for spectrometer acceptance.

Another computer program was used to calculate the acceptance corrected moments of the $K^-\pi^+$ elastic scattering angular distribution. These moments provided much insight into the resonance structure in $K\pi$ scattering but the nature of the resonance structure made it possible to investigate only the leading resonances. In order to extract a maximum of information about $K\pi$ resonances, it was necessary to perform a 2-body partial wave analysis (PWA) on the data. The PWA was an energy independent PWA, which means that it produced the $K\pi$ elastic scattering partial wave amplitudes as a function of $K\pi$ mass. From these amplitudes it was possible to immediately obtain the mass, width, and spin information for the $K\pi$ resonances.

It should be noted that a previous experiment which also involved Group B at SLAC, performed a similar analysis for the reaction $K^-p \rightarrow K^-\pi^+n$ at 13 GeV/c (that analysis included several other reactions as well, see ref. [5]). Many of the methods and computer programs developed for that previous experiment were used as a starting point for the moments analysis and partial wave analysis to be presented here.

The contents of the chapters to follow include the experimental considerations, the analytical methods, and the results of the analyses. In specific, chapter II will describe the experimental apparatus. The experimental trigger and other electronics will be discussed in

chapter III followed by a summary of the event reconstruction procedure in chapter IV. Chapter V will contain a description of the kinematics of the $K^-p \to K^-\pi^+n$ reaction, a synopsis of the data processing sequence, and a discussion of the uncorrected (for acceptance) $K^-\pi^+n$ data sample. The topics of resolution, backgrounds, and normalization will be presented in chapter VI. Chapter VII covers the method used to obtain the moments of the $K\pi$ scattering angular distribution and the results obtained in that moments analysis. A short discussion of the resonance interpretation of the moments will also be included in chapter VII. In chapter VIII, the partial wave analysis procedure will be described in detail. Also in this chapter, the results of the PWA will be presented and discussed. Finally, in chapter IX, the results of the analysis will be summarized and compared with existing results, and then will be interpreted in terms of the quark model. The remainder of the last chapter will be a discussion of the present status of the leading strange meson resonances and the spin-orbit splittings predicted by the quark model.

Chapter II

EXPERIMENTAL APPARATUS

A. The Experiment

This study was performed on data taken with the Large Aperture Solenoidal Spectrometer (LASS) facility at SLAC. The experiment was performed using an 11 GeV/c negative kaon beam incident on a liquid hydrogen target. The trigger was designed to accept events with greater than or equal to two charged tracks which was essentially the total inelastic cross-section ($\sigma_{trigger} \sim 17$ mb). For this study, the events likely to be from the reaction $K^-p \rightarrow K^-\pi^+n$ were selected offline from the 42 million good events written to tape. What follows is a brief overview of the spectrometer and then a more detailed description of each of the important sections of the experimental apparatus.

B. Overview of the Spectrometer

A schematic diagram of the spectrometer is shown in fig. 3. The coordinate system used in the experiment was defined as follows; the positive z direction was defined as the beam travel direction; the positive y direction was defined as normal to the earth's surface pointing upward and the x direction then defined to obtain a right handed coordinate system. The terms upstream and downstream will often

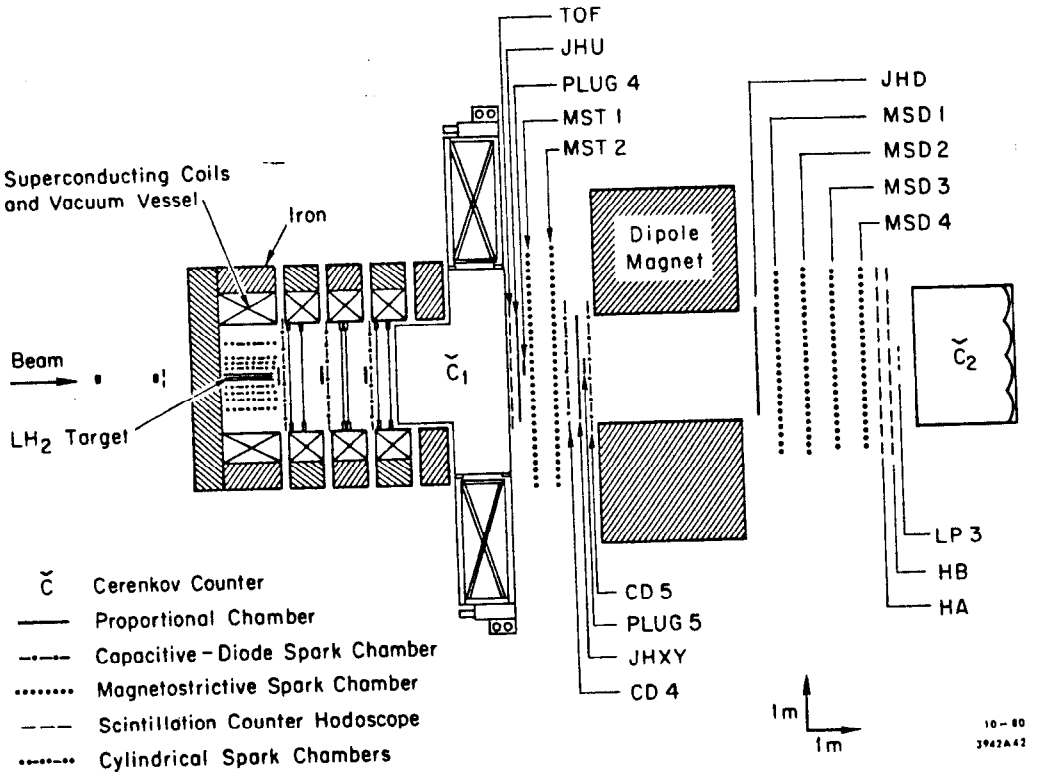

Figure 3 -- Plan view of the LASS spectrometer.

be used and will denote direction with respect to the beam travel direction.

The beam traversed momentum, position, particle identification, and timing measurement devices before passing through a hole in the flux return mirror (endcap) of the solenoid magnet where it entered the 91.6 cm long liquid hydrogen target. The beam and target were centered on the axis of the superconducting solenoidal magnet which provided a uniform 23 kilogauss magnetic field whose direction was parallel to the z axis. Thus charged particles produced in the target described helical trajectories within the solenoid magnet volume. The trajectories of particles emerging from the target at large angles with respect to the beam were measured by the cylindrical chambers which were concentric to the target. The forward going particles were detected in the many sets of planar spark and proportional wire chambers located just downstream of the target but still within the solenoid magnet volume. A plan view of the solenoid magnet region detection devices can be seen in fig. 4.

Particles with large longitudinal momentum emerged from the downstream end of the solenoid magnet and entered what was termed the "twixt" region (the 3 meter long region between the solenoid and dipole magnets). Covering the downstream end of the magnet volume was a multi-cell threshold atmospheric Cerenkov counter (C1) used for K-π separation. Just following the C1 counter was an array of 28 time of flight scintillation counters (TOF) with a combined detection area of circular shape. The TOF counters were designed to obtain (in conjunction with the C1 counter) p-K-π separation at low to moderate momenta. The remainder of the twixt region contained planar spark and proportional

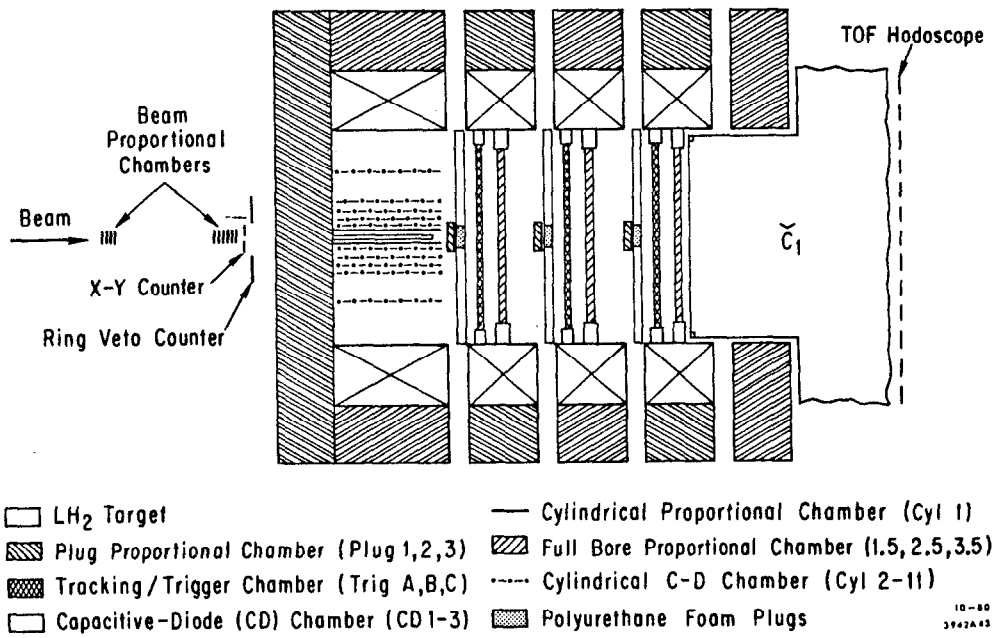

Figure 4 -- Detail of the solenoid magnet region detection devices.

chambers which were used to reconstruct the trajectories of particles that passed through the dipole magnet aperture.

The dipole magnet provided a magnetic field parallel to the y axis which caused bending in the horizontal plane. The magnet was run at maximum current which resulted in a field integral $\int B \cdot dl$ of 30 kilogauss-meters. The detection region after the magnet was known as the "downstream" region, containing a proportional wire chamber hodoscope, four spark chambers, and two planes of scintillation counter hodoscope arrays. The spark chambers and hodoscopes provided track reconstruction information for the downstream segment of particle tracks that crossed the dipole magnet gap. Just after the scintillation counter arrays was a small scintillation counter used to veto non-interacting beam particles. The last detector in the spectrometer was the 8 cell pressurized threshold Cerenkov counter (C2) used for K-π separation at higher momenta.

The solenoid magnet and its associated detection devices provided good momentum measurement for low momentum and large angle outgoing charged particles. Momentum measurement for fast forward tracks was usually not possible in the solenoid magnet. However, such fast forward tracks were very likely to pass through the dipole magnet aperture where their momentum could be accurately measured. Although the particle identification devices C1 and C2 were an important part of the experiment, their information was not required in this analysis and these devices will not be described in detail in this thesis. Time of flight information from the TOF counter array was also not used but the array was used as part of the event trigger and as a hodoscope device

for signaling in-time tracks. Particle identification was not used since the $K^-\pi^+n$ final state dominated the sample of events with two outgoing oppositely charged particles and later kinematical selection by software allowed almost complete suppression of non-$K^-\pi^+n$ backgrounds.

C. The Beam System

The beamline [6] for this experiment transported 11 GeV/c negative kaons to the LASS spectrometer at SLAC. Table 1 summarizes some of the important characteristics of the beam used in this experiment. The primary 21 GeV/c electron beam at SLAC was steered onto a beryllium target which produced a large flux of secondary particles. The flux produced at ~1° from the forward direction was focussed and directed by the beamline 20-21 transport system as shown in fig. 5. The magnets in this transport system were set to deliver an 11 GeV/c negatively charged beam. An RF separator system provided good particle type separation. For our experiment, the RF system was tuned to deliver a maximum K/π ratio which resulted in less than 5% pion contamination. The contamination from anti-protons, electrons, and other particles was negligable.

An array of scintillation counters, called the P-hodoscope, was situated at a dispersed focus of the beamline and provided a momentum measurement for beam particles with a resolution of 0.40% for dP/P. The total beam momentum dispersion was ~±1.5%. Two pressurized threshold Cerenkov counters, C_π and C_k, provided beam particle identification. All beam device and spectrometer timing was done with respect to the signal from the SE scintillation counter located just at the point where the

TABLE 1

Beam Parameters

Primary electron beam momentum	21 GeV/c
Primary production target	0.22 r.l. Cu 0.85 r.l. Be
Secondary K^- beam momentum	11 GeV/c
Momentum dispersion (dp/p)	1.5 %
Momentum hodoscope resolution (σ_p/p)	0.35 %
Beam pulse rate	$\lesssim$ 180 Hz
Beam pulse duration	1.6 μs
Number of kaons per beam pulse	~ 2.5
Pion contamination of beam	$<$ 5 %
Radius of beam spot at target	$<$ 0.5 cm

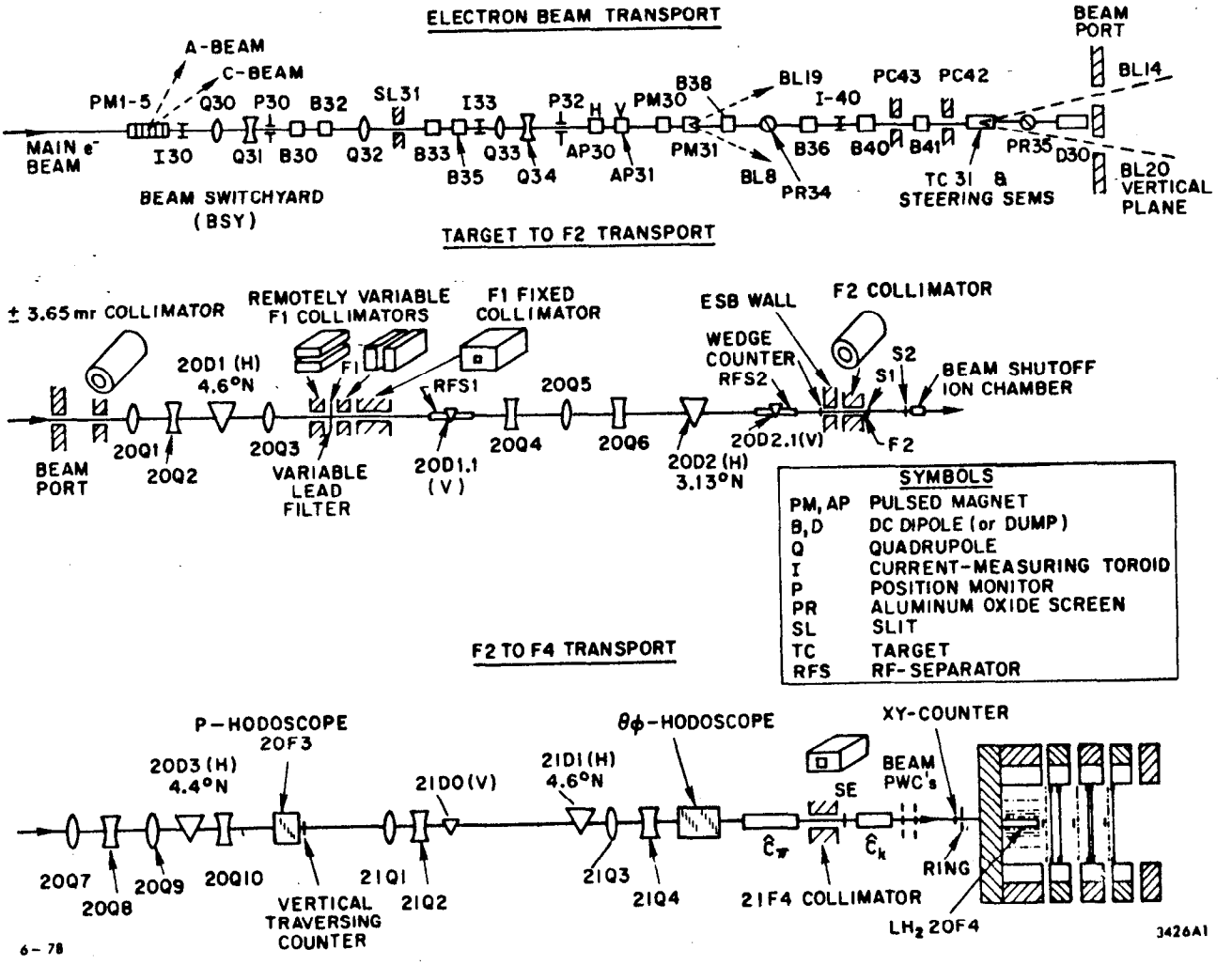

Figure 5 -- The LASS beamline.

beam enters the LASS building some 5 meters upstream of the target. Beam particle position and direction was obtained with the two proportional wire chambers (beam PWCs) and the θ and ϕ scintillation counter hodoscope arrays. The two beam PWCs were located at ~1 and at ~2 meters upstream of the target and each contained respectively, 5 and 4 planes of wires with 1 mm spacing (in all, there were 3 vertical planes, 3 horizontal planes and 3 planes rotated 45° from vertical; see fig. 8). The θ and ϕ conters were located ~14 meters upstream of the target and provided additional position information as well as better time resolution than the beam PWCs. The XY and RING conters located just upstream of the target provided position monitoring, doubles rejection, timing, and beam halo vetoing information.

Optimum beam steering resulted in a beam spot size of approximately 5 mm radius measured at F4, the final focus which was located at the downstream end of the liquid hydrogen target. In regard to time structure, the beam consisted of pulses of particles with a maximum pulse rate of 180 Hz and typical rates of 120 Hz. By adjusting the incident electron current and the collimator controlling the acceptance of the beam, each pulse was made to deliver ~2.5 kaons in a time window of 1.6 μs.

D. The Liquid Hydrogen Target

The target consisted of a cylindrical mylar cell, 91.6 cm long and 5.24 cm in radius containing the liquid hydrogen. The cell was supported by an evacuated aluminum cylinder which was inserted through the

upstream flux return mirror of the solenoid magnet (see fig. 6). The liquid hydrogen was continually cycled from the target to the cryogenic system and back to keep the temperature constant and to avoid boiling. The temperature and pressure of the liquid hydrogen in the target were continually monitored during the experiment so that density calculations could be performed later.

E. The Solenoid and Dipole Magnets

The solenoid magnet consisted of four separate superconducting coils each contained in a steel vessel. This segmentation was necessary to provide the "slots" that were occupied by the detection chambers. Flux return mirrors were located on either end of the solenoid magnet. The inner diameter of the magnet was 185 cm and the inside length along its axis was 420 cm. The magnetic field was uniform to within 1% throughout most of this volume and was measured at 22.4 kilogauss.

The dipole magnet was located some 8 meters downstream of the target and had an aperture of approximately 1 meter by 2 meters (vertical by horizontal) which was centered on the central spectrometer axis. The length of the gap (along the z direction) was nearly two meters and the resulting field integral $\int B \cdot dl$ was 30 kG-m. The field pointed in the negative y direction (down) which bent particles in the horizontal plane. In most cases, only particles with momentum greater than 1.5 GeV/c were able to cross the dipole magnet gap and be measured successfully in the downstream detector system.

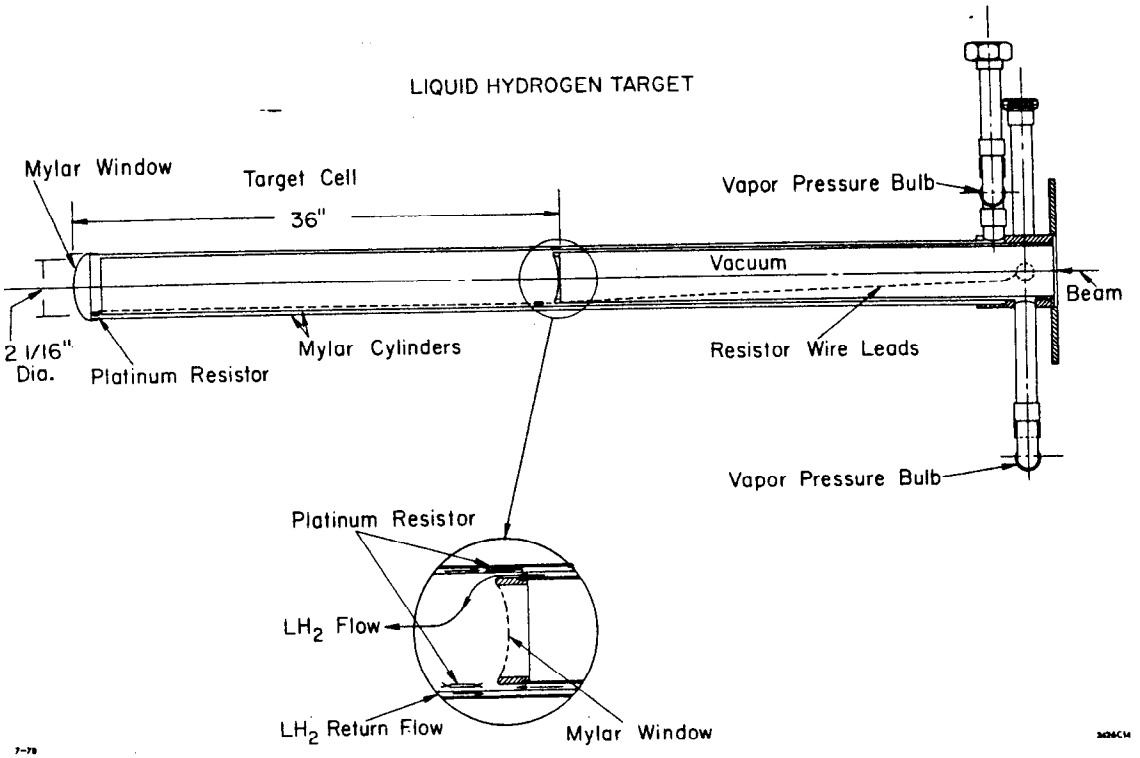

Figure 6 -- The liquid hydrogen target.

F. The Cylindrical Chamber Package

The cylindrical detector system consisted of one proportional wire chamber (the PWC cylinder) and five capacitive-diode (CD) readout spark chambers (the CD cylinders) in concentric cylindrical layers surrounding the hydrogen target. Fig. 7 depicts the important features of this system.

The innermost layer consisted of the PWC cylinder (not shown in fig. 7) containing 160 wires oriented parallel to the beam axis. This provided azimuthal angle coordinates for outgoing tracks with the good time resolution (~50 ns) associated with proportional wire chambers. This good time resolution was important in vetoing out-of-time tracks detected by the cylindrical spark chambers due to their comparitively long memory time (~1 μs). The readout system for the PWC cylinder and for all the other proportional chambers will be described in section G.5 of this chapter.

The 5 CD cylinder chambers each consisted of 3 sets of wires strung on cylindrical molds. One set of wires was strung parallel to the z axis thus providing azimuthal (ϕ) coordinates. The other two sets of wires were strung at angles of +5.7° and -5.7° from parallel, respectively, resulting in helical wire orientations. The readout from these two sets of wires provided ϕ and z coordinates by use of the known stereo angles and a simple coordinate transformation. Thus, the complete cylindrical package supplied 11 ϕ and 5 z coordinate measurements.

The cylindrical spark chambers digitized the spark coordinate by storing the signals from individual wires. Each readout wire was

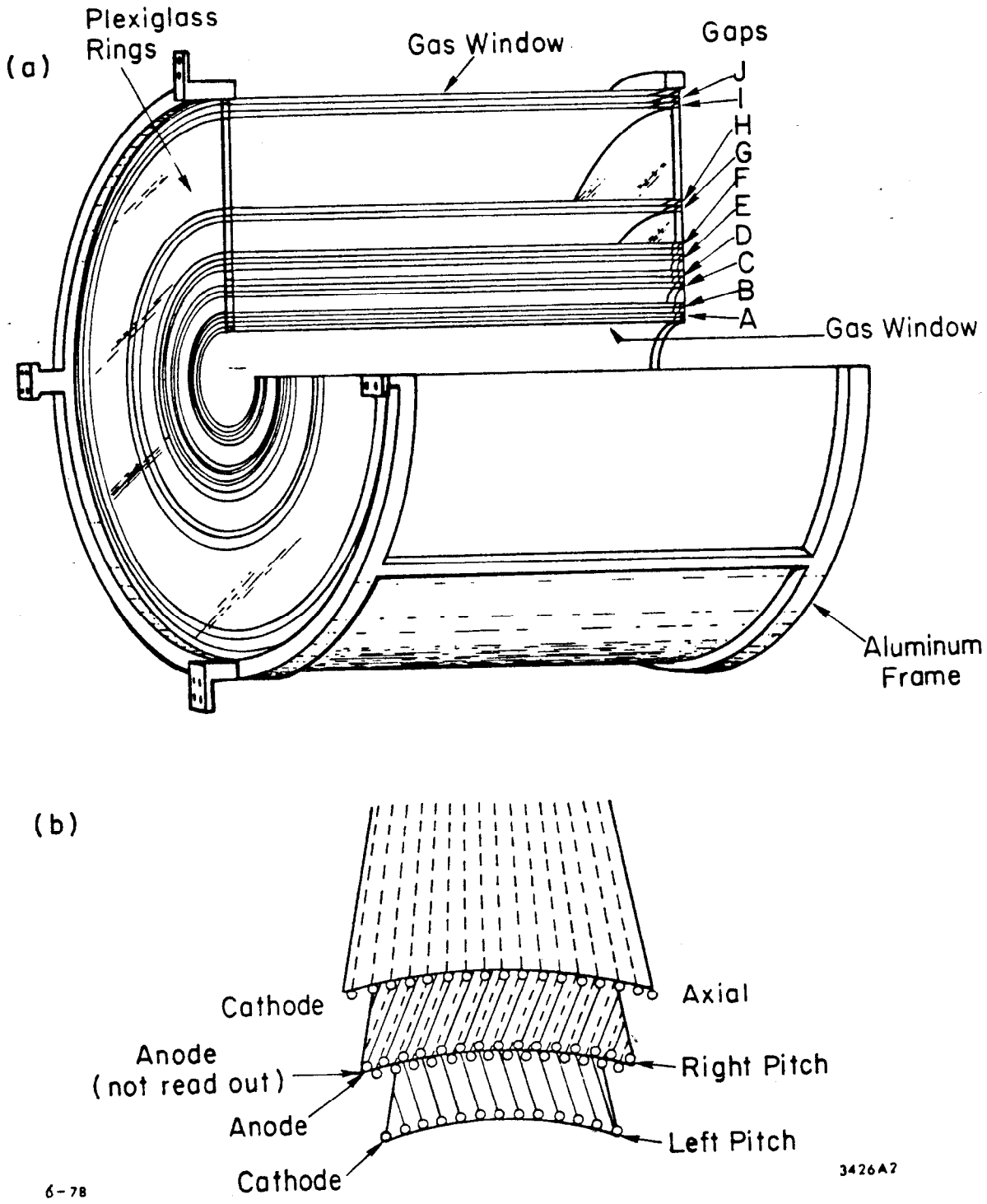

Figure 7 -- The cylindrical chamber package: (a) cut away view of entire package ; (b) detail of wire orientation of each gap

connected to its own local discriminator circuit which would enter a 1 or 0 into its assigned bit in a shift register depending on whether or not the wire had sparked. The shift registers were then strobed into the data acquisition system. A detailed description of the CD cylindrical readout system can be found in ref. [10c].

G. Planar Proportional Wire Chambers

G.1 Plug Chambers (P1 to P5)

Because of the high multiplicity of tracks expected in the forward direction, it was necessary to put a proportional wire chamber with small wire spacing in the region close to the central axis of the solenoid. These chambers, known as the plug chambers (see fig. 8), had an active area of approximately 26 x 26 cm and a wire spacing of 1 mm. Each chamber had 3 sets of wire planes, an X, Y, and E plane whose wire orientations were vertical, horizontal, and rotated 35° from vertical respectively. This provided an x, y, and one corroborating stereo coordinate. The first three plug chambers (P1, P2, and P3) were each mounted adjacent to one of the three CD spark chambers that were located in the first three gaps in the solenoid magnet. Because of the high particle fluxes existing in the region near the central axis, the three CD spark chambers were deadened in a circular region near their centers (the long memory time and poorer spatial resolution of the CD chambers would have lead to large numbers of matchpoint combinations during trackfinding). The plug chambers were designed to completely cover this

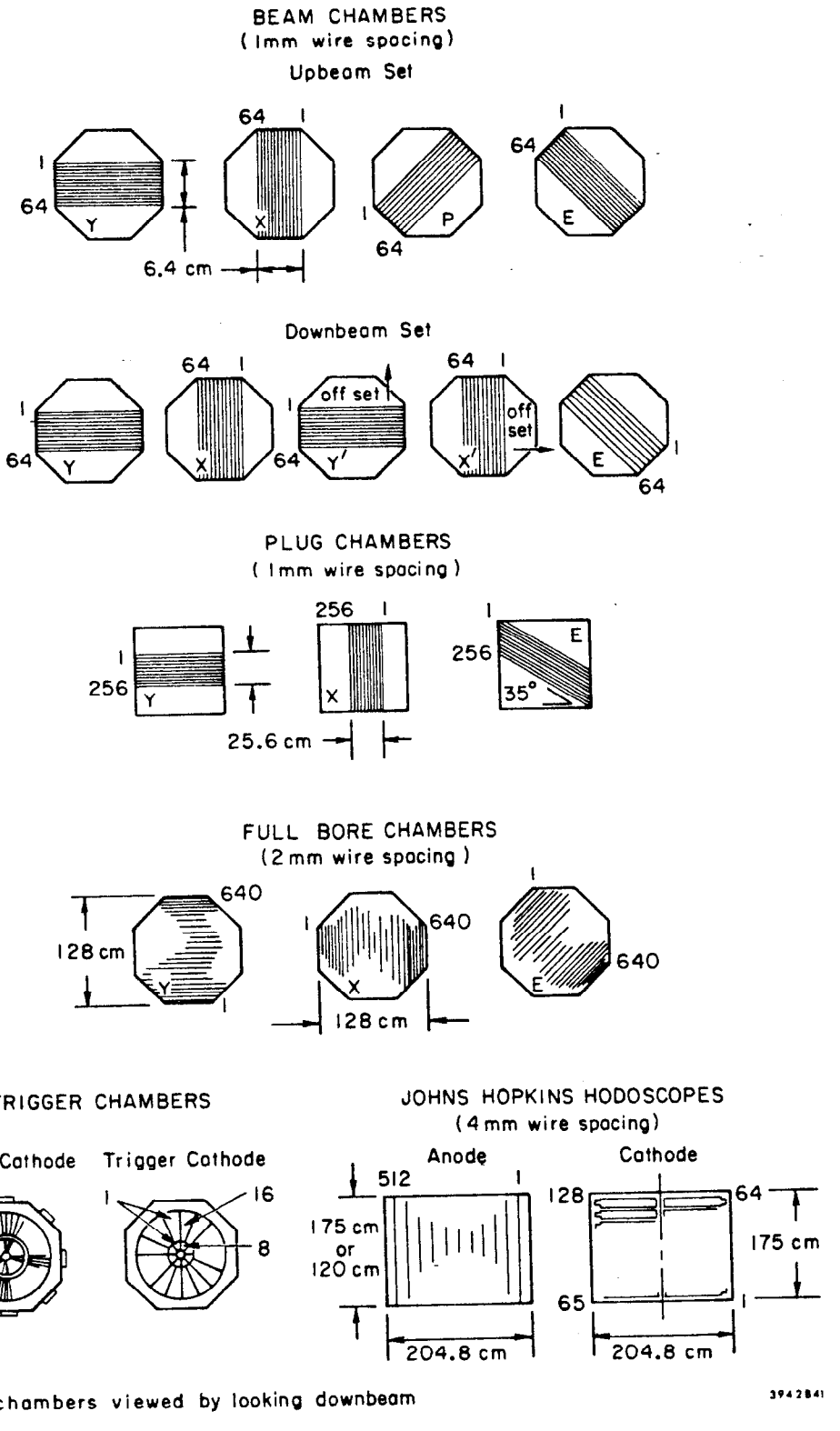

Figure 8 -- The readout planes of the proportional wire chamber (PWC) system.

deadened region and in addition they had a small region of overlap with the CD chamber active region. Thus each of these three plug-CD pairs provided an active detection area which completely covered the inner bore of the solenoid magnet. The fourth plug chamber (P4) was located adjacent to the first magnetostrictive wire spark chamber in the twixt region (MST1). The fifth plug chamber (P5) was mounted next to a CD chamber in the same fashion as the first three plug chambers but this plug-CD pair was located in the twixt region just upstream of the dipole magnet. Both P4 and P5 were centered on the central axis to cover the high flux regions that were also deadened in all of the twixt spark chambers.

G.2 The Full Bore Chambers (1.5,2.5,3.5)

The full bore proportional chambers were located halfway between the four slots in the solenoid magnet. They each consisted of three planes of wire readout, an X, Y, and E plane with wire orientations vertical, horizontal, and 45° from vertical respectively. These chambers had 2 mm wire spacing with a large octagonal active area that nearly covered the bore of the solenoid magnet (see fig. 8).

G.3 The Trigger Chambers (TA,TB,TC)

Adjacent to and just upstream of each of the three full bore chambers was a cathode readout trigger chamber, so named because they were originally designed to provide a fast logic longitudinal and/or

transverse momentum trigger for the spectrometer. In this experiment, however, the trigger chambers were used solely as hodoscopes, i.e., they were used to corroborate a track candidate but were not used for position information. Only the cathode foil "pads" were read out in the trigger chambers, the 4 mm spaced wire anodes merely provided the chamber voltage. The foil pattern consisted of 3 concentric rings each cut into sectors as shown in fig. 8.

G.4 The Johns Hopkins Hodoscopes (JHU,JHXY,JHD)

The three Johns Hopkins hodoscopes (named for the university that constructed them) were large active area proportional wire chambers with 4 mm wire spacing (see fig. 8). Their function was to provide good time resolution coordinate information in the twixt and downstream regions and to assist in track finding. The JHU chamber had only X readout (vertical wires) and was located in the twixt region just downstream of the TOF scintillation counter array. The JHXY counter had X readout wires and horizontal cathode readout strips spaced 2.8 cm apart that provided a coarse y coordinate measurement. It was also located in the twixt region about one meter downstream of the JHU chamber. Both the JHU and JHXY chambers had active areas of 175 cm (vertical) by 200 cm (horizontal) and were used primarily to differentiate between in-time and out-of-time track candidates found by the twixt spark chambers. The JHD chamber was located just downstream of the dipole magnet and had an active area of 120 cm (vertical) by 200 cm (horizontal). This chamber had only an X coordinate readout and was used for in-time track

verification for the downstream track segment of particles crossing the dipole magnet aperture.

G.5 The PWC Readout System

Every wire or cathode pad in the entire proportional wire chamber system (beam, cylinder, plug, full bore, trigger, and JH hodoscope) was electronically connected to an amplifier-discriminator circuit. These circuits were located in racks in the experimental halls and received signals from the chambers by way of specially shielded cable ribbons of up to 15 meters in length. The discriminator output was continually strobed into a 32 bit Random Access Memory (RAM) with a strobe frequency of 40 MHz. When an event occurred, the contents of the RAM for every wire (or pad) in the system was fed into the data acqusistion system. With appropriate timing adjustments, we obtained a time profile (32 time slots each of 25 ns duration) of the signal status for each readout wire or pad. This time profile system was used since the timing differences due to position of detectors, response times in amplifiers, cable lengths, etc., made precise individual wire timing too difficult for such a large system. With the time profile, the appropriate time slots could be easily selected by the offline software. A detailed description of this readout system can be found in ref. [7].

H. The Planar CD Spark Chambers (CD1 to CD5)

There were five planar CD spark chambers of identical construction used in the spectrometer. Three (CD1, CD2, and CD3) were located in the first three gaps in the solenoid magnet, the other two (CD4 and CD5) were located in the twixt region. Each of the planar CD spark chambers consisted of two spark gaps, the XY gap and the EP gap. The XY gap consisted of one plane of vertical (X) and one plane of horizontal (Y) readout wires. The EP gap had their wire planes rotated ±30° to the vertical. The readout wires were actually woven into a insulated wire mesh which was stretched across the chamber frame. Each chamber had a square active area of 160 cm by 160 cm with a 10.8 cm radius styrofoam plug in the center. This plug served to completely deaden the central region of the detector where high multiplicity would create severe matchpoint combination problems for the trackfinding algorithms. As mentioned in section G.1, the plug PWCs were installed adjacent to the CD chambers to do the particle detection in this central region. The planar CD chamber readout system was very similar to the cylindrical CD chamber readout system. Each wire was connected to a capacitive-diode discriminator circuit whose output was strobed into a shift register when an event occurred. The contents of the shift registers were then fed into the data acquisition system.

I. The Magnetostrictive Wire Spark Chambers (MST1, MST2, MSD1 to MSD4)

Because of the effect of the large magnetic field on the proper function of the readout wires, magnetostrictive wire spark chambers (MS chambers) were not used in the solenoid region. However, in the twixt and downstream regions the ambient magnetic fields were sufficiently small to allow proper operation of the MS chambers. The two large (200 cm vertical by 400 cm horizontal active area) MS chambers placed in the twixt region (MST1 and MST2) and the four smaller (150 cm by 300 cm) MS chambers placed in the downstream region (MSD1 to MSD4) each contained two spark gaps. The XY gap had vertical and horizontal planes of active wires while the EP gap had planes oriented at ±30° from the vertical. The central regions of the MS chambers were deadened by having small circular styrofoam plugs (3.8 cm radius for twixt chambers, 7.6 cm for downstream chambers) inserted into the spark gaps. This was necessary because the MS chambers, like the CD chambers, had a long memory time which caused intolerably high multilplicities in the high flux central regions of the chambers. The four downstream MS chambers were shifted horizontally by the appropriate amount to let the non-interacting beam particles that were bent by the dipole magnet pass through the centers of the styrofoam plugs.

The MS readout system consisted of the digitization of the amplified, induced magnetostrictive pulses. In specific, the pulse induced by a chamber spark in the MS wire was detected and amplified. The time delay between a fiducial (reference) pulse and the detected spark pulse gave the spark position measurement (using the speed of

sound in the wire). The MS electronics [8] digitized this time delay for each spark and fed this information into the data acquisition system.

J. Scintillation Counters (TOF, HA, HB, LP3)

There were three major types of scintillation counter systems in LASS (excluding those in the beam system), the time of flight hodoscope array (TOF), the HA and HB hodoscope arrays, and the LP3 lollipop veto counter. The TOF array was designed for identification of particles emerging from the downstream end of the solenoid. Along with Cerenkov counter C1, it provided π-K-p separation for this experiment. Since the data sample used in this analysis did not need particle identification, the TOF array was utilized solely as a highly segmented, good time resolution hodoscope counter. Fig. 9 shows the geometric configuration of the TOF array. The 24 wedge shaped scintillators each subtended 15° of the azimuthal angle about the central spectrometer axis. Along with the 4 quadrant counters which covered the central region near the axis (except for a small 3.8 cm radius beam hole), the total array gave almost complete coverage of the downstream exit of the solenoid magnet (complete TOF description in [9]).

The HA and HB hodoscope arrays were located just after the 4 downstream MS chambers and their dimensions and configuration are shown in fig. 10. Used in conjunction with the JHD hodoscope for out-of-time track rejection, the HA and HB hodoscopes consisted of 42 and 76 individual rectangular scintillation counters respectively. The large active region covered by these two arrays insured full acceptance for

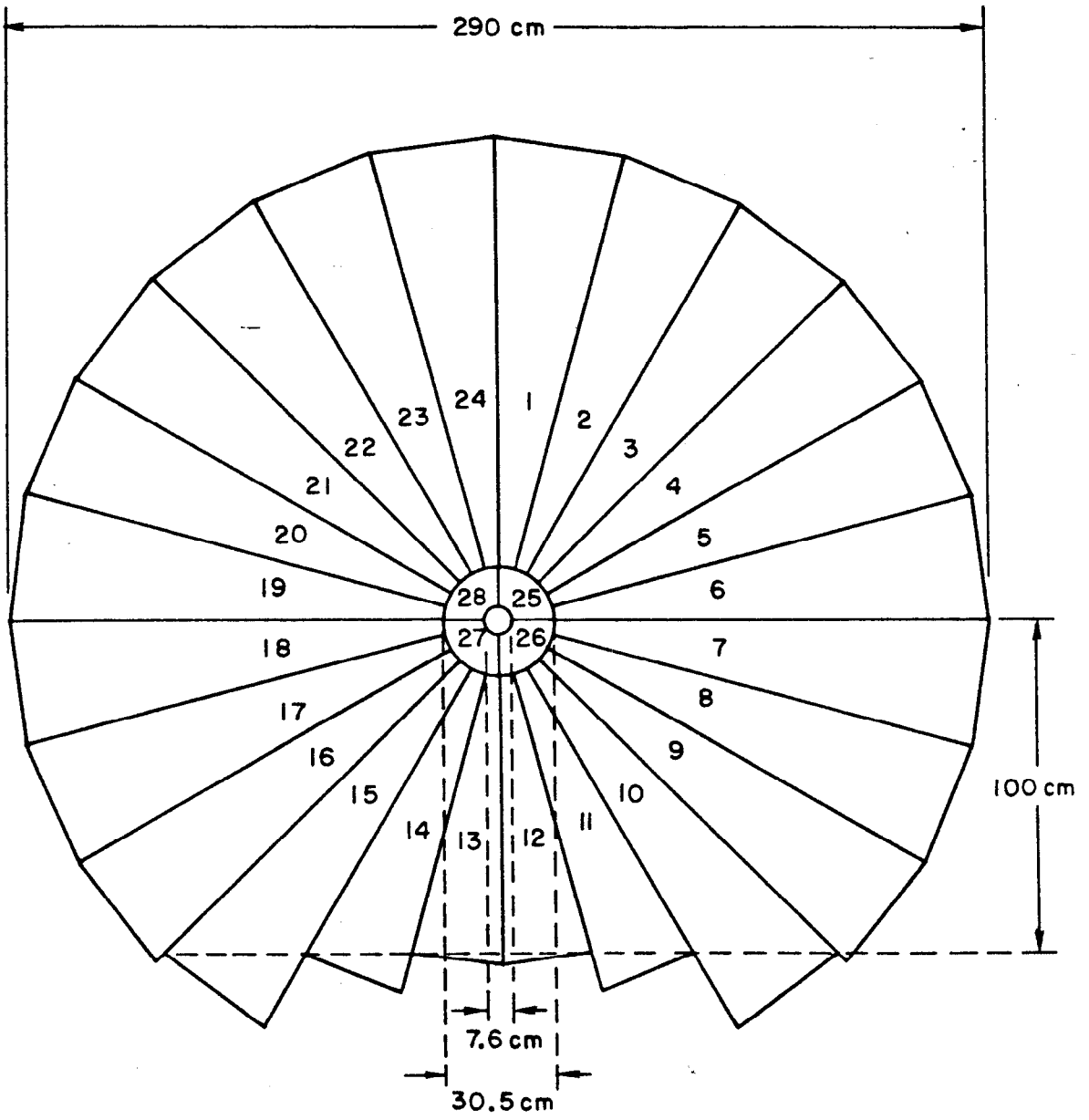

Figure 9 -- The Time-of-flight (TOF) hodoscope array.

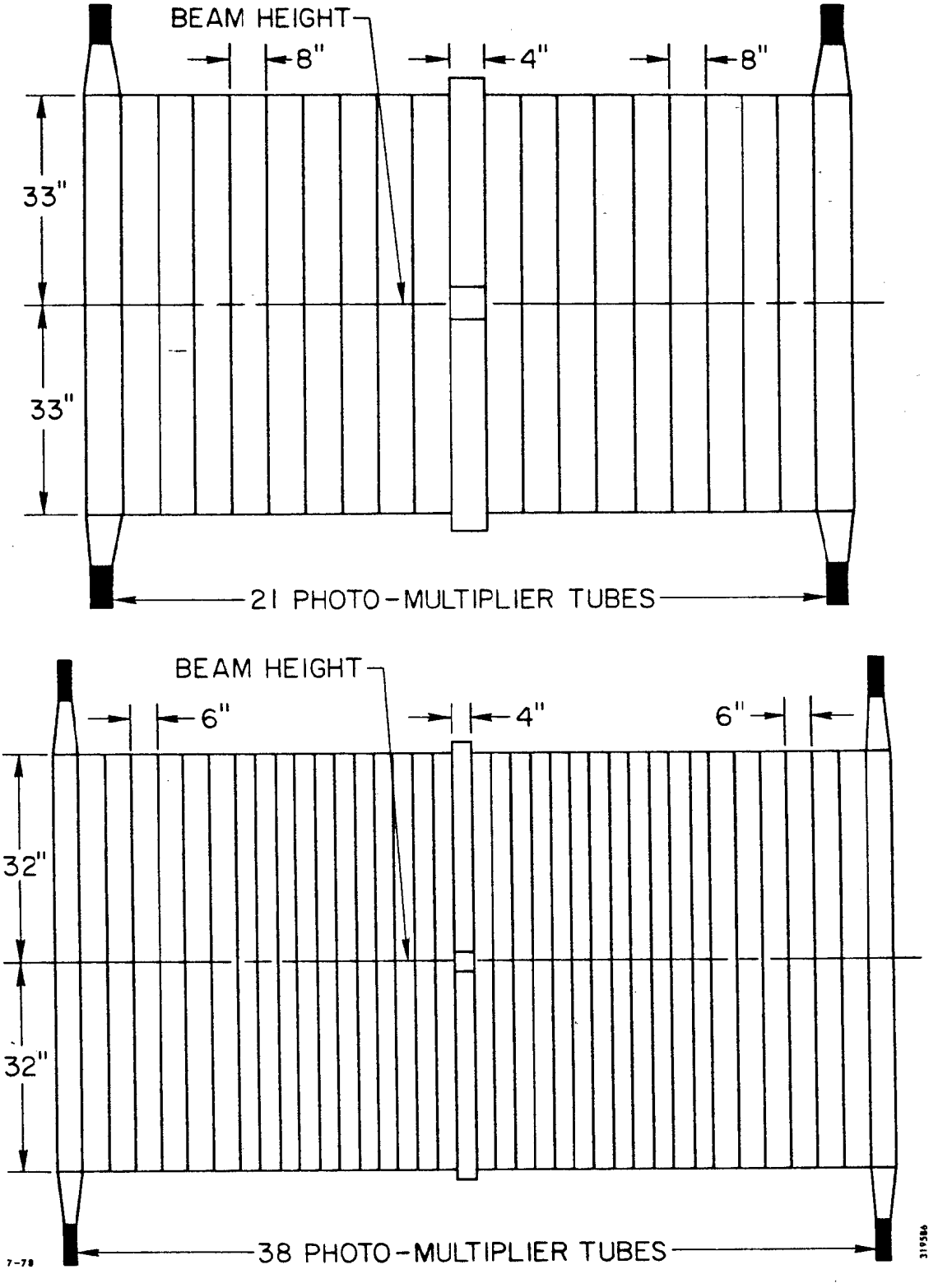

Figure 10 -- The HA and HB scintillation counter hodoscopes. Top is HA; bottom is HB.

downstream tracks. Both HA and HB had small square holes located in the center of the arrays to allow non-interacting beam particles to pass through undetected. Both arrays were shifted (like the downstream MS chambers) so that this beam hole coincided with the position of the (non-interacting) beam.

The LP3 counter was a circular scintillation counter of 9.8 cm radius that was centered on the non-interacting beam spot at a z position just downstream of the HB array. It was used to insure that non-interacting beam particles would not be coincident with an otherwise good event. Due to the short, high flux beam spill, the incidence of two beam particles that are not separable in time with scintillation counters, is not negligable. The LP3 counter vetoed two particle events where one particle interacted and one passed straight through. It also effectively removed events with forward going delta rays produced in the spectrometer.

All the scintillation counters and Cerenkov counters in the spectrometer (this includes beam related counters as well as C1, C2, TOF, HA, HB, and LP3) used standard phototubes and bases. Their output signals were sent to the logic racks where discriminator modules converted the pulses to logic signals. For the particle identification counters, pulse height and timing information was obtained from standard CAMAC ADC and TDC modules. As explained earlier, this information was not used in the analysis to be presented in this thesis. The logic signals were available for use in triggers, for monitoring functions, and for input into the data acquisition system.

K. Device Efficiency, Resolution, and Other Parameters

Summaries of some of the important quantities relating to the various spectrometer detection devices are given in Tables 2-4. Typical efficiency and resolution values were obtained from high statistic tracking studies. Other important quantities pertaining to device operation are given for purposes of comparison and reference. There are a number of excellent references [10] that provide detailed information about the various spectrometer devices. If further information about any of the experimental apparatus mentioned in this chapter is desired, it is suggested that these references be consulted.

TABLE 2

LASS Cylindrical Chamber Device Summary

cylinder number	readout type	cylinder radius†	typical trackfinding efficiency	typical spatial resolution
PWC Cylinder:				
1	ϕ	5.2 cm	98%	0.07 cm
CD Cylinders:				
2	ϕ	10.7 cm	91%	0.10 cm
	Z			0.80 cm
3	ϕ	12.7 cm	96%	0.10 cm
4	ϕ	15.7 cm	92%	0.06 cm
	Z			0.74 cm
5	ϕ	17.8 cm	93%	0.17 cm
6	ϕ	20.8 cm	93%	0.06 cm
	Z			0.71 cm
7	ϕ	22.9 cm	24%	0.12 cm
8	ϕ	31.0 cm	86%	0.13 cm
	Z			0.71 cm
9	ϕ	32.0 cm	87%	0.13 cm
10	ϕ	56.4 cm	70%	0.18 cm
	Z			1.50 cm
11	ϕ	57.4 cm	74%	0.25 cm

† Radii vary but all cylinders are 91.3 cm in length

TABLE 3: LASS Planar Chamber Device Summary

device name	# chambers in system	# planes per chamber	wire spacing	approximate active area (in cm)	typical trackfinding efficiency	typical spatial resolution
PROPORTIONAL WIRE CHAMBERS:						
Beam Chambers	2	4 and 5	1 mm	6.4 x 6.4	99%	0.28 mm
Plug Chambers	5	3	1 mm	25.6 x 25.6	94%	0.28 mm
Full Bore Chambers	3	3	2 mm	128 x 128	95%	0.55 mm
Trigger Chambers	3	2	cathode readout	71 cm radius circle	97%	Not Applicable
JHU	1	1	4 mm	200 x 175	98%	3.0 mm
JHXY (X plane)	1	1 X	4 mm	200 x 175	99%	2.5 mm
(Y plane)		1 Y	28 mm†	200 x 175	84%	8.0 mm
JHD	1	1	4 mm	200 x 120	92%	2.5 mm
SPARK CHAMBERS:						
CD	5	4	0.9 mm	160 x 160	87%	1.2 mm
MS (Twixt)	2	4	0.9 mm	400 x 200	92%	0.9 mm
(Downstream)	4	4	0.9 mm	300 x 150	97%	0.6 mm

† Y plane has 28 mm spaced cathode readout pads

TABLE 4

LASS Scintillation Counter Device Summary

name of device	number of elements	approximate active area	typical track-finding efficiency
Time-of-Flight	28	145 cm rad. circle	99%
HA	42	420 x 166 cm	95%
HB	76	459 x 162 cm	93%
LP3 (veto)	1	9.8 cm rad. circle	Not Applicable

Chapter III

FAST ELECTRONICS AND DATA ACQUISITION

A. Trigger Logic

In this experiment there were four different triggers defined, each of which would cause the spectrometer electronics and data acquisition system to record the event information on magnetic tape. One of the four triggers was the "T0" or main physics trigger, the other three "special" triggers (T2,T3,T4) were for calibration, normalization, monitoring, and other studies. Specifically, T2 was an elastic scattering trigger, T3 was a beam particle trigger, and T4 was a tau decay ($K^- \rightarrow \pi^- \pi^+ \pi^-$) trigger. The T2 and T4 triggered events were used mainly for beam momentum calibration and resolution studies as well as dipole track momentum resolution studies. The T3 triggered events were used for normalization and for studies of the properties of the beam. Due to the high triggering rate for the T2, T3, and T4 triggers it was necessary to trigger the spectrometer only a fraction of the time that the logic for these triggers was satisfied. This was accomplished by use of the Trigger Rate Equalizer module which allowed the experimenters to determine what fraction of the T2, T3, and T4 triggers would actually be used to trigger the spectrometer and the acquisition system. Events triggered by the "special" triggers were sampled concurrently with the T0 triggers to insure that the normalization and other studies would be subject to the

identical conditions (e.g., beam flux, chamber efficiency, etc.) as the physics events.

The T0 physics trigger was not subject to any rate reduction, and except for dead time limitations, a T0 trigger always produced an event trigger (an event trigger was defined as one that triggered the spectrometer devices and readout sequence). The T0 logic was designed to trigger on essentially the total inelastic K^-p cross section. The logic of the T0 trigger consisted of four main parts: 1) the kaon beam logic, 2) the 1.5 PWC cluster logic, 3) the TOF counter logic, and 4) the LP3 veto counter logic.

The beam logic (see fig. 11 for schematic diagram) was designed to produce a logic "yes" signal when one identified kaon was detected in the SE and XY scintillation counters during a beam spill with no other particles within ±32 ns. The logic notation for the kaon beam trigger was:

$$\text{KAON} = (\text{XY}=1) \cdot \overline{\text{RING}} \cdot \text{SE} \cdot C_K \cdot \overline{C_\pi} \qquad \text{(III.1)}$$

The ring counter vetoed the beam halo and the proper C_k-C_π combination insured that the particle was a kaon. It should be noted that the XY=1 logic signal indicated that one and only one of the 4 quadrants in the XY array produced a signal. However, the effects of inefficiency, or more importantly, the effect of two particles passing through the same quadrant at about the same time would also allow the XY=1 logic signal to occur. Therefore, a small percentage of KAON triggers actually permitted two beam particles, an effect that had to be corrected in the normalization calculation (the effect was less than a 3% correction).

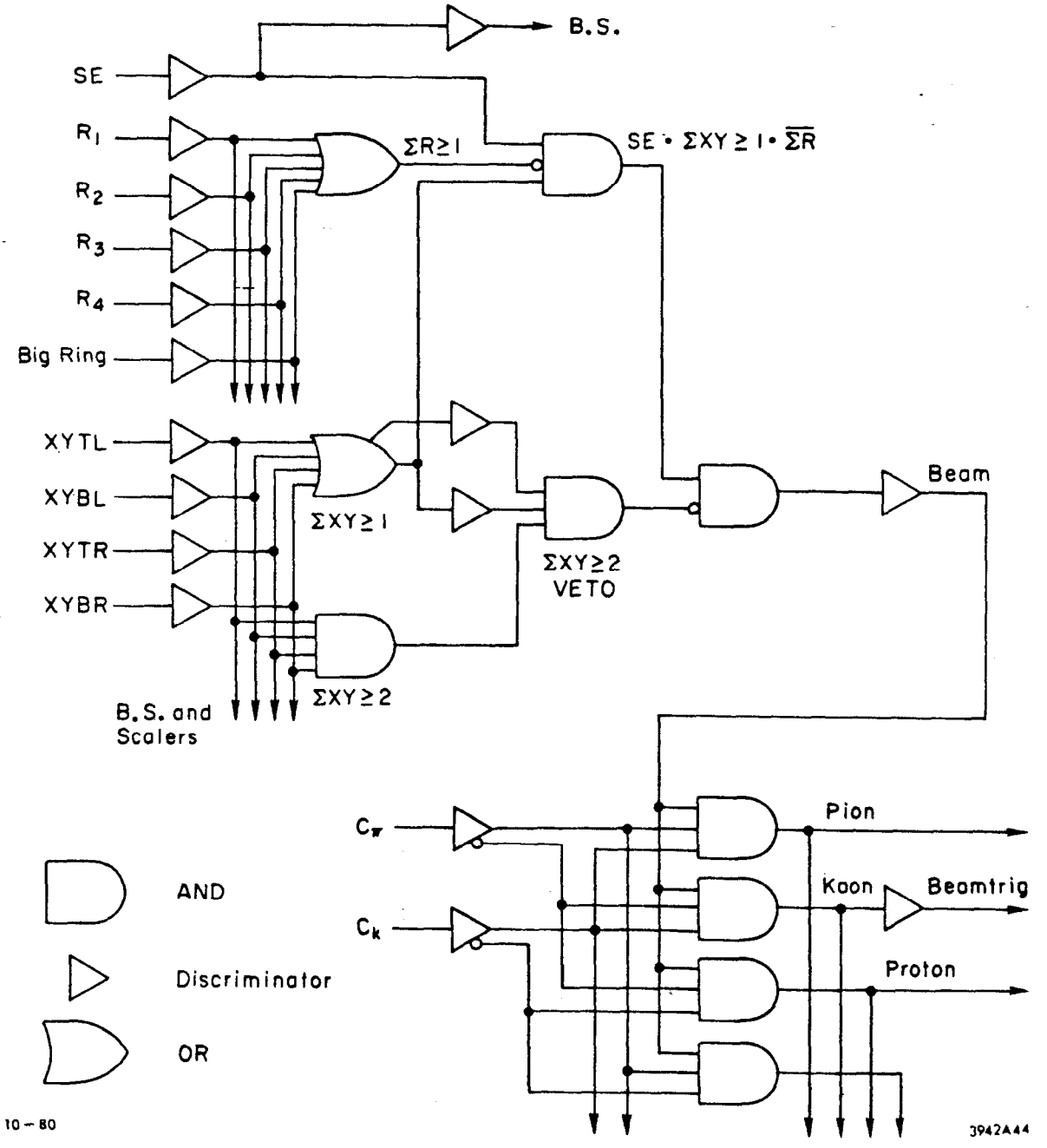

Figure 11 -- The beam logic.

The 1.5 PWC cluster logic consisted of a fast logic circuit that counted the number of "clusters" in each of the 1.5X and 1.5Y proportional wire planes. A "cluster" consisted of one or more consecutive wires that produced signals. Thus, if five consecutive wires fired, it would count as one cluster but if the pattern was two wires on, one off, two on, it would count as two clusters. Additional logic modules required that there be two or more clusters in either 1.5X or 1.5Y. Because the central region of the solenoid (along the beam) contained non-interacting beam particles, small angle elastically scattered beam particles, etc., it was necessary to exclude this region from the cluster sum in order to reduce the rate of undesired events passing the trigger logic. The wires within 1.6 cm of the central axis for the 1.5X and 1.5Y planes were therefore not included in the cluster logic for the trigger (but they were a part of the normal PWC event readout). The net result of the 1.5 PWC cluster logic was to require that two or more charged tracks emerge from the target region with trajectories away from the central axis.

The TOF counter logic was designed to count the number of individual TOF counters (out of a possible 28 counters in the array) that recorded a signal. If one or more counters had signals, the TOF logic would be satisfied. The TOF counters were used in the TO trigger because our Monte Carlo studies showed that in almost all cases, an inelastic K^-p reaction would result in one or more charged particles reaching the TOF array. Although the 1.5 PWC cluster logic did a better job of insuring that two or more charged particles emerge from the target, the much better time resolution of the TOF counters (~15 ns vs

~50 ns) helped prevent out-of-time particles from contributing to the trigger.

The LP3 counter, located at the downstream end of the spectrometer was the final element in the T0 trigger. Its signal was used in veto in order to reject events that might have had a non-interacting beam particle or a forward going delta ray which was in-time with an otherwise good event (this rejection being necessary for normalization reasons and for reducing confusion that might occur in the event reconstruction).

The logic notation for the T0 trigger was summarized as:

$$T0 = KAON \cdot ([\Sigma 1.5x] \geq 2 \text{ OR } [\Sigma 1.5y] \geq 2) \cdot ([\Sigma TOF] \geq 1) \cdot (\overline{LP3}) \qquad \text{(III.2)}$$

The logic diagram for the T0 trigger is shown in fig. 12. The T0 trigger rate (ratio of T0 triggers to KAON beam triggers) during the experiment was 6.8%. The event rate (T0 plus "special" triggers) was 7.7%.

B. The Event Trigger

The event trigger was the signal for the spectrometer devices to read out their respective event information and to transfer the data to a mass storage unit (magnetic tape). The event trigger logic consisted of the output of (T0 OR T2 OR T3 OR T4) logically ANDed with the PDP-11 OK signal (where T2, T3, and T4 above were the Trigger Rate Equalized triggers). The PDP-11 OK signal indicated that the PDP-11/20 data acquisition computer was ready to transfer the event data into its memory. When an event trigger occurred the following actions would be

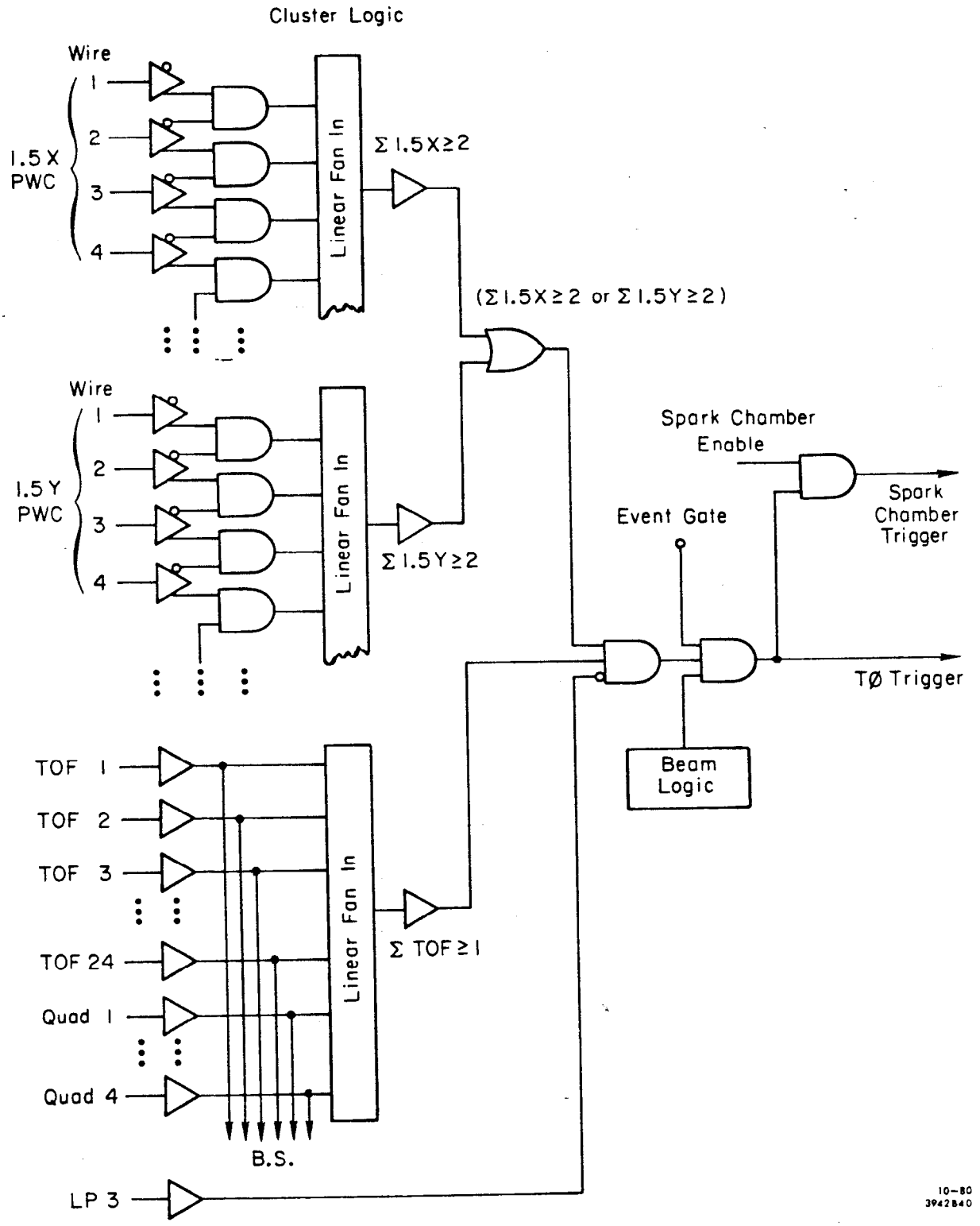

Figure 12 -- The T0 (physics) trigger logic.

initiated: 1) the PDP-11 OK signal would be switched off to block a second event trigger from occurring before it could be handled properly, 2) the scintillation counter system would have its signals strobed into buffers (the buffer strobe modules), 3) the PWC data readout system would gate and transfer its wire signal time slot records, 4) the spark chamber thyratrons would then be triggered to produce the high voltage chamber pulses (if the spark chamber high voltage pulses were delayed until all PWC readout was completed due to the deleterious effect of the spark noise on the PWC readout system), 5) the CD and MS spark chamber readout systems would digitize and store spark position information in their respective data buffers, 6) when all systems indicated that their respective devices had stored all the necessary information in their data buffers, the data buffers would be transferred to the mass storage device, 7) when this transfer was successfully completed, the PDP-11 OK signal would again be switched on and the acquisition system would then be ready to accept another event. The total amount of dead time (time between the event trigger and the time when the system is ready for the next event) was set at 21 ms. The number of beam pulses that occurred during this 21 ms dead time varied from 0 to 3 depending on the beam repetition rate delivered to the LASS beamline.

C. The Scalers and other Run Monitoring Electronics

There were a number of electronic subsystems that monitored the operation of the experimental run. These included the scaler system, the digital voltmeter (DVM) system, and the magnet monitor system. The

scaler system consisted of a large number of scaler modules that kept a running count of various quantities such as numbers of hits in scintillation counters. The signals being scaled were divided into two groups depending on how they were gated. One group of signals was event gated, this meant that the signals were counted during all of the beam spill time except for the time between an event trigger and the end of the readout sequence for that event (i.e., when the PDP-11 OK signal was off, event gated signals were not counted). Event gated quantities such as number of kaons were necessary for calculating the experimental normalization. The other group of scaled signals was run gated, which meant that the signals were counted for the full 1.6 μs beam spill for every beam spill. Run gated quantities were useful in determining absolute rates such as number of beam particles per beam spill. The DVM system monitored the voltages supplied to the phototubes in the scintillation counter system. The voltages were digitized and contiuously stored in buffer memory modules. The magnet monitor system digitized the current supplied to the beamline, solenoid and dipole magnets and stored those values in a buffer memory. All three of these monitor systems were read into the data acquisition system and written to tape on a periodic basis. In addition, all the scalers in the scaler system were reset to zero at the end of every run (a run was approximately 50,000 events and generally lasted one hour).

D. The Data Acquisition System

Figure 13 is a schematic of the overall structure of the data aquisition system. Specifically, all the major spectrometer device readout systems had their data sent to and stored in buffer memory modules when an event trigger occurred. Each readout system was governed by a device controller and each had a DMA (direct memory access) module which it used to gain control of the PDP-11 UNIBUS to transfer the data from its buffer memory to the PDP-11/20 memory. There were six readout systems that transferred data for every event. These included two systems for the CD spark chambers, one for the CD cylinders, one for the PWC system, one for the MS chambers, and one for the buffer strobe, ADC, and TDC system. In addition, there was another device controller with a DMA module that was used to transfer the scaler, DVM, and magnet monitor quantities to the PDP-11/20 memory on a periodic basis. The organization of the interface between the device controller and the PDP-11/20 acquisition computer is shown in fig. 14.

When all the DMA modules finished their data transfers, the PDP-11/20 program proceeded to send the event data (now contained in the PDP-11/20 memory) to the output device (magnetic tape) by way of a series of intermediate devices. The first step was to give control of the UNIBUS to a DMA module that quickly passed the data to an IBM SYS/7 high speed data link which in turn passed the data to a high speed input port of the SLAC computer facility. The SLAC computer facility, located approximately one kilometer from the LASS spectrometer amd control room, consisted of two IBM 370/168 computers and one IBM 360/91 computer (the

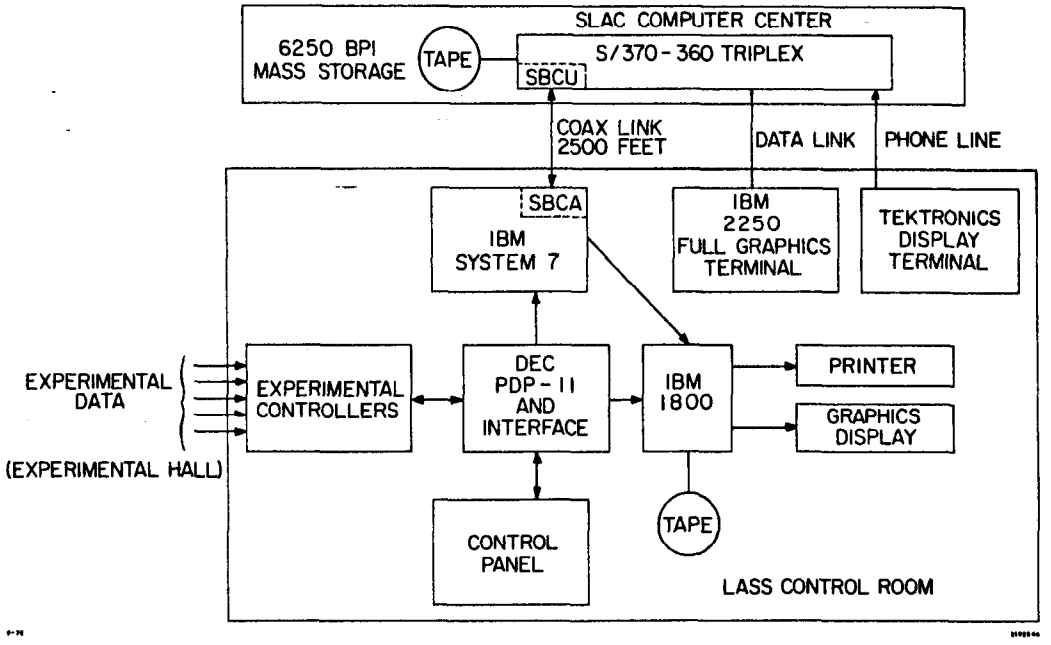

Figure 13 -- Overview of the LASS data acquisition system.

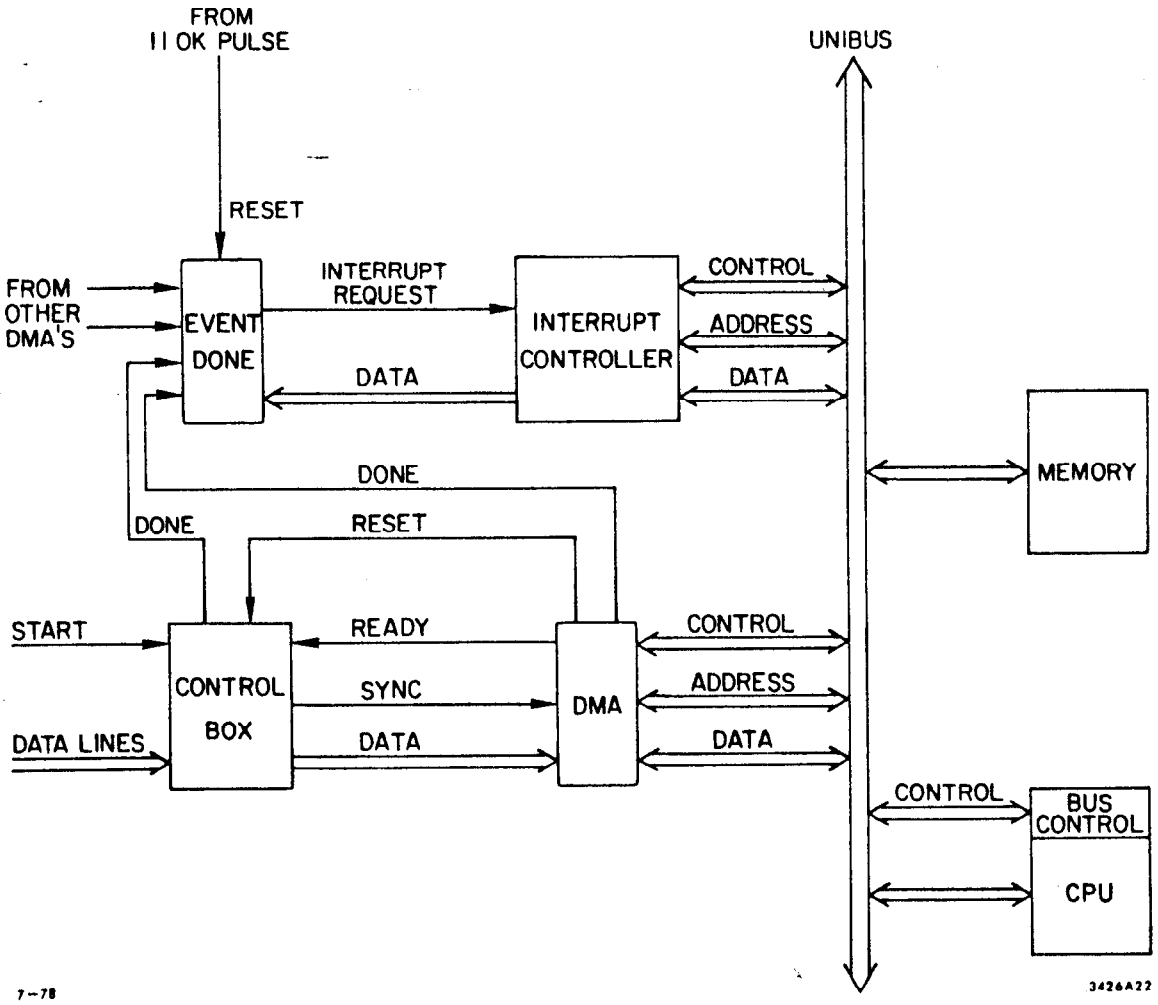

Figure 14 -- A typical device controller interface with the PDP-11/20 data acquisition computer.

Triplex system) which were all interconnected. A resident program in one of the IBM 370 computers received the data and sent it to one of the fast, 6250 bpi density tape drives attached to the Triplex system.

When the Triplex computers were not available, the PDP-11/20 acquisition computer had a backup procedure which utilized an IBM 1800 computer and its associated tape drives located in the LASS control room. The IBM 1800 computer was used only as a backup because it had slower tape drives, used lower density tapes, and provided much fewer on-line monitoring capabilities than the Triplex computers.

The PDP-11/20 data acquisition computer was also interfaced to the main control panel in the LASS control room. The control panel switches were used to start a run, stop a run, change tapes, remove devices from the data acquisition, and other functions handled by the PDP-11/20.

E. The On-Line Computer Monitoring Program

A major reason for using the Triplex system (when it was available) was the powerful software monitoring, event reconstruction, and physics analysis routines which performed limited on-line event processing for use by the experimenters in the LASS control room. These routines were part of the on-line analysis program which utilized a system supplied Realtime Network [11] that communicated with the LASS data acquisition system and with interactive terminals in the LASS control room (see fig. 15). This analysis program had four basic tasks: 1) write the event data coming from the LASS acquisition system to magnetic tape (the Spooler Task in fig. 15), 2) sample events for monitoring, event

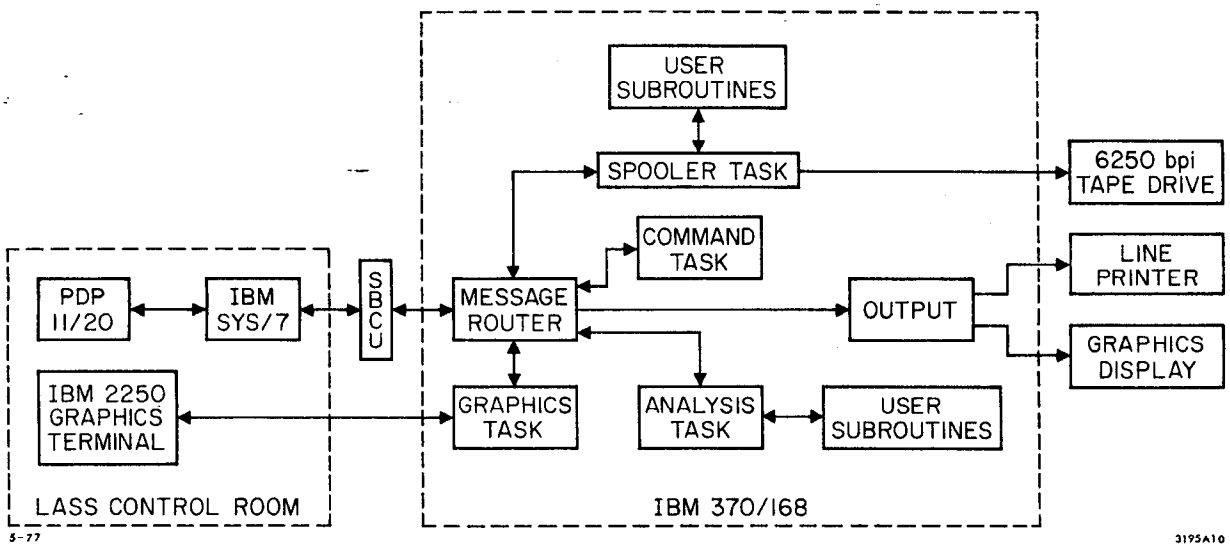

Figure 15 -- The LASS Realtime Network.

reconstruction, and analysis (the Analysis Task), 3) display sampled event data and other monitoring information on the LASS control room graphics terminal (the Graphics Task), and 4) provide additional control of the data acquisition system from the LASS control room computer terminals (the Command Task). The on-line program monitored quantities such as scalers, multiplicities, voltages, etc., which pertained to spectrometer performance. Event reconstruction and physics analysis was attempted on a small fraction of the events in order to monitor the efficiency, resolution, and stability of various devices. This program was able to display event information in numerical or pictoral form using the graphics display scope in the LASS control room. These displays were useful for locating and debugging problems with the hardware devices. Although basic control of the experiment was available at the main control panel, some of the same functions and some different functions pertaining to data aquisition were controllable from the terminals in the LASS control room by way of the on-line program. A final important task performed by the on-line program was providing hard copy output both in the control room (by use of a line printer) and at the SLAC computer center (where both text and graphics hard copy were available).

Chapter IV

EVENT RECONSTRUCTION

A. Overview

The event reconstruction procedure started with the unpacking of the raw event input record and construction of coordinates from the event data. Then a software filter, using only this coordinate information, selected the event sample that was used in this analysis. The next step involved building matchpoint combinations from the coordinate information. Then a complex series of algorithms was used to reconstruct beam tracks, solenoid region tracks, and dipole region tracks. With this information it was possible to do the alignment of the spectrometer devices. The next step was to associate the tracks with a vertex and classify the event in terms of its topology. After selecting the desired topology, a geometric fitting program (MVFIT) was used to determine the best set of track parameters for the event. This fit was based on an iterative chi-squared minimization procedure.

Before describing the event reconstruction procedure outlined above, the coordinate system and a few definitions of variables will be discussed to help clarify some of the track finding problems. The coordinate system used to parametrize all tracks in the spectrometer was the basic right-handed cartesian coordinate system described in the Chapter II overview (the origin was arbitrarily chosen to be located on the

spectrometer central axis at a point just upstream of the hydrogen target). Thus beam tracks, twixt region track segments and downstream track segments were each parametrized by just the five quantities necessary to define a straight line, namely, an intercept (x_0,y_0,z_0) and two slopes (dx/dz and dy/dz). The position of the particle as a function of z coordinate was then given by:

$$x = x_0 + (z-z_0)\, dx/dz$$
$$y = y_0 + (z-z_0)\, dy/dz \qquad \text{(IV.1)}$$

Although there was some residual magnetic field in these regions, the tracks departure from a straight line was usually as small or smaller than the measurement uncertainty of the track.

For the solenoid region (inside the magnet bore), the uniform magnetic field along the z axis caused particle trajectories to describe helices. The same (cartesian) coordinate system was used to reference points on the helical path but the parametrization of the path involved the use of cylindrical coordinates. If the helical path was projected onto the X-Y plane, one would get a cirle since the axis of the helices were parallel to the z axis. The radius of this circle was defined as one of the helix parameters. The azimuthal angle (ϕ_0) measured from the helix axis to the particle at some fixed z position was the second helix parameter. An intercept (x_0,y_0,z_0) provides three more helix parameters and the sixth and final one is the quantity $d\phi/dz$, the change in azimuthal angle with respect to the change in z position. These six quantities $(x_0,y_0,z_0,\phi,R,d\phi/dz)$ parametrized the helical path of a particle in

the solenoid, hence the x and y coordinates of the particle as a function of z position were:

$$x = x_0 + R\,(\cos(\phi_0 + (z-z_0)\,d\phi/dz))$$
$$y = y_0 + R\,(\sin(\phi_0 + (z-z_0)\,d\phi/dz)) \qquad \text{(IV.2)}$$

From Maxwell's equations it was easily shown that if the particle had momentum p and the uniform magnetic field had magnitude B, then the projections of p along the three axes x, y, and z were:

$$p_x = qBR\cos(\phi_0 + (z-z_0)\,d\phi/dz)$$
$$p_y = qBR\sin(\phi_0 + (z-z_0)\,d\phi/dz) \qquad \text{(IV.3)}$$
$$p_z = qB/(d\phi/dz)$$

where: $q = 2.998 \times 10^{-4}$ GeV/(kG-cm)

Thus a measurement of R and $d\phi/dz$ along with the knowledge of the track position in space at some z was sufficient information for specifying the particles position and momentum vector at any point along its helical path. Therefore the goal of the solenoid track finding algorithms was to measure the six parameters $(x_0, y_0, z_0, \phi, R, d\phi/dz)$ that uniquely defined a particle track.

B. Coordinate Construction

The coordinate information from the raw data tapes came in three basic forms. The PWC information consisted of a time slot profile for

each wire in the system that had a signal for that event. The CD spark chamber information was simply a sequence of wire numbers that fired for that event. The MS spark chamber information consisted of delay times between fiducial (reference) pulses and the spark pulses. Using a time slot mask, the PWC time slot profile was reduced to a yes-no determination (a study of PWC timing resulted in a table of "in-time" slots for each wire; if no signal occurred in the "in-time" slots for a given wire, a "no" determination was made). The wires determined to have signals were converted to distances (measured from the end of the wire plane) by using the wire spacing and wire number information. For the CD wires, the spacing and wire number also gave a distance measurement but this had an additional correction applied due to non-linearities in the wire cloth planes. For both PWC and CD wires, a clustering algorithm was employed to group together adjacent firing wires into a single coordinate. Studies were made to set the allowed maximum size of clusters for given chambers. The MS delay time information was converted to distance measurements by using the calculated speed of sound in the MS wires. For X and Y readout planes these distances were quickly converted to x and y coordinates by adding or subtracting the plane offsets determined in the alignment procedure (section 6 this chapter). For E and P readout planes, the number that was calculated and stored was the coordinate one would get if one rotated the E (or P) to be like an X plane and then followed the procedure for the X plane. For the cylindrical chambers, wire number information was converted into either ϕ (azimuthal) angle (for wires parallel to the z axis) or converted into (ϕ,z) pairs (for the stereo pair cylinders) using wire spacing, cylinder radius, and

crossing angle information. The scintillation counter system merely required storing a 1 or 0 for each counter depending on whether or not it recorded a signal for the event.

C. The Software Filter

It was determined that a study of events with low charge multiplicity could be accomplished relatively quickly if such events could be identified without a large amount of computing. It turned out that a simple multiplicity requirement on some of the PWC devices would reduce the data sample to 10% of original size, but leave ~80% of all good reconstructable two charged prong events in the selected data sample. Specifically, this multiplicity requirement, known as the software filter, consisted of the logic shown in fig. 16.

A study was made to compare the two prong events from this software filter sample with the full data sample. The results indicated that there was no substantial difference between the two sets of two prong events in terms of geometrical and kinematical distributions. The 20% of the good two prong events that did not pass the software filter usually failed due to showering, delta ray production, and other high multiplicity effects that were coincident with the good two prong event. The data sample obtained using this software filter was the sample used for the $K\pi$ scattering analysis to be discussed. The software filter made it possible to obtain this data sample nearly two years before the full multi-particle data sample was completely processed.

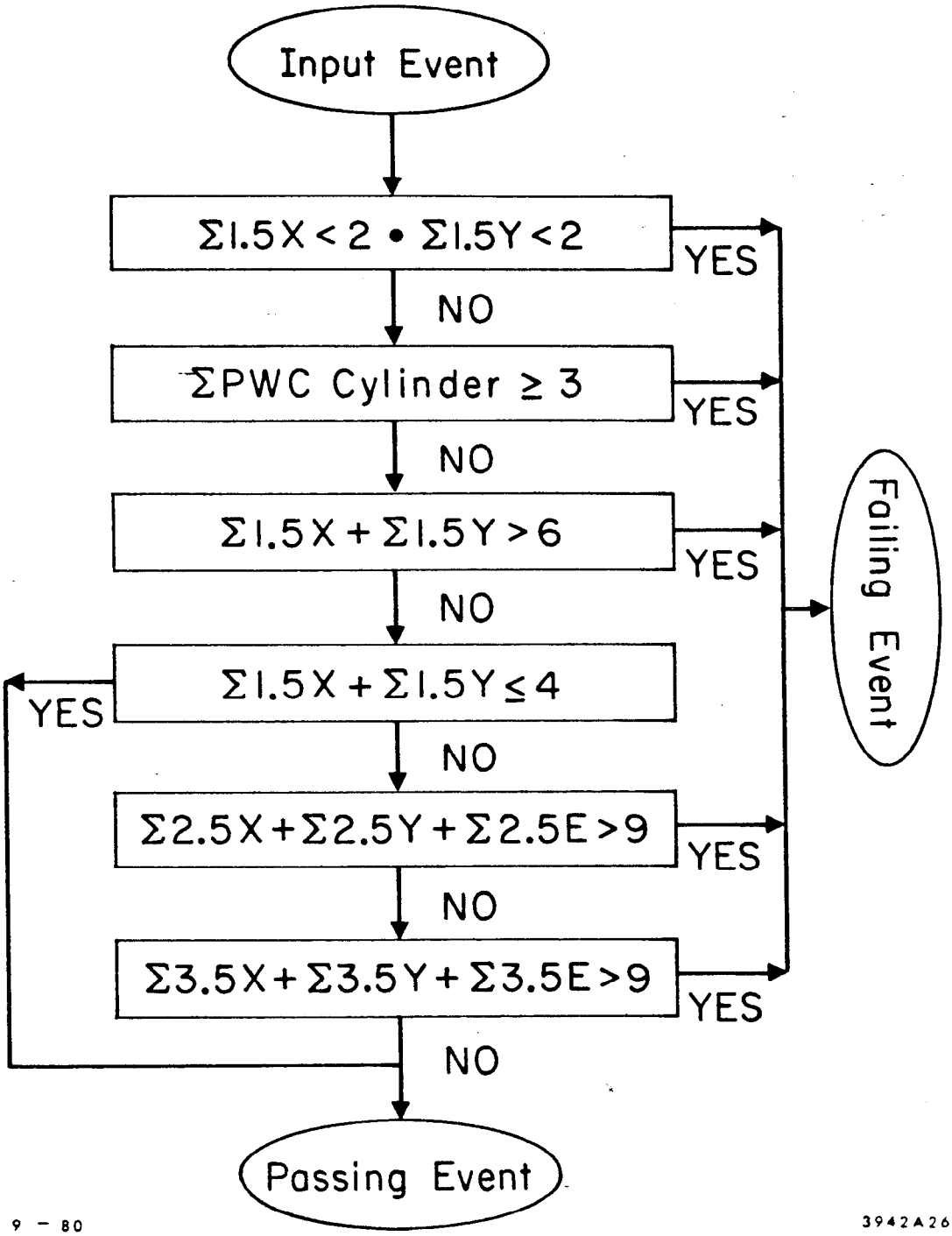

Figure 16 -- The software trigger logic.

Since this filter required only coordinate counts in the proportional devices, the event filtering took place as soon as the proportional device coordinate construction subroutines were finished. Thus all events underwent unpacking and some coordinate construction but only about 10% continued to be processed.

D. Matchpoints

Matchpoints were defined as points in a given chamber with two or more corroborating coordinates. Matchpoints were found by taking one coordinate from each of two different planes in a chamber (e.g., one X and one Y plane) and then calculating if one of more of the other planes (E or P) had a corroborating coordinate (i.e., was within some tolerance of the point defined by the first two coordinates). Thus a bank containing the (x,y,z) position of 2, 3, and 4 way match points was constructed for each chamber in the system. This match point bank was the basis for trial track determination in the track finding algorithms for beam and solenoid type tracks.

E. Track Reconstruction

As mentioned in the overview, track reconstruction was done separately for the three spectrometer regions: beam, dipole, and solenoid. Beam tracks were the first to be reconstructed, followed by dipole tracks, and then solenoid tracks. Dipole tracks were reconstructed before the solenoid tracks for the following reason. Since

there were usually many fewer dipole tracks and since their straight line parametrization made reconstruction simple, the CPU time spent for dipole track reconstruction was very small. For a dipole track to be usable it had to be extrapolated successfully into the solenoid region so it could be vertex associated. Although it would have been possible to try to join a dipole track segment to a solenoid track segment by trying all combinations of each type, it was found to be more efficient to extrapolate a dipole segment into the solenoid and look for corroborating coordinates. Then those corroborating coordinates could be removed from the bank of coordinates that would be later used for solenoid track finding (thus reducing search time for the more costly solenoid track finding algorithms).

E.1 Beam Tracks

Trial beam tracks were obtained by taking one match point from each of the two beam PWCs and calculating the parameters of the line that passed through both matchpoints. A "tube" was defined for the trial track as being a cylinder of radius r centered on the trial track. The coordinates for each of the 9 beam PWC planes that were closest to the trial track and fell within the "tube" where then used in a linear least squares fit to determine the best track parameters. This "tube" method was used in the track finding for all the various types of tracks (beam, solenoid and dipole). The method was sometimes used iteratively where bad points (far from the fit line) could be discarded and a new smaller radius tube would be defined for a coordinate search. The iterative,

point discard algorithm resulted in fitted tracks with minimum errors (for later reference, this method will be called the iterative tube search method). Tube radii and point discard criterion were determined from track finding studies of beam, solenoid, and dipole tracks.

The resulting fitted track was extrapolated upbeam into the θ-ϕ scintillation counter hodoscope and downbeam into the XY scintillation counter hodoscope to check for in-time corroboration. If more than one track was found, the tracks were ranked based on number of in-time corroborations and on number of beam PWC planes used in the fit. The momentum measurement, track parameters (intercepts, slopes), error matrix from the fit, and ranking for each track was stored for later use.

E.2 Dipole Tracks

The tracking for particles that successfully crossed the dipole magnet aperture was started from the very downstream end of the spectrometer and worked upstream to the target. The coordinates from the four downstream MS spark chambers and the JHD PWC hodoscope were used in combination to form track candidates. When a trial track was defined, the iterative tube search method was used to get coordinates for a least squares fit to a straight line. Corroboration from at least two out of the three downstream in-time devices (JHD, HA, and HB) was required for a track candidate to become a "good" downstream track segment.

All good downstream track segments were tracked across the dipole magnet aperture using a differential equation approximation technique known as the Runge-Kutta method [12]. This method utilized the magnetic field map (measured prior to the experimental run) and the differential equations of motion to calculate the approximate position of a particle as it crossed the dipole magnet aperture. The method required that the particle momentum be given and since this was not yet known, an iterative procedure was used to converge to the correct momentum. A successful dipole crossing was obtained when a downstream segment was crossed to the twixt region and an iterative tube search in the twixt region resulted in a good twixt track segment. At the end of this step the downstream and twixt track segment parameters as well as the measured dipole momentum were stored.

The final step for dipole track finding involved the continued (upstream) extrapolation of the track into the solenoid region. This step used the known momentum measurement from the previous step and used another Runge-Kutta procedure to extrapolate the good crossing tracks into the downstream end of the solenoid. This time the field map of the highly non-uniform fringe field region just downstream of the solenoid was used in the Runge-Kutta procedure. Once into the uniform field region of the solenoid volume, the standard helix parametrization was used to continue the track through the solenoid detection chambers. The iterative tube search algorithm was again used to obtain associated coordinates that were used in an iterative least squares fit to a helix. The helix parameters resulting from this fit provided an additional momentum magnitude measurement but more importantly it provided a good

measurement of particle position and direction in the solenoid. The helix parameters and the coordinates used in the fit were stored for later use.

After each step in the dipole track finding (downstream segment, twixt segment, and solenoid segment), a series of tests was applied to track candidates to select the good candidates that would continue to be processed. The tests required that a minimum total number of chamber coordinates, a minimum number of PWC coordinates, and a minimum number of scintillation counters be associated with a given track segment. These tests insured that the track was well measured and in-time with the event trigger. The long spark chamber memory time allowed collection of many out-of-time track coordinates. These coordinates would produce track candidates but the tests requiring in-time corroboration would quickly remove these candidates from further consideration.

E.3 Solenoid Tracks

The solenoid track finding consisted of two basic algorithms. The first found tracks in the planar solenoid chambers, the second found tracks in the cylindrical chamber package. The planar algorithm (plane track finding [13]) will be described first, followed by the cylindrical algorithm (cylindrical track finding).

Matchpoint combinations from the solenoid proportional chambers were formed to define trial helices. Coordinates from all solenoid chambers (CD and PWC) and all cylindrical chambers that were associated with the trial helix were found using the iterative tube search method.

By far, the majority of the trial helices were due to spurious matchpoint combinations which resulted in very few associated coordinates. These trial helices were immediately removed from consideration by imposing certain minimum requirements on the number of associated coordinates. For surviving candidates, the associated coordinates were then used in a iterative least squares fit to produce a set of parameters of the fit helix. As with the dipole tracks, some point discarding and refitting was allowed to obtain a best fit to a helix. In addition to the usual tests on minimum number of coordinates, minimum number of PWC coordinates, and minimum number of hodoscope corroborations (the TA, TB, and TC cathode readout PWC foils were used for in-time corroboration), tests on maximum number of missing coordinates were also applied. Since knowledge of helix parameters and chamber active areas allowed determination of the complete set of expected chamber coordinates, the tests on maximum number of missing coordinates removed those tracks which had many coordinates that should have been, but weren't detected. Particles that had decayed, were absorbed, or were heavily scattered during flight would often fall into this category and therefore be excluded from track reconstruction.

Cylindrical track finding used an algorithm similar to plane track finding except that it started with three cylindrical matchpoints to define a trial helix. The same iterative tube search and iterative least squares fitting procedures were used to obtain the best fit of cylindrical and planar solenoid coordinates to a helix. A set of tests, similar to those used in planar solenoid track finding, were used to remove out-of-time and other undesired track candidates.

Both the planar and the cylindrical track finding algorithms allowed use of coordinates in each others region, therefore, a fraction of the combined set of good tracks were duplicates. A subroutine that checked for uniqueness of coordinates removed such duplicate tracks. As in the case of the solenoid segment of dipole tracks, both the helix parameters and the associated coordinates used in the fit were stored. The coordinates were saved so that tracks could be refitted at a later time. For this analysis, the coordinates were used again in the event fitting stage (MVFIT) to be described later in this chapter.

F. Alignment

The alignment of the system was done before the event reconstruction job started processing the full data sample but it is described here since some knowledge of the track finding is necessary. First order alignment involved simply converting the surveyed device positions into position constants in the software coordinate system. Subsequent alignment required measured coordinates and track finding.

The main alignment procedure was accomplished with three different data samples. The first sample consisted of non-interacting beam track events recorded when both magnets were off. This sample was used to align all devices that the beam tracks passed through. The second sample was also taken with both magnets off but it contained events with outgoing tracks (large angle straight tracks) which passed through the active areas of devices that were deadened to non-interacting beam particles. The third sample contained good, reconstructed TO (physics

triggered) events taken with both magnets on which was used to align the cylinder package and to do final alignment adjustments on all the other devices.

The first data sample for alignment contained events with particles travelling in a straight line, approximately along the spectrometer axis. A iterative tube search method was again used to get coordinates associated with the track and a least squares fit to a straight line resulted in the track parameters. The residuals (residual= [measured coordinate] - [expected coordinate from fit]) for each plane were histogrammed and the mean of the residual distribution represented the alignment error for that plane. The alignment error was added (or subtracted as needed) from the offset constants for each device plane. These offset constants were used in the construction of the coordinates. All the planar chambers except for the CD chambers and the MS twixt chambers were aligned in this way (the CD and MS chambers had styrofoam plugs where the non-interacting beam particles passed through).

The tracks in the second data sample were fitted to straight lines using the usual iterative tube search followed by a least squares fit. However, only those devices that were aligned in the previous step were used in the fit. The fit lines were then extrapolated (or interpolated) to the CD and MS chambers which were not yet aligned. The alignment errors were again calculated from residual distributions and the corrections made to the offset constants.

The third data sample had tracks going in many directions so it was possible to obtain a subsample of events that had tracks passing primarily through the cylindrical chambers. The cylindrical track

finding algorithm was then used to find the helix parameters for these tracks. Residual distributions could then be used to get the rotational and translational offsets necessary to align the individual cylinders with one another. This produced proper internal alignment of the cylinder package but the alignment with respect to the rest of the spectrometer was not obtainable in this fashion. Another subsample of events that contained tracks with many planar solenoid coordinates and some cylinder coordinates was collected. Helices were fitted using only the planar coordinates, then the tracks were extrapolated into the cylinders to make residuals. A special fitting program was written to minimize the residuals by rotating and tilting the cylinder package. The tilt and rotation constants derived from this fit were then put into the cylinder coordinate construction calculations.

The third data sample was used for two more alignment functions. First, final adjustments on all detection chambers were made from residual distributions derived from all successfully reconstructed tracks. In most cases no adjustment was necessary, but in a few cases, the presence of the magnetic fields and other effects caused the need for slight realignment. The other function of the data sample was to position the various scintillation counters in the spectrometer. This was easily accomplished by extrapolating good reconstructed tracks to the counter position, then plotting the (x,y) position of those tracks for which corroboration was obtained from the counter. The resulting X-Y plot showed the outline of the counter from which the position of the counter edges was easily determined. The array of constants that contained those edge positions were then updated with the corrected

values. Thus a complete and consistent set of alignment constants was determined and was used in the event reconstruction programs.

G. Vertex Association and Event Topology Determination

Up to this point, the event reconstruction description has been completely general in the sense that it applied to all final states contained in the experimental data sample (not just the $K^-\pi^+n$ final state). However, with vertex association and event topology information now about to be available, the remaining sections will be applicable only to those events that fit a $K^-\pi^+n$ hypothesis.

Vertex association and event topology determination were interrelated and often complicated. The program that performed this task tried to mutually associate as many of the tracks as possible by searching for positions in space where all the tracks would converge. A function was defined that, when minimized, produced the (x,y,z) position of closest approach (a trial vertex) to the set of tracks given as input. The value of the function was required to be below a certain tolerance for the trial vertex to become a "good" vertex. By removing a poorly associated track from a set of tracks that defined a "bad" vertex, one could often obtain a new "good" vertex. Studies were made to determine the tolerances that would insure that the right tracks would be associated to form a vertex. The program allowed for any number of vertices, located in or out of the target, and allowed for variable numbers of tracks at a vertex.

For the $K^-\pi^+n$ data sample used in this analysis, a beam associated vertex with two oppositely charged outgoing prongs, located in the target volume was the only type of vertex to be considered. In addition, only one such vertex was allowed in each event. This topology requirement greatly reduced the sample since there were many events with fewer or greater numbers of outgoing prongs and some events with vertices outside the target (e.g., K^0 and Λ decays). The vertex tolerance criteria for this topology amounted to a requirement that the beam and the two outgoing tracks each approach the same (expected vertex) point to within ~1 cm. The expected vertex position and the closest approach parameter were added to the stored event information.

H. Event Fitting

The versatile multi-vertex fitting program MVFIT, created for the LASS software analysis job, was used to do a vertex constrained geometric fit. The MVFIT program used the measured beam track to constrain the origin of the two outgoing tracks. The individual coordinates associated with the two outgoing tracks were used in MVFIT so that a chi-squared sum of the track residuals could be calculated and minimized. The beam error matrix was also input to MVFIT so that the contribution of the beam track uncertainty to the chi-squared sum was included. The vertex constraint required the beam and the two outgoing tracks to intersect at a common point in space. The minimization of the chi-squared sum was performed by use of matrix inversion techniques. Approximate energy loss in the target was calculated for outgoing tracks

by using range-energy loss tables and the estimated path length in the target. Note that this correction required knowledge of the mass of the particles involved, so the kaon mass was assigned to the negative particle and the pion mass to the positive particle. Correction to the error matrix of the fit (which contained the error estimators of the fit parameters) was made for the effect of multiple scattering on the outgoing tracks.

The fit parameters determined by MVFIT were the helix parameters of the outgoing tracks and the vertex position. The results from the track reconstruction and the results from the vertex association were used by the MVFIT program to establish the starting values of the parameters for the first iteration of the fit. If a successful fit was obtained, the output from MVFIT contained the optimum vertex position, the momentum vectors of the outgoing tracks, and the error matrix from the fit. The error estimators of the momentum vectors were calculated from the error matrix elements. With these quantities determined, the event reconstruction program was finished.

Chapter V

KINEMATICS, Kπ DATA SELECTION, AND Kπ DATA DISTRIBUTIONS

A. Kπ Scattering Kinematics

The purpose of this analysis was to study the Kπ elastic scattering amplitudes in the reaction $K^-p \rightarrow K^-\pi^+n$. This implied that the specific exchange diagram of interest was the pion exchange diagram in fig. 17a. A reaction of this type can be completely parametrized by six independent kinematical variables. For this analysis, the choice of variables was:

1) s, the square of the center of mass energy.
2) ϕ_{lab}, the azimuthal angle of the neutron recoil direction measured in the laboratory reference frame (see fig. 17b). In a non-polarized target experiment such as this one, the physics is independent of ϕ_{lab}.
3) M(Kπ), the invariant mass of the $K^-\pi^+$ system.
4) $|t'|$, the absolute value of the square of the 4 momentum transfer minus $|t_{min}|$.
5) $\cos\theta_j$, the cosine of the polar angle of the Kπ decay in the Gottfried-Jackson [14] reference frame (see fig. 17c).
6) ϕ_j, the azimuthal angle of the Kπ decay in the Gottfried-Jackson reference frame (see fig. 17c).

It was assumed that the two outgoing particles that had been measured for each event in this analysis were correctly assigned as kaon

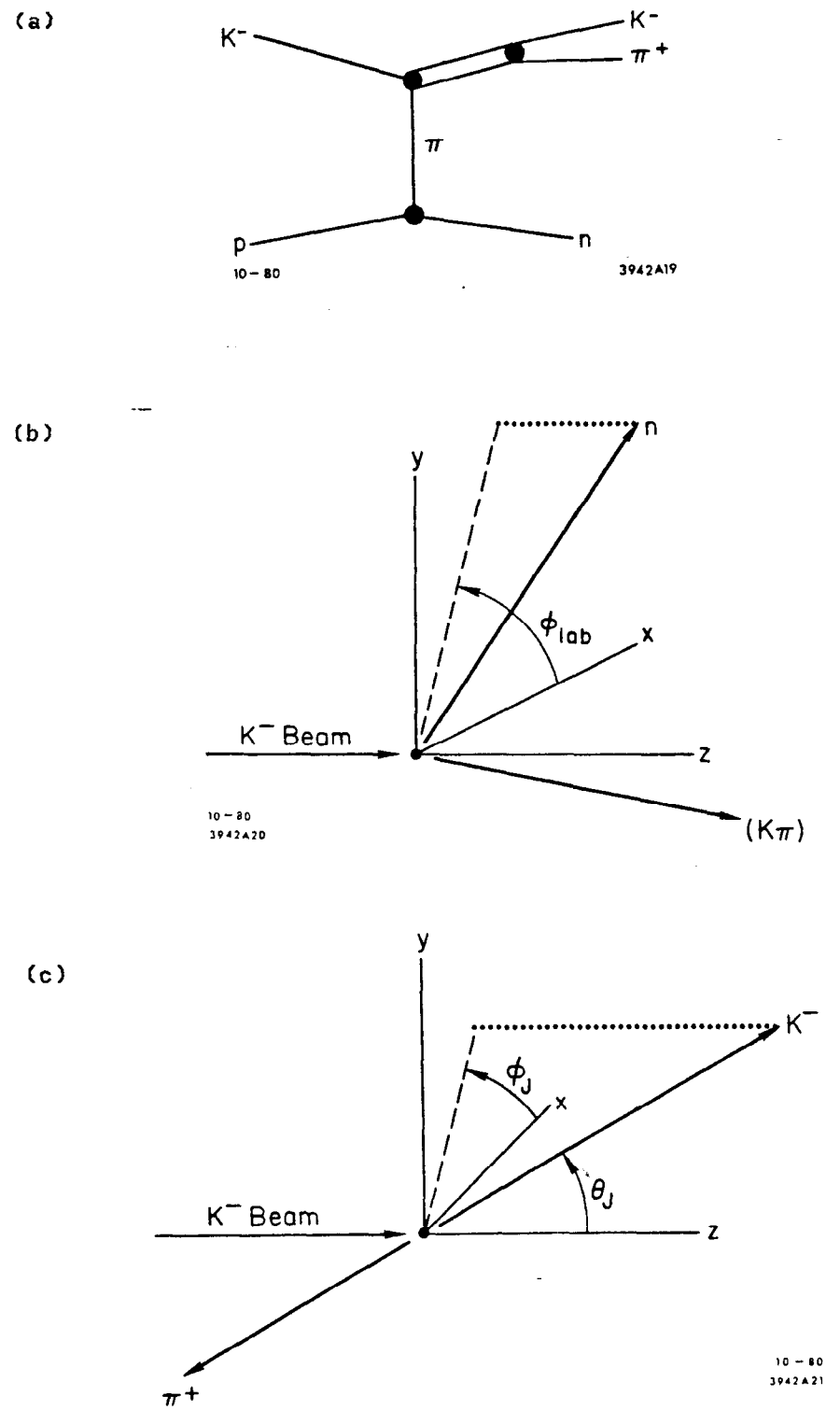

Figure 17 -- (a) Feynman diagram for Kπ scattering in the reaction $K^-p \rightarrow K^-\pi^+n$. (b) ϕ_{lab} defined in the laboratory reference frame. (c) The Gottfried-Jackson angles, θ_j and ϕ_j, defined in the Kπ center of mass reference frame.

and pion for the negative and positive particles respectively. Then for the reaction shown in fig. 17a, the 4-momentum vectors for the incoming K^-, incoming p, outgoing K^-, and outgoing π^+ were measured. By use of standard 4-vector addition, the kinematical quantities s, $|t'|$, and $M(K\pi)$ were easily calculated using the following equations.

$$
\begin{aligned}
s &= |P_b + P_p|^2 \\
|t'| &= |t| - |t|_{min} = |P_b - P_{K\pi}|^2 - |t|_{min} \\
M_{K\pi} &= |P_{K\pi}|^2 \\
\text{where:} \quad |t|_{min} &= |(E_b - E_{K\pi})^2 - (\vec{p}_b - \vec{p}_{K\pi})^2| \\
P_{K\pi} &= P_K + P_\pi
\end{aligned}
\qquad \text{(V.1)}
$$

In eq. V.1 the subscripts (b,p,K,π) refer to the beam, proton, K^-, and π^+ respectively; the P are the usual 4-momenta. Since the physics results were independent of ϕ_{lab}, this quantity was never used in the analysis and therefore was not calculated. By performing a Lorentz transformation on the outgoing K^-, π^+, and K^- beam 4-momenta from the lab to the $K\pi$ center of mass frame, and then making the proper rotations, the Gottfried-Jackson angles θ_j and ϕ_j were calculated for each event.

Another often referenced quantity was the missing mass squared opposite the $K\pi$ system. Since the neutron recoil in the reaction $K^-p \rightarrow K^-\pi^+n$ was not detected, this missing mass squared quantity (MM^2) was used to define the neutron recoil sample (using a missing mass squared cut). The MM^2 was calculated using eq. V.1 and the 4-momenta of the $K\pi$

system, beam, and target proton as follows:

$$MM^2 = | P_{K\pi} - P_b - P_p |^2 \qquad (V.2)$$

B. Data Processing

B.1 Introduction

The data processing sequence started with the many raw data tapes and ended with a single tape containing the important event information of the $K\pi$ data sample. The processing stages and intermediate tapes are shown in the flow chart of fig. 18. The number of events remaining after each processing stage are shown on the right-hand side of the flow chart. The major contributing factors to the event selection at each stage along with the percentage of the input sample removed due to those factors are listed on the far right side of the flow chart. The more important features of this processing sequence and of the selection criteria will be discussed in the following subsections.

B.2 The LASS Production Job

The LASS production job was a pseudonym for the complex computer program that performed the event reconstruction task described in the previous chapter [15]. The software filter (see IV.C) accounted for the major fraction of events not processed by this program. The main reasons

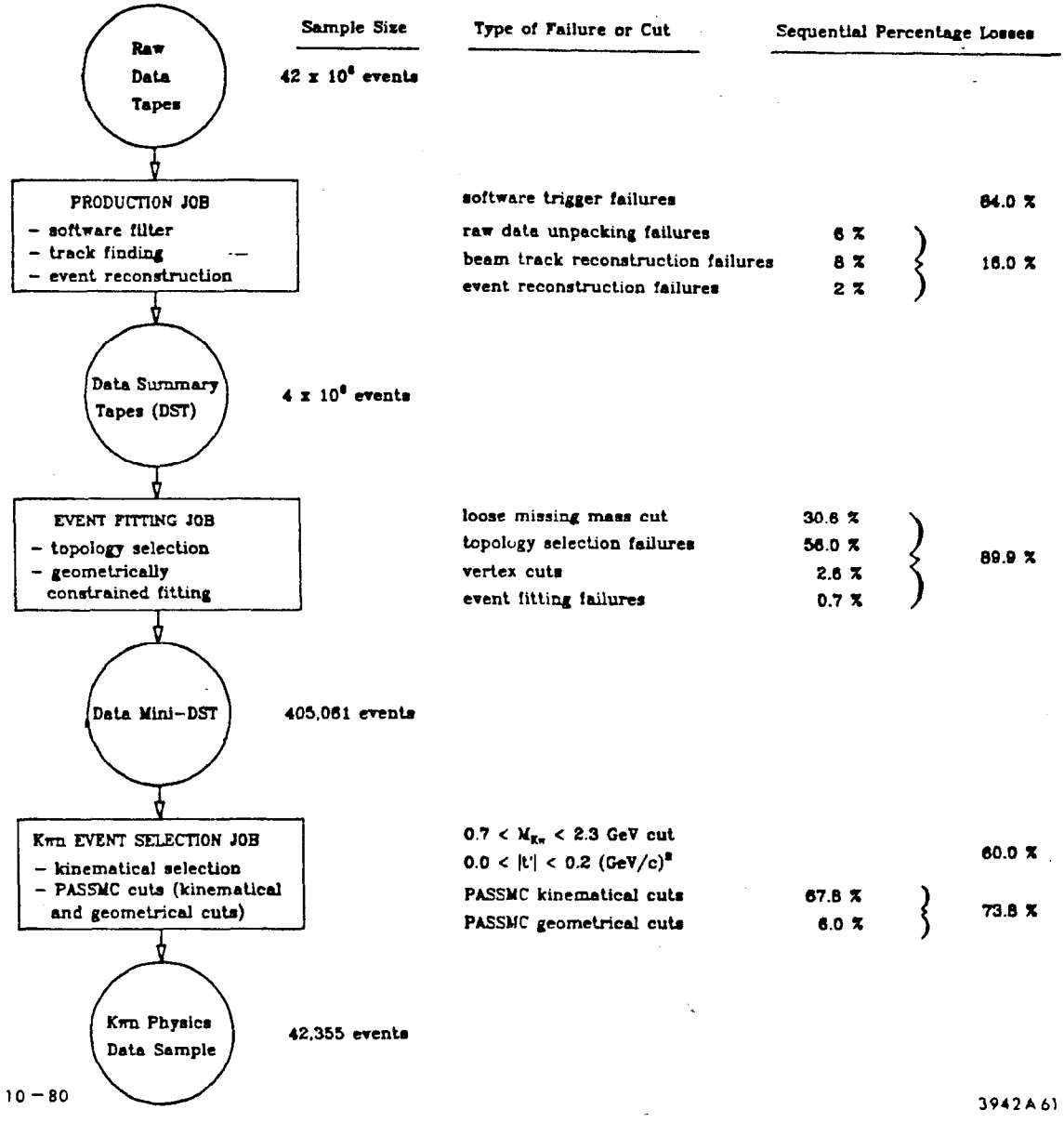

Figure 18 -- Data processing flow chart, sample size summary, failures and cuts at each processing steps, sequential percentage event loss in the processing.

for event failure were unrepairable problems with the raw data record unpacking, buffer overflows (not enough computer storage space for certain arrays; usually due to too many track candidates), and beam track failures (no suitable beam tracks found or too many candidates found). The number of failing events for each failure type was recorded so that normalization corrections could be made at a later time.

The events that survived this stage had undergone all the event reconstruction steps described in the previous chapter except for the topology selection and the event fitting (MVFIT) step. The events in this surviving sample, known as the DST (for Data Summary Tape) sample, were allowed to be of any topology and to have any number of vertices and tracks. Because of the software filter, however, the majority of these events were of the single vertex, 0 to 4 prong type. The output event record on the DST tapes contained a large number of items including track parameters, track coordinates, vertex information, topology, event hypotheses, and many other useful quantities. The track coordinates were included in the output record so that event fitting could be done at the next stage. In principle, event fitting could have taken place before writing the DST, but a sample of unfitted events was desired for various reasons, so the fitting was delayed until the next stage.

The program processed an input data set of ~42 million events and wrote ~4 million events on the DST tapes using approximately 60 CPU-days of computer time (~1 CPU-second per output event on the IBM 370/168). In terms of tape storage, the data sample represented ~1000 raw input data tapes and ~50 DST output tapes, respectively.

B.3 *Topology Selection and Event Fitting*

The second stage of the processing sequence involved reading and unpacking the DST, then selecting and fitting only the beam associated, single vertex events with two oppositely charged outgoing tracks. In addition, cuts requiring the vertex to be within the liquid hydrogen target volume were made. After the MVFIT program fitted the event, cuts were made on the confidence level of the fit to remove events with extremely poor fits. A small number of events failed to converge in the MVFIT algorithm and were also cut out of the sample. A final loose cut on missing mass squared opposite the $K\pi$ system was made to remove events that had no chance of being a $K^-\pi^+n$ event. The calculation of the MM^2 was possible because the 4-momenta necessary for the calculation were available from the MVFIT results and the DST input record. This availability of the 4-momenta also made it possible to calculate the 5 important kinematic quantities describing each event, namely, s, $|t'|$, $M(K\pi)$, $\cos\theta_j$, and ϕ_j.

A special event record format was developed for the output data sample from this stage. It was designed to contain all the necessary event information so that kinematical and geometrical quantities would be available or easily derivable. The kinematical quantities put into this output record were the five quantities mentioned above. Geometrical quantities such as track parameters for the solenoid, twixt, and downstream track segments were saved so that aperture or active area cuts could be made. Such cuts were used to remove tracks in so-called gray regions; regions where, due to measurement uncertainty, the true

path of the particle may well have hit a magnet wall or chamber frame. This gray region was difficult to handle properly in the Monte Carlo simulation program, so by cutting out such regions in both data and Monte Carlo event samples, one could feel confident that the same geometrical constraints were imposed on both data samples. Other geometrical quantities included in the output record were the vertex position, the beam momentum vector, and the momentum vectors of the two outgoing particles. A set of special code words which kept a record of which devices should have detected the track and which devices did detect the track was also put into the output record for each event. These code words were needed for tracking studies (multiplicity, efficiency, etc.) and also to repair an error that was introduced by the event reconstruction program but not discovered until after the sample was processed. The final geometrical quantities included in the output record were the errors on measured track momenta. Those errors were derived from the error matrix from MVFIT and were included so that track resolution studies and track resolution cuts could be made.

This special event record format was highly compact so that it made it possible to fit the surviving data sample (some >400,000 events) on a single magnetic tape. This one tape data sample was known as the data mini-DST. This sample allowed high statistics studies of tracking, resolution, and physics signals to be obtained in a reasonable short (in CPU time) computer job. More importantly, this sample was the input data set for the program which defined the $K^-\pi^+n$ final data sample.

B.4 Defining the $K^-\pi^+n$ Final Data Sample

As explained in the previous subsection, the event record of the data mini-DST was specially designed to make kinematical and geometrical quantities easily available. This final stage of the data processing sequence consisted of a program that read the data mini-DST tape, unpacked the event record, made some cuts to repair an error left by the trackfinding program, and called a special subroutine known as PASSMC. The PASSMC subroutine calculated a set of kinematical and geometrical quantities and then utilized user supplied kinematical and geometrical cuts to pass or fail events. The PASSMC subroutine was designed to not only operate on input from the data mini-DST but to also operate in the same way on input events from the Monte Carlo mini-DST (to be described in Chapter VII). This duality of purpose enabled the identical calculations and cuts to be applied to the data events and the Monte Carlo events which was essential for obtaining the acceptance corrected moments of the $K\pi$ angular distribution.

Before calling PASSMC, the program made a $|t'|$ cut of $0.0<|t'|<0.2$ GeV^2, since the $|t'|$ quantity was immediately available from the input record without need for calculation. The cut was intended to isolate t-channel pion exchange events.

The first step in PASSMC was the calculation of kinematical quantities used for background event removal (background removal is discussed in detail in VI.B). Cuts were applied to remove the background events due to elastic scattering and $K^-p \rightarrow \bar{K}^0 + X^0 \rightarrow \pi^+\pi^- + X^0$ reactions. A cut on missing mass squared opposite the $K^-\pi^+$ system of

$0.2<MM^2<1.1$ $(GeV/c)^2$ was applied to isolate the neutron recoil in $K^-\pi^+X^0$ final states.

In the second PASSMC step, an assortment of geometrical quantities were calculated to allow for cuts on device active areas, the dipole magnet aperture, vertex position, longitudinal and transverse track momenta, and momentum resolution. Since these geometrical cuts were usually made to remove events with tracks in gray regions (defined in subsection B.3) they resulted in a very small number of failing events (~6.5%). The kinematical cuts, however, substantially reduced the data sample, as shown in the event loss summary in fig. 18. In this figure, note that when an event first failed a cut, it was removed immediately, not getting a chance to be subject to the subsequent cuts. Thus fewer events were subject to the last cut in PASSMC than the first cut. The percentages given are not the result of the fraction (# events failing cut)/(# events reaching cut) rather they are the result of the fraction (# events failing cut)/(total # of input events processed by PASSMC).

The net purpose of these kinematical and geometrical cuts was to define the optimum sample of events for use in analyzing the angular distribution of $K\pi$ elastic scattering in the $K^-\pi^+n$ final state.

C. The $K^-\pi^+n$ Final Data Sample

The $K^-\pi^+n$ final data sample contained more than 40,000 events with good statistics in a range of $K\pi$ mass from 0.8 to 2.5 GeV. As stated before, the cuts in $|t'|$ and MM^2 used to define the sample were $0.0<|t'|<0.2$ GeV^2 and $0.2<MM^2<1.1$ GeV^2 respectively. Although the

moments analysis and partial wave analysis clearly revealed much detailed information about the Kπ scattering angular distribution, quite a lot of the structure in the distribution was evident from studying simple plots of the data sample. In this section, several of these simple plots will be presented and discusssed. In all cases, the plots shown are raw data plots, taken from the 42,355 event $K^-\pi^+n$ final data sample and uncorrected for spectrometer acceptance.

Figure 19 shows the Kπ mass distribution, where number of events is histogrammed as a function of M(Kπ). The spin 1 K*(895) resonance stands out clearly as a very narrow, tall peak. The wider spin 2 K*(1430) resonance is also quite prominent but the spin 3 K*(1780) is only hinted at by the small enhancement in the 1700 to 1800 MeV region. No features at higher (or in between) masses are obviously apparent.

The strong dependence of the mass distribution on the angular distribution can be quickly revealed by replotting the mass distribution with cuts on the $\cos\theta_j$ value. In fig. 20 the Kπ mass distribution is plotted 8 times, each plot corresponding to one of the sections obtained when the $\cos\theta_j$ range from -1 to +1 is divided into 8 equal sections. If the "forward" direction is defined as the direction opposite the recoiling neutron as seen in the Kπ center of mass frame, then $\cos\theta_j$ near +1 means the kaon is emitted in the forward direction (and the pion is emitted in the backward direction). Thus references to the "forward" and "backward" directions will imply $\cos\theta_j$ near +1 and -1 respectively. In fig. 20 there is a dramatic change in the mass distribution as one goes from the backward to forward region in $\cos\theta_j$. A close look at the position of the K*(895) and K*(1430) resonances show a slight shifting

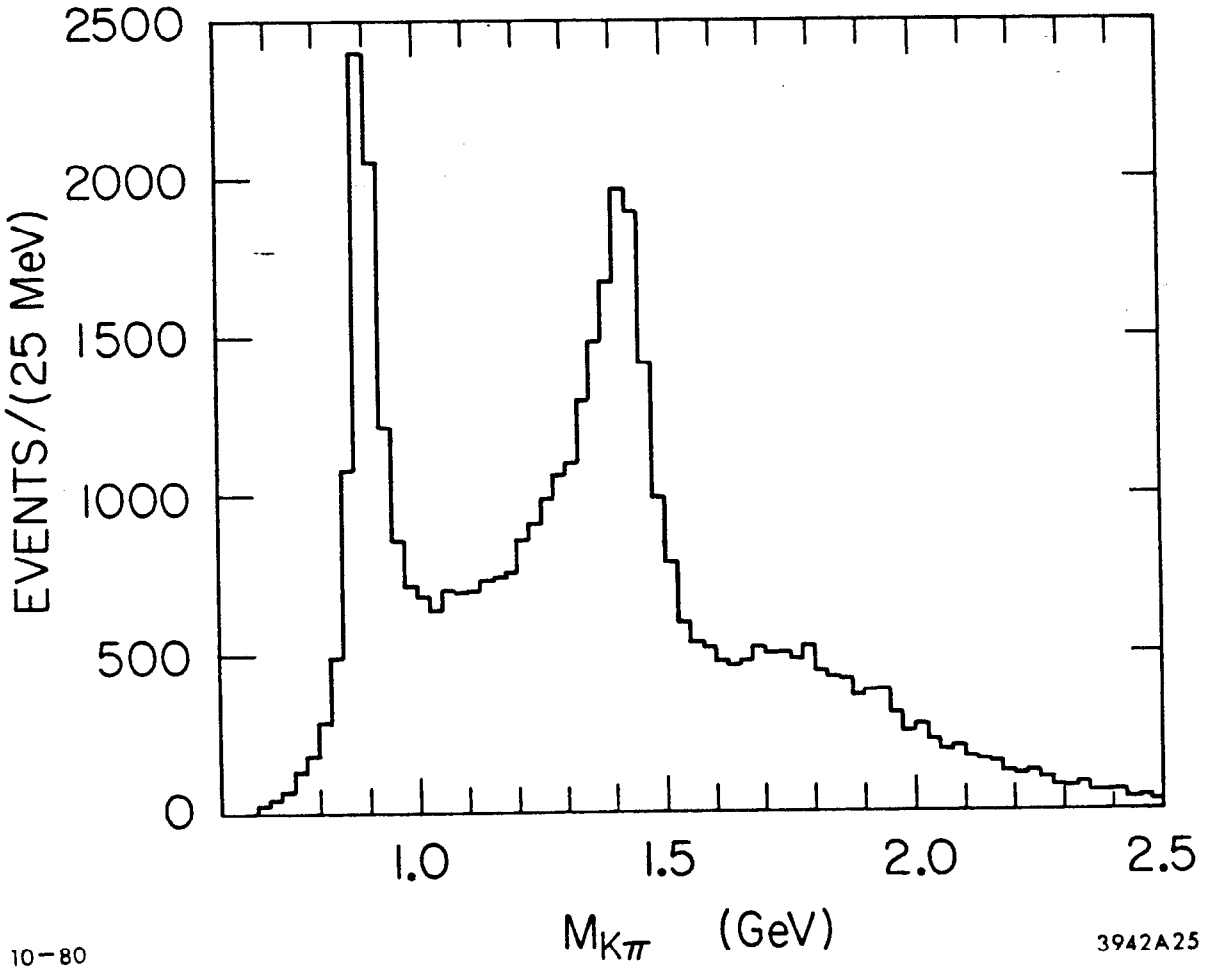

Figure 19 -- The invariant Kπ mass distribution uncorrected for acceptance.

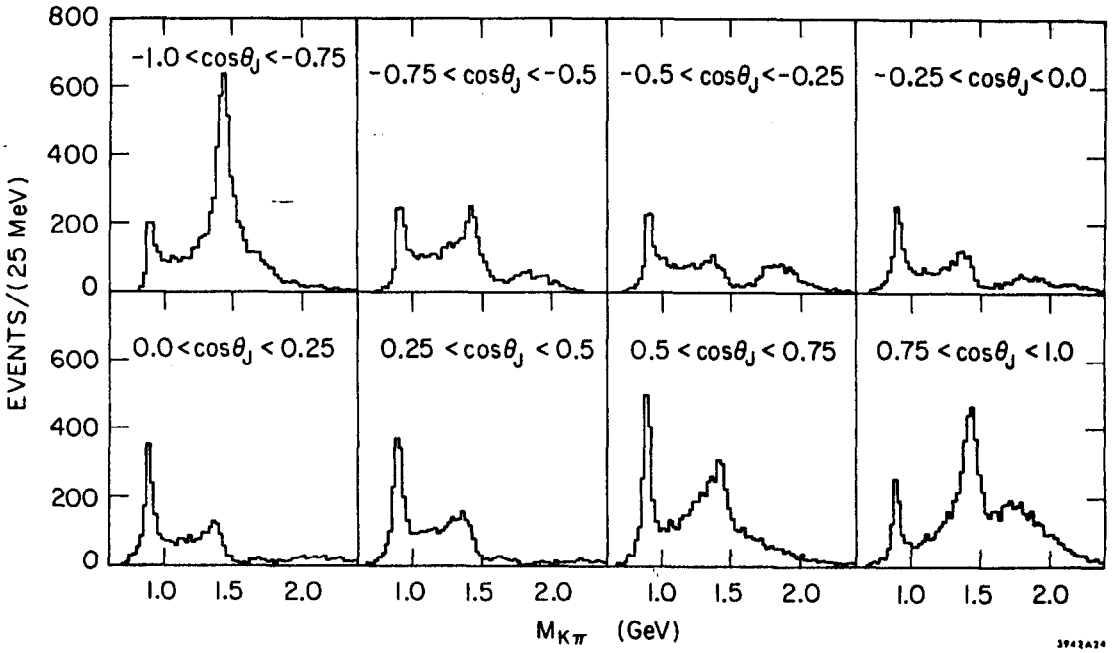

Figure 20 -- Invariant Kπ mass distributions for 8 consecutive regions in $\cos\theta_j$.

of the peaks as a function of $\cos\theta_j$. The effect is on the order of 15 MeV for the K*(895) with the mass of the peak decreasing as $\cos\theta_j$ goes from -1 to +1. For the K*(1430) resonance, the forward and backward $\cos\theta_j$ plots show a peak mear 1440 MeV while the central ($\cos\theta_j$ near 0) region shows a weak, strangely shaped bump peaked at close to 1380 MeV. As will be shown later in the partial wave analysis, this peak shifting is due to strong S-P and S-D wave interference effects. In the case of the K*(1780), not only does the apparent mass peak shift, but the resonance seems to completely vanish in some regions of $\cos\theta_j$.

Figure 21 gives the $\cos\theta_j$ distribution for M(Kπ) cuts containing the three major resonance regions. Here it can be seen quite clearly that the decay of different spin objects lead to much different angular distributions. An even more revealing plot is shown in fig. 22. In this 3D projection, the height of the plot represents the number of events and the two horizontal axes are the Kπ mass and $\cos\theta_j$ measurement values. In this plot, the shifting of the resonance peaks and changes in their magnitude and width as a function of $\cos\theta_j$ are again quite evident. In addition, more complicated angular structure can be seen in the K*(1780) and higher mass regions.

It is clear from these plots that mass and width determinations from fits to mass distributions can be very misleading. The LASS spectrometer acceptance in $\cos\theta_j$ is fairly uniform (except in the extreme forward and backward $\cos\theta_j$ regions where it drops off), therefore it affords a reasonably complete view of the mass spectrum as a function of $\cos\theta_j$. In several past experiments that looked at Kπ mass distributions with limited acceptance in $\cos\theta_j$, conflicting reports for

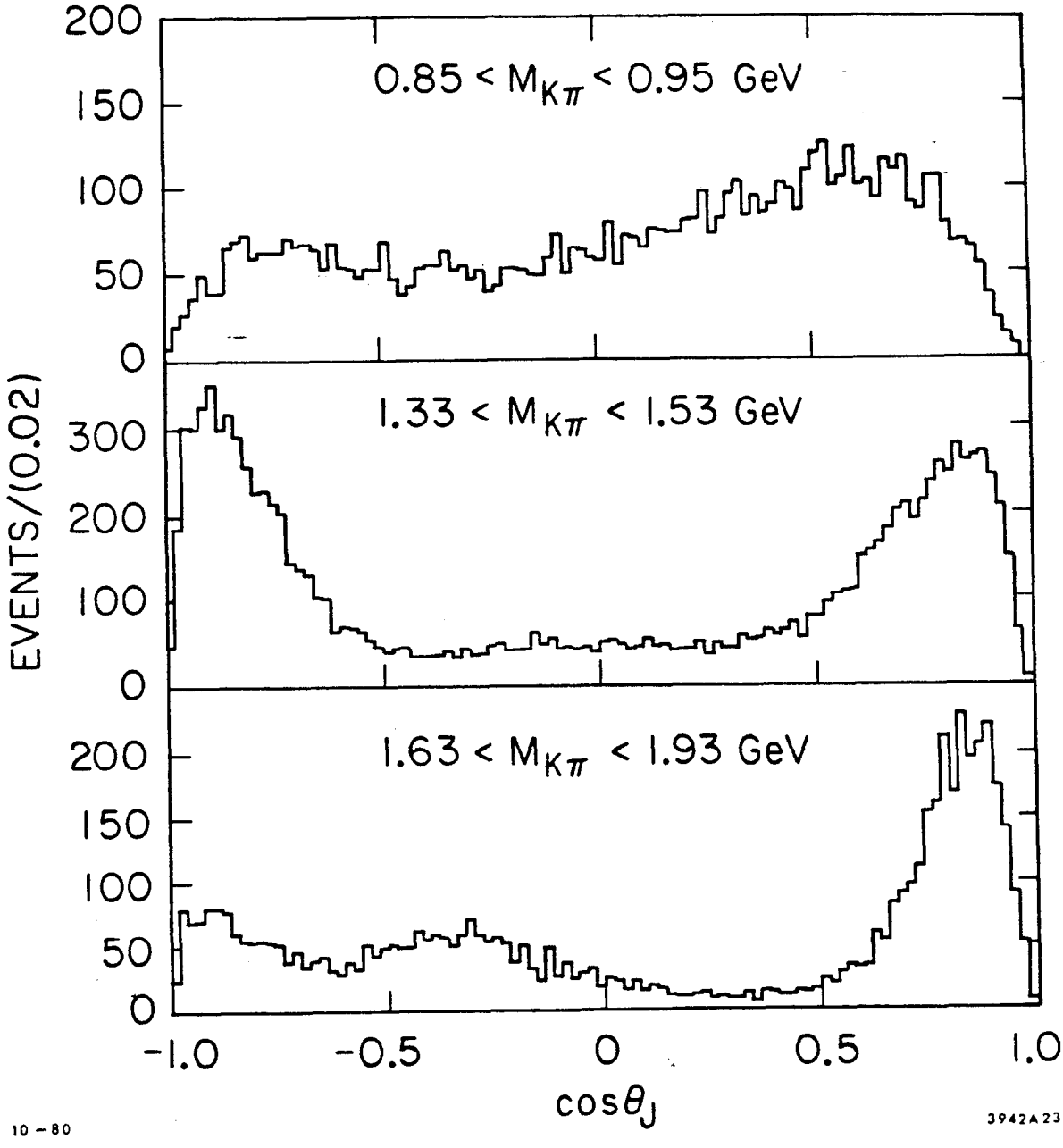

Figure 21 -- The $\cos\theta_j$ distributions for the Kπ mass regions containing the K*(895), K*(1430), and K*(1780) resonances.

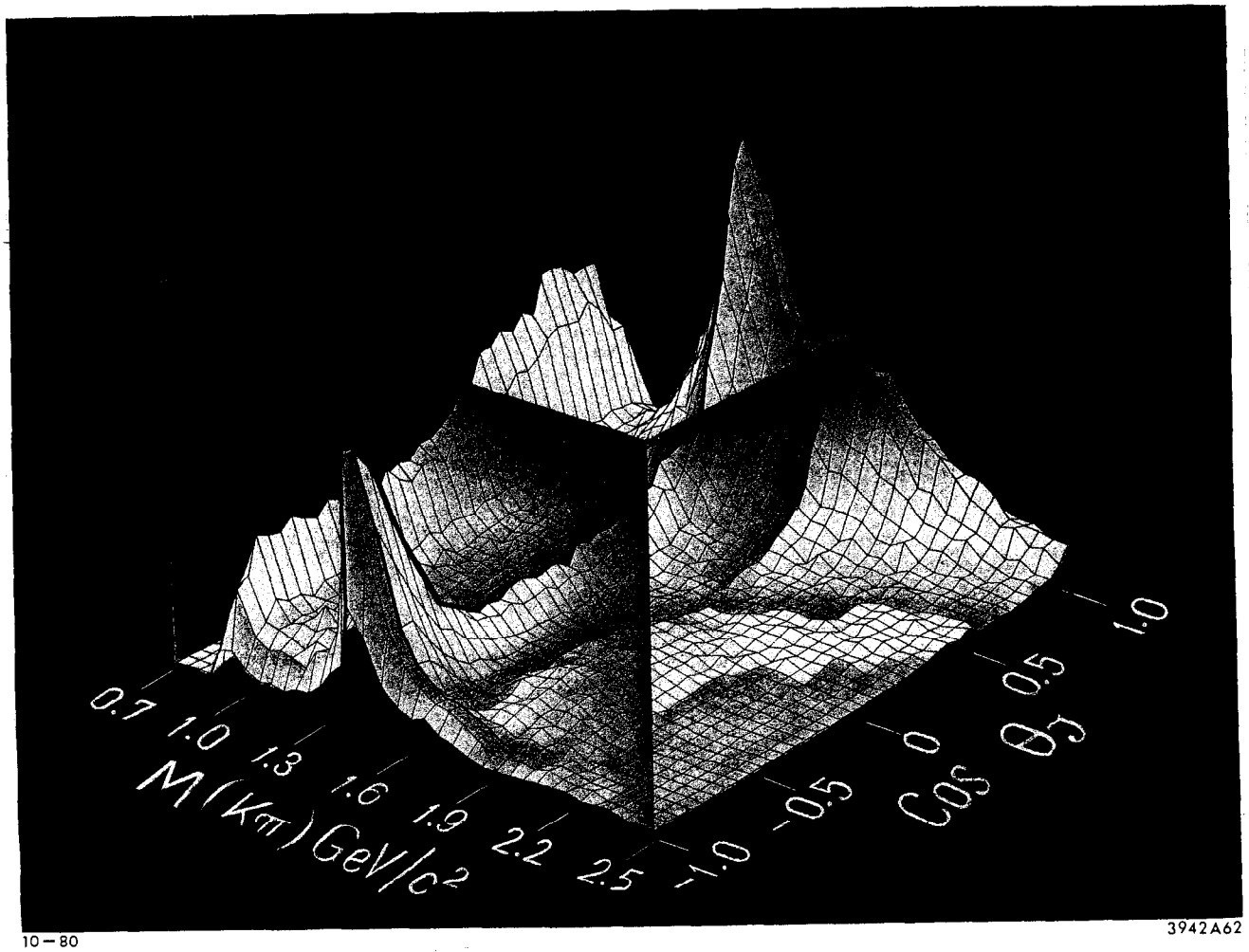

Figure 22 -- A projection of a 3 dimensional representation of the Kπ data sample. Vertical axis is number of events (scale is such that tallest bin contains about 1000 events). Horizontal axes represent Kπ mass and $\cos\theta_J$ as shown.

the mass and width of the K* resonances were presented. From the plots given here, such conflicting reports are not surprising. Although the apparent changes in magnitude of the resonance peaks as a function of $\cos\theta_j$ are merely the effect of the decay angular distribution of non-zero spin states, the shifting of the peaks is due to the interference effects of different spin states. In any case, both of these effects show the necessity for extracting the moments of the angular distribution and for attempting a partial wave analysis in order to fully understand the resonance structure.

Chapter VI

RESOLUTION, BACKGROUNDS, AND NORMALIZATION

A. Resolution

A.1 Overview

The finite resolution of the momentum measurements in the spectrometer lead to the uncertainties in the $K\pi$ scattering kinematical quantities. These uncertainties, in turn, were important in the calculation of the spectrometer acceptance (which is explained in detail in VIII.C). Thus a good understanding of spectrometer resolution was necessary for this analysis. The contributions to the total event resolution were due to the beam momentum measurement, the solenoid track measurement(s), and the dipole track measurement(s). Each of these contributions was carefully studied. The results of the studies were used to make the Monte Carlo program closely simulate the resolution properties of the spectrometer. Because of this simulation, the acceptance corrections obtained from the Monte Carlo program included the effects of spectrometer resolution. The following discussion will cover the results of these resolution studies and the method used by the Monte Carlo program to simulate the spectrometer resolution.

A.2 Track resolutions

The resolution contribution from the beam momentum measurement was due to three sources, the momentum magnitude measurement error of the P-hodoscope, the drift in the central value of the momentum magnitude (due to drifting of the calibration of the beamline magnets), and the beam position and direction measurement error. The drift of the momentum magnitude measurement was determined by selecting large samples of $K^- \rightarrow \pi^+\pi^-\pi^-$ decay events at many intervals during the experimental run then calculating the average $|P(beam)|$ for each sample. The effect of the drift was a smearing of the momentum magnitude equivalent to a resolution of $\sigma(drift) \sim 30$ MeV/c for the experimental run. The momentum magnitude resolution due to the P-hodoscope measurement was calculated as $\sigma(P\text{-hod}) = 40$ MeV/c. This was obtained from a study of forward K^-p elastic scattering events which resulted in a value for the dipole momentum measurement resolution $\sigma(dip)$ as well as $\sigma(P\text{-hod})$. The uncertainty in the position and direction of the beam for each event was easily calculated from the error matrix elements that resulted from the least squares fit which determined the beam track parameters.

As in the case of the beam tracks, the error matrix associated with the fit to a helix (MVFIT) provided the information for calculating the momentum resolution for each outgoing charged track in the spectrometer. For those tracks that were measured successfully in the dipole portion of the spectrometer (only the momentum magnitude was measured there), a momentum magnitude measurement error was calculated based on both the error matrices from the fits to the track segments and the results from the dipole magnet aperture crossing algorithm.

It should be noted that in order to obtain error matrix elements from any of the fits, the measurement error corresponding to each point used in the fit must be known and used as input to the fitting program. Thus, to obtain correct error matrices from the fits for all track types, measurement errors for all devices used in the beam, solenoid and dipole sections of the spectrometer were needed prior to the event reconstruction step. These measurement errors were obtained by an iterative procedure that was applied in a similar fashion to all trackfinding devices. In this procedure, an initial sample of events was processed using estimates of measurement errors based primarily on wire spacings. From this initial sample, a subset of well measured tracks was selected to be the new "good track" sample. Then, each of these new good tracks was reprocessed with one selected measurement plane removed from the fit. The residual distribution for that selected plane was histogrammed and the measurement resolution for the plane was defined as the rms deviation from the mean of the distribution. This procedure was repeated for every measurement plane in the spectrometer. The measurement errors from this study were then used for the calculation of the error matrix elements from the various fits used in event reconstruction (some typical values for the measurement errors for various types of devices are given in Table 3).

A.3 $M(K\pi)$, $|t'|$, MM^2 resolution

As described in Appendix A, the Monte Carlo program simulated the event reconstruction procedure used in the data to a very high degree of

accuracy. Both device efficiency and device resolution were used in the simulation of track reconstruction. Many detailed studies were performed to insure that the Monte Carlo programs properly simulated all important aspects concering track measurement. It was then possible to closely examine the effect of spectrometer resolution on the measurement of the four important kinematical quantities $|t'|$, $M(K\pi)$, $\cos\theta_j$, and ϕ_j. From the standpoint of the physics analysis to be presented, the resolution in $\cos\theta_j$ and ϕ_j was properly accounted for in the acceptance calculation. However, because the analysis divided up the $|t'|$ and $M(K\pi)$ regions into bins, it was important that the resolution be sufficiently good so that Monte Carlo events generated in a given $|t'|$ and $M(K\pi)$ bin would not end up being "measured" with a $|t'|$ and $M(K\pi)$ corresponding to a different bin. The results of this resolution study gave the following $|t'|$ and $M(K\pi)$ resolution (each averaged over all other kinematical variables; and noting that each varied as a function of $M(K\pi)$):

$$\sigma_{|t'|} = 0.003 \text{ GeV}^2$$

$$\sigma_{M_{K\pi}} = 4 \text{ MeV (low } M_{K\pi}) \text{ to } 15 \text{ MeV (high } M_{K\pi}) \qquad \text{(VI.1)}$$

This would allow for a small amount of bin crossover but since the important physical quantities were found to vary slowly from bin to bin, the small amount of crossover was found to have no significant effect on the results.

The most important quantity that was a result of the spectrometer resolution was the spread in the distribution of the missing mass squared (MM^2) opposite the $K^-\pi^+$ pair. This distributions can be seen in

fig. 23a. The MM^2 distribution as determined from a Monte Carlo event sample is also shown in fig. 23a. It is clear from the figure that the leading edge of the data distribution is well represented by the Monte Carlo distribution. The trailing edge would not be expected to coincide well since the data sample contains $K^-\pi^+\Delta^0$ as well as other background contributions. However, assuming the Monte Carlo distribution correctly represents the neutron recoil data distribution, the MM^2 resolution is:

$$\sigma_{MM^2} = 0.04 \text{ GeV}^2 \qquad \text{(VI.2)}$$

The Monte Carlo MM^2 distribution and the data MM^2 distribution were used to estimate the background contamination in the $K^-\pi^+n$ event sample which will be discussed in the next section.

B. Backgrounds

The topology requirement of two and only two oppositely charged outgoing tracks resulted in a data sample consisting largely of $K^-\pi^+n$ events. However the following final states were still able to contribute to the physics background in the data sample: 1) $K^-\pi^+\pi^0n$, 2) $\pi^+\pi^-n$ from $\bar{K}^0$ decay, 3) $\pi^+\pi^-\Lambda$ (or Σ^0), 4) $K^-K^+\Lambda$ (or Σ^0), 5) K^-p, 6) $K^-\pi^0p$, and any of the above final states with one or more π^0s added. Most of these background events were removed by the kinematical cuts in the PASSMC program. The largest background was due to elastic events but the elastic cut in PASSMC was effective in removing nearly all of these events. The elastic cut consisted of three requirements, all of which had to be satisfied to be considered an elastic event (and hence removed from the

sample). The requirements were: 1) $p_z(K^-)>8$ GeV/c, 2) MM^2 opposite the K^- between -2 and 5 GeV^2, and 3) MM^2 opposite the (K^-p) pair (assuming the positive track was a proton) between -0.2 and +0.2 GeV^2. The third requirement was quite loose but it was intentionally made less restrictive so most $K^-\pi^\circ p$ events would also be removed from the final sample. Because most elastic events had at least one dipole type track, the measurement errors on the elastic MM^2 quantities were very small hence very few true elastic events escaped this cut. The $\pi^+\pi^-n$ events where the $\pi^+\pi^-$ pair resulted from $\bar{K}^\circ$ decay were explicitly removed by cutting out events whose $(\pi^+\pi^-)$ invariant mass hypothesis was within 5 MeV of the K° mass. Events with final states of two charged mesons and a neutral baryon which was not a neutron (e.g. $K^-\pi^+\Delta^\circ$, $\pi^+\pi^-\Lambda$, $K^-K^+\Lambda$) were suppressed by both the trigger and the two prong hypothesis since only the neutral decay modes of the baryon could have satisfied the topology requirement (the vertex requirements also removed many of the hyperon recoil events). The hyperon recoil events have much smaller K^-p cross-sections which further limited their contribution to the background. However, it is likely that most of the events with a missing mass (opposite a $K^-\pi^+$ hypothesis) larger than a neutron mass are due to these other neutral baryon recoil events as well as due to $K^-\pi^+\pi^\circ n$ events. The majority of these background events were removed with the $0.2<MM^2<1.1$ GeV^2 cut.

Two methods were used to estimate the amount of background events remaining in the $K^-\pi^+n$ final data sample. The first method consisted of a fit to the data MM^2 distribution using the Monte Carlo MM^2 distribution and a parametrization of the expected background contributions (using a low order polynomial). This fit is shown in fig. 23a and the results from the fit give an estimated background contribution of 8 ± 4 %.

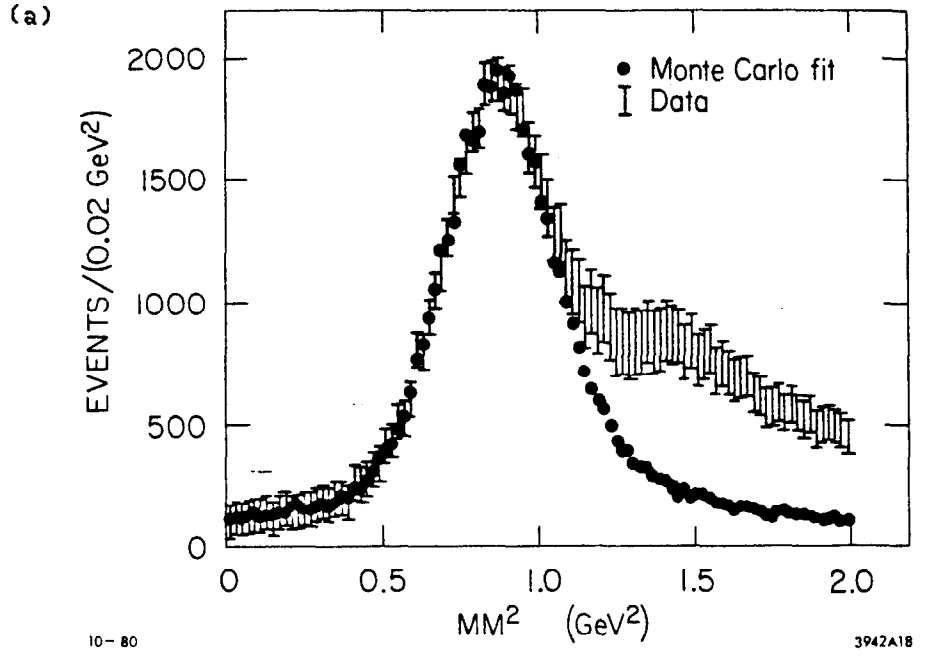

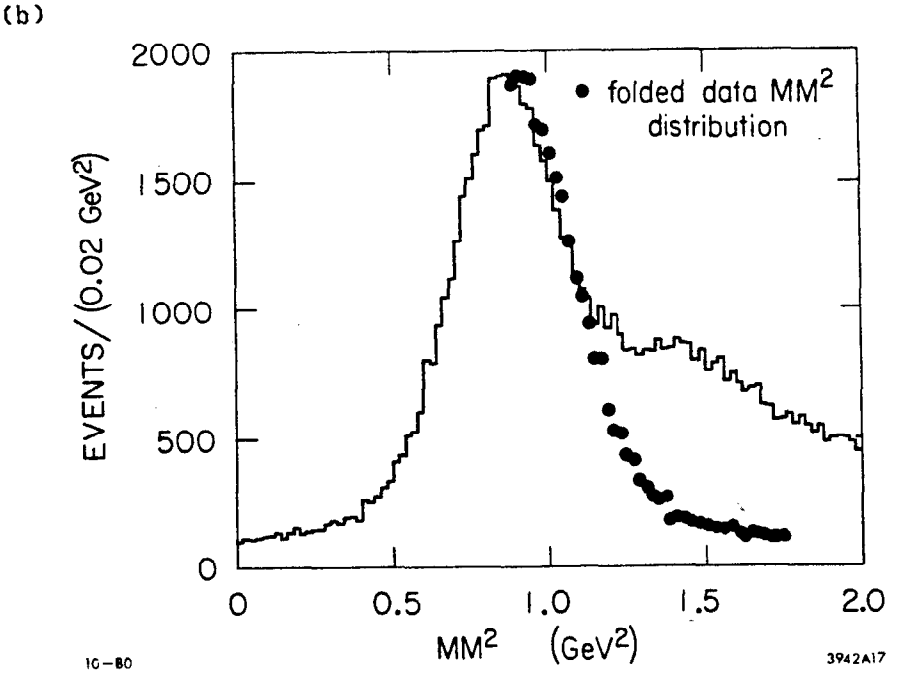

Figure 23 -- (a) Comparison of MM^2 (opposite $K^-\pi^+$) distributions for data events (error bars) and the Monte Carlo fit (●). (b) Comparison of MM^2 (opposite $K^-\pi^+$) distribution for data (histogram) with reflected data distribution (●), see text for explanation.

The second fit was based on the assumption that the data MM^2 distribution due to true neutron recoil events was symmetric about the neutron mass squared value (0.88 GeV^2). The justification for this assumption came from the very symmetric Monte Carlo MM^2 distribution (as can be seen in fig. 23a). By reflecting the leading edge of the data MM^2 distribution about the neutron mass squared value, one obtains the expected shape of the trailing edge of the distribution due to pure neutron recoil events. This comparison is shown in fig. 23b and resulted in a background contribution estimate of 0±4 %.

The two methods probably reflect the upper and lower limits of the background, so for the purposes of this thesis, the background contribution was assumed to be 4±4 %. Any residual background was most likely to come from $K^-\pi^+\Delta^0$ with small amounts of $K^-\pi^0 p$, $\pi^+\pi^-\Lambda$, $K^+K^-\Lambda$, and $K^-\pi^+\pi^0 n$ events as well.

It should be noted that a small fraction of good $K^-\pi^+ n$ events were removed along with background events in the elastic, $\bar{K}^0$, and MM^2 cuts. However, since these cuts were also applied to the $K^-\pi^+ n$ Monte Carlo events which were used to calculate the acceptance corrections, any biases due to these cuts were properly corrected in the angular moments results.

C. Normalization and Estimate of $\sigma(K^-p \rightarrow K^-\pi^+ n)$

Although not crucial to either the moments analysis or partial wave analysis, the determination of the absolute experimental normalization provides a rough check of the accuracy of the experimental acceptance.

In what follows, the sensitivity of the experiment will be calculated. This will be used to obtain the $K^-p \to K^-\pi^+n$ cross-section as measured by this experiment. The cross-section will then be compared to the existing world data as a rough check of the normalization.

The sensitivity is the product of the beam flux, the number of target particles and an acceptance correction term. There are a number of correction factors that go into each of the above three terms. These factors are given in Table 5 along with their errors. The acceptance correction term is a product of the spectrometer acceptance (which includes kinematical cuts) and the software loss factors from Table 5. The spectrometer acceptance is determined primarily from the Monte Carlo study. The sensitivity to be quoted will not include the spectrometer acceptance but will include the software loss factors. Given a K^- beam particle count of 4.05×10^8, a target density of .07082 gm/cm^3 (the density varied with time during the experiment but this effect was properly accounted for), and the aforementioned correction factors, the sensitivity associated with the raw data sample for this analysis is calculated to be:

$$S_0 = 1004 \text{ events}/\mu b \pm 12.5\% \text{ (in quadrature)} \pm 24.5\% \text{ (linear)} \quad \text{(VI.3)}$$

where the two estimates of the systematical error are obtained by adding the individual errors in quadrature and linearly. It is likely that the "true" error is close to the error from the quadrature method although not all of the factors were independent. The error from the linear sum best represents an upper limit to the actual error.

TABLE 5

Normalization Correction Factors

Type of Correction	Correction Factor and Error
Beam Correction Factors:	
a) beam deadtime and doubles	0.976 ± 0.013
b) trigger deadtime	0.990 ± 0.005
c) kaon beam decay	0.973 ± 0.003
d) kaon beam absorption	0.958 ± 0.005
Target Correction Factor:	
a) vertex cut	0.984 ± 0.010
Software Loss Factors:	
a) production job efficiency†	0.840 ± 0.100
b) software filter efficiency	0.820 ± 0.060

† Losses due to raw data unpacking failures, beam track reconstruction failures, and various other event reconstruction failures.

To calculate the total cross-section for the reaction $K^-p \to K^-\pi^+n$, the following relation is used:

$$N = \sigma \cdot S_0 \quad \text{thus} \quad \sigma = N / S_0 \tag{VI.4}$$

As stated above, the sensitivity value of 1004 events/μb does not include the spectrometer acceptance. In this calculation of the cross-section, this acceptance factor has been absorbed into the N term, i.e., the number of events used is the acceptance corrected number of events. But the acceptance corrected number of events does not include corrections for the kinematical cuts: $0.0 < |t'| < 0.2$ GeV^2 and $0.8 < M(K\pi) < 2.3$ GeV. Thus the cross-section calculation needs to include correction terms for these cuts and therefore is written as follows:

$$\sigma = N / (S_0 \, \epsilon_{|t'|cut} \, \epsilon_{M_{K\pi}cut}) \tag{VI.5}$$

The t' cut factor is calculated to be:

$$\epsilon_{|t'|cut} = 0.80 \pm 6\% \tag{VI.6}$$

assuming that:

$$(d\sigma/dt') \propto e^{-8|t'|} \quad \text{and} \quad \epsilon_{|t'|cut} = \frac{\int_0^{0.2} (d\sigma/dt') \, dt'}{\int_0^{\infty} (d\sigma/dt') \, dt'}$$

The M(Kπ) cut factor is determined by estimating the number of $K^-\pi^+n$ events outside the range $0.8 < M(K\pi) < 2.3$ GeV by looking at the full mass range from other $K^-p \to K^-\pi^+n$ experiments [16] with acceptance for the full mass range and with similar beam momenta. Then by scaling the mass plots from these other experiments to the number of events in the mass region 0.8 to 2.3 GeV^2 from this experiment, the number of events outside this

mass region can be estimated. The loss factor was calculated to be:

$$\epsilon_{M_{K\pi}cut} = 0.67 \pm 15\% \qquad \text{(VI.7)}$$

The value for N, the acceptance corrected number of $K^-\pi^+n$ events obtained from the moments analysis is 175,573 events hence the cross-section for $K^-\pi^+n$ is:

$$\sigma\,(K^-p \rightarrow K^-\pi^+n) = 326\ \mu b \pm 20\%\ \text{(quadrature)} \qquad \text{(VI.8)}$$

The error shown is the systematical error obtained by adding the errors from the individual terms in quadrature (the error for the sensitivity was the quadrature error of 12.5%). This value for the cross-section compares favorably with the known existing world data taken from CERN-HERA [17] as shown in fig. 24.

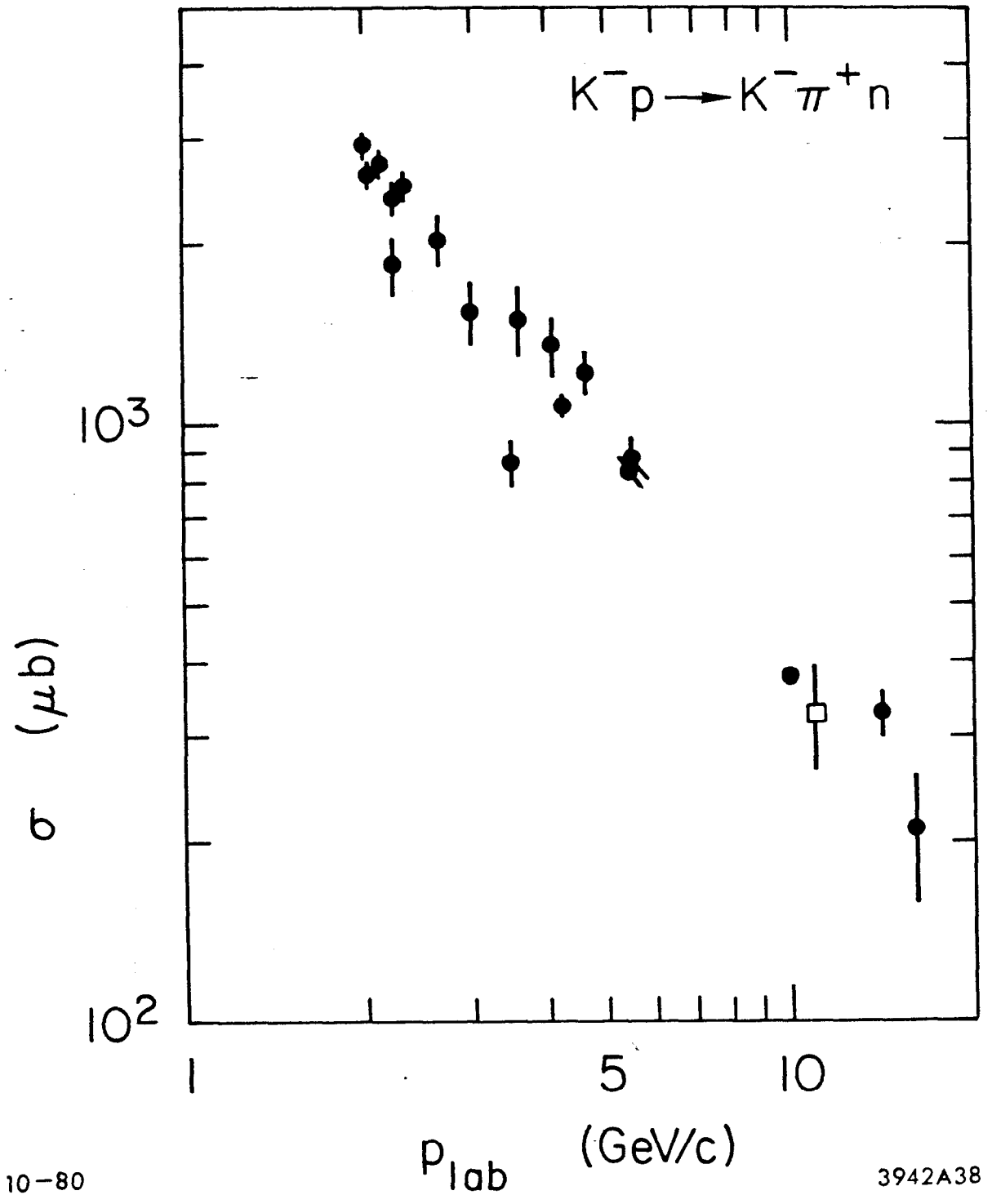

Figure 24 -- Comparison of $\sigma(K^-p \rightarrow K^-\pi^+n)$ from this experiment (□) with existing world data (●).

Chapter VII

ANALYSIS OF THE MOMENTS OF THE ANGULAR DISTRIBUTION

A. Overview

In this chapter, the moments of the Kπ angular distribution will be defined and the procedure used to obtain those moments will be described in section B. There were two independent methods that were used to obtain the moments, the maximum likelihood method and the method of moments (a linear algebra method). The maximum likelihood method will be described in detail in this chapter while the method of moments will be only briefly discussed since it was used primarily to provide an independent check of the first method. The details of the method of moments will be found in Appendix B. An essential part of obtaining the moments is the calculation of the spectrometer acceptance. This was an involved and fairly complicated process utilizing a sophisticated Monte Carlo program and will be discussed in section C of this chapter. The final set of Kπ elastic scattering moments obtained from this analysis will then be presented in section D. Special attention to the checks of stability, the error handling, and the physics implications will be given in the discussion of the moments. Finally, fits to the moments in terms of leading K* resonances will be presented and discussed.

B. Obtaining the Angular Moments

B.1 Statement of the Problem

The angular distribution produced in Kπ elastic scattering is denoted by I_{prod} and can be expanded in a series of spherical harmonic functions as shown in eq. VII.1:

$$I_{prod}(\Omega,x) = (4\pi)^{-1/2} \sum_{lm} t_{lm}(x)\, Y_{lm}(\Omega) \qquad \text{(VII.1)}$$

where the following shorthand has been used:

$$x = (M_{K\pi} , |t'|)$$
$$\Omega = (\cos\theta_J , \phi_J) \qquad \text{(VII.2)}$$

Determining the coefficients, t_{lm}, is the object of this part of the analysis since they are the acceptance corrected moments of the Kπ angular distribution.

The angular distribution that is observed in the experiment, I_{obs}, is not the same as I_{prod} but related as follows:

$$I_{obs}(\Omega,x) = A(\Omega,x)\, I_{prod}(\Omega,x) \qquad \text{(VII.3)}$$

The function A is the experimental acceptance function which in this analysis is determined by use of the Monte Carlo spectrometer simulation program. Then by using the observed experimental distributions and knowledge of the acceptance, the optimum set of moments, t_{lm}, can be obtained by various fitting techniques. The technique used to obtain the

$K\pi$ angular moments given in this analysis is known as the maximum likelihood method and is described in the next subsection.

In the analysis that follows, both the observed distribution function $I_{obs}(\Omega)$ and the acceptance distribution function $A(\Omega)$ will also be expanded in series of spherical harmonics. Three simplifications can be made to reduce the number of parameters in the equations that describe the spherical harmonic series for the produced, observed, and acceptance distributions. These simplifications are:

1) By invoking parity conservation it can be shown that the imaginary parts of the spherical harmonics do not contribute to the sum. Therefore we can rewrite eq. VII.1 as follows:

$$I_{prod}(\Omega,x) = (4\pi)^{-1/2} \sum_{lm\geq 0} t_{lm}(x)\,(2-\delta_{m0})\,\mathrm{Re}(\,Y_{lm}(\Omega)\,) \qquad \text{(VII.4)}$$

$$\text{where:}\quad \delta_{m0} = \begin{cases} 1, & m=0 \\ 0, & m>0 \end{cases}$$

It is possible however that the acceptance distribution $A(\Omega)$, if also expanded in a series of spherical harmonics, could contain non-zero imaginary terms which would then allow for imaginary terms in $I_{obs}(\Omega)$. From the Monte Carlo study it was shown that the imaginary terms in an expansion of $A(\Omega)$ were consistent with zero. Therefore, all the spherical harmonic expansions used in the following methods will be justifiably restricted to real terms only.

2) If the $M(K\pi)$ and t' space is subdivided into a grid of small bins, one can make the approximation that t_{lm} is constant throughout any small $(M(K\pi),t')$ bin. Then eq. VII.4 can be rewritten as follows for

each (M(Kπ), t′) bin:

$$I_{prod}(\Omega) = (4\pi)^{-1/2} \sum_{lm\geq 0} t_{lm} (2-\delta_{m0}) \, Re(Y_{lm}(\Omega)) \qquad \text{(VII.5)}$$

This same subdivision of M(Kπ) and t′ will be applied to the I_{prod} and A distributions.

3) The final simplification involves limiting the values of l (in the sums over l and m) to $\leq l_{max}$, where l_{max} is set to the highest value of l for which t_{lm} is non-zero. This requires trying various values of l_{max} until one obtains t_{lm} consistent with zero for all $l>l_0$, then l_{max} is set to l_0. In practice, $l_{max}=2J$, where J is the highest spin Kπ resonance that contributes to the angular distribution for that particular (M(Kπ), t′) bin. For example, for M(Kπ) much less than the mass of the spin 2 K* (1430 MeV), one sets l_{max} to 2 since the highest possible contributing resonance is spin 1 (J=1, so l_{max} = 2J = 2). The produced distribution can now be written as shown in eq. VII.6:

$$I_{prod}(\Omega) = (4\pi)^{-1/2} \sum_{lm=0}^{l_{max}} t_{lm} (2-\delta_{m0}) \, Re(Y_{lm}(\Omega)) \qquad \text{(VII.6)}$$

Because of the orthogonality of the spherical harmonic functions and the relation in eq. VII.4, it is clear that the l_{max} limit can also be applied to the expansions for I_{obs} and A.

At this point some additional shorthand will be useful to further simplify the equations. Let:

$$\mu = (l,m) \qquad \text{(VII.7)}$$

with the summation for $0 \leq l \leq l_{max}$, $0 \leq m \leq l$ understood in the definition of μ and then define:

$$Y_\mu'(\Omega) = (2-\delta_{m0})\, \mathrm{Re}(\, Y_\mu(\Omega)\,)$$

so finally:

$$I_{prod}(\Omega) = (4\pi)^{-1/2} \sum_\mu t_\mu\, Y_\mu'(\Omega) \qquad \text{(VII.8)}$$

In both the maximum likelihood method and in the method of moments, the above three simplifications will be assumed.

B.2 The Maximum Likelihood Method

In the maximum likelihood method one must define a likelihood function which can be maximized with respect to a set of parameters (in this case the parameters are the moments t_{lm}) so that the maximized function will result in the optimum set of parameters (the best set of moments t_{lm}). To apply this to the problem at hand, one must first introduce the normalization condition for the observed distribution.

$$n = \int I_{obs}(\Omega)\, d\Omega \qquad \text{(VII.9)}$$

In eq. VII.9, n is the expected number of observed events. One can now define a quantity p_i, the probability for observing event i, which occurs with coordinate Ω_i.

$$p_i = \frac{I_{obs}(\Omega_i)}{\int I_{obs}(\Omega)\, d\Omega} \qquad \text{(VII.10)}$$

Then using eq. VII.4 and eq. VII.7 this can be rewritten as:

$$p_i = \frac{1}{n} I_{prod}(\Omega_i) A(\Omega_i) \qquad \text{(VII.11)}$$

The next step requires expanding the acceptance function $A(\Omega)$ in terms of spherical harmonics.

$$A(\Omega) = \sum_{\mu} a_\mu Y_\mu(\Omega) \qquad \text{(VII.12)}$$

Then using this expansion and the expansion for I_{prod} (eq. VII.8) one obtains eq. VII.13:

$$p_i = \frac{1}{n} \sum_{\mu} t_\mu Y_\mu'(\Omega_i) \sum_{\mu} a_\mu Y_\mu(\Omega_i) \qquad \text{(VII.13)}$$

One now defines a likelihood function L, as the probability of observing a sample of N events each with probability p_i.

$$L = \left(\prod_{i=1}^{N} p_i \right) \left(e^{-n} n^N / N! \right) \qquad \text{(VII.14)}$$

The second term in eq. VII.14 is the probability of observing N events given a Poisson distribution with a mean of n. In this case n is the expected number of observed events from eq. VII.9. Rather than maximize L, it turns out to be easier to maximize $w=\log(L)$. This value w is known as the loglikelihood function and will be maximized with respect to the parameters t_{lm}, the angular moments. Using the definition of w and eq. VII.13 and eq. VII.14 one obtains eq. VII.15:

$$w = \sum_{i=1}^{N} \log \left[\left(\sum_{\mu} t_\mu Y_\mu'(\Omega_i) \right) \left(\sum_{\mu} a_\mu Y_\mu(\Omega_i) \right) \right] - n - \log N! \qquad \text{(VII.15)}$$

Going back to the definition of n (eq. VII.9) and substituting for I_{obs} with eq. VII.3 one arrives at eq. VII.16:

$$n = \int I_{prod}(\Omega)\, A(\Omega)\, d\Omega \qquad \text{(VII.16)}$$

Then by inserting the spherical harmonic expansions of I_{prod} and A and using the orthogonality property of the spherical harmonics, one obtains the series in eq. VII.17:

$$n = \sum_{\mu} t_{\mu}\, a_{\mu} \qquad \text{(VII.17)}$$

Now one can easily see that the log N! term in eq. VII.15 is independent of t_{μ} and will be omitted since it won't effect the maximization result. Similarly if the first log term is divided into two log terms, the log of the $a_{\mu}Y_{\mu}$ sum is also independent of t_{μ} and can also be omitted. The final representation of w becomes:

$$w = \sum_{i=1} \log\Big(\sum_{\mu} t_{\mu}\, Y'_{\mu}(\Omega_i) \Big) \; - \sum_{\mu} t_{\mu}\, a_{\mu} \qquad \text{(VII.18)}$$

In order to compute w, one needs to supply the acceptance distribution coefficients a_{μ} and also one needs the Y_{μ} value for each event in the data sample. The acceptance coefficients are determined by the Monte Carlo simulation procedure and will be described in detail in the next subsection. The Y_{μ} value for each event is easily calculated from the Gottfried-Jackson angles $\cos\theta_j$ and ϕ_j which are kept in the event output record on the data mini-DST tape.

The FORTRAN fitting program OPTIME [18] was used to maximize the value of w. This produced the optimum set of parameters t_{μ}, which are the $K\pi$ angular moments to be discussed in section D. The error matrix E

for the fit parameters t_μ, was given by the following formula:

$$E = D^{-1} C (D^{-1})^\dagger \qquad \text{(VII.19)}$$

where: $$D_{\mu\mu'} = \frac{\partial^2 w}{\partial t_\mu \partial t_{\mu'}}$$

$$C_{\mu\mu'} = \frac{\sum_{i=1}^{N} Y_\mu'(\Omega_i)\, Y_{\mu'}'(\Omega_i)}{\left[\sum_{\mu''} t_{\mu''} Y_{\mu''}'(\Omega_i) \right]^2}$$

The programs used to perform the initialization, setup, and output presentation of the OPTIME fit were modified versions the programs used by the SLAC group that performed the $K\pi$ scattering analysis in [5].

B.3 The Method of Moments

The method of moments was used to provide an independent check of the angular moments obtained from the maximum likelihood method. The method of moments is described in detail in Appendix B. What follows is a brief discussion of the basic principles of the method.

The method of moments starts with the basic relation of eq. VII.3 and by substituting the series expansion for I_{obs}, I_{prod}, and A, then by multiplying both sides by $Y_\mu(\Omega)$ and integrating over Ω one can set up a matrix equation of the form:

$$b_\mu = \sum_{\mu'} A_{\mu\mu'} t_{\mu'} \qquad \text{(VII.20)}$$

The b_μ are the coefficients of the spherical harmonics from an expansion of the observed distribution I_{obs}. $A_{\mu\mu'}$ is the acceptance correlation matrix and the $t_{\mu'}$ are the angular moments as before. By use of more

equations than unknowns in this matrix equation, a fit can be performed to reduce the errors in t_μ. A chi-squared function is defined and is minimized by standard matrix algebra techniques. One obtains the optimum set of parameters t_μ and the error matrix for t_μ as a result of this procedure. The computer programs used to obtain the moments by this method were once again modified versions of the programs used in the analysis of [5]. The moments obtained by this method and the moments obtained by the likelihood method in all cases agreed with each other to within the statistical errors from the fits (see the figures and the corresponding discussion of the stability of the moments in Appendix C).

C. The Acceptance Calculation

A standard method of determining spectrometer acceptance goes as follows. One expands the acceptance function in spherical harmonics.

$$A(\Omega) = \sum_\mu a_\mu Y_\mu(\Omega) \qquad \text{(VII.21)}$$

By multiplying both sides by $Y_\mu(\Omega)$, integrating over Ω, and using orthogonality of spherical harmonics, one obtains:

$$a_\mu = \int A(\Omega)\, Y_\mu(\Omega) \qquad \text{(VII.22)}$$

In a large statistics sample one can approximate this integral by a sum over events,

$$a_\mu \cong \sum_i^N w_i\, Y_\mu(\Omega_i) \qquad \text{(VII.23)}$$

where w_i is the probability (weight) that event i can be detected. In the usual case w_i is a product of trackfinding efficiency for each track and vertex reconstruction efficiency as determined from a Monte Carlo simulation of the detection apparatus. If the events are generated randomly in the angle variables Ω, the coefficients a_μ can be calculated to any degree of accuracy by selecting the sample size. However, the values of Ω (and $M(K\pi)_-$ and t') that one measures differ from the Monte Carlo generated values due to the finite resolution of the detection device. Unless the measurement errors are very small, the above method may not be accurate. Another approach to the problem is to go back to eq. VII.3, and rewrite it as:

$$A(\Omega) = \frac{I_{obs}(\Omega)}{I_{prod}(\Omega)} \qquad \text{(VII.24)}$$

Now replacing $A(\Omega)$ by its Y_μ expansion, multiplying both sides by $Y_\mu(\Omega)$, integrating over Ω, and using orthogonality gives:

$$a_\mu = \int \frac{I_{obs}(\Omega)}{I_{prod}(\Omega)} Y_\mu(\Omega)\, d\Omega \qquad \text{(VII.25)}$$

Now if the produced physics distribution is completely understood, one could generate Monte Carlo events with that distribution and obtain the I_{obs} distribution from the set of events that are successfully detected by the Monte Carlo spectrometer simulation program. With a large statistics sample, the a_μ can then be approximated by:

$$a_\mu \cong \sum_i^N \frac{w_i\, Y_\mu(\Omega_i)}{I_{mcprod}(\Omega_i)} \qquad \text{(VII.26)}$$

where w_i is the probability of being detected in the Monte Carlo simulator and N is the total number of Monte Carlo generated events.

Now the I_{prod} term in eq. VII.25 is not known exactly since it is the produced physics distribution. However, if a good approximation to I_{prod} can be made, one can employ an iterative procedure to get the best set of acceptance moments. This approximated distribution, called I_{mcprod}, is the distribution used by the Monte Carlo program to generate events.

For this analysis the iterative procedure began by approximating the I_{prod} distribution with a completely flat I_{mcprod} distribution in the variables $\cos\theta_j$ and ϕ_j (i.e., randomly generated in the ranges $-1 \leq \cos\theta_j \leq 1$, $-\pi \leq \phi_j \leq \pi$). The distribution in t' was generated using the simple exponetial form $e^{-\beta t'}$. The acceptance moments a_μ were then calculated and used as described in the maximum likelihood method to obtain a first order set of angular moments, t_μ. This set of moments was then used to make a more accurate approximation of I_{prod} as follows:

$$I_{mcprod}(\Omega) = N\,(4\pi)^{1/2} \sum_{\mu} (t_\mu/t_0)\, Y_\mu(\Omega_i) \qquad \text{(VII.27)}$$

where: N = total number of Monte Carlo generated events

$t_0 = t_{lm}$ for $l=0, m=0$

A second iteration was then performed which resulted in a new set of acceptance moments a_μ and subsequently a new set of physics distribution moments t_μ. A third iteration was performed to check that the procedure was indeed converging, i.e., that the a_μ and t_μ from the third iteration did not differ (within the statistical errors) from the second iteration. This was confirmed and the iterative procedure was terminated after the third iteration.

As pointed out earlier, the difference between the generated and the measured kinematical variables which was due to the spectrometer resolution was the main reason for this special procedure for calculating the acceptance moments. The iterative procedure, described above, properly accounts for measurement resolution effects on t', $\cos\theta_j$, and ϕ_j. However, there are also some measurement resolution effects on $M(K\pi)$. Since all our determinations of acceptance moments and physics moments were made in small $M(K\pi)$ bins, there was a possiblilty of having events generated in one $M(K\pi)$ bin but measured in another $M(K\pi)$ bin. Events crossing over into different $M(K\pi)$ bins were ignored in this analysis because the small number of events of this type did not alter the acceptance moments results.

A versatile acceptance calculation program was created so that the acceptance coefficients, a_μ (for the likelihood method) and the $A_{\mu\mu'}$ (for the method of moments) could be determined. This program read the tape of Monte Carlo events described in Appendix A and selected the appropriate $M(K\pi)$ and t' range for the sample. The sample was then required to pass the same geometrical and kinematical cuts that were to be applied to the data events (the PASSMC program). The events that successfully passed all cuts were then used to compute the acceptance coefficients using the sums of eq. VII.26 and eq. B.9.

A good indication of the basic spectrometer acceptance is shown in fig. 25, where the percent acceptance is given in a contour plot as a function of $M(K\pi)$ along the x-axis and $\cos\theta_j$ along the y-axis. The acceptance shown here includes the geometrical acceptance of the spectrometer, losses due to device inefficiency, decays, absorpton,

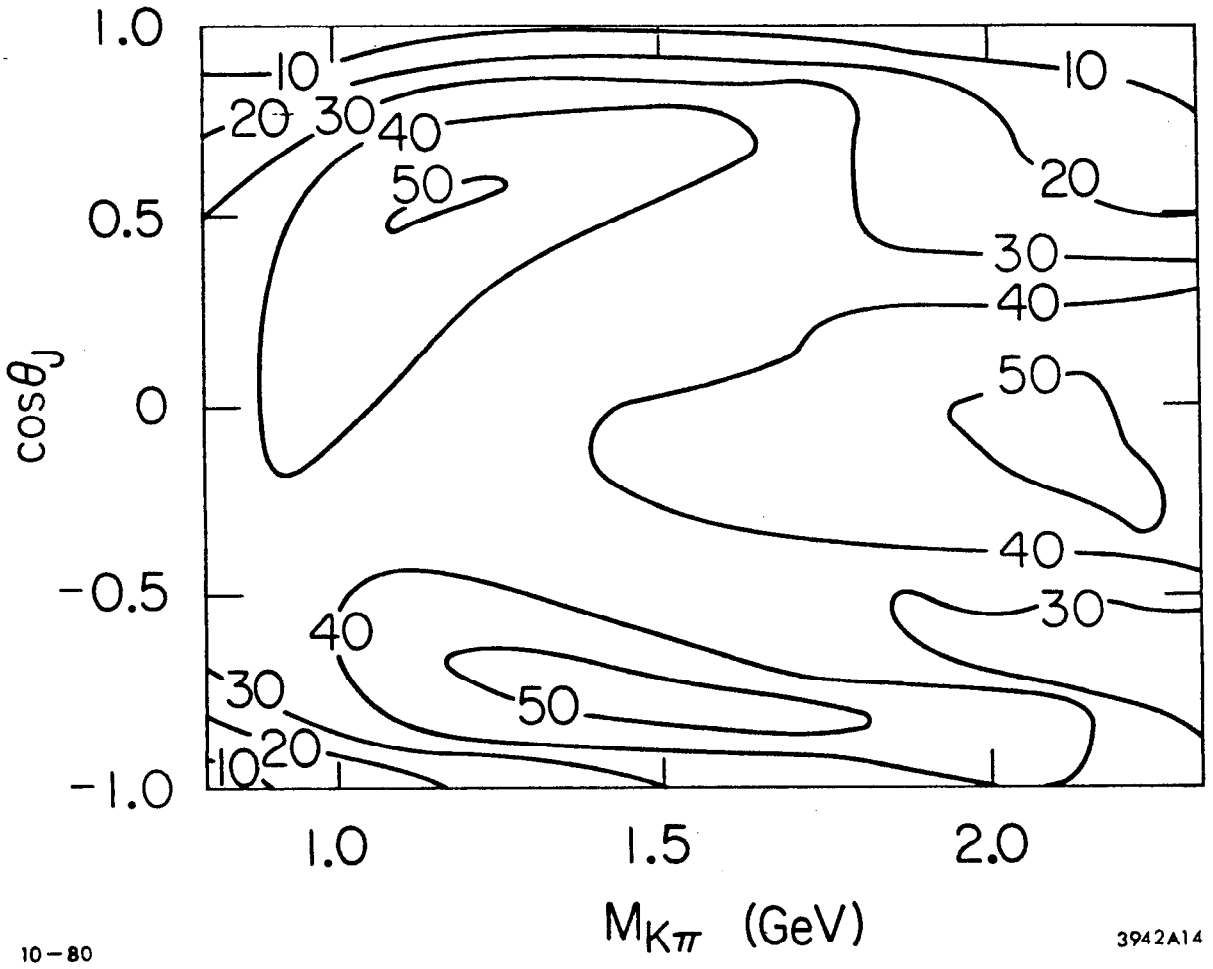

Figure 25 -- Acceptance contour plot. Contours denote percent acceptance for the reaction $K^-p \to K^-\pi^+n$ as determined by the Monte Carlo simulation program.

trackfinding inefficiency, event reconstruction inefficiency, and also losses due to geometrical and kinematical cuts. The geometrical and kinematical cuts used to produce the plot in fig. 25 are identical to those used to define the angular moments data sample (the PASSMC cuts of fig. 18). In most regions of M(Kπ), the acceptance is fairly high and relatively flat except in the forward ($\cos\theta_j$=1) region and sometimes in the backward ($\cos\theta_j$=-1) region. There is also a drop in acceptance for all $\cos\theta_j$ at low mass (M(Kπ)<0.8 GeV) and at high mass (M(Kπ)>2.3 GeV). This acceptance cut off at low and high mass essentially determine the range of M(Kπ) that was used in this analysis. These regions of poorer acceptance are for the most part due to the effect of the trigger requirements. However, the good acceptance in the vast majority of the kinematical regions allows for accurate acceptance corrections in the determination of the angular moments.

D. The Kπ Elastic Scattering Angular Moments

The unnormalized angular moments obtained from the procedure described in this chapter are shown as a function of M(Kπ) in figs. 26-28. The values for the moments and their errors are listed in Table 6. Note that in the region from 0.8 to 1.6 GeV the moments consist of 40 MeV wide bins plotted every 40 MeV and in the region from 1.6 to 2.3 GeV the moments consist of 80 MeV wide bins plotted every 40 MeV (overlapping bins). The moments were plotted in overlapping bins in the high mass region to help guide the eye. Where moments are not shown (at lower masses), they have been found to be consistent with zero. For the

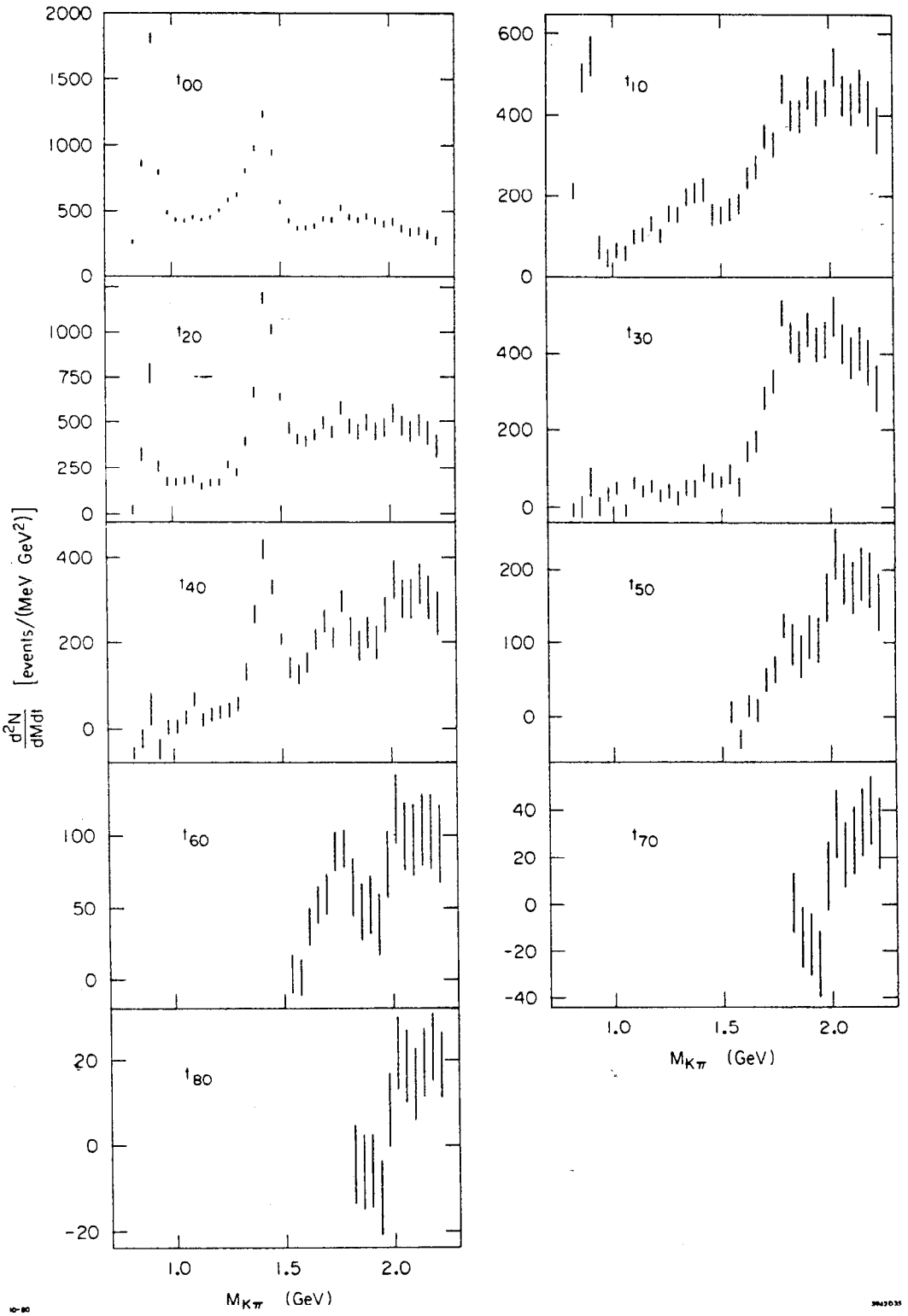

Figure 26 -- The unnormalized moments of the Kπ scattering angular distribution, t_{lm}, for l=0,...,8 ; m=0. Where no moments are shown, moments were found to be consistent with zero. Errors are statistical only.

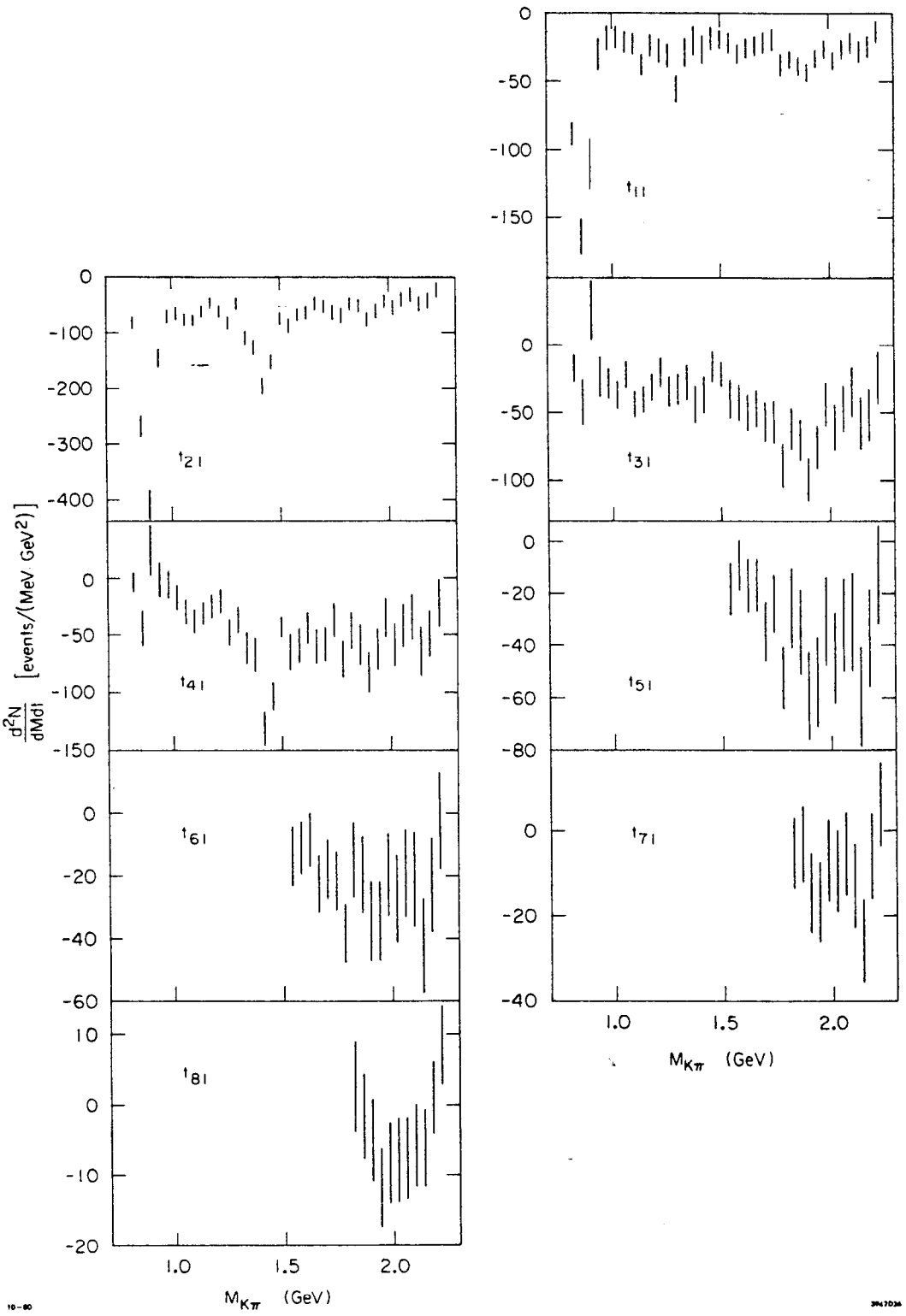

Figure 27 -- The unnormalized moments of the Kπ scattering angular distribution, t_{lm}, for l=1,...,8 ; m=1. Where no moments are shown, moments were found to be consistent with zero. Errors are statistical only.

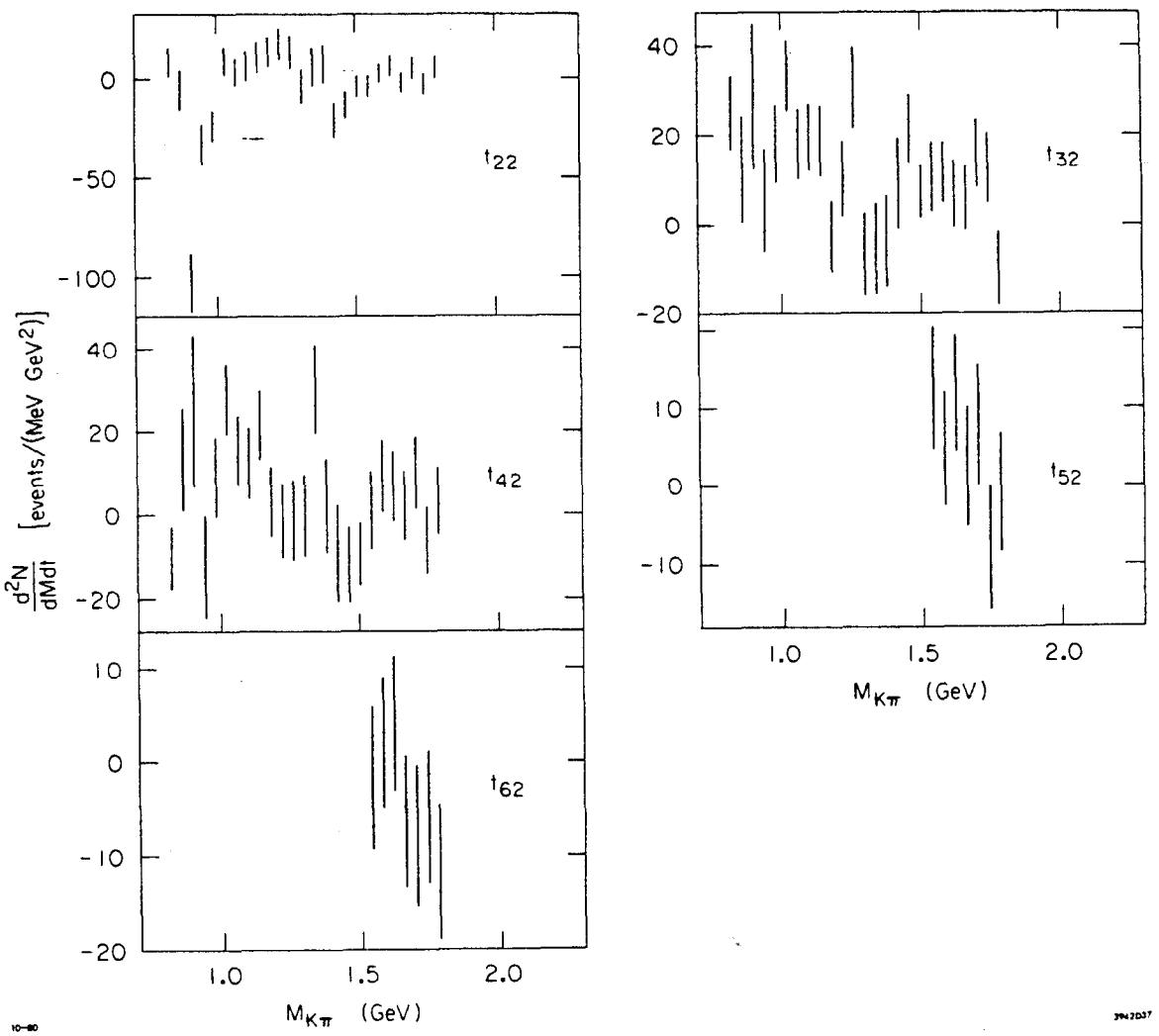

Figure 28 -- The unnormalized moments of the Kπ scattering angular distribution, t_{lm}, for l=2,...,6 ; m=2. Where no moments are shown, moments were found to be consistent with zero. Errors are statistical only.

TABLE 6

Unnormalized Acceptance Corrected Angular Moments

All masses are in GeV. Moments are in units of events/(MeV·Gev^2). Below each moment is the statistical error for that moment.

M(Kπ)	t_{00}	t_{10}	t_{11}	t_{20}	t_{21}	t_{22}	t_{30}	t_{31}	t_{32}	t_{40}	t_{41}	t_{42}	t_{50}	t_{51}	t_{52}	t_{60}	t_{61}	t_{62}
0.82	272.1	212.7	-87.9	22.0	-82.9	8.6	-7.1	-17.1	25.1	-56.3	-3.7	-10.1	- -	- -	- -	- -	- -	- -
	15.9	20.6	8.8	23.2	11.2	7.2	17.9	10.4	8.4	16.6	8.6	7.6	- -	- -	- -	- -	- -	- -
0.86	862.3	490.1	-164.2	326.4	-269.3	-5.6	0.5	-42.2	12.3	-24.4	-44.1	13.6	- -	- -	- -	- -	- -	- -
	27.5	37.0	13.7	38.5	19.5	10.5	28.5	16.8	12.0	24.0	15.7	12.4	- -	- -	- -	- -	- -	- -
0.90	1808.8	544.7	-110.5	776.7	-410.4	-103.1	65.5	26.4	28.6	44.3	24.8	25.2	- -	- -	- -	- -	- -	- -
	38.1	50.3	18.7	54.7	26.4	14.7	39.1	22.1	16.5	37.3	22.2	18.3	- -	- -	- -	- -	- -	- -
0.94	797.8	74.1	-30.1	260.6	-146.9	-32.9	2.2	-23.3	5.4	-47.1	-1.3	-12.3	- -	- -	- -	- -	- -	- -
	23.1	29.7	12.0	32.4	16.5	10.1	24.3	14.5	11.5	24.4	15.3	12.4	- -	- -	- -	- -	- -	- -
0.98	494.7	46.2	-18.1	174.2	-72.1	-23.7	32.1	-28.1	18.1	3.6	-5.9	9.2	- -	- -	- -	- -	- -	- -
	17.4	21.8	9.0	23.8	12.4	7.8	18.0	11.1	8.7	18.2	11.7	9.6	- -	- -	- -	- -	- -	- -
1.02	435.3	66.3	-17.4	173.1	-66.6	8.7	48.5	-36.9	33.2	5.3	-17.3	28.0	- -	- -	- -	- -	- -	- -
	16.3	20.3	8.2	22.1	11.3	7.0	16.7	10.4	7.9	16.6	11.0	8.6	- -	- -	- -	- -	- -	- -
1.06	427.4	57.6	-20.9	179.3	-76.9	3.8	-7.8	-21.8	18.0	25.8	-29.7	15.7	- -	- -	- -	- -	- -	- -
	16.0	19.1	8.0	22.0	10.9	6.9	16.0	9.9	7.7	16.4	10.8	8.5	- -	- -	- -	- -	- -	- -
1.10	455.0	101.0	-22.2	188.4	-78.2	6.2	61.1	-43.5	19.6	67.8	-38.3	12.7	- -	- -	- -	- -	- -	- -
	15.9	18.7	7.9	21.1	10.3	7.3	16.0	10.1	7.5	16.0	10.8	8.5	- -	- -	- -	- -	- -	- -
1.14	436.7	106.4	-37.9	149.9	-63.5	10.9	40.8	-40.4	18.6	19.7	-31.6	21.6	- -	- -	- -	- -	- -	- -
	14.9	17.6	8.1	19.4	10.0	7.4	15.7	9.9	7.9	15.3	10.3	8.4	- -	- -	- -	- -	- -	- -
1.18	455.7	133.2	-23.4	167.5	-47.8	13.6	54.0	-31.0	-2.8	30.1	-25.3	3.3	- -	- -	- -	- -	- -	- -
	15.2	18.2	8.3	20.3	10.1	7.5	16.4	10.2	8.0	16.0	10.4	8.3	- -	- -	- -	- -	- -	- -
1.22	506.4	103.7	-27.1	172.3	-63.7	17.5	29.2	-20.3	10.2	37.2	-20.8	-1.2	- -	- -	- -	- -	- -	- -
	15.5	18.2	9.0	20.3	10.5	8.1	16.6	10.8	8.4	16.5	10.9	8.9	- -	- -	- -	- -	- -	- -
1.26	585.8	157.6	-31.1	269.8	-83.5	13.4	41.5	-34.4	30.6	41.9	-48.1	-1.2	- -	- -	- -	- -	- -	- -
	16.8	20.3	9.2	22.7	11.5	8.4	18.0	11.4	9.1	17.5	11.6	9.6	- -	- -	- -	- -	- -	- -
1.30	624.2	154.8	-65.2	227.4	-48.7	-3.6	23.4	-32.7	-6.7	56.0	-37.4	-0.0	- -	- -	- -	- -	- -	- -
	16.9	20.0	9.6	22.2	11.3	8.9	18.8	11.7	9.4	17.9	11.8	9.9	- -	- -	- -	- -	- -	- -
1.34	807.3	198.8	-29.0	398.1	-109.4	6.1	50.9	-27.7	-5.4	131.1	-62.0	30.4	- -	- -	- -	- -	- -	- -
	19.3	23.2	10.7	26.2	13.2	9.7	20.9	13.1	10.2	20.4	13.6	10.8	- -	- -	- -	- -	- -	- -
1.38	976.9	208.7	-19.9	672.5	-127.5	7.5	47.1	-44.0	-3.7	264.0	-67.6	2.2	- -	- -	- -	- -	- -	- -
	21.1	26.3	10.8	29.7	13.9	9.6	22.4	13.9	10.3	22.3	14.5	11.3	- -	- -	- -	- -	- -	- -
1.42	1231.3	216.5	-26.5	1189.1	-196.5	-20.9	88.9	-37.1	9.2	416.0	-132.0	-9.0	- -	- -	- -	- -	- -	- -
	23.8	30.7	10.4	35.0	15.3	9.0	24.1	13.8	10.2	23.8	15.2	11.6	- -	- -	- -	- -	- -	- -
1.46	943.3	154.5	-18.4	1018.0	-153.6	-13.1	68.4	-15.9	21.5	326.9	-104.0	-11.8	- -	- -	- -	- -	- -	- -
	20.7	27.2	8.6	30.3	13.5	6.9	19.9	11.3	7.8	19.8	12.2	9.2	- -	- -	- -	- -	- -	- -
1.50	568.6	153.8	-19.1	645.0	-74.8	-3.6	64.7	-21.5	7.5	205.3	-43.9	-9.2	- -	- -	- -	- -	- -	- -
	16.3	21.8	6.8	23.7	10.8	5.3	14.7	9.1	5.9	15.4	9.3	7.5	- -	- -	- -	- -	- -	- -
1.54	428.0	167.1	-21.9	469.1	-88.3	-3.5	85.1	-39.7	10.7	139.2	-65.5	1.3	6.0	-18.3	12.5	3.6	-13.8	-1.7
	19.3	27.8	7.6	31.2	12.7	5.4	26.6	14.5	7.8	25.1	15.6	9.3	14.8	10.1	7.9	13.6	9.5	7.6
1.58	373.6	181.0	-29.6	410.2	-69.1	3.0	51.8	-42.4	11.5	124.1	-60.0	9.2	-31.1	-9.1	4.8	0.8	-11.2	2.0
	17.3	25.2	7.1	28.0	11.9	4.8	23.7	13.6	6.9	22.1	14.4	8.6	13.5	9.8	7.3	12.6	8.4	7.0
1.62	376.0	245.6	-25.7	398.2	-65.9	6.6	143.6	-50.1	6.8	151.2	-44.9	6.9	14.4	-17.1	11.8	36.6	-8.7	4.1
	18.7	26.9	7.4	30.0	12.1	5.1	26.4	13.7	7.4	23.7	14.1	8.4	14.7	10.4	7.5	13.3	8.7	7.3
1.66	389.5	272.3	-23.9	433.3	-48.9	-1.6	171.1	-46.9	5.9	204.1	-60.9	2.4	7.9	-16.7	2.6	51.2	-22.9	-6.4
	19.8	28.6	7.3	32.5	12.2	5.1	27.6	13.9	7.3	25.0	14.5	8.3	15.8	10.2	7.7	13.2	9.1	7.0
1.70	443.4	347.4	-21.4	496.1	-54.3	5.2	283.2	-56.9	15.8	246.8	-59.3	10.1	50.2	-34.5	7.7	58.8	-17.9	-7.9
	21.3	31.1	7.6	34.6	12.7	5.4	30.0	14.6	7.6	26.3	14.7	8.6	16.7	11.3	7.7	14.3	9.4	7.5
1.74	439.1	328.3	-19.3	446.5	-64.9	-2.4	326.9	-57.3	12.5	207.4	-38.1	-6.0	63.6	-24.1	-7.9	88.3	-21.9	-5.9
	22.0	31.6	8.1	34.9	13.1	5.6	31.3	15.4	7.8	26.0	15.1	8.1	17.3	11.2	7.9	13.9	9.4	7.1
1.78	524.2	464.9	-37.9	581.3	-70.1	5.8	504.0	-88.8	-10.0	291.8	-71.6	3.3	122.6	-52.6	-0.9	89.9	-38.6	-11.8
	25.1	36.3	8.5	39.6	13.9	5.7	34.7	16.4	8.2	26.9	15.3	8.0	17.0	11.8	7.6	13.6	9.5	7.2

TABLE 6 (cont.)

M(KB)	t_{00}	t_{10}	t_{11}	t_{20}	t_{21}	t_{30}	t_{31}	t_{40}	t_{41}	t_{50}	t_{51}	t_{60}	t_{61}	t_{70}	t_{71}	t_{80}	t_{81}
1.82	457.2	399.8	-34.2	478.3	-49.4	440.1	-62.0	221.9	-47.3	97.8	-25.7	63.3	-15.0	0.2	-5.4	-4.7	2.6
	23.7	37.5	6.7	42.2	11.8	40.6	15.0	35.9	16.6	28.4	15.6	20.5	12.0	12.8	8.4	9.4	6.4
1.86	434.6	398.1	-38.8	446.9	-52.4	416.1	-70.6	187.3	-59.6	81.3	-34.7	46.2	-19.8	-14.4	-3.2	-6.3	-1.6
	24.3	38.6	6.9	43.4	12.2	41.6	15.4	36.5	17.1	28.8	16.2	20.2	12.3	13.1	8.9	9.0	6.1
1.90	463.1	455.6	-43.6	497.9	-77.1	460.6	-99.3	217.0	-83.5	107.7	-59.3	51.2	-34.8	-17.3	-14.7	-6.1	-5.0
	25.8	41.0	6.9	45.8	12.6	43.7	15.9	37.8	17.7	29.7	16.8	20.2	12.8	13.4	9.3	8.7	5.9
1.94	426.3	418.3	-33.4	450.8	-62.4	421.3	-75.7	195.9	-63.8	103.4	-53.9	37.7	-34.7	-25.8	-16.8	-12.4	-11.7
	26.7	42.5	7.0	47.6	12.7	45.5	16.1	39.6	17.8	31.1	16.9	21.5	12.8	14.2	9.4	8.9	5.6
1.98	404.8	442.6	-26.1	468.8	-45.1	433.7	-43.7	258.7	-36.6	161.3	-30.8	79.4	-19.8	11.6	-7.1	8.1	-8.2
	27.6	43.9	6.8	49.8	12.6	47.9	16.0	42.1	17.8	33.2	16.9	23.3	13.3	14.6	9.5	8.8	5.6
2.02	422.7	517.9	-35.0	550.7	-56.4	496.3	-60.9	341.0	-59.6	219.8	-44.7	117.0	-27.7	33.9	-9.4	21.4	-7.8
	30.2	48.0	7.0	54.3	13.1	51.9	16.8	45.1	18.5	35.0	17.4	24.3	14.0	14.5	9.7	8.6	6.1
2.06	371.5	448.7	-26.7	479.3	-41.6	423.7	-47.0	298.3	-42.9	185.8	-32.0	98.3	-19.5	20.7	-5.4	18.2	-7.6
	30.8	49.0	7.2	55.5	13.6	52.8	17.3	45.5	19.0	34.9	17.7	24.1	14.1	14.1	9.7	8.5	5.9
2.10	343.9	427.1	-21.7	448.6	-33.2	386.9	-34.8	297.4	-35.9	173.9	-31.0	95.7	-21.3	26.7	-13.0	13.9	-5.8
	32.0	50.9	7.4	57.5	14.0	54.7	18.4	47.0	20.3	35.8	18.7	25.0	15.1	14.5	9.9	8.4	6.0
2.14	352.2	459.5	-28.0	481.3	-49.8	410.8	-57.5	330.8	-65.7	193.0	-58.6	102.9	-42.4	34.5	-26.0	19.0	-6.2
	34.2	54.4	7.7	60.9	14.6	57.5	19.3	48.9	21.0	36.8	19.1	25.6	15.3	14.3	9.9	8.0	5.6
2.18	324.7	429.7	-24.4	439.6	-44.3	375.0	-51.7	301.3	-50.1	184.2	-37.2	101.5	-23.2	39.6	-5.9	22.9	1.1
	35.1	55.9	7.7	62.9	14.6	59.6	18.9	50.8	20.5	38.6	18.7	26.3	15.0	14.6	10.0	8.0	5.2
2.22	277.4	363.4	-13.4	366.6	-24.9	307.8	-24.6	261.6	-24.2	154.6	-12.8	93.2	-2.5	29.6	6.3	18.3	8.5
	35.9	57.6	7.9	64.7	14.8	61.4	19.5	52.3	21.0	39.4	19.2	27.1	15.5	15.2	9.9	7.7	5.6

lower M(Kπ) range (0.8 to 1.8 GeV) the moments were allowed to have values for the m index ranging from 0 to 2 since the moments with m>2 were shown to be consistent with zero. For M(Kπ)>1.8 GeV, the moments with m>1 were shown to be consistent with zero and thus only m=0 and m=1 moments are shown.

The error bars shown in these plots correspond to the appropriate diagonal matrix elements of the error matrix of eq. VII.19 (a statistical significance of one standard deviation). It should be noted that the angular moments are highly correlated (an effect due to the non-uniformity of the acceptance) which means that the off-diagonal error matrix elements are non-zero. This indicates that the errors given in figs. 26-28 and Table 6 are not independent and thus any fits to the moments must use the full error matrix in order to obtain statistically correct results.

As mentioned previously, the moments presented here were obtained using the maximum likelihood method. These moments were found to be consistent within statistical errors with the moments obtained from the method of moments. Also, many tests were performed that demonstrated that these moments were stable with respect to a variety of geometrical and kinematical cuts. This stability with respect to cuts indicated that the Monte Carlo program accurately simulated the spectrometer acceptance. A discussion of tests of stablility of the moments as well the results from three of the more important tests is given in Appendix C.

By examining the even l, m=0 moments, the resonance structure in Kπ scattering can be quickly seen. A resonance with mass M and spin J

should show up as a peak-like structure in the l=2J moment at a mass M with no structure at that mass for any higher l moments. In the case of a leading resonance, one would expect the l=2J moment to be consistent with zero for masses below M and one would expect the higher l moments to also be consistent with zero for masses up to M. Using this criteria, there is clear evidence for the spin 1 K*(895) from the strong peak in the t_{20} moments at 895 MeV and no structure in higher moments. The same reasoning leads to the assignment of the resonances near 1430 MeV and 1780 MeV as spin 2 and 3 respectively. Parity conservation requires that the parity assignment of a spin J Kπ resonance decaying into $K^-\pi^+$ to be $P=(-1)^J$. Thus the angular moments give confirmation of the $J^P = 1^-$ K*(895), the 2^+ K*(1430) and the 3^- K*(1780) resonances.

Additional support to this resonance interpretation comes from the behavior of the odd l, m=0 moments. The effects of interference between resonances of differing angular momentum can be seen as a slight drop followed by a rapid rise in the proper odd l moment in the mass region between the interfering resonances. One example of this can be seen clearly in the 1.5 to 1.7 GeV region of the t_{50} moment indicating the interference between the spin 2 K*(1430) and the spin 3 K*(1780).

In order to determine the masses and widths for these resonances, a simple Breit-Wigner resonance model was fit to the leading 2J moment (t_{20}, t_{40}, and t_{60} for the spin 1, 2, and 3 resonances). The fits are shown as the curves in figs. 29a-c. The values for the masses and widths are listed in Table 7. The exact Breit-Wigner parametrization used in these fits is described in Appendix E. The mass and width measurements for the K*(895) and K*(1430) resonances from the partial wave analysis

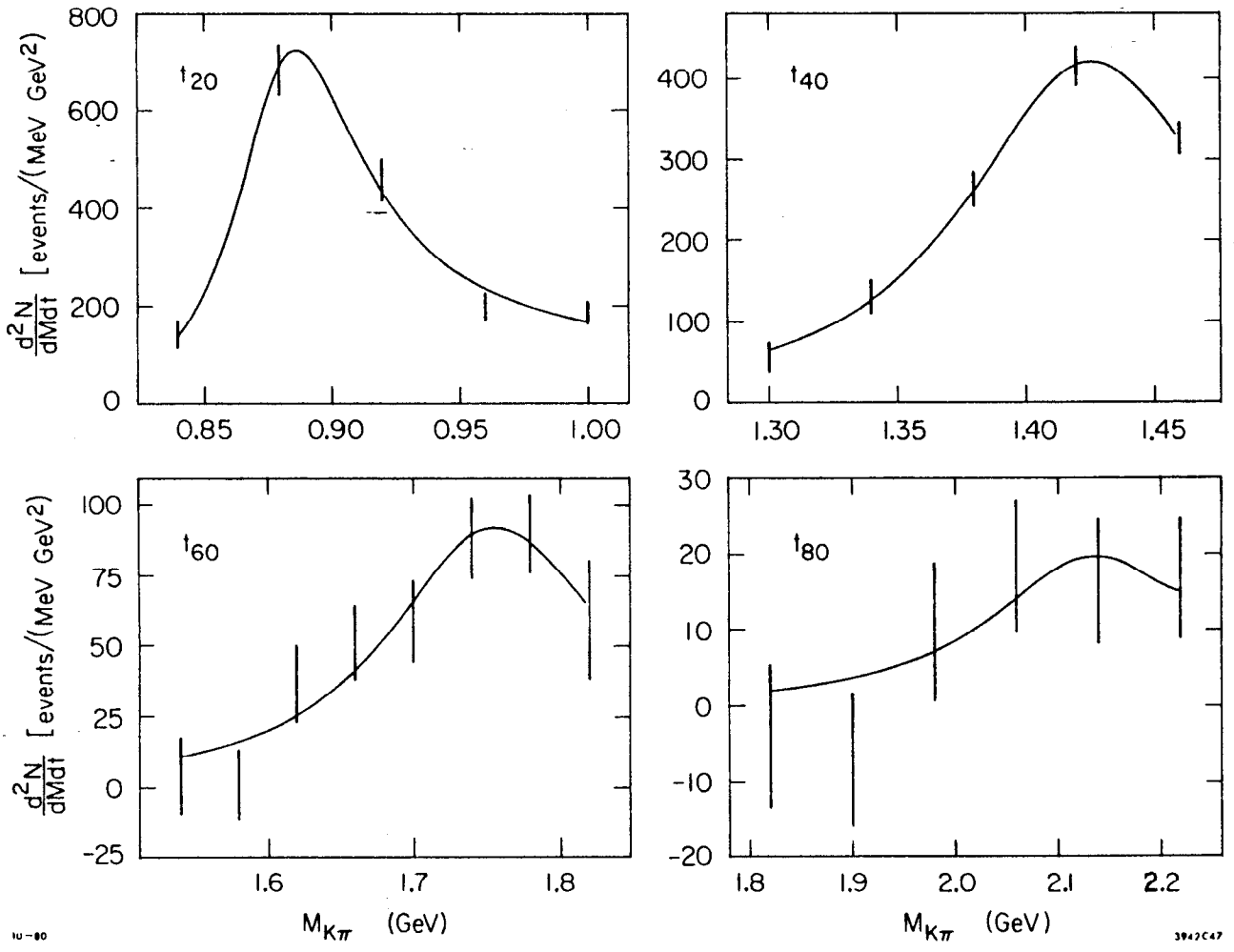

Figure 29 -- Breit-Wigner resonance fits to the leading m=0 moments. Plotted points are the moments from fig. 26, curves are the results from the fits. (a) Spin 1 fit to t_{20} moment. (b) Spin 2 fit to t_{40} moment. (c) Spin 3 fit to t_{60} moment. (d) Spin 4 fit to t_{80} moment.

TABLE 7

Breit-Wigner Resonance Parameters from Fits to Moments

(a) Spin 1 fit to t_{20} moment. (b) Spin 2 fit to t_{40} moment. (c) Spin 3 fit to t_{60} moment. (d) Spin 4 fit to t_{80} moment. (e) Special simplified spin 4 amplitude fit to the t_{60}, t_{70}, and t_{80} moments.

(a)	Parameter	Fit Result
	Mass	887.0 ± 3.3 (± 2.0)* MeV
	Width	58.8 ± 7.1 MeV
	χ^2/DOF†	2.9/1

(b)	Parameter	Fit Result
	Mass	1426 ± 3 (± 4)* MeV
	Width	118 ± 13 MeV
	χ^2/DOF†	0.32/2

(c)	Parameter	Fit Result
	Mass	1756 + 17 − 13 (± 20)* MeV
	Width	185 + 53 − 38 MeV
	χ^2/DOF†	3.4/5

(d)	Parameter	Fit Result
	Mass	2140 + 140 − 60 (± 30)* MeV
	Width	250 + 300 − 130 MeV
	χ^2/DOF†	2.5/3

(e)	Parameter	Fit Result
	Mass	2075 + 40 − 30 (± 30)* MeV
	Width	240 + 400 − 80 MeV
	χ^2/DOF†	15.7/13

* Estimated systematical error
† DOF = # of degrees of freedom

(Chapter VIII) were more accurate and used a more proper parametrization than these simple fits to the moments. Thus the mass and width values shown here should only serve as a test that the method of fitting to the leading moment gives reasonably reliable results. However, due to the effect of backgrounds and the limited statistics at higher masses, the mass and width of the K*(1780) may be as well determined or possibly better determined in the fit to the leading moment than the fit to the partial wave amplitude. In all three cases the Breit-Wigner fit to the leading moment produces a resonance mass and width that agrees reasonably well with the expected values from the existing world data (see Table 13 for comparison to PWA fit results and Particle Data Group [2] values).

In addition, due to the high statistics and good acceptance at high $K\pi$ masses in this experiment, it was possible to extract the I=7 and I=8 moments for $M(K\pi)>1.8$ GeV. For the t_{80} plot, the moment is seen to rise from zero with a peak occurring near 2100 MeV and a slight drop at higher masses. A similar peaking at the same mass is seen in the t_{60} plot. A look at the t_{70} moment in the 1.8 to 2.0 GeV region reveals a drop followed by a rapid rise, structure indicative of interference between a spin 3 and a spin 4 object. As can be seen in fig. 30, the t_{90} and $t_{10\ 0}$ moments were also obtained and are consistent with zero for the entire $K\pi$ mass range used in this analysis (up to 2.3 GeV). All of these facts are interpreted as evidence for a new leading K* resonance near 2100 MeV with a spin-parity assignment of 4^+.

Because of the possibility of sizeable backgrounds in the high mass region, the determination of the exact mass and width of this spin 4

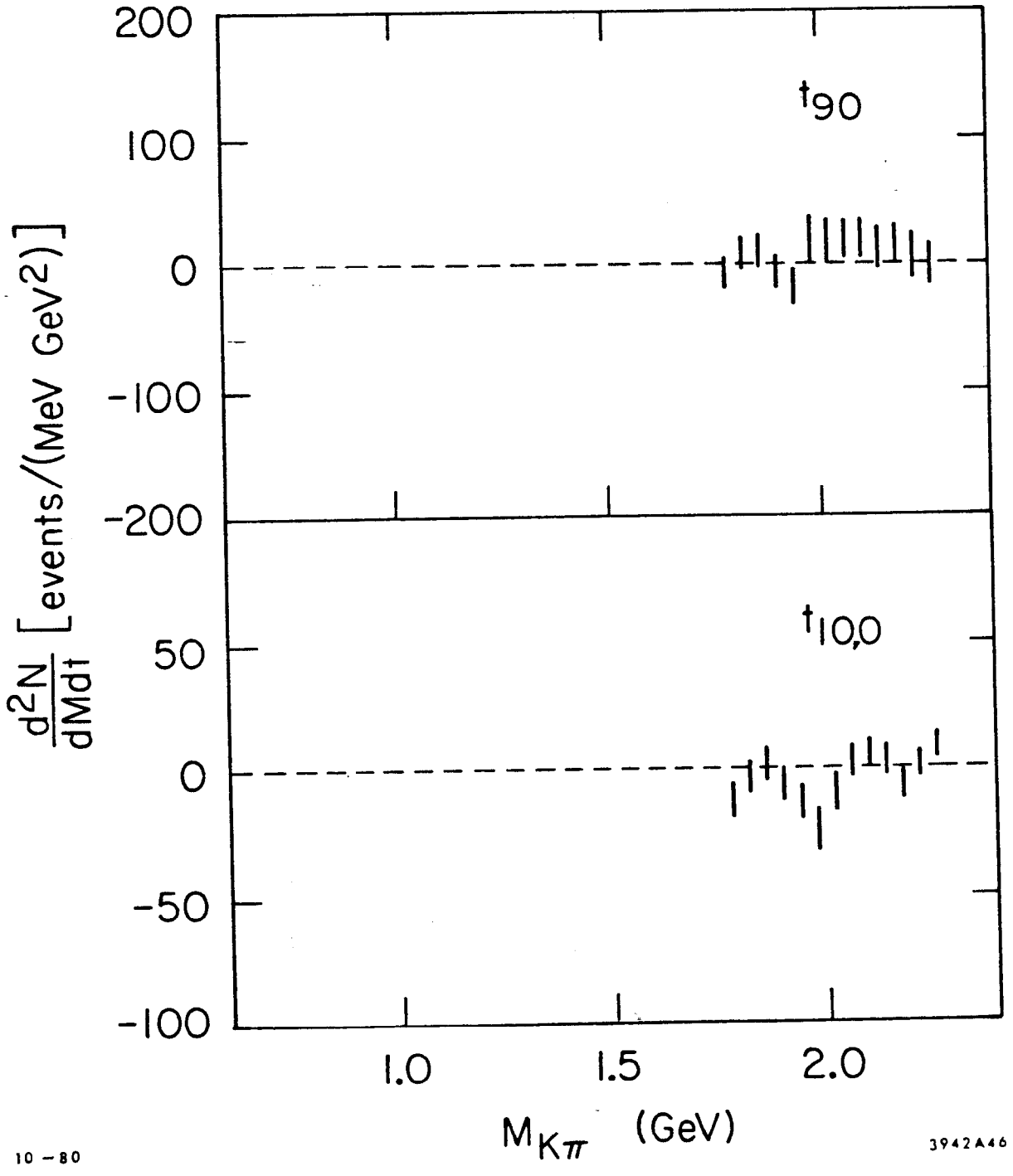

Figure 30 -- The t_{90} and $t_{10,0}$ moments (from a separate moments fit with $l \leq 10, m \leq 1$ moments allowed).

resonance was rather difficult. A simple Breit-Wigner fit to the leading t_{80} moment was performed and the results shown in fig. 29d. The values for the mass and width of this resonance as determined from this fit are given in Table 7. A more sophisticated mass dependent fit to the t_{60}, t_{70}, and t_{80} moments based on a relativistic Breit-Wigner resonance parametrization for both the spin 3 and spin 4 resonances including simple polynomial background terms for the D, F, and G waves (using spectroscopic notation for the J=2, 3, and 4 angular momentum waves) was also performed. In this fit the mass and width of the leading spin 3 resonance were fixed at $M(K\pi)$=1753 MeV and Γ=185 MeV respectively. These values were taken from the fit to the t_{60} moment mentioned above. Although the mass and width of the spin 3 resonance was not well determined, the results obtained for the spin 4 resonance were found to be not very sensitive to the exact values of the fixed spin 3 mass and width. The spin 4 fit is shown in fig. 31 and the values for the mass and width are presented in Table 7. A detailed analysis of this spin 4 resonance based on a slightly larger data sample also taken from this experiment (defined by a less restrictive MM^2 cut) has been presented in ref. [19]. The mass and width quoted in that study were M=2086 MeV and Γ=180 MeV. As in the case of the lower spin resonances, a comparison of all the leading $K\pi$ resonance fits (using moments and using partial wave amplitudes) is given in Table 13. The resonance parametrizations for the fits to the spin 4 object are described in Appendix E. A more detailed discussion of the results from the various resonance fits can be found in VIII.G.6).

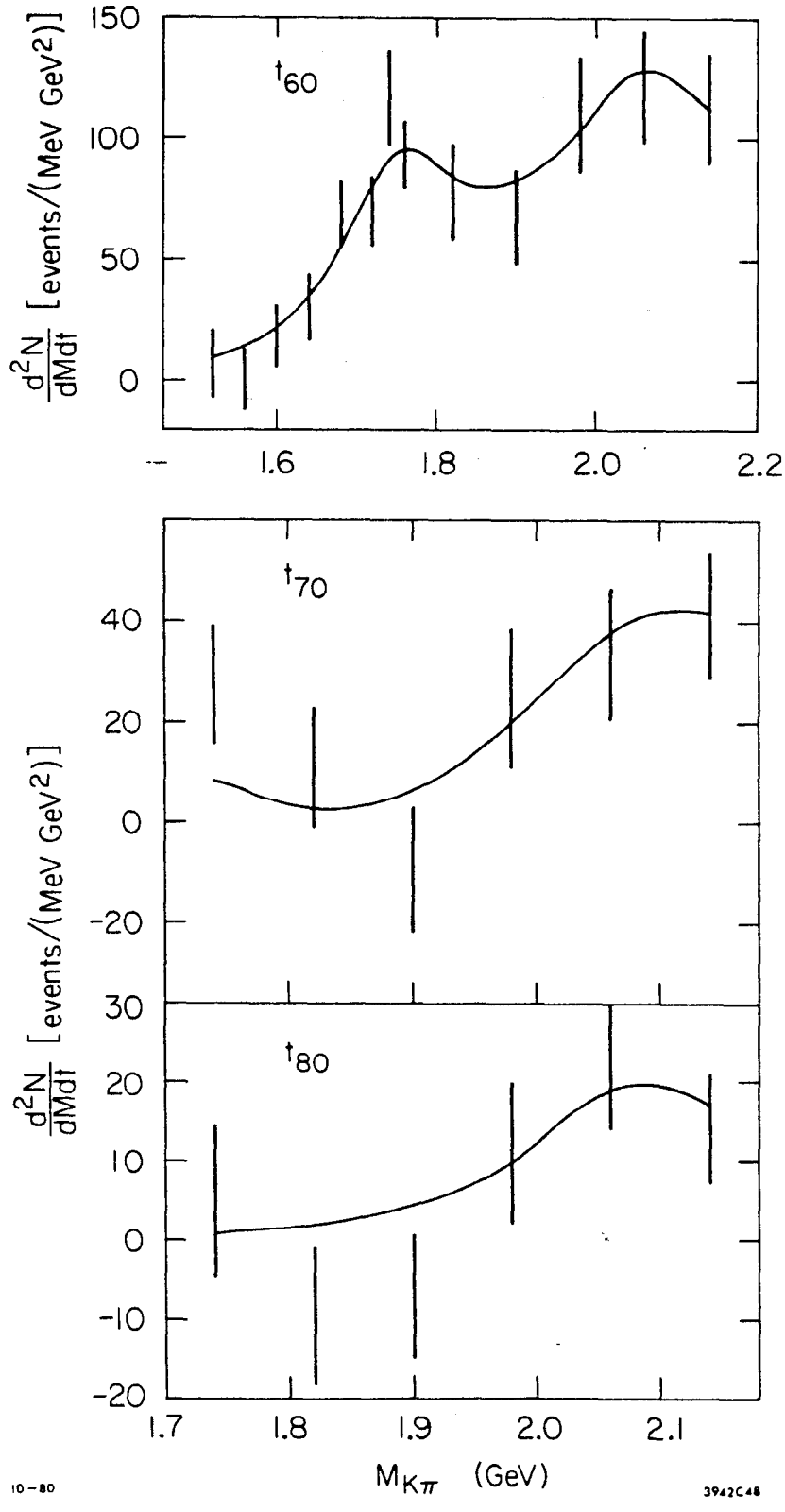

Figure 31 -- Special simplified Breit-Wigner amplitude fit to the t_{60}, t_{70}, and t_{80} moments. Plotted points are the moments from fig. 26, curves are results from the fit. See text for details.

Chapter VIII

PARTIAL WAVE ANALYSIS

A. Introduction

The angular moments of the $K\pi$ scattering angular distribution show clear structure indicating the leading $K\pi$ resonance behavior. In order to obtain the masses, widths, and spin assignments of these leading resonances and in order to reveal any underlying resonance structure, one must apply a partial wave analysis (PWA) to the data.

The goal of this analysis was to obtain the $K\pi$ elastic scattering partial waves. The first step in the procedure was to isolate the pure $K\pi$ scattering amplitude from the $K\pi$ production amplitude. This required a model which related the scattering amplitude to the production amplitude using a parametrization of the t' dependence of the production amplitude. Then a partial wave fit was performed to the angular moments in several consecutive small t' bins in order to determine the values of the parameters describing the t' dependence. This step was known as the multi-t' bin partial wave analysis. It was then possible to integrate the amplitudes over the entire t' range (0.0 to 0.2 GeV^2) and perform a second, more detailed series of partial wave fits to the angular moments (this step was called the single t' bin partial wave analysis). The results from these fits are the $K\pi$ elastic scattering partial waves given as a function of $K\pi$ mass. The structure and features of these partial waves clearly reveal the mass, width, and spin of $K\pi$ resonances.

In this chapter, the model relating the Kπ elastic scattering amplitude to the production amplitude will be the first topic discussed. Then the partial wave fitting procedure used to obtain the parameters expressing the t' dependence of the model will be described in detail. The results of the fits, the parameter values from the fits, and the implications of the results will then be presented. The next step will be the description of the single t' bin partial wave fitting procedure. A special section explaining some of the assumptions used in the fits and explaining some of the conventions used in the presentation of the partial wave results will follow. Finally the Kπ elastic scattering amplitudes will be presented and discussed in terms of their resonance structure.

B. The Kπ Scattering Model

The procedure used to partial wave analyze the Kπ scattering data involved selecting a model which would best describe the small t', $K^-p \to K^-\pi^+n$ reaction and would isolate the contribution from π exchange. A suitable model was chosen which required parametrization of the t' dependence of the Kπ scattering amplitude. The model used to describe the Kπ scattering production amplitude in this analysis was a simplified Regge pole exchange model used in a similar Kπ scattering PWA from [5]. The model was found to provide an excellent description of Kπ scattering data in several previous analyses. For each Kπ mass bin the t' dependence of the Kπ production amplitudes $L_{\lambda\pm}$, with angular momentum L and t-channel helicity λ by natural (+) or unnatural (-) parity exchange was

given by:

$$L_0 = g_L \frac{\sqrt{-t}}{\mu^2 - t}$$

$$L_{1-} = \frac{1}{\sqrt{2}} g_L \sqrt{L(L+1)}\, \gamma_c \qquad \text{(VIII.1)}$$

$$L_{1+} = \frac{1}{\sqrt{2}} g_L \sqrt{L(L+1)}\, (\gamma_c - 2i\gamma_a |t'|)$$

$$L_{\lambda\pm} = 0 \quad , \lambda \geq 2$$

where g_L was related to the $K\pi$ scattering amplitudes a_L by:

$$g_L = \eta \frac{M_{K\pi}\, a_L\, e^{b(t-\mu^2)}}{\sqrt{q}} \qquad \text{(VIII.2)}$$

and where γ_a and γ_c were the ρ-A_2 exchange coefficient and Regge cut (absorption correction) coefficient, respectively. This parametrization was a low t' simplification of a more general $K\pi$ production model discussed in ref. [20].

The relationship between the t_{lm} and the a_L was determined in the following way. The produced $K\pi$ scattering intensity for an unpolarized target for a given value of $M(K\pi)$ and t' can be written as,

$$I(\Omega) = \frac{1}{2} \sum_{\lambda_1 \lambda_3} | H_{\lambda_3 \lambda_1} |^2 \qquad \text{(VIII.3)}$$

where H is the production helicity amplitude with initial nucleon helicity λ_1 and final nucleon helicity λ_3. This can also be written in terms of a production density matrix as follows:

$$I(\Omega) = \frac{1}{2} \sum_{\lambda_3 \lambda_1} \sum_{j_1 m_1} \sum_{j_2 m_2} \rho^{j_1 j_2}_{m_1 m_2} Y^*_{j_1 m_1}(\Omega)\, Y_{j_2 m_2}(\Omega) \qquad \text{(VIII.4)}$$

where:

$$\rho^{j_1 j_2}_{m_1 m_2} = \frac{1}{2N} \sum_{\lambda_3 \lambda_1} H^{*j_1 m_1}_{\lambda_3 \lambda_1} H^{j_2 m_2}_{\lambda_3 \lambda_1} \qquad \text{(VIII.5)}$$

and the helicity amplitude in eq. VIII.3 has been decomposed into a sum of contributions for helicity amplitudes of different spin j and helicity m states.

The production amplitudes $L_{\lambda\pm}$ can now be associated with the helicity amplitudes H as follows:

$$L_{\lambda\pm} = \frac{1}{\sqrt{2}}\left[H^{L\lambda}_{\lambda_2\lambda_1} \pm (-1)^{L+1} H^{L-\lambda}_{\lambda_2\lambda_1} \right] \qquad \text{(VIII.6)}$$

Thus the density matrix ρ can be written in terms of the production amplitudes $L_{\lambda\pm}$ and hence be written in terms of the scattering amplitudes a_L.

By using the following identity relation for a product of spherical harmonics,

$$Y_{j_1m_1}(\Omega)\, Y_{j_2m_2}(\Omega) = (4\pi)^{-1/2} \sum_{jm} \left\{ \left[(2j_1+1)\,(2j_2+1)\,(2j+1) \right]^{1/2} \times \begin{pmatrix} j_1 & j_2 & j \\ m_1 & m_2 & m \end{pmatrix} Y^*_{jm}(\Omega) \begin{pmatrix} j_1 & j_2 & j \\ 0 & 0 & 0 \end{pmatrix} \right\} \qquad \text{(VIII.7)}$$

eq. VIII.4 can be rewritten as:

$$I(\Omega) = (4\pi)^{-1/2} \sum_{\substack{jm \\ j_1m_1 \\ j_2m_2}} \rho^{j_1j_2}_{m_1m_2} (-1)^{m_1+m} \left[(2j_1+1)\,(2j_2+1)\,(2j+1) \right]^{1/2} \times \begin{pmatrix} j_1 & j_2 & j \\ m_1 & m_2 & m \end{pmatrix} Y^*_{jm}(\Omega) \begin{pmatrix} j_1 & j_2 & j \\ 0 & 0 & 0 \end{pmatrix} \qquad \text{(VIII.8)}$$

where the terms in curved brackets are Wigner 3-j symbols as defined in ref. [21]. Now the original expansion of the Kπ production intensity in terms of the angular moments (eq. VII.1) was given by:

$$I(\Omega) = (4\pi)^{-1/2} \sum_{lm} t_{lm}\, Y_{lm}(\Omega) \qquad \text{(VIII.9)}$$

and hence the angular moments t_{lm} can be written in terms of the density matrix by equating coefficients of the spherical harmonics in eqs. VIII.7 and VIII.8.

$$t_{lm} = \sum_{\substack{j_1 m_1 \\ j_2 m_2}} (-1)^{m_1+m} \left[(2j_1+1)(2j_2+1)(2l+1) \right]^{1/2} \times \begin{pmatrix} j_1 & j_2 & l \\ -m_1 & m_2 & m \end{pmatrix} \mathrm{Re}(\rho^{j_1 j_2}_{m_1 m_2}) \begin{pmatrix} j_1 & j_2 & l \\ 0 & 0 & m \end{pmatrix} \qquad \text{(VIII.10)}$$

C. The Multi-t′ Bin Partial Wave Fitting Procedure

Equations VIII.5 and VIII.6 give the relation between the density matrix ρ and the production amplitudes $L_{\lambda\pm}$. Equation VIII.10 then relates the moments to the $L_{\lambda\pm}$. This allows a fit to be done to the angular moments, t_{lm}, in order to determine the coefficients b, γ_c, γ_a, and the Kπ scattering amplitudes a_L that give the t′ dependence of the production amplitudes $L_{\lambda\pm}$. The fit performed was a chi-squared minimization fit with the chi-squared defined as:

$$\chi^2 = \sum_{i=1}^{N_{bins}} \sum_{l,m} \frac{(t_{lm;i} - t^{exp}_{lm;i})^2}{\sigma^{exp\,2}_{lm;i}} \qquad \text{(VIII.11)}$$

where t^{exp}_{lm} were the experimental angular moments obtained in a series of special large M(Kπ), small t′ bin angular moments fits similar to fits described in the previous chapter. The σ_{lm} were the diagonal error matrix elements from the fit that determined the t^{exp}_{lm}. The sum over the i index represented a sum over t′ bins. The range of t′ from 0.0 to

0.2 GeV^2 was divided into 6 bins and it was assumed that the angular moments were nearly constant within a t' bin. To provide sufficient statistics, the range of M(Kπ) was made fairly large (from 40 to 120 MeV) which implied the additional assumption that b, γ_c, γ_a, and a_L varied slowly as a function of M(Kπ).

The fit was accomplished by a partial wave fitting program based on the MINUIT [22] multi-parameter minimizing routines. This program was a modified version of the fitting program used in the PWA of ref. [5]. The parameters of the fit were b, γ_c, γ_a, and the amplitudes a_L but only b, γ_c, and γ_a were of interest since the single t' bin fit (the next step) would obtain a new set of amplitudes with a finer Kπ mass dependence.

D. Results from the Multi-t' Bin Fits

The results from the fit for the mass bin ($0.92 \leq M(K\pi) \leq 0.96$ GeV) are presented in fig. 32. In this figure, the points represent the moments obtained in the special multi-t' bin moments analysis and the curves are the best fit to these moments using the parametrization in eqs. VIII.1 and VIII.2. Fits were performed for a total of 14 mass bins and the resulting production parameters are shown in fig. 33 and Table 8. The points in fig. 33 represent the production parameters obtained from the fits for each mass bin and the curves shown are the parametrizations used to provide the production parameter values for the single t' bin analysis. The production parameter b is seen to be fairly constant for all masses whereas both γ_c and γ_a approach zero for increasing mass. The implication is that the ρ-A_2 and cut contributions are significant for

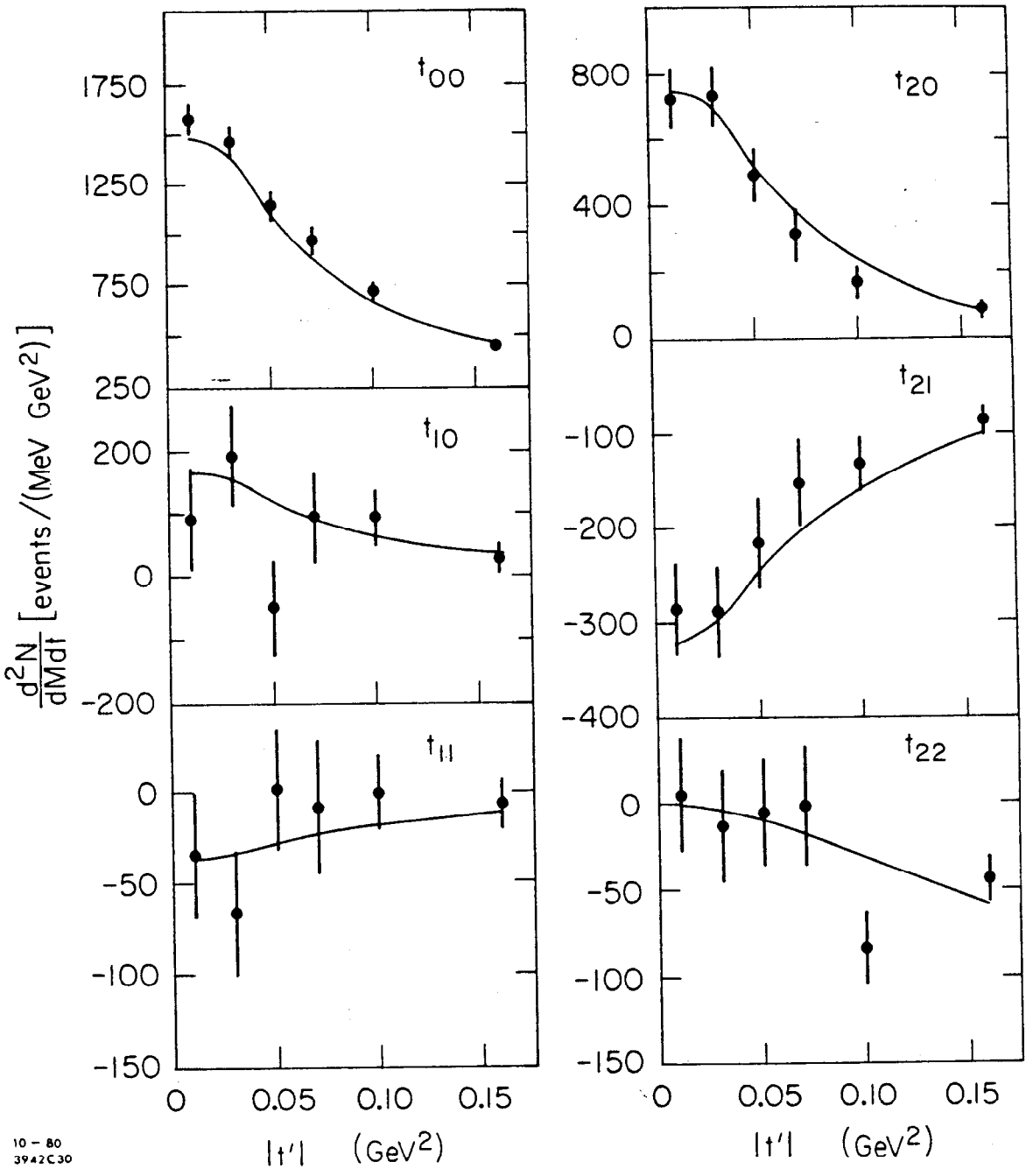

Figure 32 -- Multi-t′ bin partial wave fit to the t_{1m} for $1 \leq 2, m \leq 1$ as a function of t′. This fit was performed in the Kπ mass bin 0.92 to 0.96 GeV. Plotted points are the moments, curves are the results from the fit.

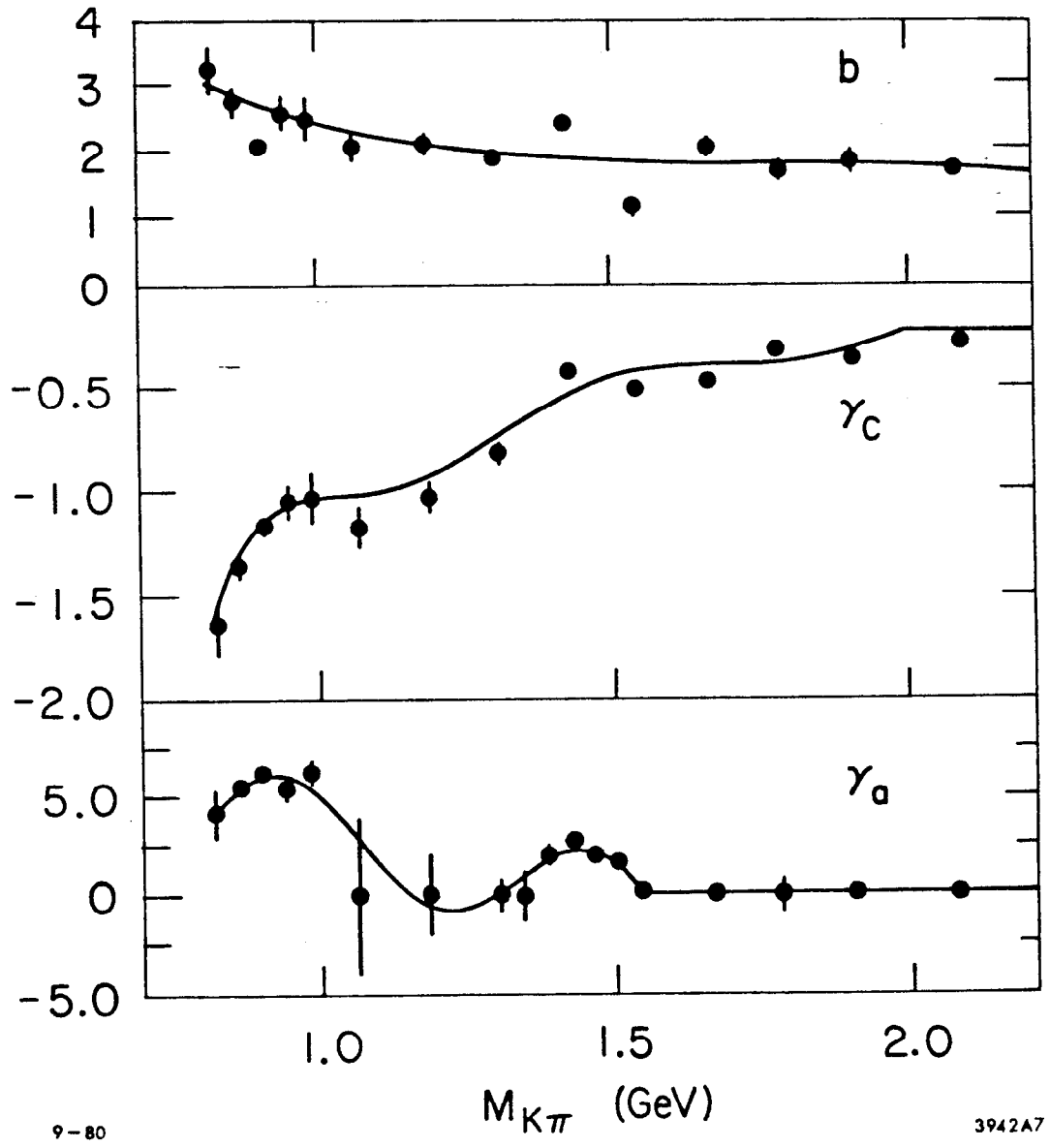

Figure 33 -- The parameters b, γ_c, and γ_a that describe the t′ dependence of the Kπ production amplitude. Plotted points are the values and errors for b, γ_c, and γ_a from the fit, the smooth curves are the parametrizations for b, γ_c, and γ_a as a function of M(Kπ) used in the next step (the single t′ bin PWA).

TABLE 8

Results for b, γ_c, and γ_a from Multi-t′ PWA Fits

M(Kπ)	b	γ_c	γ_a
0.82	3.25 ±0.34	-1.66 ±0.13	4.24 ±1.21
0.86	2.76 ±0.21	-1.36 ±0.06	5.54 ±0.47
0.90	2.09 ±0.12	-1.17 ±0.05	6.11 ±0.32
0.94	2.58 ±0.26	-1.04 ±0.08	5.40 ±0.56
0.98	2.51 ±0.33	-1.02 ±0.12	6.17 ±0.79
1.06	2.06 ±0.20	-1.17 ±0.10	0.00 ±3.91
1.18	2.16 ±0.15	-1.02 ±0.08	0.00 ±2.02
1.18	2.16 ±0.15	-1.02 ±0.08	0.00 ±2.02
1.30	1.90 ±0.12	-0.81 ±0.05	0.00 ±0.79
1.42	2.43 ±0.10	-0.42 ±0.02	2.14 ±0.21
1.54	1.18 ±0.15	-0.49 ±0.03	0.00 ±0.37
1.66	2.10 ±0.15	-0.46 ±0.02	0.00 ±0.26
1.78	1.74 ±0.15	-0.32 ±0.02	0.00 ±0.88
1.90	1.90 ±0.16	-0.34 ±0.02	0.00 ±0.30

low masses but become less important at high masses. The results from this multi-t′ bin analysis are in good agreement with the results from the similar analysis in ref. [5].

E. The Single t′ Bin Partial Wave Fitting Procedure

With production parameters b, γ_c, and γ_a obtained from the previous step, it was then possible to insert the parameters into eqs. VIII.1 and VIII.2 so that the amplitudes $L_{\lambda\pm}$ could be integrated over the full t′ range from 0.0 to 0.2 GeV^2. A new chi-squared was defined:

$$\chi^2 = \sum_{lm} \frac{(t_{lm} - t_{lm}^{exp})^2}{\sigma_{lm}^{exp\,2}} \qquad \text{(VIII.12)}$$

where the experimental moments t_{lm}^{exp} and the error matrix elements σ_{lm} are the regular (small M(Kπ) bin, full t′ range) moments and error matrices obtained in the moments fits described and presented in the previous chapter. The parameters of this single t′ bin fit are the complex amplitudes a_L. The fitting program for this step in the PWA was a sophisticated chi-squared minimization program based on the MINUIT routines. This program was quite similar to the program used in the multi-t′ bin fitting procedure and was also a modified version of the fitting programs used in ref. [5].

The amplitude a_L measured in $K^-\pi^+$ scattering contains an isospin 1/2 component and an isospin 3/2 component as shown in eq. VIII.13.

$$a_L = a_L^{I=1/2} + \frac{1}{2} a_L^{I=3/2} \qquad \text{(VIII.13)}$$

In the elastic region, the amplitudes were written as:

$$a_L = \sqrt{2L+1}\,\epsilon_L \sin\delta_L\, e^{i\delta_L} \qquad \text{(VIII.14)}$$

with ϵ and δ representing the elasticity and phase shift of the amplitude respectively. The requirement of purely elastic scattering (elastic unitarity) was equivalent to setting ϵ=1 hence the amplitude was determined by a single (real) parameter δ. In the inelastic region, the amplitude was parametrized as:

$$a_L = |a_L|\, e^{i\phi_L} \qquad \text{(VIII.15)}$$

where $|a_L|$ was called the magnitude and ϕ_L called the phase of the L-wave amplitude.

F. Special Comments on the Procedure and Results of the Single t′ Bin PWA

The single t′ bin fits were performed on the full mass range $0.8 \leq M(K\pi) \leq 2.3$ GeV. However, a number of conventions, exceptions, assumptions, and special procedures were applied to different mass regions for these fits. Many of these conventions, exceptions, etc., are very important for understanding and interpreting the results of the single t′ bin partial wave fits and will be explained in the following subsections prior to the presentation and discussion of the results. The topics in the following subsections are:

1) Definition of terms

2) The normalization constant

3) The number of waves used in the fits

4) The mass binning convention

5) Overall phase determination

6) The I=3/2 amplitudes and elastic unitarity

7) The $n\pi$ cut

8) Ambiguous solutions and Barrelet zeroes

F:1 Definition of terms

The following conventions will be used in the description of the PWA results. The partial waves will be defined by the standard spectroscopic notation convention of S, P, D, etc., for angular momentum L= 0, 1, 2, etc. Thus the amplitude, a_L, for L=1 will be written a_P. As noted in eq. VIII.13, a_L is a sum of the I=1/2 and I=3/2 amplitudes. When either the I=1/2 or I=3/2 amplitude is to be considered by itself, it will be written $a_L^{1/2}$ or $a_L^{3/2}$. Since the amplitude is often expressed as:

$$a_L = |a_L| e^{i\phi_L} \qquad \text{(VIII.16)}$$

the spectroscopic notation letters will be used in the subscripts for $|a_L|$, ϕ_L, and δ_L.

F.2 The normalization constant

The normalization constant was a number that was directly proportional to the overall experimental normalization with several other miscellaneous constants included as well. An initial guess for

this constant could be made based on the known absolute experimental normalization (see chapter VI), but due to the sizeable error in this normalization, the constant would not be accurately determined. To obtain a more precise value for this constant, a known physics signal, in this case the K*(895) resonance, was used to determine the value. The assumption that the K*(895) was a completely elastic resonance was the significant factor in determining the normalization constant in this procedure. The determination was accomplished by trying a number of values for the constant close to the initial guess and then applying the full PWA machinery to the 890 MeV mass region for each of the trial values for the constant. Then two methods were used to select the optimum value for the constant. The first method summed the chi-squared from the partial wave fits for each mass bin in the 890 region. The value of the constant associated with the smallest chi-squared sum was considered the optimum value. The second method took the P-wave phases from the PWA fits and fit them with a Breit-Wigner spin 1 resonance model. The optimum constant was that which resulted in the best fit to the resonance model. The two "optimum" values obtained were nearly identical and the final value used for all the PWA fits to be presented was the average of the two "optimum" values.

F.3 The number of waves used in the fit

Using some mathematics, it can be shown that a given partial wave amplitude a_L, when expressed in terms of moments t_{lm}, can only have moments up to l=2L in the expression. Thus the criterion for deciding

how many waves should be used in the fit is based on what the highest l non-zero moment happens to be for the mass bin in question. Applying this criterion, it was determined that in the mass region from 0.8 to 1.24 GeV, only the S and P-waves were required. Above 1.24 GeV the D-wave was added and at 1.56 GeV and 1.86 GeV, the F and G-waves, respectively, were included in the fit. For the mass region from 0.8 to 1.56 GeV the moments t_{1m} with m=0,1,2 were being fit but above 1.56 GeV, only the moments with m=0,1 were fit. The m=2 moments were consistent with zero in this upper mass range and several checks showed that the results were not affected by this limiting of the m value (such checks are discussed in Appendix C). This elimination of unnecessary l and m moments reduced the number of degrees of freedom in the fit and resulted in smaller errors in the fit parameter as well as better stability in the fits.

F.4 The mass binning convention

For the mass region from 0.8 to 1.0 GeV, 20 MeV wide bins were used in the PWA fits. The small number of degrees of freedom and the large number of events in this resonance region allowed the bin width to be reduced to this size. From 1.0 to 1.64 GeV, 40 MeV wide bins were used. The decreasing number of events for increasing $K\pi$ mass coupled with the larger number of degrees of freedom (number of moments) in the fit required the increase of bin size to 80 MeV above 1.64 GeV. At 2.26 GeV, the lack of statistics effectively established this point as the end of the PWA mass range. The binning given above was used for the plots of

the magnitude and phase of the amplitudes as presented in figs. 35-39, 44, and Table 10. However, for the Argand plots of figs. 40-43 and in Table 11, a second pass over the high mass region (M(Kπ)>1.6 GeV) was performed using 80 MeV wide bins offset by 40 MeV from the original PWA set. This resulted in a high mass sweep of overlapping 80 MeV bins at 40 MeV intervals. This overlapping set was created to help guide the eye and also to allow for smoother, more continuous Argand plots. However, all resonance fits to the amplitudes were properly performed with the non-overlapping set of mass bins.

F.5 The overall phase determination

Because the physics distributions are related to the square of the amplitude, the overall phase of the total amplitude is indeterminate. However, it is necessary to fix the overall phase for the sake of studying the mass dependence of the amplitudes. It should be noted that the choice of overall phase is arbitrary, the conventions used here are chosen to make the interpretation of the result straightforward.

The PWA fit results in values for the magnitude of the partial wave amplitudes and the relative phases between the amplitudes. In other words, if the fit used 3 waves, then $\phi_D-\phi_S$ and $\phi_D-\phi_S$ can be determined but the absolute values for each of the ϕ_S, ϕ_P, and ϕ_D phases will not be determined. An exception occurs when elastic unitarity (described in subsection F.6) is imposed in the fit. In that case the absolute phases can be determined. However, when elastic unitarity cannot be imposed (in this analysis elastic unitarity was imposed for the Kπ mass range of

0.8 to 1.24 GeV) the overall phase must be determined by another method. The standard method for phase fixing used in previous analyses uses a leading resonance to determine the overall phase. This is accomplished by fitting the magnitude of the resonating wave to a model which does not need the phase information. The standard Breit-Wigner resonance parametrization of eq. E.1, explained in detail in Appendix E, is suitable for this purpose. When the resonance parameters are obtained from the fit, the absolute phase for the resonating wave can be easily calculated as a function of mass. Then by measuring the phase of all other waves relative to the resonating wave (this can be set up in the PWA fit) one can obtain absolute phases for all waves.

The phase fixing procedure just described (the resonance fit method) has several important assumptions built in, any of which can lead to inaccuracies in the overall phase determination. The first assumption is that the Breit-Wigner parametrization correctly models the resonance behavior. A second assumption is that no other nearby resonances occur in the same wave, a possibility that would invalidate the model if the amount of overlap between the resonances was significant. A third assumption is that no other factors (such as backgrounds) contribute to the amplitude, and thus possibly altering the phase. Because these assumptions cannot be met with absolute certainty, the phase determination using the resonance fit method cannot be considered totally correct. In this analysis, the phase determination from the resonance fit method was used as the primary guide for fixing the overall phase. However, a small amount of additional phase rotation was allowed, especially in mass regions where either the resonance fit

method was not expected to be totally accurate or where the large phase errors from the PWA fit showed that the phases were not well determined. In such cases, smoothness and continuity of the Argand diagrams was used as the criterion for the allowed phase rotations. Where such additional rotations were made, the amount of rotation is given in the ϕ_{rot} column in Table 11. In all other cases, either elastic unitarity or the resonance fit method was used to determine the overall phase. Where no errors are given for the phase for a particular wave (in Table 11 and in figs. 35-39), that phase was set by the resonance fit method.

F.6 The I=3/2 amplitudes and elastic unitarity

As stated earlier, the partial wave amplitudes that will be presented in section G have isospin 1/2 and 3/2 components. However, the results from other analyses, specifically that of ref. [5], have measured the I=3/2 $K^-\pi^+$ partial wave amplitudes. The I=3/2 amplitudes for the P, D and higher L-waves were found to be consistent with zero (up to $M(K\pi)$=1.9 GeV, the limit of that experiment). Thus $a_L = a_L^{1/2}$ for P, D, and higher L-waves at all masses (assuming the I=3/2 contribution remains zero above 1.9 GeV).

The I=3/2 S-wave amplitude was found to be accurately parametrized by the effective range parametrization of [5]:

$$q = \cot\delta_S = \frac{1}{a} + \frac{1}{2} r q^2 \qquad \text{(VIII.17)}$$

where: $a = 2.4\ \text{GeV}^{-1}$

$r = -1.8\ \text{GeV}^{-1}$

and where q is the momentum in the Kπ center of mass and δ_s is the I=3/2 elastic S-wave phase shift as defined in the elastic region amplitude:

$$a_S = \sin\delta_S \, e^{i\delta_s} \qquad \text{(VIII.18)}$$

The I=3/2 Kπ scattering was assumed to be purely elastic, allowing elastic unitarity to be imposed. From eq. VIII.17, the phase shift δ_s could be calculated as a function of mass, thus making it possible to calculate $a_s^{3/2}$. With knowledge of $a_s^{3/2}$, one can immediately obtain $a_s^{1/2}$ since a_s has been measured.

The ability to isolate $a_L^{1/2}$ is important because one expects resonance structure only in $a_L^{1/2}$ (not $a_L^{3/2}$) and because elastic unitarity can only be imposed on $a_L^{1/2}$ (or $a_L^{3/2}$) but not on a_L. The reason one wants to impose elastic unitarity is to be able to fix the phase. The reason why imposing elastic unitarity fixes the phase can be seen in eq. VIII.19:

$$a_L = \sqrt{2L+1}\, \epsilon_L \sin\delta_L \, e^{i\delta_L} \qquad \text{(VIII.19)}$$

Elastic unitarity implies ϵ=1 hence only one parameter, δ, determines a_L. From the PWA fit, one obtains $|a_L|$ which for elastic unitarity is $|\sin\delta|$. The absolute phase, δ, is therefore determined.

In the partial wave fits, where elastic unitarity has been imposed, it was necessary to use eq. VIII.18 to calculate $a_s^{3/2}$ so that it could be subtracted from a_s to obtain $a_s^{1/2}$. Then elastic unitarity could be easily imposed on $a_s^{1/2}$. Elastic unitarity was also imposed on the P-wave amplitude but no I=3/2 subtraction was necessary since $a_p^{3/2}$ was found to be consistent with zero (as stated earlier). The validity for

imposing elastic unitarity comes from the fact that previous measurements have indicated that the onset of inelastic $K\pi$ scattering occurs somewhere above a $K\pi$ mass of 1.3 GeV. In the PWA results to be presented, elastic unitarity was imposed on the S-wave from 0.8 to 1.24 GeV and on the P-wave from 0.8 to 1.12 GeV. This allowed the absolute phase to be determined up to 1.24 GeV. From there the resonance fit method based on the D, F, and G-wave resonances was used to fix the phase.

F.7 The $n\pi$ cut

An important additional kinematical cut was made to define the data sample used in both the elastic region and the low mass inelastic region. This cut, known as the $n\pi$ cut, removed events with an invariant $n\pi$ mass of less than 1.8 GeV in order to remove diffractively produced $K^-p \rightarrow K^-N^{*+} \rightarrow K^-\pi^+n$ events. Such diffractively produced events contributed strongly to the background, primarily in the low $M(K\pi)$ kinematical regions. This diffractive background was not expected to contribute strongly for high $M(K\pi)$ so the cut was not applied in the high mass inelastic region. In fact, the $n\pi$ cut drastically reduced the event sample for $M(K\pi) > 1.6$ GeV. A careful study of the effects of the $n\pi$ cut was made and the results of this study showed that the cut was effective in removing N* backgrounds for $M(K\pi) < 1.6$ GeV. For $M(K\pi) > 1.6$ GeV, the cut had no major effect on the physics results other than the severe loss of data. The details of the study of the $n\pi$ cut are presented in Appendix D.

F.8 Ambiguous solutions and Barrelet zeroes

An important feature of the partial wave analysis is the possible existence of multiple ambiguous solutions. If partial waves from 0 to L are used to describe the data, there will be a total of 2^L discrete sets of amplitudes, each of which results in the same observed scattering distribution. An easy way to demonstrate the existence of these ambiguous solutions starts with the Legendre function expansion of the full scattering amplitude $f(\theta)$, given in eq. VIII.20:

$$f(\theta) = C' \sum_{l=0}^{L} (2l+1)\, a_l\, P_l(\cos\theta) \qquad \text{(VIII.20)}$$

The sum over l in eq. VIII.20 has been truncated at L, representing L+1 contributing waves. It was first shown by Barrelet [23] that a convenient way to represent this amplitude was to extend the $z=\cos\theta$ variable into the complex plane ($Z=\cos\theta + i\sin\theta$). Then the above sum could be rewritten as a polynomial in Z by reexpressing the Legendre functions in terms of polynomials in Z. Then for L>0, eq. VIII.20 could be rewritten as:

$$f(Z) = C \prod_{i}^{L} (Z - Z_i) \qquad \text{(VIII.21)}$$

where C is a complex constant and the Z_i are the complex zeroes of the polynomial, often called the Barrelet zeroes. It can be easily shown that replacement of any Z_i by its complex conjugate does not affect the observable physics given by $|f|^2$. Thus 2^L different combinations of the Z_i and their conjugates can give rise to identical distributions $|f|^2$.

When one imposes elastic unitarity for the case when L=1 (S and P-waves), the restriction results in a choice of one of the ambiguous solutions. In this analysis, elastic unitarity has been imposed from 0.8 to 1.24 GeV in mass (as explained in the previous subsection). From eqs. VIII.20 and VIII.21 one can calculate the Z_i from knowledge of the partial wave amplitudes, a_L, and thus plot the Kπ mass dependence of the Z_i. Using elastic unitarity, the choice between Z_1 and Z_1^* was determined automatically. When elastic unitarity is no longer applicable (for M(Kπ)>1.24 GeV) a unique value for Z_1 is still possible as long as Im(Z_1) does not approach zero. This statement uses continuity to argue that the value of a Barrelet zero would not take a large jump between mass bins as would be the case to go from Z_1 to Z_1^*. This argument is applied to all Barrelet zeroes and it implies that as long as a unique choice exists for all Barrelet zeroes Z_1 through Z_L, no ambiguities will arise until a mass bin is reached where one of the Im(Z_i) approaches zero. At masses above the point where a Z_i approaches zero (called a crossing point), the number of solutions is doubled (both Z_i and Z_i^* are allowed). But when a new wave is included in the PWA, a new Barrelet zero appears and there is no way of deciding which of the two complex conjugate representations of the new Barrelet zero should be used. This problem is resolved by requiring that leading resonances rotate counterclockwise in an Argand diagram (equivalent to the Wigner condition [24]). This rotation requirement is equivalent to choosing the new Barrelet zero to have Im(Z)<0. Therefore, when the D, F, and G-waves are included in the PWA, each of the new Barrelet zeroes introduced by each new wave is required to have Im(Z)<0. Thereafter,

continuity is used to keep the choice of zeroes unique at least until one or more of the $Im(Z_i)$ approach zero.

In this analysis, the results of a partial wave fit produced the partial wave amplitudes, a_L, which were used to calculate the Z_i (using eqs. VIII.20 and VIII.21). It was quite possible that the solution from the fit represented the wrong choice of the complex conjugate zeroes. The fitting program was therefore designed to calculate the other 2^L-1 possible combinations of zeroes (by complex conjugating the first set of zeroes). Then it reversed the procedure by calculating the amplitudes from the zeroes. These calculated a_L values were given as initial values to the fitting program which was then allowed to refit the data. In most cases the fitting program immediately converged to the "conjugate" solution which was given as input. The final result was the 2^L sets of ambiguous amplitude solutions.

Figure 34 shows the 4 Barrelet zeroes obtained in this analysis. As stated previously, when each new Z_i appears, it starts with a negative imaginary part. Although $Im(Z_1)$ approaches and crosses zero near 0.9 GeV, elastic unitarity kept the choice of Z_1 unique. The mass dependence of all the Z_i appears quite smooth and continuous, thus no ambiguitites are proposed until $Im(Z_3)$ approaches zero near 1.86 GeV. At 2.02 GeV, $Im(Z_1)$ also approaches zero. Thus in the region 1.86 to 2.02 GeV two ambiguous solutions exist and in the region above 2.02 GeV four ambiguous solutions exist. It could even be argued that $Im(Z_1)$ remains close enough to zero that additional ambiguities could arise from recrossing above 2.02 GeV. This is unlikely but even assuming that it is true, the difference between the resulting two ambiguous solutions

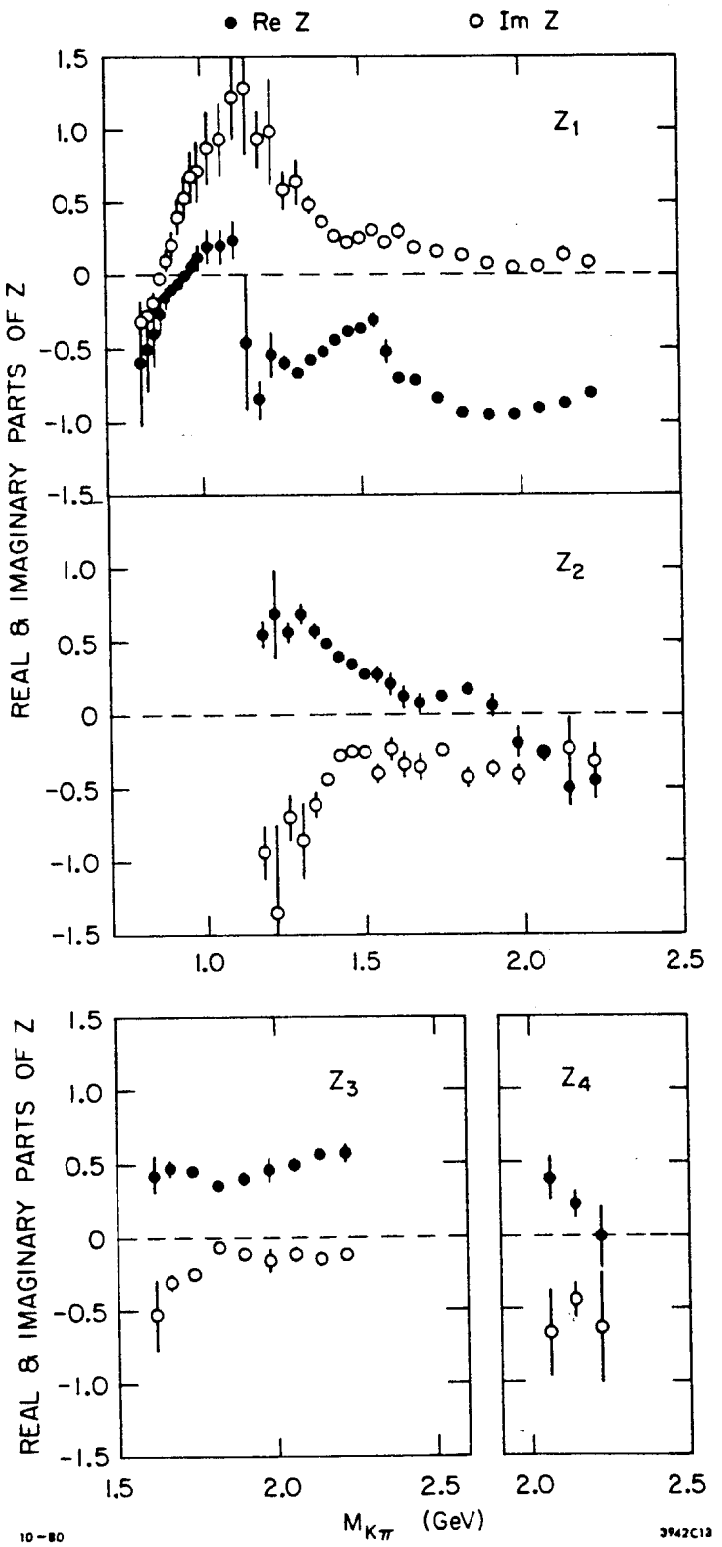

Figure 34 -- The real and imaginary parts of the four Barrelet zeroes as a function of M(Kπ) obtained in the single t′ bin PWA (see text for explanation).

would be small. This is due to the fact that as $Im(Z_i) \rightarrow 0$ the two solutions (represented by Z_i and Z_i^*) become identical. The ambiguous solutions are classified by the sign of the imaginary parts of the ambiguous Barrelet zeroes as shown in Table 9 for the results of this analysis. The labelling convention for the solutions given in Table 9 will be used in the presentation of the partial wave amplitudes in section G.

The calculation of the errors for the Barrelet zeroes is crucial for determining if $Im(Z_i)$ approaches zero. The errors for Z_i were calculated with a Monte Carlo gaussian distribution generating routine. The errors on the magnitude and phases of the amplitudes for the various waves were obtained from the results of the PWA fit. It was assumed that statistical distributions for the magnitudes and phases had a gaussian shape. This assumption allowed each magnitude and phase to be offset by an amount determined by the Monte Carlo generator (which used the error as the sigma of the gaussian). The new "offset" magnitudes and phases were used to calculate new "offset" zeroes using eqs. VIII.20 and VIII.21. This procedure was repeated one thousand times so that a "distribution" of Barrelet zeroes was produced. The rms deviation from the original Barrelet zero (calculated from the non-offset magnitudes and phases) was determined from this generated distribution. This deviation was used as the error for the Barrelet zero. The important assumptions made in this procedure are that the magnitude and phase distributions resembled gaussian distributions and that the generated Barrelet zero distribution resembled a gaussian distribution. In most cases, these assumptions were well justified. However, in a few cases,

TABLE 9

Labelling Convention for Ambiguous Solutions

Solution	$Im(Z_1)$	$Im(Z_3)$	
for $-1.86 < M(K\pi) < 2.02$ GeV :			
A	+	+	
B	+	-	
C	+	+	(same as Solution A)
D	+	-	(same as Solution B)
for $M(K\pi) > 2.02$ GeV :			
A	-	+	
B	-	-	
C	+	+	
D	+	-	

the error in the Barrelet zeroes are likely to be either slightly underestimated or overestimated.

G. Single t′ Bin Partial Wave Analysis Results

The results from the single t′ bin partial wave fits are presented in figs. 35-39 in plots of magnitude and phase for each solution of each partial wave as a function of $K\pi$ mass. For the mass regions where elastic unitarity was imposed on the S and P waves, the phase shifts as a function of mass bin are given in Table 10. Table 11 contains the amplitudes and phases for each solution of each partial wave for the inelastic $K\pi$ mass regions. The partial wave amplitudes expressed in Argand diagram form are shown in figs. 40-43. The important features of the partial wave amplitudes will now be discussed sequentially by wave.

G.1 The S-wave amplitude

In the region from 0.8 to 1.24 GeV where elastic unitarity has been imposed on the S-wave amplitude, the magnitude and phase shown in fig. 35 are not independent. The magnitude is related to the phase shift by $|a_s|=|\sin\delta_s|$ (the phase ϕ_s and the phase shift δ_s are identical but it should be stressed that the amplitude shown in fig. 35 is the sum of the I=1/2 and I=3/2 components). The phase is seen to rise slowly in the elastic region. Above the elastic region, the magnitude and phase are independent. At 1.3 GeV, the magnitude continues to rise, then just below 1.4 GeV, it peaks and drops precipitously to nearly zero magnitude

Figures 35-43 -- Some supplementary comments pertaining to the figures on the following 9 pages are given below.

Figures 35-39 : The magnitude and phase of the S, P, D, F, and G wave $K^-\pi^+$ elastic scattering amplitudes as a function of M(Kπ) for the four ambiguous solutions. All solutions are identical in the M(Kπ) region left of the dotted line. The curves (in figs. 37, 38, and 39) represent the regions in M(Kπ) where the overall phase is expected to be determined by the dominating resonance in the wave shown in the figure. The curve is the phase resulting from a Breit-Wigner resonance parametrization based on a fit to the amplitude of the given wave. The open circles represent the actual value of the phase fixed in this analysis by the method described in VIII.F.5. Errors shown are statistical only. See text for further explanations.

Figures 40-43 : The Argand plots for each of the partial wave amplitudes for the four ambiguous solutions (A, B, C, and D). The diameters of the unitarity circles are $\sqrt{2L+1}$. The points for M(Kπ)<1.6 GeV are plotted in 40 MeV steps with 40 MeV wide bins. The points for M(Kπ)>1.6 GeV are plotted in 40 MeV steps with 80 MeV wide overlapping bins (see VIII.F.2 for explanations).

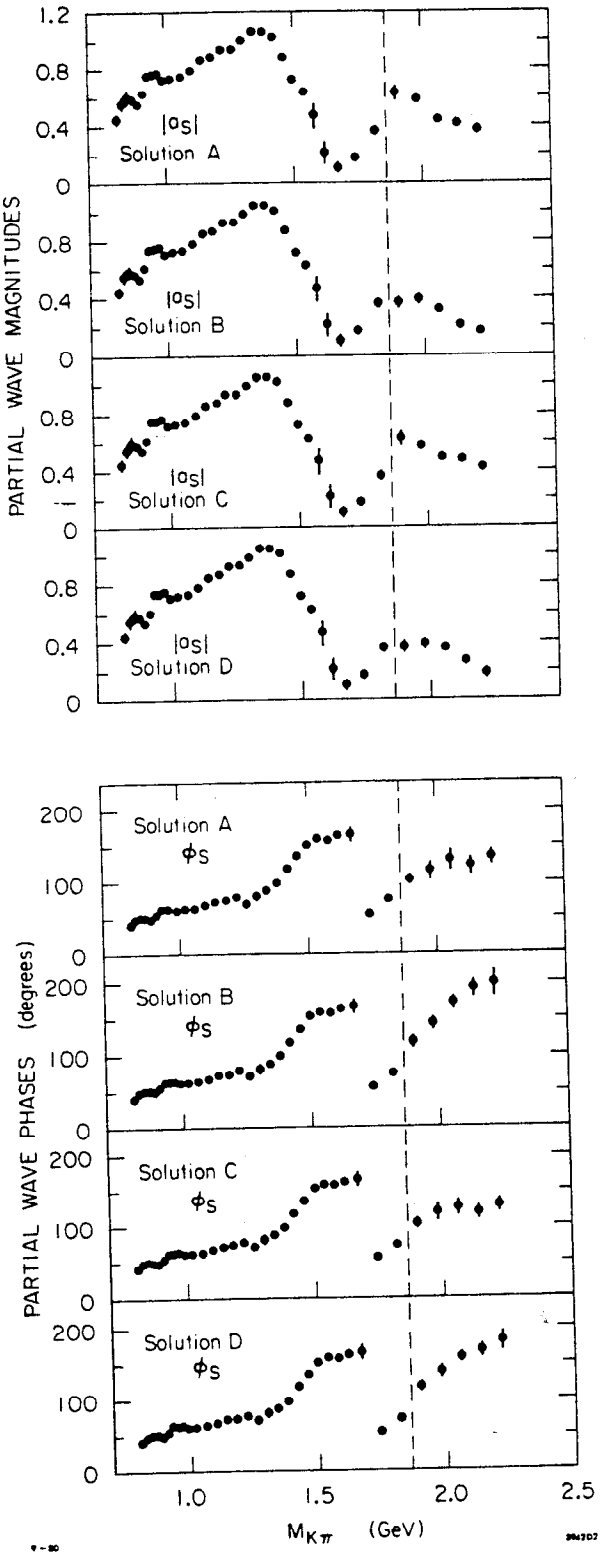

Figure 35 -- The magnitude and phase of the S-wave amplitude.

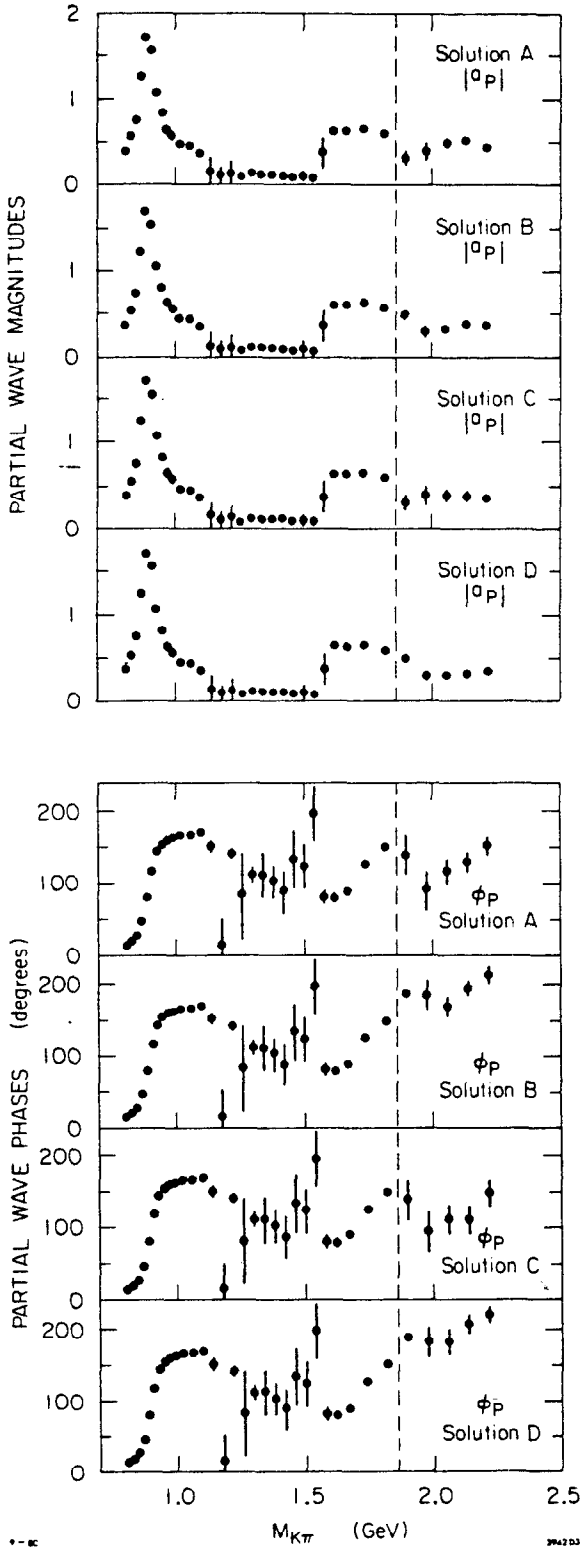

Figure 36 -- The magnitude and phase of the P-wave amplitude.

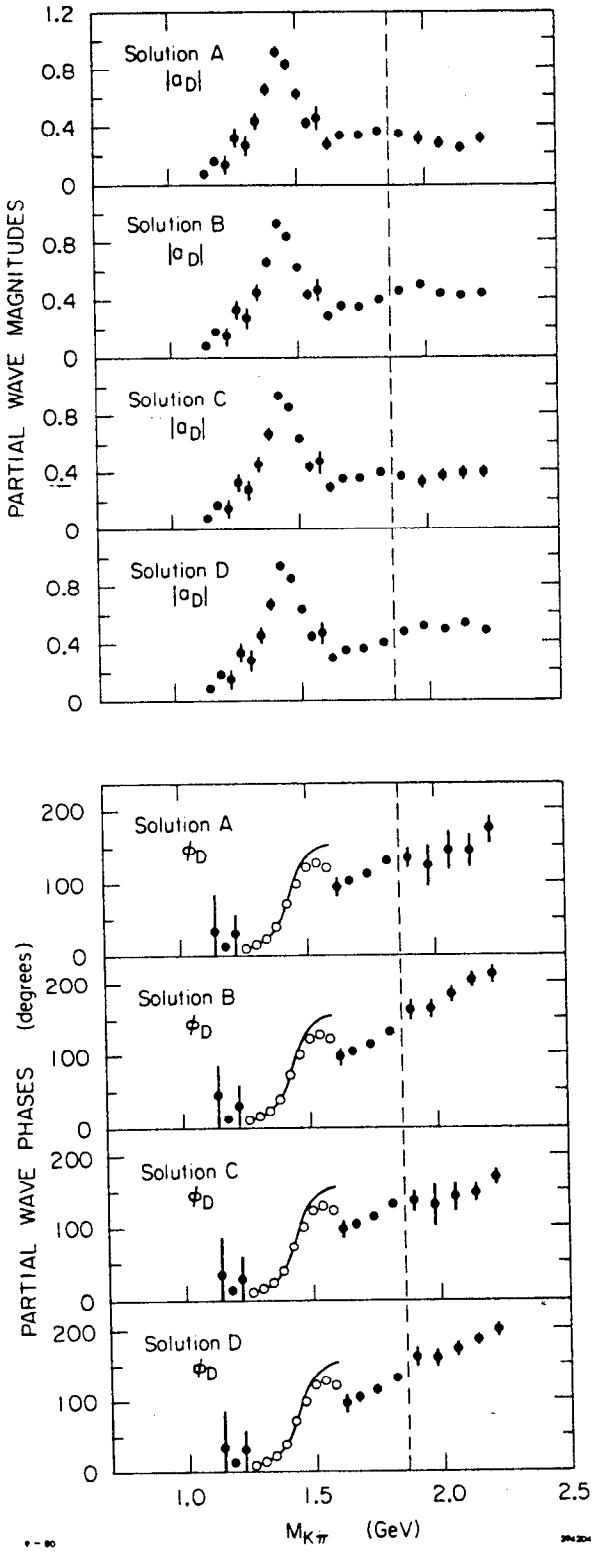

Figure 37 -- The magnitude and phase of the D-wave amplitude.

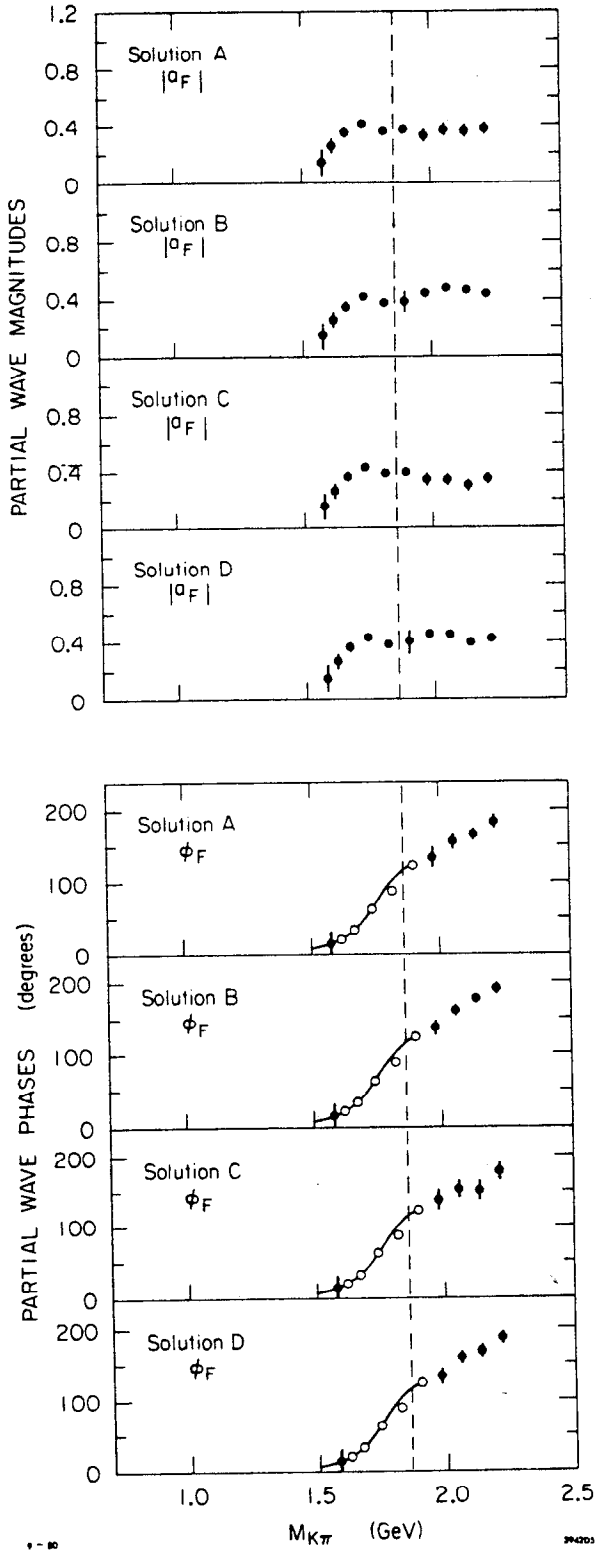

Figure 38 -- The magnitude and phase of the F-wave amplitude.

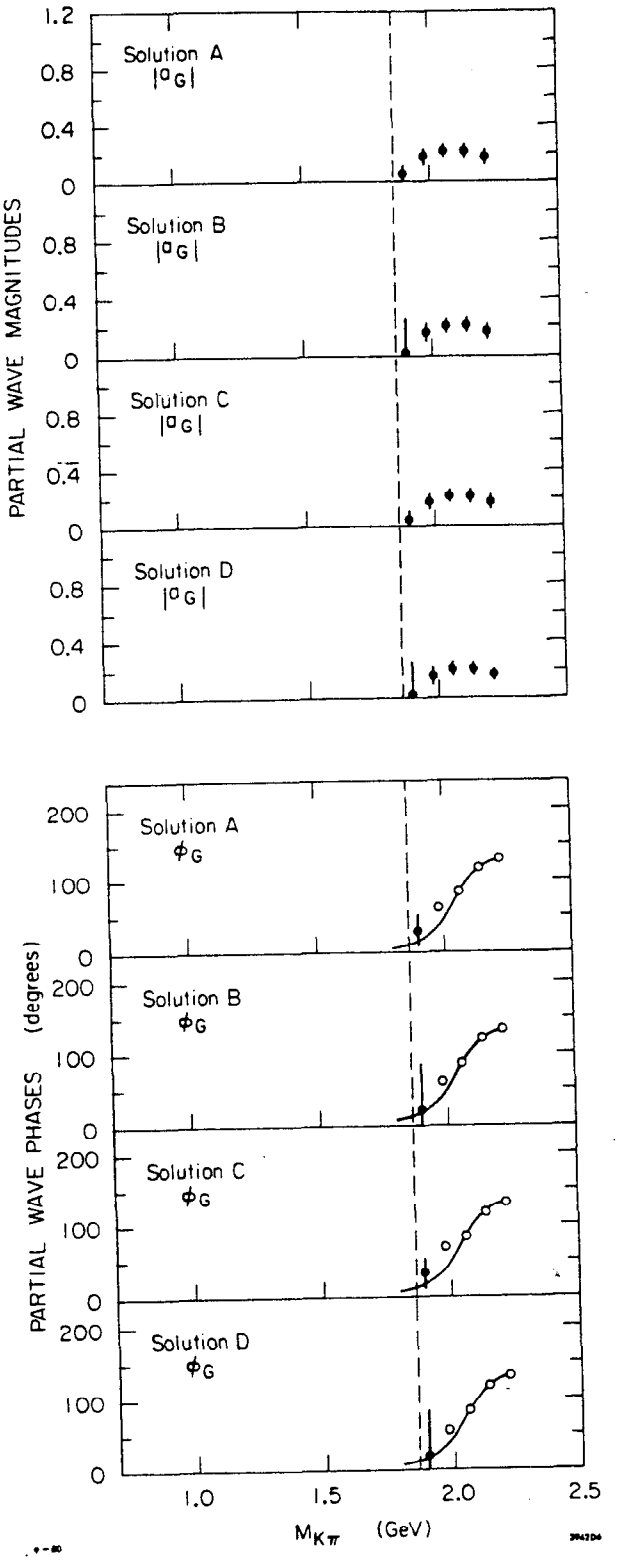

Figure 39 -- The magnitude and phase of the G-wave amplitude.

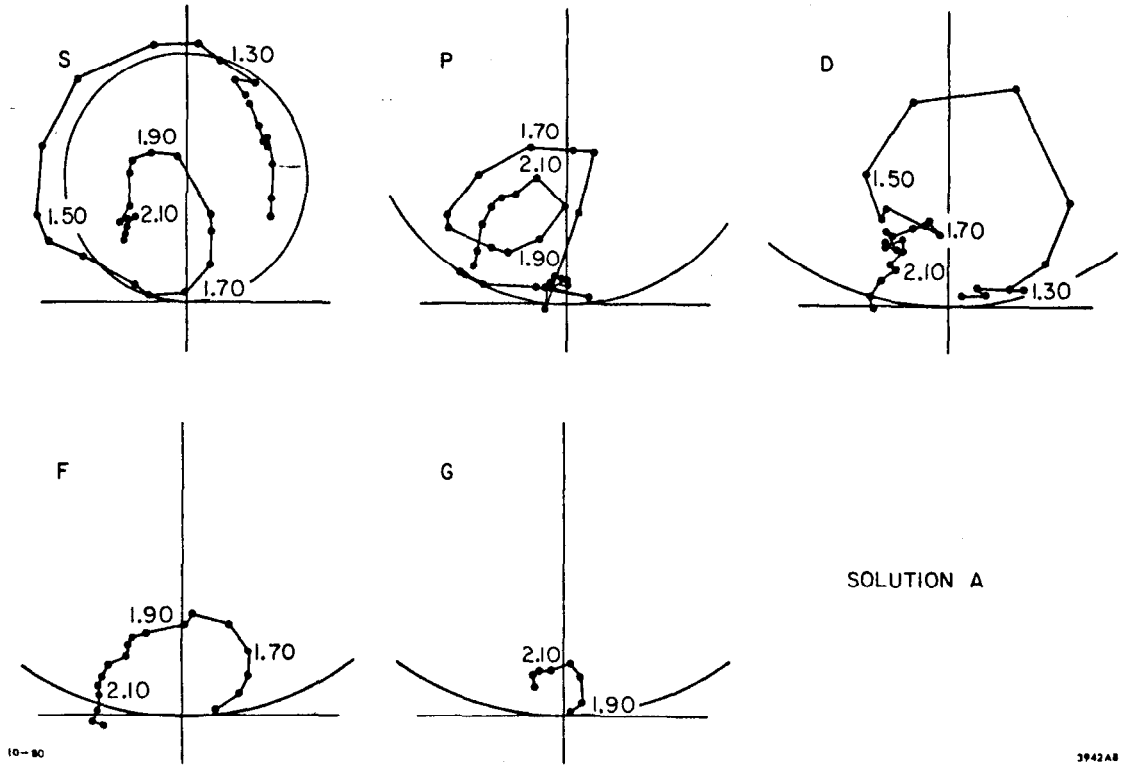

Figure 40 -- Argand plots for solution A.

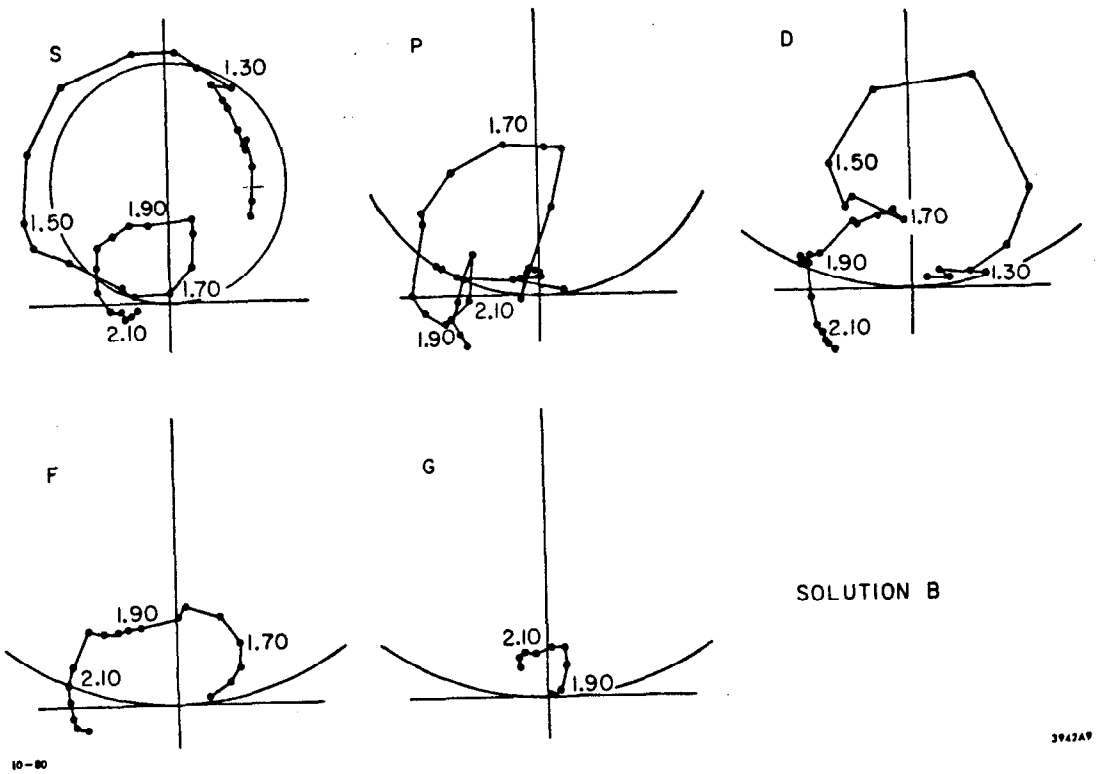

Figure 41 -- Argand plots for solution B.

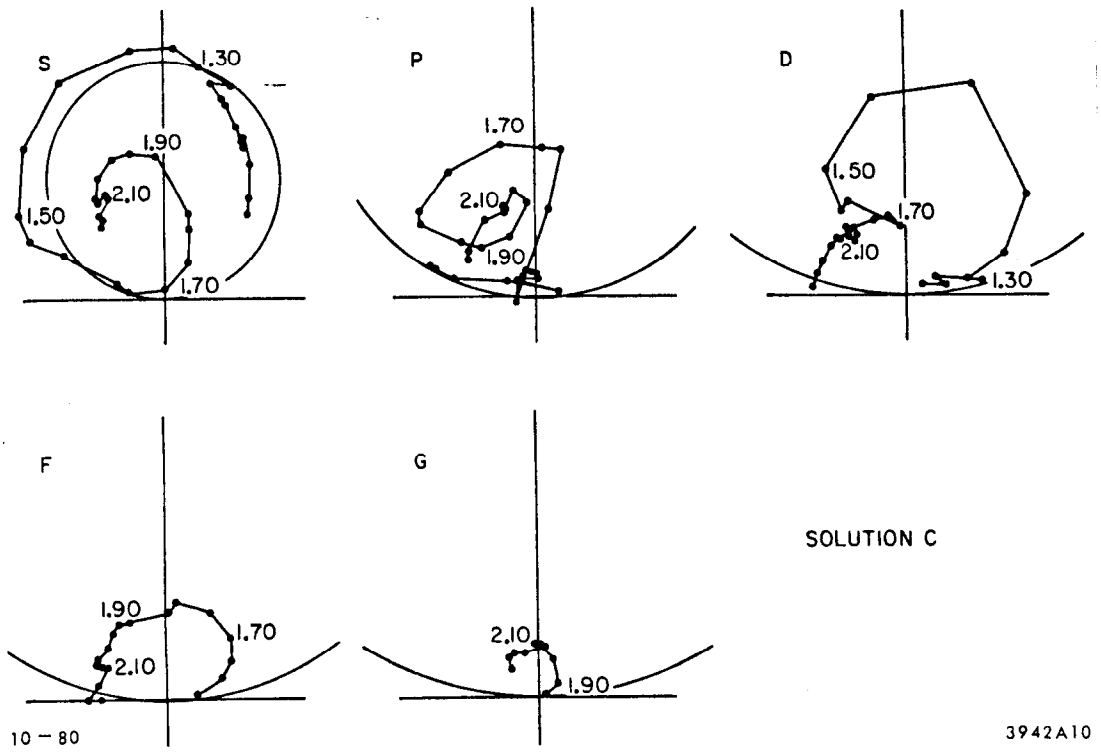

Figure 42 -- Argand plots for solution C.

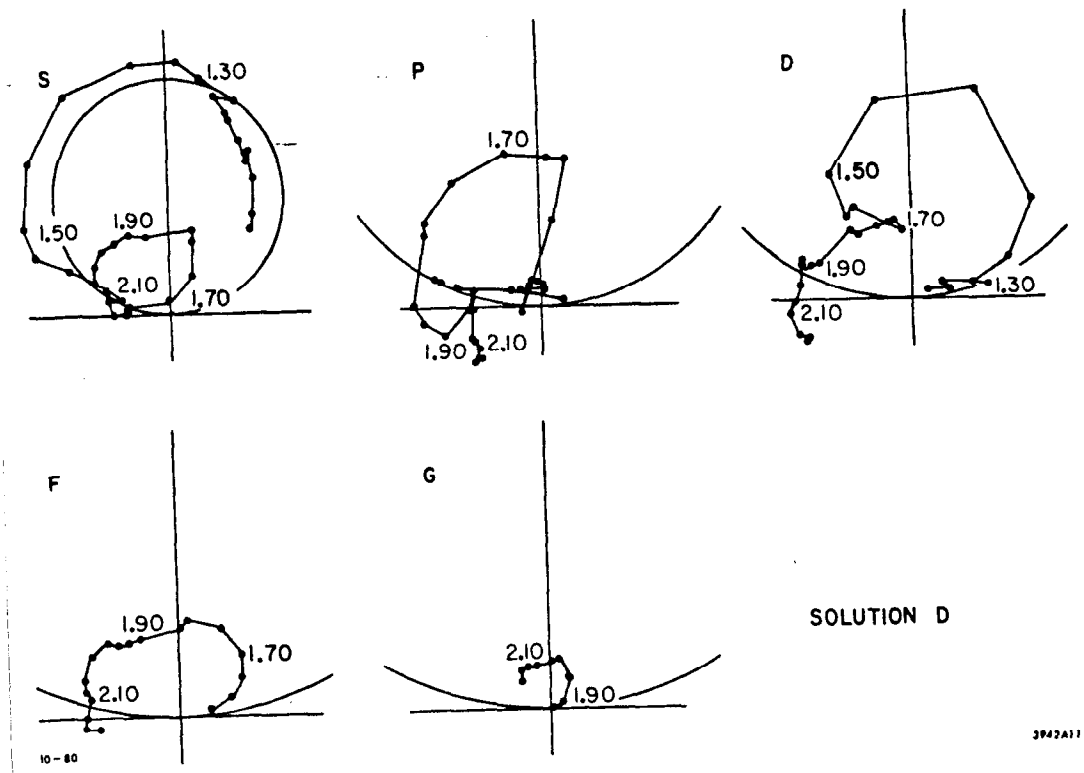

Figure 43 -- Argand plots for solution D.

TABLE 10

Single t′ bin PWA Results for the Elastic Region

The elastic region phase shifts. The phase shifts (δ) are defined in eq. VIII.14. The I=1/2 S and P-wave phase shifts were determined from the PWA in this analysis by the method described in VIII.F.6. The I=3/2 S and P-wave phase shifts shown here were taken from the results of the PWA of [5]. Masses are in GeV; phase shifts are in degrees.

	δ_S		δ_P	
M(Kπ)	I=1/2	I=3/2	I=1/2	I=3/2
0.81	31.1 ± 2.8	-12.8	12.6 ± 1.4	0.0
0.83	37.7 ± 3.8	-13.6	18.2 ± 1.6	0.0
0.85	40.8 ± 4.4	-14.3	25.7 ± 1.6	0.0
0.87	39.9 ± 2.5	-15.1	45.6 ± 1.1	0.0
0.89	37.1 ± 2.0	-15.8	79.5 ± 3.4	0.0
0.91	42.3 ± 2.7	-16.4	116.9 ± 2.1	0.0
0.93	51.3 ± 2.8	-17.1	142.3 ± 1.4	0.0
0.95	51.6 ± 3.1	-17.7	151.9 ± 1.5	0.0
0.97	52.4 ± 3.3	-18.3	158.2 ± 1.7	0.0
0.99	49.0 ± 3.0	-18.9	160.8 ± 1.7	0.0
1.02	49.2 ± 1.9	-19.8	164.6 ± 1.3	0.0
1.06	50.1 ± 1.7	-20.9	165.2 ± 1.3	0.0
1.10	53.4 ± 1.7	-21.9	168.0 ± 1.6	0.0
1.14	59.0 ± 3.5	-22.8		
1.18	60.1 ± 1.2	-23.7		
1.22	64.5 ± 2.0	-24.5		

TABLE 11

Single t′ bin PWA Results for the Inelastic Region

The magnitude and phases of the partial wave amplitudes in the M(Kπ) region above 1.12 GeV. (a) Solution A. (b) Solution B. (c) Solution C. (d) Solution D. Masses in GeV; phases in degrees.

M(Kπ)	ϕ_{rot}	S Magnitude	S Phase	P Magnitude	P Phase	D Magnitude	D Phase	F Magnitude	F Phase	G Magnitude	G Phase
1.14	0	0.85 ± 0.02	72 ± 4	0.13 ± 0.17	151 ± 8	0.08 ± 0.02	33 ±53				
1.18	0	0.87 ± 0.01	73 ± 1	0.10 ± 0.09	13 ±38	0.17 ± 0.03	13 ± 5				
1.22	0	0.92 ± 0.01	78 ± 2	0.11 ± 0.09	141 ± 7	0.14 ± 0.07	30 ±28				
1.26	0	0.93 ± 0.03	72 ± 6	0.08 ± 0.03	82 ±59	0.33 ± 0.06	10				
1.30	0	0.99 ± 0.02	82 ± 7	0.12 ± 0.02	112 ±10	0.27 ± 0.07	15				
1.34	0	1.05 ± 0.02	88 ± 3	0.11 ± 0.04	111 ±31	0.45 ± 0.05	23				
1.38	0	1.05 ± 0.03	98 ± 2	0.10 ± 0.02	102 ±22	0.67 ± 0.04	39				
1.42	0	1.02 ± 0.03	117 ± 1	0.10 ± 0.02	87 ±29	0.93 ± 0.03	72				
1.46	-14	0.87 ± 0.03	148 ± 1	0.08 ± 0.02	147 ±40	0.85 ± 0.03	114				
1.50	-14	0.71 ± 0.02	165 ± 2	0.10 ± 0.03	136 ±30	0.63 ± 0.03	137				
1.54	-19	0.62 ± 0.02	177 ± 4	0.08 ± 0.05	215 ±38	0.44 ± 0.04	148				
1.58	-31	0.46 ± 0.09	188 ± 5	0.37 ± 0.18	112 ± 9	0.46 ± 0.08	153	0.14 ± 0.09	42 ±21		
1.62	0	0.21 ± 0.08	163 ± 6	0.63 ± 0.03	80 ± 6	0.29 ± 0.04	97 ±12	0.25 ± 0.05	21		
1.66	0	0.15 ± 0.04	172 ± 5	0.62 ± 0.02	87 ± 3	0.34 ± 0.02	102 ± 6	0.32 ± 0.03	30		
1.70	0	0.04 ± 0.02	94 ±47	0.65 ± 0.01	103 ± 2	0.33 ± 0.01	105 ± 6	0.38 ± 0.03	44		
1.74	0	0.18 ± 0.03	55 ± 5	0.64 ± 0.02	126 ± 2	0.34 ± 0.01	114 ± 5	0.41 ± 0.02	63		
1.78	0	0.31 ± 0.03	70 ± 3	0.61 ± 0.02	145 ± 3	0.36 ± 0.01	129 ± 4	0.41 ± 0.02	85		
1.82	-14	0.36 ± 0.03	87 ± 3	0.58 ± 0.02	163 ± 3	0.38 ± 0.02	145 ± 4	0.37 ± 0.03	103		

TABLE 11 (cont.)

(a) SOLUTION A

M(Kπ)	ϕ_{rot}	S Magnitude	S Phase	P Magnitude	P Phase	D Magnitude	D Phase	F Magnitude	F Phase	G Magnitude	G Phase
1.86	0	0.59 ± 0.03	94 ± 3	0.38 ± 0.04	145 ± 8	0.31 ± 0.03	134 ± 8	0.37 ± 0.02	116		
1.90	0	0.62 ± 0.05	104 ± 7	0.31 ± 0.08	139 ±27	0.36 ± 0.03	135 ±13	0.38 ± 0.02	124	0.04 ± 0.07	32 ±22
1.94	0	0.62 ± 0.03	112 ± 8	0.27 ± 0.04	114 ±35	0.35 ± 0.05	136 ±13	0.36 ± 0.02	129	0.10 ± 0.08	33 ±26
1.98	26	0.57 ± 0.02	89 ±12	0.39 ± 0.10	64 ±26	0.32 ± 0.05	99 ±28	0.33 ± 0.05	109 ±14	0.17 ± 0.06	38
2.02	26	0.44 ± 0.02	97 ±13	0.52 ± 0.05	77 ±14	0.29 ± 0.03	103 ±25	0.37 ± 0.04	122 ± 9	0.23 ± 0.04	59
2.06	0	0.42 ± 0.02	130 ±14	0.49 ± 0.05	116 ±16	0.29 ± 0.04	146 ±27	0.37 ± 0.04	156 ±10	0.21 ± 0.05	84
2.10	0	0.41 ± 0.02	127 ±14	0.50 ± 0.03	123 ±14	0.25 ± 0.03	146 ±29	0.37 ± 0.04	162 ± 9	0.19 ± 0.05	105
2.14	0	0.40 ± 0.02	123 ±12	0.50 ± 0.02	129 ±12	0.26 ± 0.03	144 ±23	0.36 ± 0.04	166 ± 8	0.21 ± 0.05	119
2.18	0	0.39 ± 0.02	131 ±11	0.47 ± 0.02	138 ±12	0.29 ± 0.04	159 ±18	0.35 ± 0.04	177 ± 8	0.21 ± 0.05	127
2.22	0	0.37 ± 0.03	134 ±10	0.42 ± 0.02	151 ±12	0.32 ± 0.04	174 ±16	0.38 ± 0.04	184 ± 9	0.17 ± 0.05	132
2.26	0	0.36 ± 0.03	137 ± 9	0.41 ± 0.02	160 ±10	0.30 ± 0.04	182 ±13	0.34 ± 0.04	188 ± 8	0.17 ± 0.04	135

(b) SOLUTION B

M(Kπ)	ϕ_{rot}	S Magnitude	S Phase	P Magnitude	P Phase	D Magnitude	D Phase	F Magnitude	F Phase	G Magnitude	G Phase
1.86	0	0.33 ± 0.03	107 ± 3	0.55 ± 0.02	179 ± 3	0.42 ± 0.02	159 ± 4	0.37 ± 0.02	116		
1.90	0	0.37 ± 0.04	118 ± 7	0.50 ± 0.05	188 ± 6	0.45 ± 0.02	162 ±14	0.38 ± 0.08	124	0.02 ± 0.24	21 ±64
1.94	0	0.37 ± 0.09	130 ± 6	0.43 ± 0.14	196 ± 9	0.47 ± 0.02	166 ± 8	0.39 ± 0.06	129	0.06 ± 0.08	17 ±42
1.98	21	0.39 ± 0.03	122 ± 9	0.30 ± 0.06	164 ±21	0.49 ± 0.02	142 ±12	0.44 ± 0.03	116 ±10	0.16 ± 0.06	38
2.02	11	0.35 ± 0.02	142 ± 7	0.34 ± 0.02	138 ±11	0.45 ± 0.02	154 ± 9	0.50 ± 0.02	129 ± 6	0.22 ± 0.05	59
2.06	0	0.31 ± 0.02	171 ±10	0.34 ± 0.02	169 ±14	0.43 ± 0.02	185 ±12	0.48 ± 0.02	161 ± 7	0.21 ± 0.05	84
2.10	0	0.26 ± 0.02	187 ±10	0.36 ± 0.02	187 ±12	0.43 ± 0.03	201 ±11	0.48 ± 0.03	170 ± 7	0.19 ± 0.05	105
2.14	0	0.21 ± 0.02	191 ±12	0.39 ± 0.02	195 ± 9	0.42 ± 0.02	205 ±10	0.47 ± 0.02	177 ± 6	0.21 ± 0.05	119
2.18	0	0.20 ± 0.02	199 ±14	0.38 ± 0.02	204 ±11	0.43 ± 0.02	210 ±11	0.45 ± 0.02	187 ± 6	0.21 ± 0.05	127
2.22	0	0.17 ± 0.03	198 ±19	0.37 ± 0.02	213 ±12	0.43 ± 0.02	212 ±12	0.44 ± 0.03	191 ± 8	0.17 ± 0.05	132
2.26	0	0.14 ± 0.03	194 ±21	0.37 ± 0.02	214 ±12	0.41 ± 0.02	216 ±13	0.40 ± 0.03	195 ± 8	0.17 ± 0.05	135

TABLE 11 (cont.)

(c) SOLUTION C

M(Kπ)	ϕ_{rot}	S Magnitude	S Phase	P Magnitude	P Phase	D Magnitude	D Phase	F Magnitude	F Phase	G Magnitude	G Phase
1.86	0	0.59 ± 0.03	94 ± 3	0.38 ± 0.04	145 ± 8	0.31 ± 0.03	134 ± 8	0.37 ± 0.02	116		
1.90	0	0.62 ± 0.05	104 ± 7	0.31 ± 0.08	139 ±27	0.36 ± 0.03	135 ±13	0.38 ± 0.02	124	0.04 ± 0.07	32 ±22
1.94	0	0.62 ± 0.03	112 ± 8	0.27 ± 0.04	114 ±35	0.35 ± 0.05	136 ±13	0.36 ± 0.02	129	0.10 ± 0.08	33 ±26
1.98	31	0.57 ± 0.02	89 ±12	0.39 ± 0.10	64 ±26	0.32 ± 0.05	99 ±28	0.33 ± 0.05	109 ±14	0.17 ± 0.06	38
2.02	32	0.50 ± 0.03	93 ±11	0.45 ± 0.07	70 ±17	0.36 ± 0.03	102 ±19	0.34 ± 0.04	119 ±11	0.23 ± 0.04	59
2.06	0	0.49 ± 0.02	126 ±11	0.39 ± 0.07	110 ±20	0.37 ± 0.04	141 ±19	0.33 ± 0.04	154 ±12	0.21 ± 0.04	84
2.10	0	0.51 ± 0.02	120 ±10	0.37 ± 0.06	110 ±21	0.38 ± 0.04	141 ±14	0.31 ± 0.04	154 ±12	0.19 ± 0.05	105
2.14	0	0.48 ± 0.03	119 ± 9	0.38 ± 0.06	110 ±19	0.38 ± 0.04	146 ±12	0.29 ± 0.04	152 ±13	0.21 ± 0.05	119
2.18	0	0.45 ± 0.02	129 ± 9	0.38 ± 0.05	125 ±17	0.38 ± 0.04	159 ±12	0.30 ± 0.04	168 ±12	0.21 ± 0.05	127
2.22	0	0.42 ± 0.03	129 ± 9	0.35 ± 0.02	147 ±18	0.39 ± 0.04	168 ±11	0.34 ± 0.04	179 ±12	0.17 ± 0.05	132
2.26	0	0.40 ± 0.03	132 ±11	0.33 ± 0.03	151 ±23	0.40 ± 0.05	175 ±12	0.28 ± 0.04	179 ±16	0.17 ± 0.05	135

(d) SOLUTION D

M(Kπ)	ϕ_{rot}	S Magnitude	S Phase	P Magnitude	P Phase	D Magnitude	D Phase	F Magnitude	F Phase	G Magnitude	G Phase
1.86	0	0.33 ± 0.03	107 ± 3	0.55 ± 0.02	179 ± 3	0.42 ± 0.02	159 ± 4	0.37 ± 0.02	116		
1.90	0	0.37 ± 0.04	118 ± 7	0.50 ± 0.05	188 ± 6	0.45 ± 0.02	162 ±14	0.38 ± 0.08	124	0.02 ± 0.24	21 ±64
1.94	0	0.37 ± 0.09	130 ± 6	0.43 ± 0.14	196 ± 9	0.47 ± 0.02	166 ± 8	0.39 ± 0.06	129	0.06 ± 0.08	17 ±42
1.98	17	0.39 ± 0.03	122 ± 9	0.30 ± 0.06	164 ±21	0.49 ± 0.02	142 ±12	0.44 ± 0.03	116 ±10	0.16 ± 0.06	38
2.02	17	0.38 ± 0.02	131 ± 6	0.29 ± 0.02	149 ±16	0.49 ± 0.02	144 ± 8	0.46 ± 0.02	127 ± 7	0.22 ± 0.05	59
2.06	0	0.35 ± 0.02	158 ± 8	0.29 ± 0.02	181 ±18	0.48 ± 0.02	173 ± 9	0.44 ± 0.02	160 ± 8	0.21 ± 0.05	84
2.10	0	0.30 ± 0.04	162 ±10	0.33 ± 0.05	204 ±14	0.50 ± 0.03	181 ± 9	0.41 ± 0.02	165 ± 9	0.19 ± 0.05	105
2.14	0	0.27 ± 0.03	168 ± 9	0.32 ± 0.04	206 ±13	0.53 ± 0.03	186 ± 7	0.38 ± 0.03	169 ± 9	0.21 ± 0.05	119
2.18	0	0.25 ± 0.03	182 ±10	0.32 ± 0.03	213 ±14	0.51 ± 0.03	196 ± 8	0.39 ± 0.03	182 ± 8	0.21 ± 0.05	127
2.22	0	0.19 ± 0.04	181 ±13	0.36 ± 0.04	220 ±10	0.47 ± 0.03	200 ± 9	0.40 ± 0.03	188 ± 9	0.17 ± 0.04	132
2.26	0	0.18 ± 0.05	177 ±14	0.34 ± 0.05	219 ±14	0.48 ± 0.04	201 ±11	0.34 ± 0.04	189 ±12	0.17 ± 0.05	135

at 1.7 GeV. Significantly, the phase varies rapidly in this 1.3 to 1.6 GeV region, a strong indication of resonance structure. Above 1.7 GeV the four solutions have different detailed structure but all show a peak in the magnitude near 1.9 GeV with rapidly varying phase motion. The apparent jump in the phase at 1.7 GeV is not a cause for concern, it is merely a discontinuity introduced by the definition of the phase. This can be seen in the Argand diagrams in figs. 40-43 where the amplitude is seen to vary smoothly across the 1.7 GeV region. Since a physical amplitude should remain inside the unitary circle, its phase is restricted to the region 0° to 180°. If the amplitude passes through the origin (Im(a)=Re(a)=0), a discontinuity of phase from 180° to 0° can be expected. The Argand diagrams also strongly support the assertion that there are two S-wave resonant structures, one near 1.4 and the other near 1.9 GeV. The circular motion of the amplitude is indicative of classic resonance behavior.

The S-wave Argand plots show a number of mass bins outside the unitary circle in the mass regions 1.3 to 1.6 GeV and for M(Kπ)>2.0 GeV in solutions B and D. As explained in subsection F.5, the S-wave amplitude presented in these figures contains both I=1/2 and I=3/2 components, and unitarity is expected only for each component separately. Using the parametrization for the I=3/2 S-wave amplitude from ref. [5] given in eq. VIII.17 (valid for the Kπ mass range 0.7 to 1.6 GeV), the subtraction was made to isolate the I=1/2 S-wave amplitude. This I=1/2 amplitude is shown in an Argand diagram in fig 44. Here it can be seen that the I=1/2 S-wave amplitude remains inside the unitary circle as expected. For the mass region near and above 1.6 GeV,

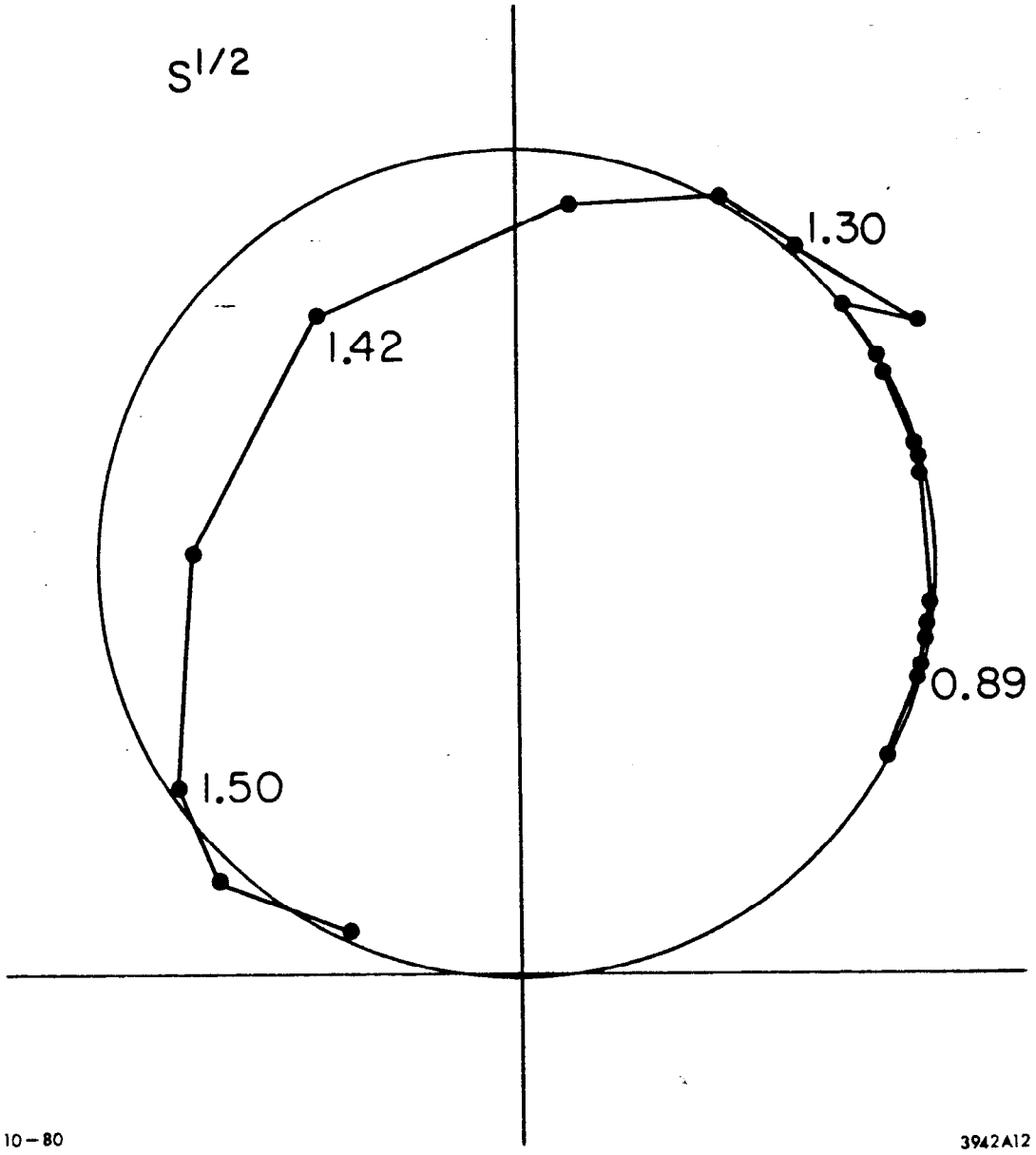

Figure 44 -- Argand plot for the I=1/2 S-wave amplitude. This was obtained by subtracting the I=3/2 S-wave component from the S-wave amplitude of fig. 35. The I=3/2 component was determined from an effective range parametrization (eq. VIII.17) taken from ref. [5].

it is not known if the parametrization of eq. VIII.17 is valid since this was near the limit of the mass region for that analysis. The I=1/2 S-wave amplitude is therefore not shown above 1.6 GeV although there are indications from the high mass data from ref. [5] that the I=3/2 S-wave amplitude may slowly decrease in magnitude for M(Kπ)>1.6 GeV. The interpretation of the S-wave amplitudes will assume that the I=3/2 contribution is slowly varying over the entire Kπ mass range (this is known to be true up to 1.8 GeV).

G.2 The P-wave amplitude

In the P-wave, the elastic unitarity region extends from 0.8 to 1.2 GeV. The well known spin 1 K*(895) is quite evident from the classic Breit-Wigner resonance phase motion. A fit was performed to this phase to determine the resonance parameters. Fits were performed for all leading resonances to determine the mass, width, etc., and will be presented in a separate subsection after all partial waves are described (subsection G.5). The results of the P-wave resonance fit agreed to within errors with the existing world data. This was an excellent check of the performance of the spectrometer and the analysis.

Above 1.12 GeV, in the inelastic region, the P-wave magnitude drops to nearly zero. When this occurs, the phase becomes nearly indeterminate as is obvious from the large error bars on the P wave phase in the 1.12 to 1.56 GeV region. At 1.56 GeV, the magnitude increases, accompanied by rapid phase motion. The magnitude plateaus at a value of 0.6 for nearly

200 MeV after which it drops slowly. The trailing edge of this "bump" varies with the different solutions. In the Argand diagrams (fig. 39), the P-wave shows a somewhat ragged circular motion in the 1.6 to 1.9 GeV region for all solutions. However solutions A and C show a second smaller circular loop at higher mass which may indicate another resonant structure near 2.1 GeV. In solutions B and D, the high mass Argand points move outside the unitary circle by a small amount. This is cause for some concern, but as explained previously in subsection F.5, there are several effects that would allow for phase rotations that could bring the points back into the unitary circle. The high mass behavior of the amplitude in solutions B and D show very little structure. The phase motion is quite slow and the magnitude remains nearly constant. A cusp-like structure near 2.0 GeV is evident but may only be a reflection of the uncertainty of the absolute phase.

G.3 The D-wave amplitude

The D-wave magnitude clearly shows the presence of the well established spin 2 K*(1430). A Breit-Wigner fit was performed to the D-wave magnitude and the resulting mass, width, and elasticity compared favorably to the existing world values (see subsection f). At masses above the 1430 resonance, the magnitude is seen to remain at values near 0.4 for the rest of the high mass region. The detailed structure of each ambiguous solution is different at high mass but all show a smoothly varying magnitude with a slow, steady increase in the phase. In the Argand plots for the D-wave, the classic circular resonance shape

for the K*(1430) is immediately apparent. At 1.7 GeV, there is a cusp followed by an arc shaped path for the mass range above 1.7 GeV. Such a cusp-like structure is often due to the presence of another nearby resonance as can be seen in the case of some baryon resonances (e.g., πN S11 amplitude or πΣ D13 amplitude in ref. [2]). The interpretation of this structure as a second resonance is not strongly justifiable due to large phase determination uncertainty. It can be stated however that the data is not inconsistent with such a resonant structure interpretation.

G.4 The F-wave amplitude

At 1.56 GeV, where the F-wave is first introduced, the magnitude rises steadily to a peak near 1.75 GeV then drops only slightly at higher masses. In fact, for solutions B and D, the magnitude rises again to an even larger value. In solution A and C the magnitude remains nearly constant for masses above 1.9 GeV. The initial peaking in the F-wave magnitude is confirmation of the spin 3 K*(1780). A Breit-Wigner resonance fit was performed using the F-wave magnitude and the results can be seen in subsection G.5. The F-wave phase was fixed in the vicinity of the resonances as described in subsection F.5. At Kπ masses above 1.9 GeV, each solution shows a steadily increasing phase. The F-wave Argand diagrams have the initial clear circular motion expected of a resonance but at 1.86 GeV, the phase slows and the magnitude remains large. Thus the circular phase motion is not completed. The amplitude behavior for masses above 1.86 GeV could be due to background contributions or could be due to the presence of one or more additional

nearby F-wave resonances. It is a feature of a Breit-Wigner resonance that the magnitude of the amplitude drop more slowly on the high mass side of a high spin object (due to the centrifugal barrier factor). Thus some of the large magnitude on the high mass side of these higher spin resonances may be explained by this feature.

G.5 The G-wave amplitude

In this analysis, five mass bins with non-zero G-wave amplitude were obtained before the upper limit of the mass range of the data was reached. In these five bins the G-wave magnitude can be seen to rise from zero, reach a peak near 2.1 GeV and drop slightly at higher mass. This gave excellent confirmation of the spin 4 resonance first postulated from the evidence from the angular moments. A Breit-Wigner fit to this resonance was performed and is presented in the next subsection. The Argand plot shows that the G-wave amplitude does indeed have the circular motion characteristic of a resonance. It is also clear that the elasticity of this resonance is extremely small.

G.6 The Breit-Wigner resonance fits

Breit-Wigner resonance fits were performed using the P-wave phase and the D, F, and G-wave magnitudes. The exact parametrizations used in these fits are discussed in Appendix E. The results are shown in fig. 45 where the points are the phase or magnitudes from the PWA and the curves are the Breit-Wigner fits. The resonance parameters

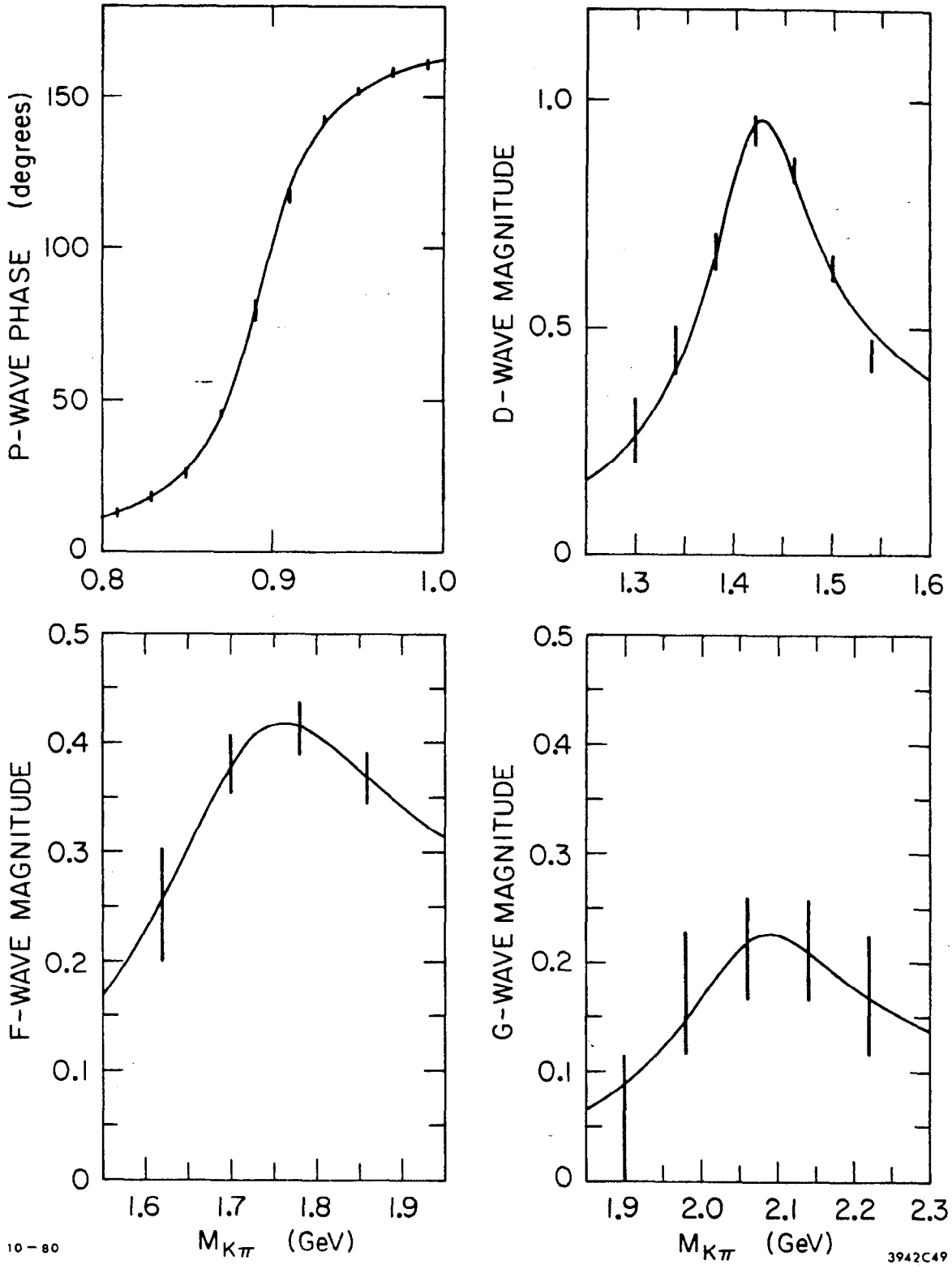

Figure 45 -- Breit-Wigner resonance fits to the partial wave phase or magnitudes. (a) Spin 1 fit to P-wave phase. (b) Spin 2 fit to the D-wave magnitude. (c) Spin 3 fit to the F-wave magnitude. (d) Spin 4 fit to the G-wave magnitude. Plotted points are partial wave phase or magnitudes of figs. 36-39, curves are results from fits.

determined by the fits are presented in Table 12. The statistical errors were obtained from the fit, the systematic errors are estimates based on the spectrometer momentum measurement accuracy and on other expected systematic sources.

In Table 13 the resonance parameters from these PWA Breit-Wigner fits are compared with the results from the fits to the angular moments and also compared to the Particle Data Group 1980 values [2] for the first three established resonances. The agreement for the spin 1 K*(895) and the spin 2 K*(1430) is quite good. The mass of the spin 3 resonance from the fits presented in this analysis are somewhat low compared to the PDG value of 1785 MeV. The widths from both the PWA and the moments fits are quite large (although not well determined) and not at all close the the PDG value of 126 MeV. However, the width agrees reasonably well with width measurements made by other moments or PWA fits (e.g., references [5,25]). The mass and width of the new spin 4 resonance is fairly consistent between the moments and PWA fits. The width is not well determined by either method largely due to the large errors and small number of data points. In all the resonance fits, the chi-squared per degree of freedom is found to be quite good.

G.6 Underlying resonance parameter estimates

Several major difficulties arise when one attempts to determine the exact mass, width, and elasticity of these underlying resonances. One problem in obtaining the resonance parameters is the large indeterminancy of the overall phase of the partial wave amplitudes.

TABLE 12

Resonance Parameters from Fits to PWA Amplitudes

(a) Breit-Wigner spin 1 fit to P-wave phase. (b) Breit-Wigner spin 2 fit to D-wave magnitude. (c) Breit-Wigner spin 3 fit to F-wave magnitude. (d) Breit-Wigner spin 4 fit to G-wave magnitude.

(a) Parameter	Fit Result
Mass	894.6 ± 0.8 (± 2.0)* MeV
Width	49.8 ± 1.2 MeV
R	7.8 ± 3.2
χ^2/DOF†	3.9/7

(b) Parameter	Fit Result
Mass	1428 ± 3 (± 4)* MeV
Width	98 ± 8 MeV
Elasticity	0.43 ± 0.01
χ^2/DOF†	3.8/4

(c) Parameter	Fit Result
Mass	1753 $^{+25}_{-18}$ (± 20)* MeV
Width	300 $^{+170}_{-80}$ MeV
Elasticity	0.16 ± 0.01
χ^2/DOF†	0.06/1

(d) Parameter	Fit Result
Mass	2070 $^{+100}_{-40}$ (± 30)* MeV
Width	240 $^{+500}_{-100}$ MeV
Elasticity	0.07 ± 0.01
χ^2/DOF†	0.86/2

* Estimate of systematical error
† DOF = # of degrees of freedom

TABLE 13

Comparison of All Resonance Fits and PDG Values

(a) The leading spin 1 resonance. (b) The leading spin 2 resonance.
(c) The leading spin 3 resonance. (d) The leading spin 4 resonance.

(a)	Breit-Wigner Fit to P-Wave Phase				Breit-Wigner Fit to t_{20} Moment				PDG Table Value*		
Parameter	Fit Result	Stat. Error	Syst. Error		Fit Result	Stat. Error	Syst. Error		Table Value	Error	
Mass	894.6	± 0.8	± 2.0	MeV	887.0	± 3.3	± 2.0	MeV	896.1	± 0.3	MeV
Width	49.8	± 1.2		MeV	58.8	± 7.1		MeV	52.2	± 0.5	MeV
R	7.8	± 3.2			--	--					
x^2/DOF†	3.9/7				2.9/1						

(b)	Breit-Wigner Fit to D-Wave Magnitude				Breit-Wigner Fit to t_{40} Moment				PDG Table Value*		
Parameter	Fit Result	Stat. Error	Syst. Error		Fit Result	Stat. Error	Syst. Error		Table Value	Error	
Mass	1428	± 3	± 4	MeV	1426	± 3	± 4	MeV	1434	± 5	MeV
Width	98	± 8		MeV	118	± 13		MeV	100	± 10	MeV
Elasticity	0.43	± 0.01			--	--			0.49	± 0.02	
x^2/DOF†	3.8/4				0.32/2						

(c)	Breit-Wigner Fit to F-Wave Magnitude				Breit-Wigner Fit to t_{60} Moment				PDG Table Value*		
Parameter	Fit Result	Stat. Error	Syst. Error		Fit Result	Stat. Error	Syst. Error		Table Value	Error	
Mass	1753	+ 25 - 18	± 20	MeV	1756	+ 17 - 13	± 20	MeV	1785	± 6	MeV
Width	300	+ 170 - 80		MeV	185	+ 53 - 38		MeV	126	± 20	MeV
Elasticity	0.16	+ 0.01			--	--			0.19	± 0.05	
x^2/DOF†	0.06/1				3.4/5						

(d)	Breit-Wigner Fit to G-Wave Magnitude				Breit-Wigner Fit to t_{80} Moment				Simplified Amplitude Fit to t_{00}, t_{70}, t_{80} Moments			
Parameter	Fit Result	Stat. Error	Syst. Error		Fit Result	Stat. Error	Syst. Error		Fit Result	Stat. Error	Syst. Error	
Mass	2070	+ 100 - 40	± 30	MeV	2140	+ 140 - 60	± 30	MeV	2075	+ 40 - 30	± 30	MeV
Width	240	+ 500 - 100		MeV	250	+ 300 - 130		MeV	240	+ 400 - 80		MeV
Elasticity	0.07	± 0.01			--	--			--	--		
x^2/DOF†	0.86/2				2.5/3				15.7/13			

* Reference [2]
† DOF = # of degrees of freedom

Knowledge of the absolute phase is crucial since a simple fit to the partial wave magnitude would not be proper if additional nearby resonances or backgrounds contribute strongly to that particular mass region of the partial wave amplitude in question. Resonance fits requiring both magnitude and phase information will be necessary and thus substantial phase uncertainty (which is expected as explained in VIII.) can lead to inaccurate resonance parameter determination. Similarly, the effects of non-resonant backgrounds (I=3/2, $n\pi$, etc.) could also produce minor inaccuracies in the resonance parameter determination.

A method was devised to obtain rough estimates of the masses, widths, and elasticities that was believed to be at least partially immune to the problems just stated. For the 0^+ resonance near 1400 MeV the method consisted of setting the resonance mass to the value of $M(K\pi)$ where the speed of the phase motion as a function of $M(K\pi)$ was greatest (maximum phase motion is another method of determining the resonance mass; it is especially useful where slowly varying non-resonant backgrounds contribute). This was possible because the absolute phase was believed to be well determined in this mass region. The width was obtained by taking the value of $M(K\pi)$ needed to go from ϕ_r-45° to ϕ_r+45°, where ϕ_r is the phase of the resonating wave at the resonance mass. The elasticity was estimated by ascribing circular motion to the S wave Argand plot and using the diameter of the circle as the elasticity value. This method of estimating the elasticity was used for all the other underlying resonances but the masses and widths were determined differently. The masses and widths were obtained by estimating where

the maximum phase motion occurs by examining the Argand projection of the real part of the resonating amplitude (see figs. 46-50 for Argand projections of the partial wave solutions). The maximum motion was assumed to occur at the M(Kπ) value halfway between the two points where the real part of the amplitude is nearly constant just outside of the region where it changes rapidly. Thus, for the 1^- resonance near 1700 MeV in solution A, the two points are chosen as 1600 MeV (where $Re(a_p)$ starts its rapid motion in the negative direction) and 1800 MeV (where $Re(a_p)$ stops its rapid motion). The mass and width are therefore estimated as 1700 MeV and 200 MeV respectively. This method was repeated for all the remaining underlying resonant structures for all applicable solutions and the results are presented in Table 14. No errors are given since this method was not a fit and did not provide errors. This method used to estimate the resonance parameters is nearly independent of background effects if those effects are slowly varying as a function of Kπ mass. However, the method is highly sensitive to the choice of overall phase as a function of M(Kπ) and this is the main reason for the large expected errors. It should also be noted that any of the underlying resonant structures could in fact be due to two resonances that are very close in mass. The resonance parameters in Table 14 are based on the assumption that each structure is due to a single resonance.

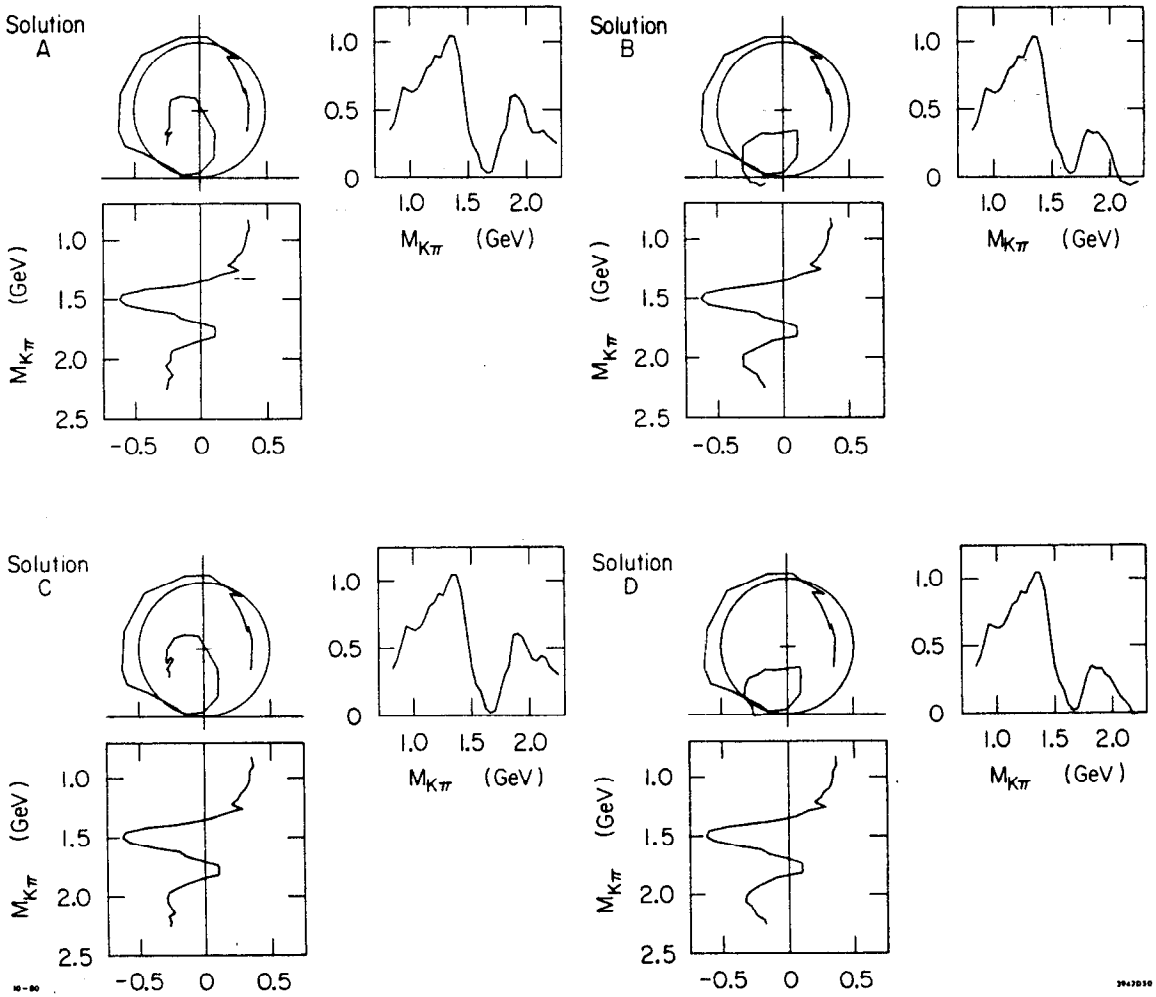

Figure 46 -- Argand plot with real and imaginary projections for the four S-wave amplitude solutions. The underlying resonance parameters were determined from these projections as explained in the text.

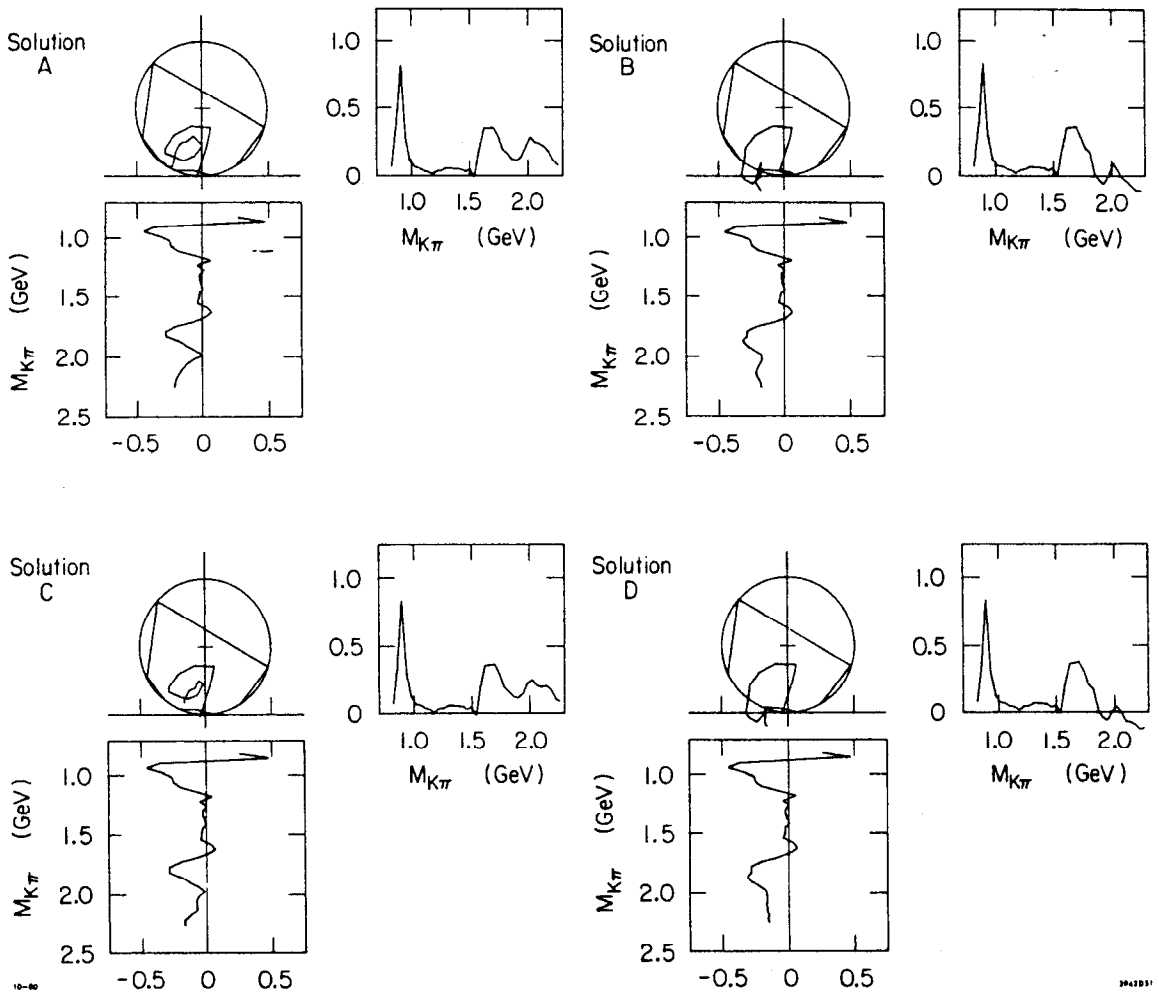

Figure 47 -- Argand plot with real and imaginary projections for the four P-wave amplitude solutions. The underlying resonance parameters were determined from these projections as explained in the text.

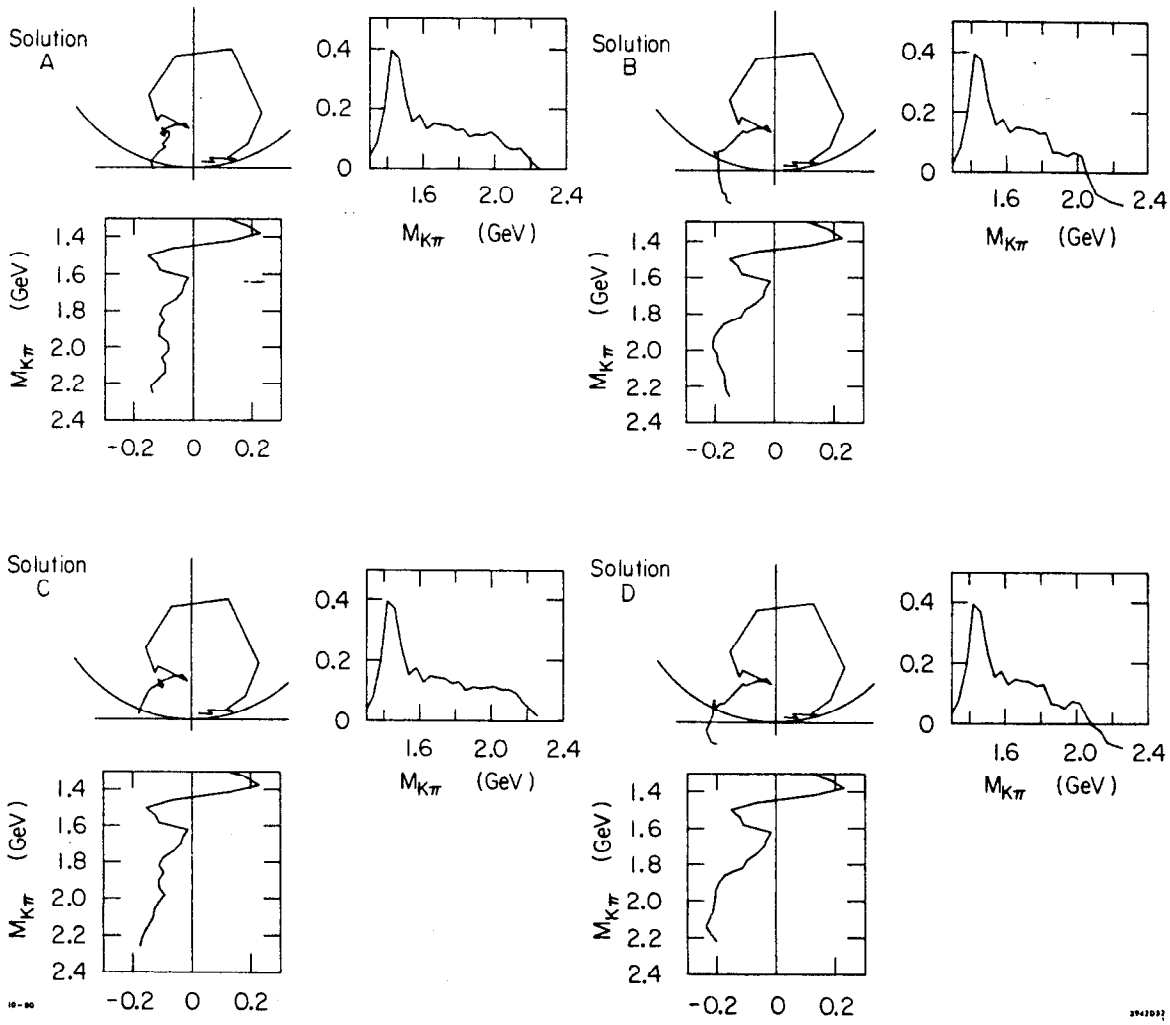

Figure 48 -- Argand plot with real and imaginary projections for the four D-wave amplitude solutions.

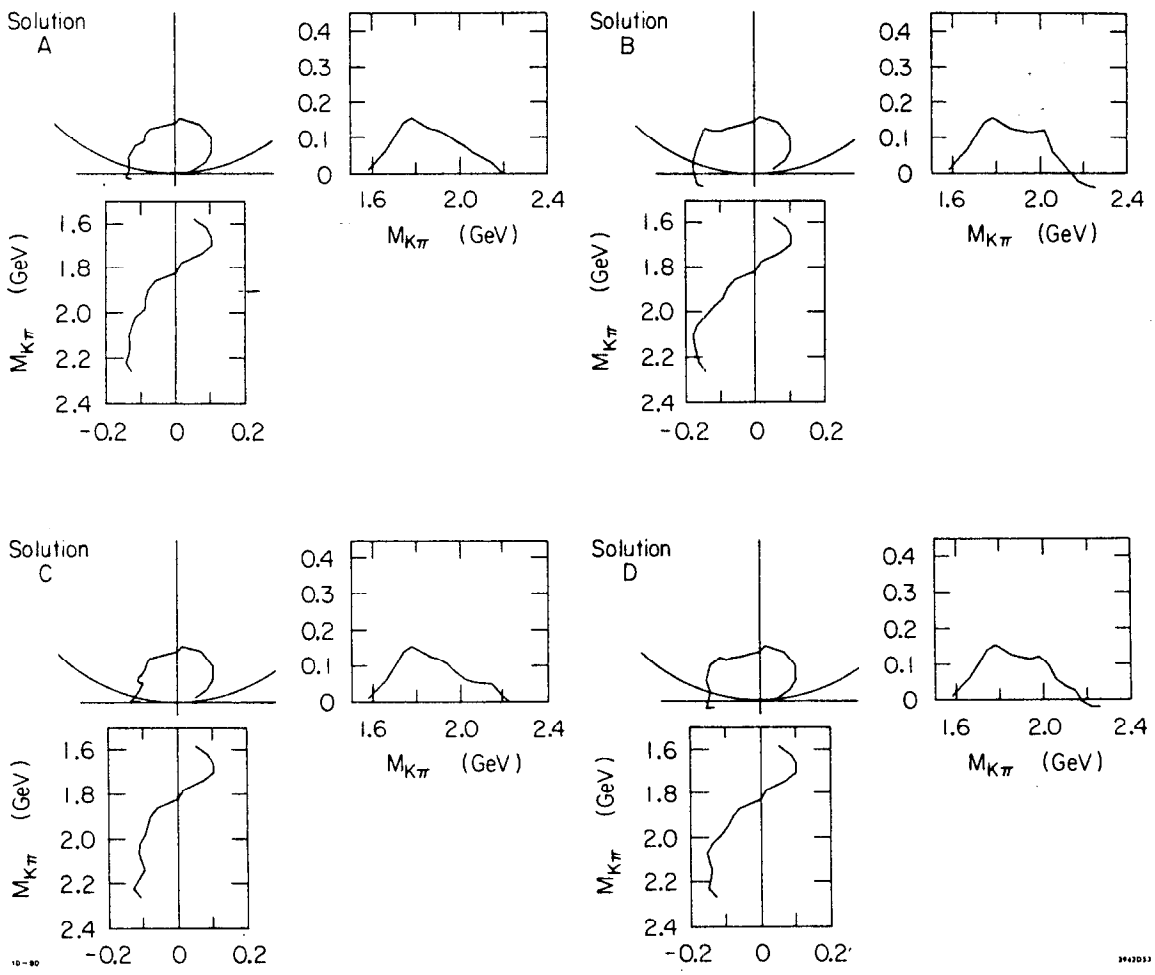

Figure 49 -- Argand plot with real and imaginary projections for the four F-wave amplitude solutions.

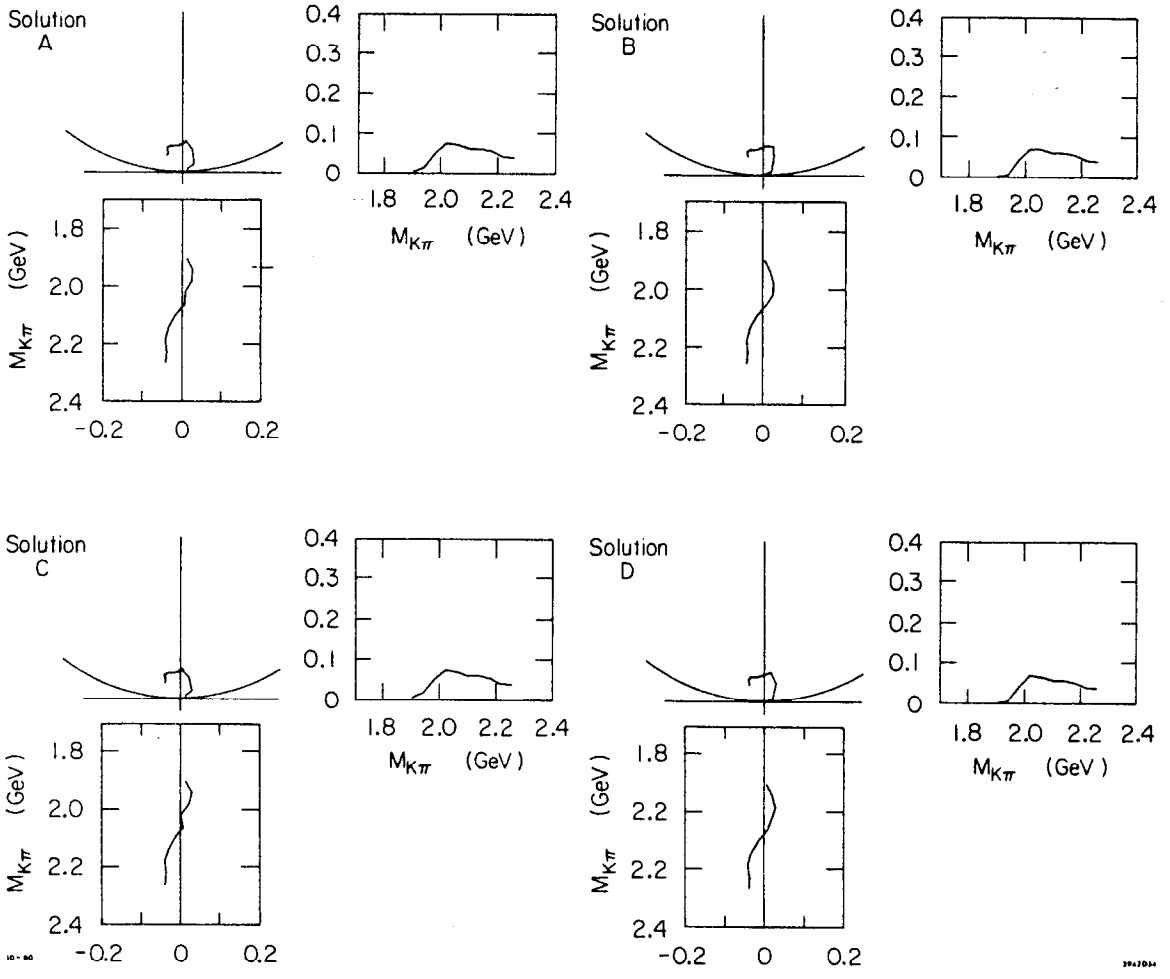

Figure 50 -- Argand plot with real and imaginary projections for the four G-wave amplitude solutions.

TABLE 14

Underlying Resonance Parameter Estimates

Estimates for mass, width, and elasticity of the underlying S and P-wave resonances using the method described in the text.

S wave resonances:

Parameter	Value
Mass (MeV)	1420
Width (MeV)	240
Elasticity	0.85

	SOLUTION			
	A	B	C	D
Mass (MeV)	1880	1900	1880	1900
Width (MeV)	200	240	220	240
Elasticity	0.45	0.35	0.45	0.35

P wave resonances:

Mass (MeV)	1700	1720	1700	1720
Width (MeV)	200	200	200	200
Elasticity	0.35	0.35	0.35	0.35
Mass (MeV)	2100		2100	
Width (MeV)	240		240	
Elasticity	0.2		0.2	

Chapter IX

DISCUSSION OF QUARK MODEL, LEADING STATES, AND L·S SPLITTINGS

A. Discussion of the Results

The results from the moments analysis and from the partial wave analysis contain much new information pertaining to $K^-\pi^+$ resonance structure. The first important result is the confirmation of the three existing leading K* resonances, the K*(895), K*(1430), and the K*(1780). Of particular interest is the confirmation of the fact that the spin 2 resonance has a mass closer to 1430 MeV rather than 1420 MeV (a fact first established by the results from ref. [5]). The analyses utilizing angular information have shown that the mass assignment obtained in the past from fits to overall mass distributions is too low due to the presence of the large S wave background which peaks at 1380 MeV.

There has been much confusion as to the mass and width of the spin 3 K* resonance, especially the width determination, which varies from less than 100 MeV to nearly 300 MeV. The results from this analysis indicate that the width is indeed difficult to determine, primarily because of the possibility of either strong resonant or non-resonant backgrounds just above the K*(1780) mass. The fit to the leading moment (t_{60}) and the fit to the F wave magnitude both agree that the K*(1780) width is much larger than the 126 MeV quoted in the PDG tables [2]. A value closer to 200 MeV for the width is supported by the results from

this analysis, in general agreement with the estimates made by the two other partial wave analyses of refs. [5] and [25].

The evidence for a K* resonance near 2080 MeV from both the angular moments and the PWA is the first observation (actually simultaneous with ref. [26]) of a $J^P=4^+$ K* resonance. The behavior of the G wave amplitude shows typical resonance behavior in an Argand diagram and the lack of t_{90} and $t_{10,0}$ moments at the same mass indicate that the J=4 spin assignment of this resonance is correct. The mass and width determination of this resonance have sizeable errors, primarily due to the dwindling statistics at high $K\pi$ masses. The extremely small elasticity (~0.07) of the resonance also contributes to the difficulty of measuring the mass and width. When placed on a Chew-Frautschi plot (see fig. 46), this new 4^+ resonance falls very close to the line defined by the first three leading resonances (the natural spin-parity strange meson trajectory). The K*(2080) is naturally interpreted as the I=1/2 SU(3) partner of the I=0 4^+ h(2040) meson (the quark model interpretation will be discussed in more detail in the next section). It is also noteworthy that no evidence was found for any higher spin ($J\geq 5$) resonance structure in the entire $K\pi$ mass range of this analysis (0.8 to 2.24 GeV) [27]. An upper limit to the elasticity of a spin 5 resonance, assuming a width similar to the spin 4, in the mass range of this analysis is estimated to be 0.05.

Another significant result from the PWA in this study is the fact that the elastic $K\pi$ scattering amplitude has a unique solution up to a $K\pi$ mass of 1.8 GeV. The previous PWA of ref. [5] found a unique solution up to 1.5 GeV. Due to the higher statistics and improved acceptance at

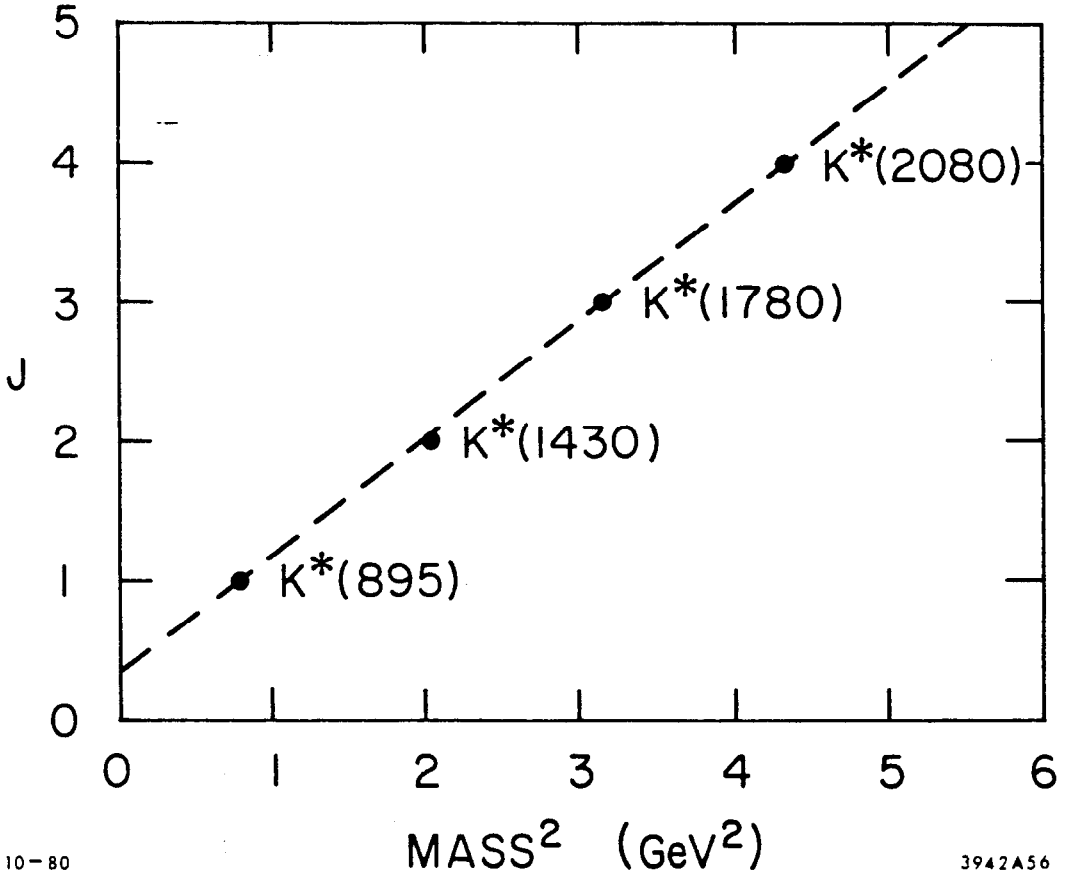

Figure 46 -- Leading natural spin-parity strange meson trajectory on a Chew-Frautschi plot.

high $K\pi$ mass, this analysis was able to ascertain that the imaginary parts of the Barrelet zeroes did not approach zero until 1.8 GeV (where Z_3 approached zero) and 2.0 GeV (where Z_1 approached zero). The unique solution that was determined by this analysis corresponds to solution B in ref. [5] and thus the features in that solution can be directly compared with the results presented here. Thus the unique solution from this analysis verifies the spin 1 underlying resonance structure in the mass region near 1.7 GeV that was first indicated in solution B of ref. [5] (this resonance structure will be discussed later). A comparison of the results for the region of overlap between this analysis and the analysis of ref. [5] has shown no major conflicts. This is taken as a confirmation of the results of ref. [5] and also provides additional confidence in the results from this analysis.

A second important result based on the behavior of the Barrelet zeroes is that due to the proximity of $Im(Z_1)$ to zero, solutions A and C have nearly identical structure for the amplitudes (the same is true for solutions B and D). Thus for $M(K\pi)>1.8$ GeV, there are really only two solutions that differ significantly in the structure of their partial wave amplitudes.

One of the primary motivations for performing a PWA on the $K\pi$ elastic scattering data was to unravel the underlying (i.e., non-leading) resonance structure. The PWA presented here was quite successful in attaining this goal by verifying an underlying 0^+ resonance near 1420 MeV, by verifying a 1^- resonant structure near 1700 MeV and establishing it uniquely (i.e., not just in two of four ambiguous solutions), by observing a second high mass 0^+ resonant

structure near 1900 MeV in all solutions, and by observing a second high mass 1^- resonant structure near 2100 MeV in two of the four solutions.

The underlying structure in the high mass regions of the D and F waves is intriguing but cannot be unambiguously interpreted as resonant structure. However, the large amount of magnitude in both the D and F waves at $K\pi$ masses above their respective leading resonances is interesting. It is possible that with a more accurate phase determination and better understanding of the possible non-resonant backgrounds, the high mass D and F waves may also yield underlying resonances.

This concludes the summary of the major results from this analysis. What follows is a brief review of some of the problems that still exist in the analysis of $K\pi$ elastic scattering and some suggestions of how these might be solved.

1) The uncertainty in the width of the 3^- and 4^+ leading resonances: More statistics would pin down the width of the 4^+ resonance to a large degree (and to a smaller degree for the 3^-) but it is likely that a better understanding of the resonant and non-resonant backgrounds will be necessary before these resonances can be properly parametrized.

2) I=3/2 amplitudes: The I=3/2 $K\pi$ partial wave amplitudes must be measured at high mass to insure that the amplitudes shown in this analysis are pure I=1/2 component. This is expected to be accomplished in the near future as a result of the analysis of K^+p data taken concurrent to the K^-p data of this analysis (the I=3/2 amplitude can be isolated with the additional information from a PWA of $K^+p \rightarrow K^+\pi^+n$) [28].

3) Backgrounds: Non-Kπ scattering backgrounds are likely to play a small role leading to systematic errors in the results of this analysis. Specially designed experiments could result in a purer $K^-\pi^+n$ final state sample but effective removal of the entire diffractive $N^*\rightarrow\pi^+n$ background is not likely to be easily solved.

4) Phase determination: All three previous problems contribute signficantly to this problem, thus reducing their effects will reduce the magnitude of this problem. As noted in the last chapter, the overall phase is completely indeterminate in that the physics is unaffected by the choice of overall phase (only the phase differences between partial waves is physically important). However, for the purposes of fitting individual partial wave amplitudes and for other mass independent interpretations of the amplitudes, the overall phase determination is important. One way to bypass this problem is to create a mass dependent model that incorporates resonances (and/or backgrounds) for each wave for the entire mass region of the analysis. Such a model would use only the phase differences between waves and thus be independent of the choice of overall phase for each mass bin. It is quite possible that if the backgrounds are fairly well understood, such a model could be designed that would result in a good fit to the PWA results presented here. However, the large number of parameters resulting from the large number of potential resonances (anywhere from 7 to 12) makes such a model extremely difficult to fit. Several attempts have been already made but problems with stability, multiple solutions, and other multi-parameter fitting difficulties have thus far prevented success.

5) Measurement of the resonance parameters of the underlying resonances: This problem is also dependent on the previously described problems, especially 4). Of course, a successful mass dependent model would solve this problem immediately but in lieu of that, a sound method of phase determination is prerequisite for obtaining believable underlying resonance parameters.

6) Multiple ambiguous solutions: Three possibilities exist that could reduce the ambiguities. First, higher statistics would reduce the error bars on the Barrelet zeroes so those $Im(Z_i)$ that came close to but didn't actually "cross" zero could be spotted (this could well be the case for the "crosses" obtained in this analysis; to within errors it could not be determined if Z_1 and Z_3 were consistent with zero for some $M(K\pi)$). On the other hand, if an $Im(Z_i)$ did actually pass through zero, no amount of statistics could reduce the ambiguity. Then one would have to resort to the second possibility which involves measuring the partial wave amplitudes in other $I=1/2$ strange meson inelastic channels such as $K\pi\pi$. If structures are uniquely observed in those other inelastic channels but are not observed at the same mass in some of the solutions in $K\pi$ elastic scattering, those solutions could be ruled out. The third possibility requires measuring the moments of the angular distribution of the $K^0\pi^0$ final state produced via π exchange. Because this final state has a different relative coupling between the $I=1/2$ and $I=3/2$ components than that for $K^-\pi^+$, a slightly different angular distribution would be expected. Each of the ambiguous solutions from this analysis would result in different predictions for the angular

distributions for $K^0\pi^0$ scattering hence a measurement of the $K^0\pi^0$ angular distribution could resolve the ambiguity (a discussion of the possible resolution of the ambiguities is given in refs. [5,29].

B. Quark model interpretation of the observed Kπ resonances

B.1 The model

With the success of the quark model in providing an accurate representation of meson states, it is desirable to see what the model predicts for strange meson states with the quantum numbers allowed for a $K^-\pi^+$ decay. The allowed quantum numbers for a $q\bar{q}$ meson system are $J=L+S$, and $P=(-1)^{L+1}$, where L and S are the total $q\bar{q}$ angular momentum and total spin as shown in fig. 1. The expected spectrum of states can be displayed as a function of L and mass squared, M^2, as shown in fig. 52. The recurrence of states in the same column but with higher values of M^2 are taken to be radial excitations. In the S=1 half of the plot, the triplet states are due to the spin-orbit (L·S) splitting.

In the specific reaction $K^-p\rightarrow K^-\pi^+n$ produced by π exchange, the (Kπ) scattering state is limited to natural spin-parity, $(P=(-1)^J)$. This is because the Kπ final state has parity $P=(-1)^L$, where L is the angular momentum between the K and π. Since both K and π have zero spin, $J=L+S=L$, and by parity conservation $P=(-1)^J$ for the (Kπ) state. This restriction added to the allowed J and P from the quark model implies that only S=1 $q\bar{q}$ states are allowed in the Kπ elastic scattering reaction. Thus the states predicted by the quark model for this reaction

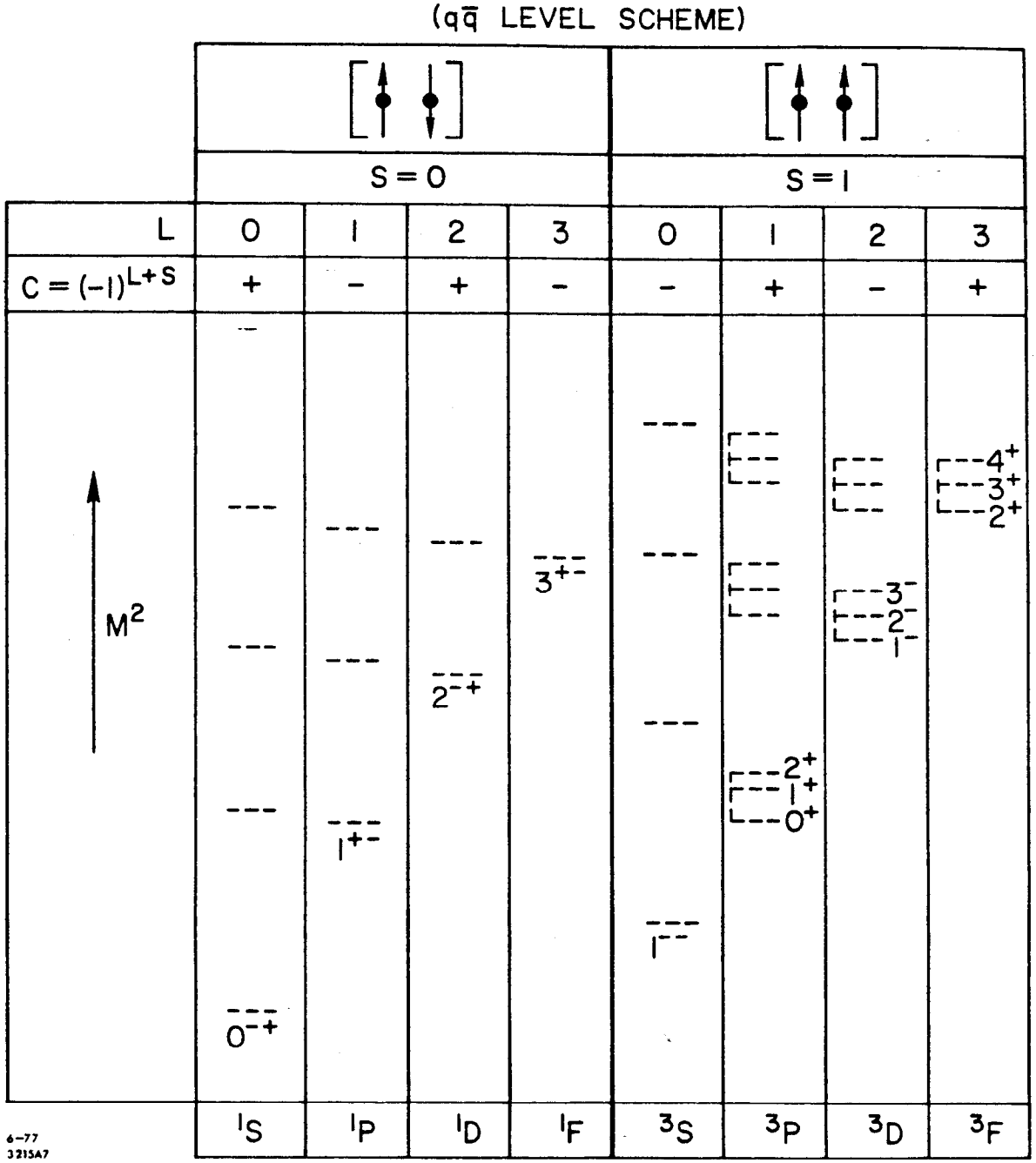

Figure 52 -- Energy level plot of meson spectrum arising from $q\bar{q}$ system. Level splittings are loosely based on simple harmonic oscillator potential model.

are limited to those in the S=1 half of the energy level plot. In addition, only the highest and lowest spin members of the triplet states are allowed by the natural J^P requirement.

The quark content of a $(K^-\pi^+)$ state is $s\bar{d}$. In Table 15, the predicted $(s\bar{d})$ states that have been experimentally observed prior to this analysis are presented. The status of the full light quark meson spectrum prior to this analysis has already been presented in fig. 2 in chapter I.

B.2 Identifying the observed resonances with quark model states

It is now possible to see how well the resonances observed in this analysis fit into the predicted quark model states. The leading $1^-,2^+,3^-$ states as well as the 0^+ ground state have been observed. In addition, the 4^+ resonance can be identified with the 4^+ member of the L=3 triplet. The second 0^+ resonance (at 1900 MeV) can only be a radial excitation (n=2) if the quark model is valid. This would be the first unambiguous evidence for a radial excitation in the natural parity strange $q\bar{q}$ spectrum. Evidence for a 0^- radial excitation, the K'(1400), has been presented (refs. [30,35]) and a similar radially excited state candidate in the non-strange $q\bar{q}$ spectra, the $\rho'(1600)$, has been observed.

The 1^- resonance near 1700 MeV is now unambiguously verified but its position in the quark model is ambiguous since the next 1^- state could be a radial excitation of a L=0 state or the 1^-, L=2 triplet state. It is also possible that the 1^- resonance structure contains both

TABLE 15

Previously Existing Strange Meson Resonances

(Masses in MeV)

J^P	$n^\dagger$	Name	Mass	Comment
S=0 states: (not accessible in this analysis)				
0^-	1	K	497	Well established
1^+	1	Q_B	1355	Well established
0^-	2	K′	1400	Not well established
S=1 states: (all but Q_A are accessible)				
1^-	1	K*	895	Well established
1^+	1	Q_A	1340	Well established
2^+	1	K*	1430	Well established
0^+	1	κ	1490?	Not well established
3^-	1	K*	1780	Well established

† n = radial quantum number

of these states if they are nearly degenerate in mass. If the $1^-(1700)$ resonant structure is really two resonances, and if solution A or C is correct, then the $1^-(2100)$ resonant structure could be the n=3 radial excitation of the L=0 state or the n=2 radial excitation of the 1^-, L=2 triplet member (or both). Otherwise, the $1^-(2100)$ structure may be whatever 1^- state that is available after the $1^-(1700)$ state has been determined.

B.3 Problems with resolving quark model states

Clearly, there are two very important problems that need to be resolved in order to clean up the $s\bar{d}$ natural spin-parity spectrum. The first problem is how to find out if there are one or two resonances in the $1^-(1700)$ structure. The second problem is how to determine whether a resonance is a radial excitation or a L=2 triplet member. The first problem may be solved by higher statistics, better background removal, and proper phase determination. If the two states are almost exactly on top of one another, it may be possible to determine this based on elasticity arguments (but this may require other theoretical assumptions).

The second problem is much more difficult but two methods have been proposed for resolving the radial vs. L=2 ambiguity. The first method is based on the assumption that the theory (i.e., binding potential, QCD, or whatever) will be sufficiently understood so that simple mass splittings can be predicted and thus the states can be properly associated. The second method is based on a theory of pionic decays in

the quark model (ref. [31]). In this theory, the relative sign of the amplitude for the 1^-, L=0 radial state decaying into a vector meson and a pion is opposite the relative sign of the amplitude for the 1^-, L=2 triplet state decaying the same way. The theory can therefore predict the relative sign between the amplitude for:

$$1^- \; K^*(1700) \rightarrow 1^- \; K^*(895) + \pi$$

$$\text{and } 3^- \; K^*(1780) \rightarrow 1^- \; K^*(895) + \pi$$

Thus a PWA of some other inelastic final states such as $K\pi\pi$ is needed to make this determination.

B.4 Mass splittings between states

Although most of the meson resonances have been successfully associated with states expected in the quark model, the quark model theory has not yet been able to predict the quantitative parameters of the states such as mass, width, branching ratios, etc., in a general way for all $q\bar{q}$ multiplets. Nevertheless, it is important to verify that all the expected quark states do occur in nature. Furthermore, any measurements obtained will be very useful in checking the validity of candidates for a theory of light quark meson spectroscopy. A theory based on a central potential for the (more or less) non-relativistic $q\bar{q}$ states containing charmed or bottom quarks is being developed. This theory accurately accounts for most of the known $c\bar{c}$ and $b\bar{b}$ spectra. However, when dealing with the three lighter quarks (u,d,s), the $q\bar{q}$ system is expected to be relativistic and as yet no theory can account for the light quark meson spectra. Despite the lack of a precise

theory, many features of the light quark meson spectra show general regularities which give rise to a structure similar to that expected of a simple harmonic oscillator model for the potential. This accounts for the notation and level diagrams which anticipate such structure. There are a number of important questions about the details of the $q\bar{q}$ spectra that may contribute significantly to the understanding of the structure and may provide insight that will enable a complete theory to be devised that successfully incorporates the known light quark meson spectra. The most obvious regularities in the spectra that should be directly predicted by a theory are the mass splittings. There are a great many splittings that are of interest, such as the ground state - radial splittings, the leading trajectory (e.g., $1^-,2^+,3^-$, etc.) splittings, the S=0 vs. S=1 (for the same L) splittings, the natural vs. unnatural spin-parity member splittings (e.g., 0^- vs. 1^- ground states, 1^+ vs. 2^+, etc.), and the spin-orbit (L•S) triplet splittings (e.g., $2^+,1^+,0^+$ triplet splittings for the L=1, S=1 $q\bar{q}$ state). Although much can be said about all these splittings, only the leading trajectory and the L•S triplet splittings will be examined here (a discussion of the role of the resonances found in this analysis in terms of the radial state splittings of the strange meson system can be found in ref. [32]).

B.5 Leading resonance splittings

Prior to this analysis, the leading trajectory natural strange mesons consisted of the 1^- K*(895), 2^+ K*(1430), and 3^- K*(1780). As shown in the Chew-Frautschi plot of fig. 46, these three states lie very close to a Regge trajectory with slope $a=0.82\ GeV^{-2}$.

The newly discovered 4^+ K*(2080) falls almost exactly on this trajectory. So now the I=1/2 and one of the I=0 natural J^P light quark meson trajectories both contain four measured states which all lie nearly on a straight line. How this $J=aM^2$ relationship fits into a quark model framework is still not known but the well established pattern is seen to continue at least to J=4 (and recently there are indications that it holds true for J=5 [27]). Continuation of the strange meson natural J^P trajectory would predict a $J^P=5^-$ K* state near 2380 MeV (which is just above the endpoint of this analysis). A comparison of leading trajectories of light quark mesons is presented below:

Trajectory	# states found	slope (GeV^{-2})
K* (I=1/2)	4	0.82
ω (I=0)	4	0.95
ϕ (I=0)	2	0.78
ρ (I=1)	3	0.88

B.6 The spin-orbit (L·S) splittings

The very beautiful L·S triplet splittings in the $c\bar{c}$, L=0, S=1 state (see fig. 53) is a strong motivation for checking if the same is true for the $s\bar{d}$, L=0, S=1 state. In this analysis, the 0^+ and 2^+ members were accessible, the 1^+ member was inaccessible but a previous analysis [33] has identified a $K\pi\pi$ state that is believed to be the 1^+ member of the triplet. The 2^+ K*(1430) has been established for quite some time and it represents the most solid and accurately measured member of the triplet. The 1^+ Q_A(1340) from ref. [33] has been confirmed recently and can be

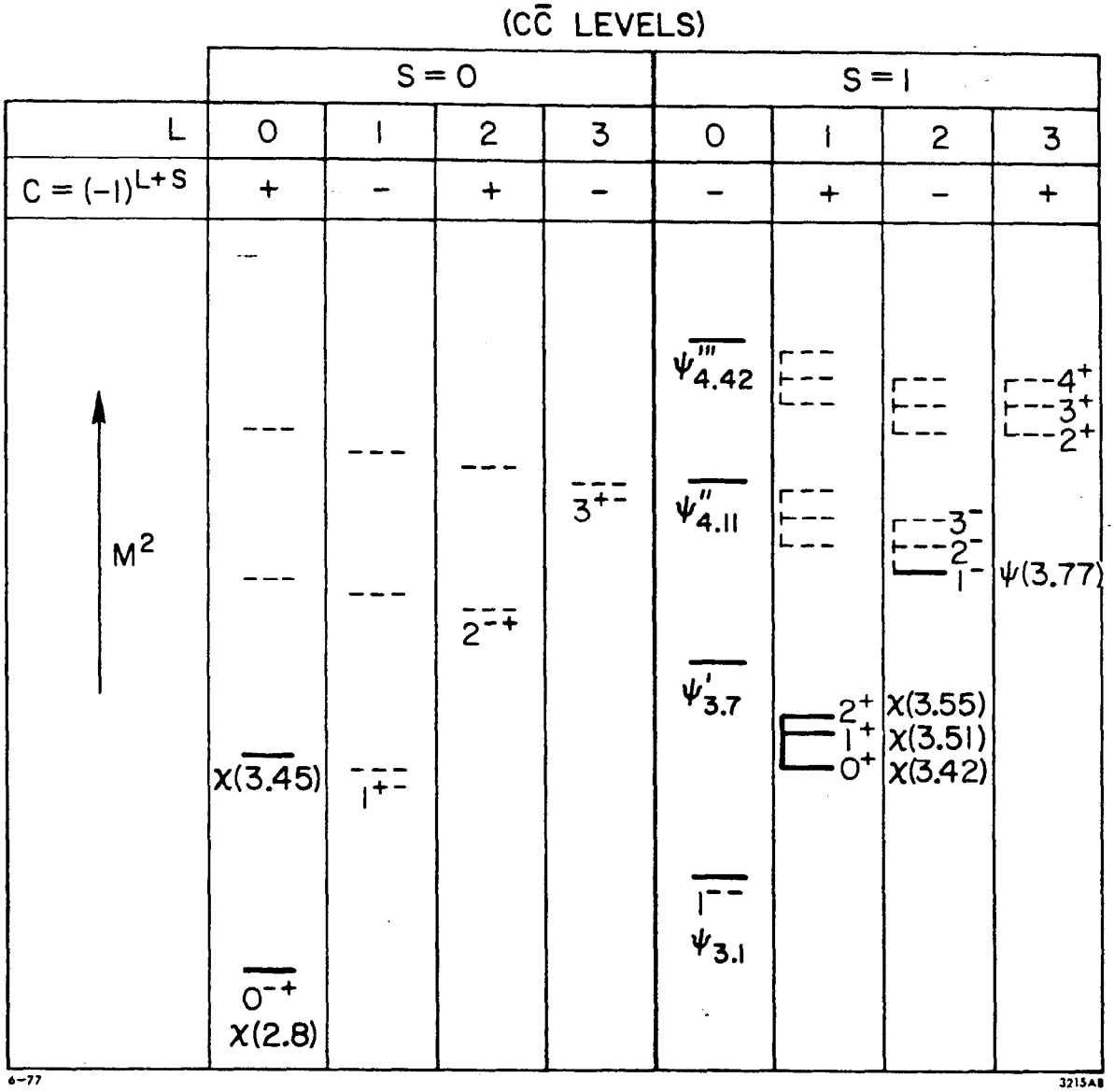

Figure 53 -- Energy level plot of meson spectrum arising from $c\bar{c}$ system. Possible assignments of current observed states are denoted by solid lines and labels. In particular, note the one complete L•S triplet.

considered as quite solid. The 0^+ meson state has recently been restudied and the $\kappa(1490)$ is believed to be the proper candidate for this member. A detailed study of all of the light quark scalar (0^+) mesons has been performed in ref. [34]. The result from a mass dependent fit of the $K\pi$ S wave amplitude from the PWA of ref. [5] was obtained in that study. The result indicated that there was only one low mass 0^+ strange resonance with a mass near 1490 MeV (rather than the preliminary result of 1425 MeV) and width between 120 and 400 MeV depending on which of the four possible ambiguous solutions (from ref. [5]) was chosen. Since this analysis found that solution B from the PWA of ref. [5] was the correct solution, the resulting 0^+ parameters are 1490 and 400 MeV for the mass and width respectively (as mentioned previously, the S wave amplitude results from solution B of ref. [5] and the S wave results from this analysis are nearly identical; therefore, the 0^+ parameters given here are expected to be consistent with the values that would result from use of the data from this analysis).

In summary, the triplet members are 0^+ $\kappa(1490)$, 1^+ $Q_A(1340)$, and 2^+ K*(1430). The assertion that the 0^+ is higher in mass than the 1^+ and the 2^+ is an intriguing feature whose explanation will not be attempted here. Whether this is an anomaly of the strange meson multiplet or is true of all light quark mesons can be checked by examining the I=0 or I=1, L=1, S=1 triplet.

In Table 16, the L=1, S=1 triplet splittings for $c\bar{c}$ and for the four light quark isospin multiplets are presented for comparison. In the first I=0 triplet, the f, D, and ϵ masses appear to be inversely related to the total spin J. Such a reverse ordering is interesting but

TABLE 16

Current Status of Selected L•S Triplet Splittings

(a) L=1, S=1 $c\bar{c}$ triplet (b) I=1/2,0,0,1 light quark meson triplets for L=1, S=1 (c) predicted I=1/2 triplet for L=2, S=1

(a)	J^P	State
	2^+	$\chi(3550)$
	1^+	$\chi(3510)$
	0^+	$\chi(3415)$

(b)	J^P	I=1/2	I=0	I=0	I=1
	2^+	K*(1430)	f(1270)	f′(1515)	$A_2(1310)$
	1^+	$Q_A(1340)$	D(1285)	E(1420)	$A_1(1250?)$
	0^+	$\kappa(1425\text{-}1490?)$	$\epsilon(1300)?$	$\epsilon(1425)$ or S*(980)	$\delta(980)?$

(c)	J^P	State	predicted mass based on L=1, S=1 triplet
	3^-	K*(1780)	--
	2^-	L	~1690
	1^-	?	~1775 to 1840

the uncertainty in the experimentally determined masses and the fact that the masses are nearly identical makes it difficult to say anything definite about the mass splittings in this triplet. The second I=0 triplet contains the f′, E, and either the S*(980) or the new ϵ(1425). Until recently, the scalar member was considered to be the S* resonance. However, a recent amplitude analysis of $\pi\pi \rightarrow K\bar{K}$ resonances [39] presented evidence for a 0^+ ϵ(1425). That analysis also asserted that the S*(980) is a broad effect, possibly a $K\bar{K}$ virtual bound state. If true, this triplet would be in general agreement with the I=1/2 triplet, namely, containing a scalar member that may be more massive than the 1^+ member. The I=1 triplet contains the A_2, A_1, and δ resonances. If this triplet follows the trend of having a heavier scalar meson member as seen in the I=1/2 and the I=0 triplets, then one would expect an I=1 scalar meson near 1200 MeV.

The interpretation of the scalar mesons remains somewhat cloudy due to the possibility of glueball, 4-quark, and >4-quark 0^+ states. In fact the very broad S-wave enhancement at low mass (900-1300 MeV) in this analysis (formerly believed to be the 0^+ κ(1200)) may well be one of these exotic meson states. Such an assertion is not entirely without reason since the trend seems to be toward discovery of heavier scalar mesons states which are being associated with the L=1, S=1 0^+ triplet member. The lower mass enhancements seen in the S-wave spectra could be interpreted as 4-quark or other exotic mesons.

It is certainly clear that no simple L·S splitting structure can be inferred from the four L=1, S=1 light quark meson triplet states. However, if the internal splitting of the lowest mass triplet applies to

the next triplet in the same trajectory, i.e., for L=2, S=1 (1^-,2^-,3^-), then predictions can be made for the 1^- and 2^- triplet members since the 3^- is relatively well measured. For the I=1/2 L=2, S=1 triplet, with the 3^- K*(1780), the previous triplet splittings would imply a slightly lighter 2^- and a slightly heavier 1^- based on the L=1, S=1 splittings (see Table 16). It is likely that the analysis of the inelastic final states (to be performed on the data from this experiment) will shed light on the 2^- member of the triplet (often called the L meson). The 1^- state may well be one of the 1^- resonances found in this analysis as stated earier, but resolving the radially excited L=1, S=0 1^- from this triplet member will be necessary (see subsection B.3).

The current status of the L•S splittings in the strange meson spectrum shows that progress has been made but many unanswered questions still exist. The uncertainty in the assignment of the scalar mesons puts the L=1, S=1 triplet splittings for all the isospin multiplets (I=0,0,1,1/2) in doubt. If the 0^+ does indeed have a higher mass than the 1^+ or even the 2^+, the implication is that factors such as spin-spin or other quark forces may play an important role in the light quark meson L•S splittings. It is also important to discover if this is the case for the L≥2, S=1 triplets and the radial excitations of the triplets as well. Resolving the triplet mass splittings remains a key goal in experimental meson spectroscopy but it is certainly not an easy task. It is hoped that with the information from the analysis of the inelastic final states ($K2\pi$, $K3\pi$) at high mass combined with the information from this analysis, a more complete picture of the L•S and radial splittings of the $q\bar{q}$ spectrum for $M(K\pi)$ up to 2.2 GeV can be obtained.

B.7 Summary

In summary, the $K\pi$ elastic scattering resonances resulting from this analysis have natural interpretations in terms of a general $q\bar{q}$ model meson spectrum. The new states that have been observed and the old states that have been confirmed by the results from this analysis are summarized in Table 17. Based on the preceding discussions, these states can be included in the full light quark meson spectrum resulting in the box plot of fig. 54. Specifically, the new 4^+ K*(2080) is associated with the leading L=3, S=1 $s\bar{d}$ state and is seen to fit well on the existing natural J^P strange meson Regge trajectory as seen in a Chew-Frautschi plot. The new $K'(1900)$ resonance is identified with the first radial excitation of the 0^+ L=2, S=1 triplet member. The interpretation of the $1^-(1700)$ is not clear, being able to be associated with the radial excitation of the 1^- L=0, S=1 state or the 1^- L=2, S=1 triplet member (or both). Similarly, if solution A or C is correct, the $1^-(2100)$ resonance could be identified with up to 4 possible quark model 1^- states. In addition to these new states, the leading 1^-, 2^+, and 3^- states have been confirmed and the $K(1490)$, a 0^+ L=1, S=1 triplet member has been confirmed. Some interesting features in the high mass D and F waves indicate that there may be underlying 2^+ and 3^- resonance structure but nothing quantitative can be presented. Further progress is expected when high statistics 3 and 4 body analyses are performed for the strange meson system. An accurate description of radial and L·S splittings may not be possible until the scalar meson picture is cleared up and until the radial L=0, S=1 vs. triplet member L=2, S=1 identity

TABLE 17

$K\pi$ Resonances Observed in this Analysis

(Masses in MeV)

J^P	$n^\dagger$	Name	Mass	Comment
1^-	1	K*	895	Observed
2^+	1	K*	1430	Observed
3^-	1	K*	1780	Observed
4^+	1	K*	2080	New
0^+	1	κ	~1420?	Verify previous observation
0^+	2	κ'	~1900	New
1^-	1	?	~1700	Unambiguous verification
1^-	1-2?	?	~2100	In 2 of 4 solutions

† n = radial quantum number

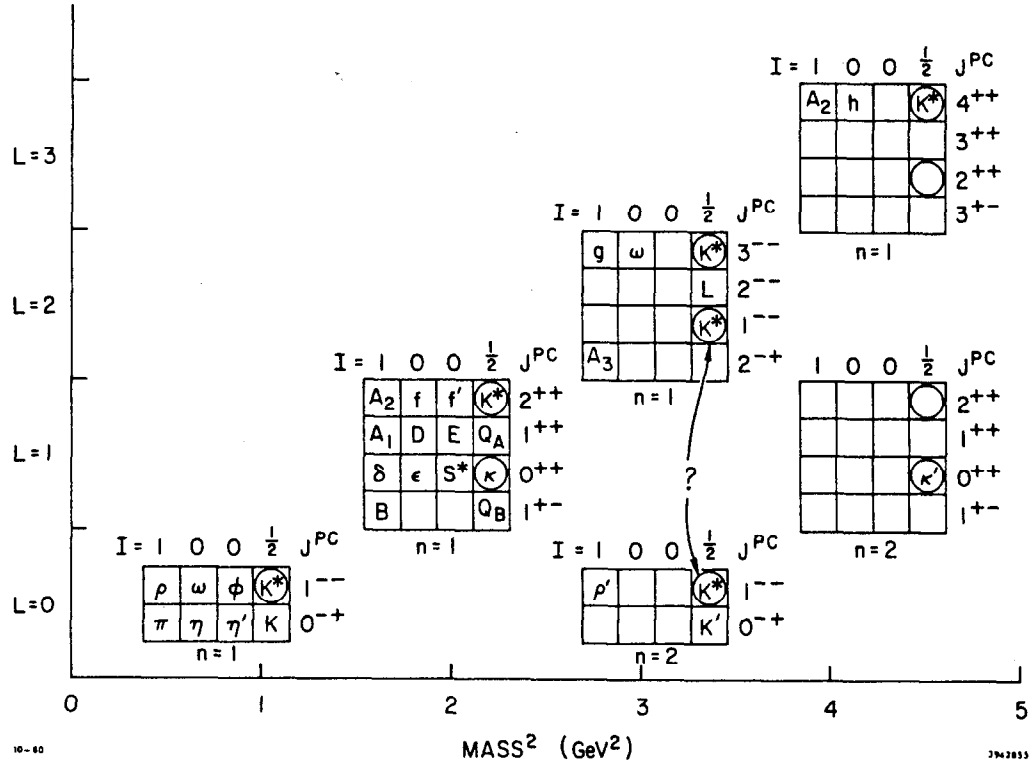

Figure 54 -- Box plot of current meson spectrum. This plot is identical to fig. 2 except that the new states observed in this analysis are included. Circled states depict those accessible to this analysis.

problem is resolved. However, this analysis has made much progress in strengthening and broadening the existing picture for the strange meson spectrum.

Appendix A

THE MONTE CARLO PROGRAM

1. Motivation for the Monte Carlo Program

The primary reason for a Monte Carlo program in this analysis was to calculate the acceptance moments of the LASS spectrometer in order to obtain acceptance corrected moments of the $K\pi$ scattering angular distribution. Secondary reasons for this program was to study device and spectrometer resolutions and performance. The program was also sufficiently adaptable for study of spectrometer acceptance for many other physics processes and for study of backgrounds.

To fulfill these basic objectives, the following guidelines were used in the design of the Monte Carlo program.

1. Generate $K^-p \to K^-\pi^+n$ events with kinematical distributions as close as possible to the true physics $K\pi$ scattering distributions.
2. Simulate the spectrometer's geometrical acceptance accurately (this includes proper physical boundaries, detector active areas or volumes, proper magnetic field tracking, simulation of hardware trigger, absorption, etc.).
3. Include device inefficiency effects.
4. Simulate the data event reconstruction programs (software tracking algorithms).
5. Reproduce track resolution.

6. Create a large sample of Monte Carlo events that can be easily processed to obtain acceptance moments.

The size and content of the large sample of Monte Carlo events to be created was determined by the following criteria:

1. For each Monte Carlo event there had to be sufficient information saved so that the acceptance moments could be calculated, so that cuts could be made on kinematical quantities (e.g. missing mass or mass hypotheses of backgrounds), and so that studies could be carried out on geometrical and kinematical cuts (to check the sensitivity of the physics to those cuts).
2. Sample size was determined such that the statistical errors in the data dominated the statistical errors from the Monte Carlo sample. For this analysis a Monte Carlo event sample was generated that was large enough to have the ratio (# Monte Carlo events)/ (# data events) to be approximately equal to 10 for any kinematical region. To avoid kinematical regions with data but (for statistical and other reasons) no Monte Carlo events, a fraction of the event sample was generated with a flat angular distribution (as opposed to the physics-like angular distribution). This was necessary to avoid problems with the fitting programs that calculated the acceptance corrected angular moments.

2. Program Structure

2.a Overview

The Kπ Monte Carlo program was set up to generate $K^-p \rightarrow K^-\pi^+n$ events where the beam particle (K^-) and the outgoing charged particles were tracked and measured by a method that emulates as closely as possible the spectrometer and track reconstruction software used in this data analysis. The flow chart in fig. 48. gives the basic procedure followed by the program for each Monte Carlo event. At any step where one or both of the tracks were shown to be unmeasureable (as for decays, absorption, insufficient number of intersections with detection devices, etc.) the event was flagged as bad and further processing was halted. All events (whether flagged as bad or not) were written to an output storage device so that the acceptance moments could be calculated.

2.b Generation of kinematical variables

As explained previously, the four kinematical variables $M(K\pi)$, $|t'|$, $\cos\theta_j$, and ϕ_j completely describe a Kπ scattering event (there are actually six variables but s is fixed for fixed beam momentum and ϕ_{lab} is not important in the physics). Since it was desired that a distribution be produced that simulated the physics distribution, the intercorrelation of these four variables had to be taken into account. This was done by first selecting a value for $M(K\pi)$ then using random generator procedures to obtain $|t'|$, $\cos\theta_j$, and ϕ_j from previously measured distributions as a function of $M(K\pi)$.

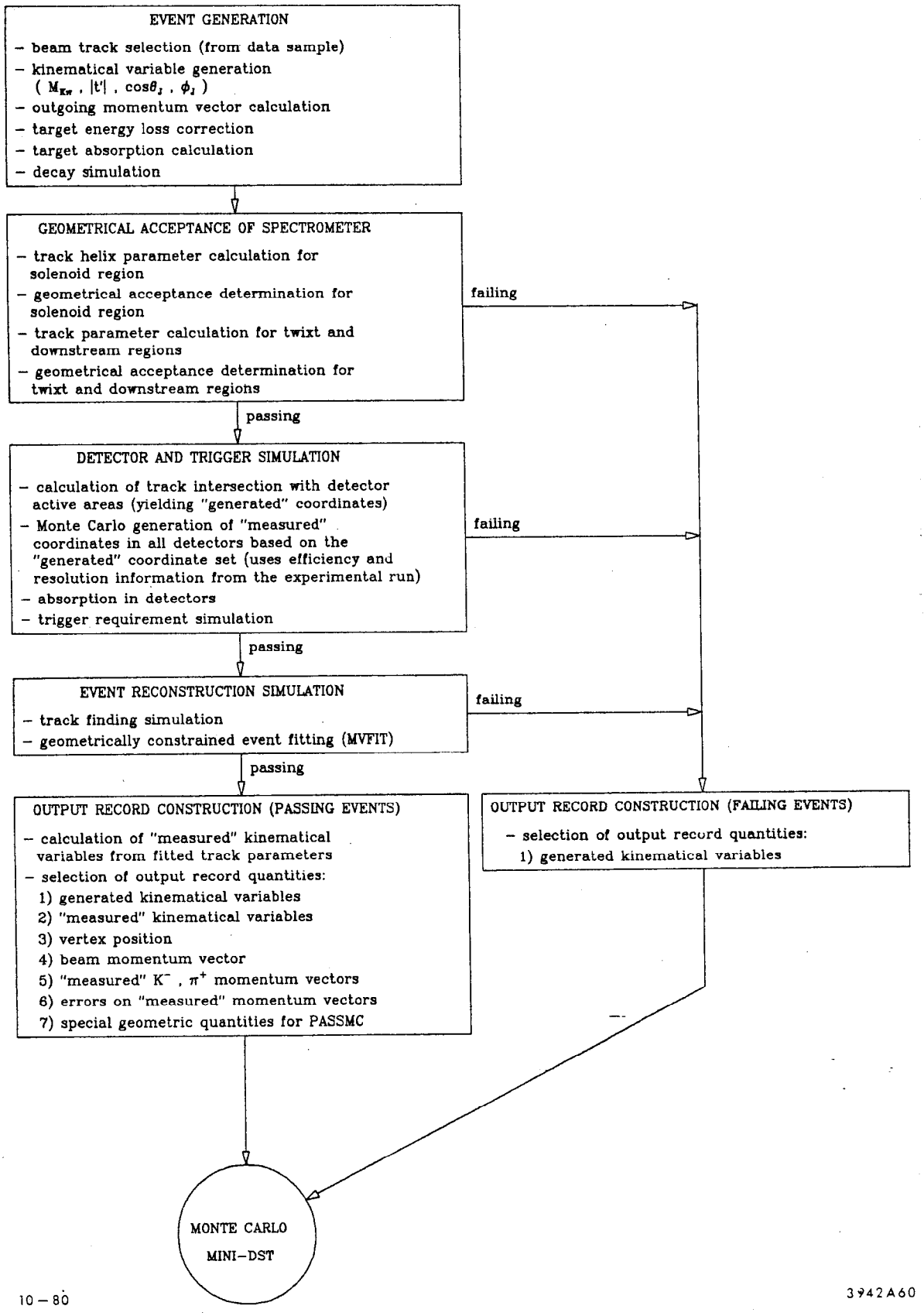

Figure 55 -- Flow chart depicting the basic structure and function of the $K^-p \to K^-\pi^+n$ Monte Carlo simulation program.

The distribution of events as a function of $|t'|$ has a functional form very close to $e^{-\beta t'}$. This form was used to generate $|t'|$ distributions for Monte Carlo events on the first iteration of the partial wave analysis procedure. After the first pass through the partial wave analysis procedure $K\pi$ scattering amplitudes were obtained as a function of $M(K\pi)$ and $|t'|$. Using the functional form of the $|t'|$ distribution obtained from these amplitudes, the random generator procedure was used to generate events that would simulate that $|t'|$ distribution. Thus for the second iteration of the partial wave procedure, the $|t'|$ distribution had a functional form closely resembling that of the data and had the dependence on $M(K\pi)$ included.

In a similar way, the angular distribution of the data as a function of $M(K\pi)$ from the first iteration was used as input to obtain $\cos\theta_j$ and ϕ_j for Monte Carlo events. By generating a random $\cos\theta_j$ and ϕ_j, the probability that such an event would be produced based on the first iteration angular distribution of $K\pi$ data was calculated. Then the random generator procedure was used to accept events so that the resultant Monte Carlo event angular distribution closely simulated the physics angular distribution.

The net effect (averaged over large numbers of events) produced $|t'|$ and angular distributions very similar to the physics distributions with proper dependence on $M(K\pi)$. The only dependence not taken into account was the coupling of $|t'|$ with the angular variables ($\cos\theta_j$ and ϕ_j) which was believed to be a small effect.

2.c Beam, vertex, momentum vectors, decays

Because the beam phase space varied as a function of time during the experiment, it was decided to use reconstructed data beam tracks (obtained from a special sample of events taken during the exprerimental run) as input beam particles for the Monte Carlo events. Hence, drifts or fluctuations of the beam during the experimental run were automatically taken into account in the Monte Carlo program. To simulate the difference between the physical beam track and the reconstructed beam track, a Monte Carlo "reconstructed" beam track was generated by changing the position, direction and momentum of the input beam track (using a random generator) by amounts as prescribed by the known resolutions of those quantities. Thus, one track was used to produce the event (the physics Monte Carlo beam track) and one track with a phase space slightly offset from the first was used for event reconstruction (the measured Monte Carlo beam track).

A vertex was created by extrapolating the physical beam track to a z position within the known target volume limits. This position was determined by a random generator which was properly corrected to give a distribution that accounted for beam attenuation due to target absorption.

Using the beam momentum vector, the vertex position and the four kinematical variables, the 4-vectors for the outgoing particles were then calculated. Since the neutron was not detected in this experiment, no further neutron tracking took place in the Monte Carlo program. The outgoing K^- and π^+ were fully tracked so arrays were created to store

the important parameters of their trajectories. At this time the K^- and π^+ were decayed (using the random generator and knowledge of their lifetimes) and their decay lengths (as measured in the lab starting from the vertex) were saved in their respective storage array. The treatment of decays chosen for the Monte Carlo program was to stop tracking the particle at the point it decayed. Thus the particle effectively vanished at the decay point. In reality, the kaon or pion would decay into one charged and two neutral particles (or possibly three charged particles for the kaon), hence could still leave a measureable track. However, the choice of stopping trackfinding at the decay point was a good first approximation to the treatment of a decay by the trackfinding algorithms in the data event reconstruction code.

2.d Geometrical acceptance, tracking through magnetic fields

Given the momentum vectors for the two outgoing charged particles, the particles were then tracked through the full length of the spectrometer. The walls of the magnets, frames of the detectors and other high mass objects that the particles would intercept were considered to be total absorbers, i.e., all tracking stopped at first contact with such an object. For the region in the solenoid magnet where the magnetic field was fairly uniform, the particles were tracked assuming a perfectly uniform field parallel to the z axis. This resulted in particles following helical paths. When the particles approached the downstream end of the solenoid magnet, the field lines diverged and the particles followed more complicated trajectories. Utilizing a detailed

map of the field (obtained from direct measurements prior to the experimental run) it was possible to closely approximate the particle trajectory by use of a numerical finite difference technique known as the Runge-Kutta method [12]. In this case the Runge-Kutta method was used to solve (approximately) for the particle position and direction using the equations of motion determined from Maxwell's equations and the known field map.

Upon exit of the solenoid magnet, if the particles were still in the detection region they were linearly extrapolated through the twixt region (as the magnetic field there was sufficiently small to be neglected). In the region encompassed by the magnetic field of the dipole magnet, those surviving particles were once again tracked using the Runge-Kutta method. Just downstream of the dipole magnet, a linear extrapolation of the particle trajectory was again used to determine its path through the final downstream magnetostrictive wire spark chambers and scintillation counter hodoscopes after which tracking was halted.

2.e Absorption and energy loss

In order to correct for absorption and energy loss, the spectrometer was divided into sections and the amount of material through which a given particle would pass was calculated in terms of absorption length and dE/dx. The sections of the spectrometer were: 1) the target system, 2) the cylinder chambers, 3) the solenoid devices, 4) the C1 Cerenkov counter, 5) the dipole region. The absorption length in the target determined an overall event weight (i.e., probability) for

the event, the weight varied between 0 and 1 depending on the probability of successfully escaping the target system. For the other four sections of the spectrometer the absorption length was used to calculate the probability of successful passage but unlike in the target, a random number was generated to determine if this particular particle was to be absorbed. In principle, one could include the absorption probabilities for these sections in the overall event weight instead of this yes-no absorption procedure but the complicated method used by the data trackfinding algorithms made the assignment of event weight too difficult. The yes-no procedure was straightforward and it best represented the results one would obtain based on the physics of the spectrometer and based on the methods of the trackfinding software. If a particle was to be aborbed, tracking was halted at the beginning of the spectrometer section in which absorption occurred.

Given the mass, energy, and path length of a particle, the energy loss was determined by means of range-energy loss tables. Energy loss was computed for the target system (the liquid hydrogen, the mylar target jacket, and the aluminum support tube) but not for the other sections of the spectrometer due to the difficulty of tracking a particle with continually decreasing momentum and also due to the fact that the correction was found to be quite small.

2.f Generation of device coordinate banks

At this point the basic path of the particles through the spectrometer had been deterimined and had been corrected for losses due

to decay and absorption. It was then necessary to ascertain that the particles could be found by the trackfinding algorithms. This was accomplished by calculating the intersection of the particle path with the active detection area in each device. These "virtual" coordinates were stored in an array for later use. To simulate the inefficiencies of the detectors, the experimental efficiency for each device was used. This efficiency was determined from the software data monitoring routines (averaged over the entire experimental run). Then, a random number was generated to decide if a given particle was "detected" in that device. An array was created which indicated if a given "generated" coordinate was actually detected (thus becoming a "measured" coordinate).

2.g Simulation of software trackfinding

A brief description of the software trackfinding procedure used in the data reconstruction program (see also chapter IV) will follow so that the Monte Carlo simulation can be more easily understood.

The software trackfinding program took device coordinates, formed matchpoints, then took sets of matchpoints to define "trial" tracks. The coordinate banks were searched for all coordinates that were close to the trial track. An array that contained all the device coordinates associated with the trial track was then created. A complex series of tests based on the number of coordinates and the type of coordinates was used to determine if a trial track was to be considered a real detected track.

Because the Monte Carlo program also kept track of numbers and types of detected coordinates for each particle, it only required reproducing the part of the (data) program containing the series of tests in order to simulate the software trackfinding. Thus, both data and Monte Carlo tracks were required to meet the same criteria to be judged "detectable". In this same series of tests it was also determined if a track was to be labelled a "dipole" track (i.e., a track detected both upstream and downstream of the dipole magnet hence momentum analyzed to high precision) or a "solenoid" track (i.e., detectable in the solenoid region but not in the dipole region). This dipole-solenoid distinction had to be accurately reproduced in the Monte Carlo because of the substantial track resolution differences between the two types.

2.h Trigger requirements

A Monte Carlo event was required to pass the same criteria as those imposed by the trigger logic used in the experimental run. Specifically, this implied that the following requirements be satisfied.

1. At least two "hits" in either the 1.5X PWC plane or the 1.5Y PWC plane.
2. At least 1 "hit" in the TOF counter.
3. No "hit" in the LP3 counter.

The word "hit" meant the Monte Carlo particle had to have a detectable ("measured") coordinate associated with that particular device. Thus, trigger losses due to device inefficiencies were properly taken into account.

2.i Device Resolution

At this point in the Monte Carlo program, it was known whether a generated event could trigger the spectrometer and could be successfully reconstructed. However, since it was necessary to make some resolution cuts on the data, it became necessary to simulate the device resolution in the Monte Carlo to enable corrections to be made for the effects of such cuts. There were basically three different types of tracks defined for resolution considerations: 1) beam tracks, 2) dipole tracks and 3) solenoid tracks.

As described in section c (Beam, vertex, momentum vectors, decays), the beam tracks for Monte Carlo events were obtained from a sample of special beam event data records. These records contained the parameters of the reconstructed beam tracks from the experimental run. The beam tracks were reconstructed by a least squares fit to a straight line using the coordinates from the two beam proportional chambers. The error matrix from the fit was also stored in the beam record. Thus the resolution of the beam due to position measurement resolution was taken into account by using the error matrix information. Finite momentum resolution of the momentum hodoscopes and momentum smearing due to electronic drift (probably thermal effects on the magnet calibrations) were also accounted for in the Monte Carlo by including terms for these effects in the beam momentum resolution calculation.

The momentum resolution of "dipole" tracks was calculated from a formula obtained from a detailed study of $K^- \rightarrow \pi^- \pi^- \pi^+$ decays. The formula

was:

$$\sigma_p = 6.53 \times 10^{-4} p^2 + 1.15 \times 10^{-3} p \qquad (A.1)$$

where p was the momentum measured in the dipole magnet in GeV/c. The study showed that the resolution of the dipole magnet momentum measurement had a shape consistent with a gaussian distribution with a sigma given in the formula above. For use in the Monte Carlo resolution calculations, the true momentum of the particle was offset by an amount obtained from a gaussian distribution random generator (with the above sigma) and that new momentum was stored as the "measured" momentum.

For the type of track termed as "solenoid" tracks, no simple resolution formula was obtainable. This was due to the strong dependence of track resolution on the type of device detecting the track and on the number of coordinates associated with the track. To simulate the solenoid region resolution, the method of generating "measured" coordinates was used. This method required picking up the detected device coordinates (as explained in section f), then offsetting them by an amount produced by a gaussian distribution random generator. The sigma of the gaussian was taken to be the resolution of the particular device as determined by a study using the experimental data (see VI.A.2 for device resolution study). This offsetting resulted in a set of points that were scattered away from the exact particle trajectory in a quasi-random fashion that should have closely simulated the measurement errors in the physical devices. These new coordinates were used as input to the same event fitting program (MVFIT) as used in the data processing program. This coordinate offsetting procedure was also used for detected

coordinates in the solenoid region that were associated with the "dipole" type tracks . This was necessary because when the events were fitted (in MVFIT), the dipole momentum measurement was used for the magnitude of the momentum vector of the "dipole" type track but the direction could only be well determined from the coordinates in the solenoid region (which were close to the interaction vertex).

This procedure took nearly all resolution effects into account except for multiple scattering. The handling of multiple scattering will be described in the next subsection.

2.j Event fitting

As implied in the previous section, the event fitting program for the Monte Carlo events was nearly identical to the MVFIT program used in the data processing as described in IV.H. Reviewing the MVFIT program briefly, a geometrical fit was made to the input tracks assuming an interaction of the type a+b→c+d+X where a,b,c and d are the tracks input to the fit program. The program used an iterative chi-squared minimization procedure which resulted in an output containing the track parameters of the best fit. For the Monte Carlo events, the input track data consisted of 1) the beam track and its error matrix, 2) the "measured" coordinates in the solenoid region associated with a "dipole" track and the coordinate errors, 3) the dipole momentum measurement for "dipole" tracks and its error, 4) the "measured" coordinates of "solenoid" tracks and the coordinate errors.

In addition to the best fit track parameters, the MVFIT output included the error matrix from the fit (whose elements were the best estimators of the correlated errors of the fit parameters). From the various error matrix elements, it was possible to construct quantities which accurately represented the resolution of individual tracks. These quantities were useful for making cuts to get rid of very poorly measured tracks.

The only difference between the fitting program used in the Monte Carlo and the one used in the data was that the data version included a correction algorithm for multiple scattering (which changed the error matrix). The Monte Carlo event had no multiple scattering of its tracks, hence needed no such corrections in the fitting program. Multiple scattering in the Monte Carlo was omitted because the small increase in accuracy gained was greatly overshadowed by the large amount of time and difficulty involved in including it correctly (to first order, the multiple scattering was actually included since the offsets used in generating coordinates were derived from the measured device resolutions which had some of the multiple scattering error folded in).

2.k Output record

The format of the output record (which was written to magnetic tape) was designed to satisfy the following requirements: 1) accessibilty of large numbers of events (hence a desire for minimal record size), 2) all kinematical variables (both generated and "measured") available, 3) all important geometrical quantities available

for hypothesis testing (i.e. beam and outgoing particle momentum vectors), 4) other geometrical quantities and fit results for making geometrical and other cuts (e.g., vertex position for vertex cuts, position at dipole magnet for aperture cuts, track measurement error estimators for resolution cuts), 5) event status information available (i.e., passed or failed reconstruction, "dipole" or "solenoid" type track, etc.). With the information contained in this output record, it was possible to run a fairly quick (in CPU time) program that could read a large number of the Monte Carlo events, make a set of selected geometrical and kinematical cuts, and have the group of events that pass those cuts available for calculating the acceptance moments. It was important that many of the geometrical quantities were made available in the output record because it was important to check that the physics results obtained were not sensitive to variations in the geometrical cuts. For instance, it was desirable to cut out tracks that came within 5 centimeters of the dipole magnet aperture to insure that absolutely no tracks might have hit the magnet walls due to position uncertainty or due to slight misalignments. By having the necessary quantities available to make such cuts it was possible to produce new sets of acceptance moments with which to study the effects of the cuts on the physics.

Appendix B

THE METHOD OF MOMENTS

The first step of the method of moments is the statement of the problem. The relationship between the observed and produced angular distribution is:

$$I_{obs}(\Omega,x) = A(\Omega,x)\, I_{prod}(\Omega,x) \tag{B.1}$$

where I_{prod} can be written as:

$$I_{prod}(\Omega,x) = \sum_{lm>0} t_{lm}(x)\,(2-\delta_{m0})\,\mathrm{Re}(\,Y_{lm}(\Omega)\,) \tag{B.2}$$

The simplifications mentioned in VII.B.1 can be applied here so eq. B.2 can be written for a given M(Kπ) and t′ bin as:

$$I_{prod}(\Omega) = (4\pi)^{-1/2} \sum_{\mu} t_{\mu}\, Y'_{\mu}(\Omega) \tag{B.3}$$

Inserting eq. B.3 into eq. B.1, then multiplying both sides of the resulting equation by $Y'_{\mu}(\Omega)$ and finally integrating both sides over Ω, one obtains:

$$(4\pi)^{-1/2} \sum_{\mu} t_{\mu} \int Y'_{\mu}(\Omega)\, Y'_{\mu'}(\Omega)\, A(\Omega)\, d\Omega = \int I_{obs}(\Omega)\, Y_{\mu'}(\Omega)\, d\Omega \tag{B.4}$$

By defining the two quantites:

$$A_{\mu\mu'} = (4\pi)^{1/2} \int Y'_{\mu}(\Omega)\, Y'_{\mu'}(\Omega)\, A(\Omega)\, d\Omega \tag{B.5}$$

$$M_{\mu'} = \int I_{obs}(\Omega)\, Y_{\mu'}(\Omega)\, d\Omega \tag{B.6}$$

eq. B.4 can be rewritten as:

$$\sum_{\mu} A_{\mu\mu'} t_{\mu} = M_{\mu'} \tag{B.7}$$

Now $M_{\mu'}$ can be approximated by replacing the integral in eq. B.6 with a sum over the event data sample.

$$M_{\mu'} = \sum_{i=1}^{N_{events}} Y'_{\mu'}(\Omega_i) \tag{B.8}$$

In the limit of infinite statistics, eq. B.8 is equivalent to eq. B.6.

The acceptance matrix $A_{\mu\mu'}$ is calculated using the Monte Carlo event sample. The integral in eq. B.7 is approximated by a sum over accepted Monte Carlo events in the following manner:

$$A_{\mu\mu'} \cong \sum_{i=1}^{N_{passing}} \frac{4\pi\, w_i\, Y'_{\mu}(\Omega_i)\, Y'_{\mu'}(\Omega_i)}{I_{MC}(\Omega_i)} \tag{B.9}$$

where w_i is the event weight and

$$I_{MC}(\Omega_i) = N_{generated} \sum_{\mu} (4\pi)^{1/2} (t_{\mu}/t_0)\, Y_{\mu}(\Omega_i) \tag{B.10}$$

The procedure used to obtain the matrix $A_{\mu\mu'}$ is the same iterative procedure that was used to derive the acceptance coefficients a_{μ} as explained in VII.C.

The matrix equation B.7 consists of N equations in M unknowns where N and M are determined by the number of l and m indices that are used in determining $M_{\mu'}$ and by the number of l and m indices to be allowed for the angular moments. If N≥M, the equation can be solved uniquely. Using standard matrix inversion techniques the equation is solved resulting in the values for the angular moments t_{μ}.

The error matrix E for the t_μ solution is given by the matrix equation:

$$E = A\,D\,(A^{-1})^{\dagger} \tag{B.11}$$

where the A matrix is the acceptance matrix described above and the D matrix represents the statistical errors of the quantity $M_{\mu'}$ defined as:

$$D_{\mu\mu'} = \sum_{i=1}^{N_{events}} Y_{\mu}^{*}(\Omega_i)\, Y_{\mu'}^{*}(\Omega_i) \tag{B.12}$$

The program used to solve for the moments and the corresponding error matrices were modifications of existing FORTRAN programs which were originally developed for the $K\pi$ scattering analysis of ref. [5]. The results obtained using the method of moments are presented and discussed in Appendix C.

Appendix C

TESTS OF THE STABILITY OF THE MOMENTS

An extensive series of tests were made to insure that the $K\pi$ scattering angular moments obtained in this analysis were stable with respect to geometrical and kinematical cuts. Additional tests were made to reveal if biases were introduced by the choice of mass bin, by the assumptions imposed on the acceptance calculations, or by the removal of high l and high m moments that were seen to be consistent with zero.

If the Monte Carlo simulation program and the acceptance calculation were not functioning properly, a change in the geometrical or kinematical cuts (cuts that were applied to both the data and Monte Carlo event samples) could lead to a change in the angular moments. The following comparisons between sets of angular moments were made to test this possibility.

1) standard cuts vs. tighter MM^2 (opposite $K\pi$) cut ($0.2<MM^2<1.1$ GeV^2 vs. $0.4<MM^2<1.0$ GeV^2)
2) standard cuts vs. different elastic event cut
3) standard cuts vs. forward $\cos\theta_j$ cut (accept only $\cos\theta_j<0.9$)
4) standard cuts vs. tighter geometric aperture cuts (reduction of active area of trigger and of other chambers, reduced magnet aperture, reduced target volume, etc.)

The moments obtained from the "standard cuts" are those presented in VII.D with the geometrical and kinematical cuts described in Chapter

V. In each of the four comparisons above, the two sets of moments being compared agreed with each other to within the statistical errors from the fits. These results demonstrated that the original results were not sensitive to the precise values for the cuts thus giving confidence in the Monte Carlo simulation. Some of the other tests on the stability of the moments included:

1) standard moments vs. those obtained with imaginary moments allowed to contribute
2) standard moments vs. moments obtained using a smooth parametrization of the acceptance moments as a function of $K\pi$ mass (to see if the statistical fluctuations of the acceptance moments affected the angular moments results)
3) standard moments vs. moments obtained in $K\pi$ mass bins offset by 1/2 bin width from the standard set
4) standard moments vs. moments obtained with more l or more m moments in the fit, i.e., $(l \leq 6, m \leq 2)$ vs. $(l \leq 8, m \leq 3)$
5) moments obtained using the first 1/2 of the event sample (i.e. taken during the first 1/2 of the experimental run) vs. those from the second 1/2 of the sample (to test for any time dependence)
6) standard moments (maximum likelihood method) vs. moments obtained using the method of moments

None of the tests showed any statistically significant differences between the moments being compared. The comparisons for the maximum likelihood vs method of moments, for the standard vs. tight MM^2 cut, and for the standard vs. tight aperture cuts were considered especially

important and are shown in figures 49-51. The comparisons shown represent the three mass bins 1.40-1.44 GeV, 1.74-1.78 GeV, and 2.04-2.12 GeV respectively (i.e., the mass regions of the spin 2, spin 3, and spin 4 resonances).

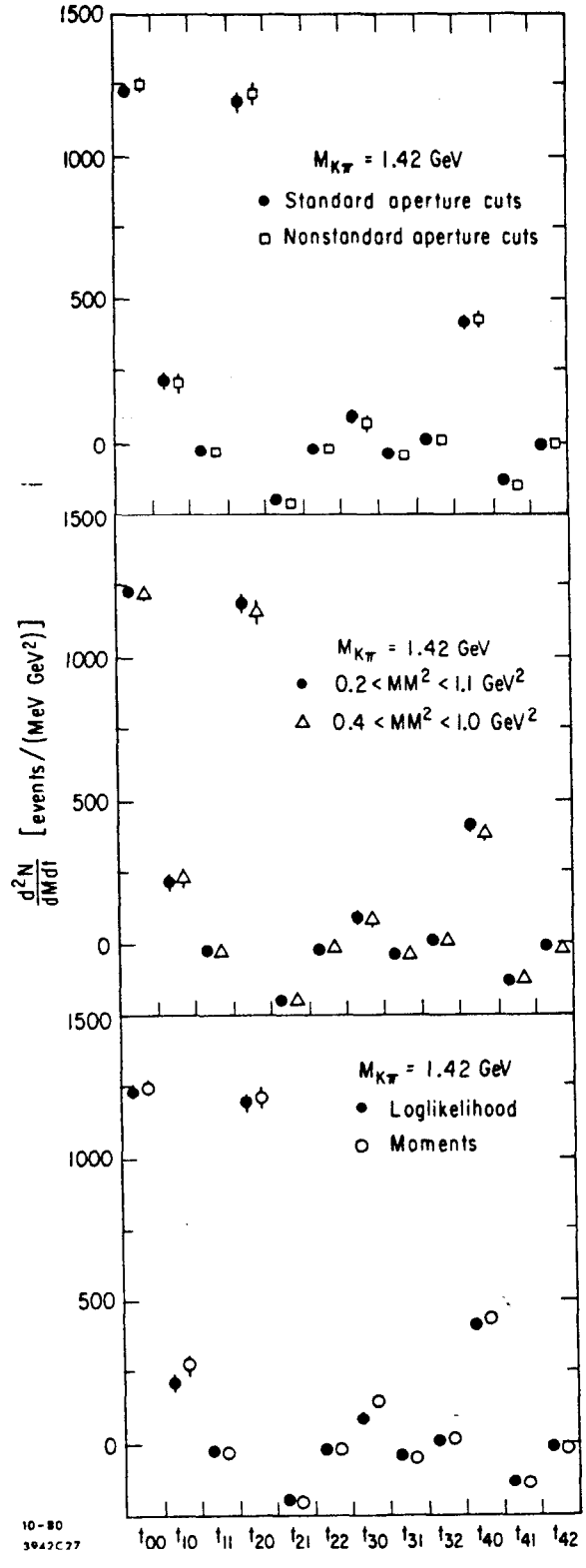

Figure 56 -- Three comparisons of the standard angular moments with moments obtained under differing conditions. The agreement indicates the stability of the standard set of moments. The moments in these three plots are for the Kπ mass bin 1.40-1.44 GeV.

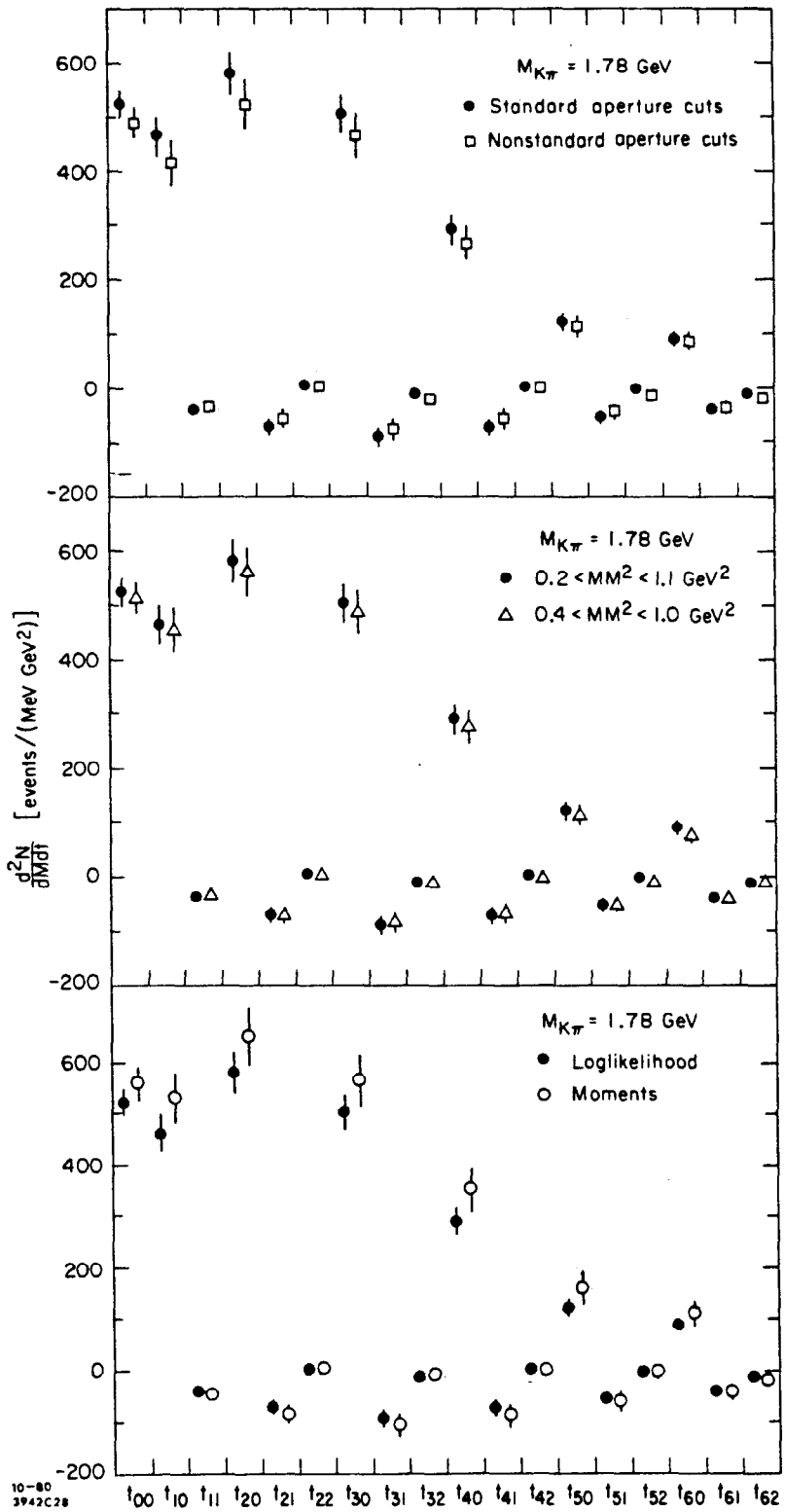

Figure 57 -- Three comparisons of the standard angular moments with moments obtained under differing conditions. The agreement indicates the stability of the standard set of moments. The moments in these three plots are for the Kπ mass bin 1.76-1.80 GeV.

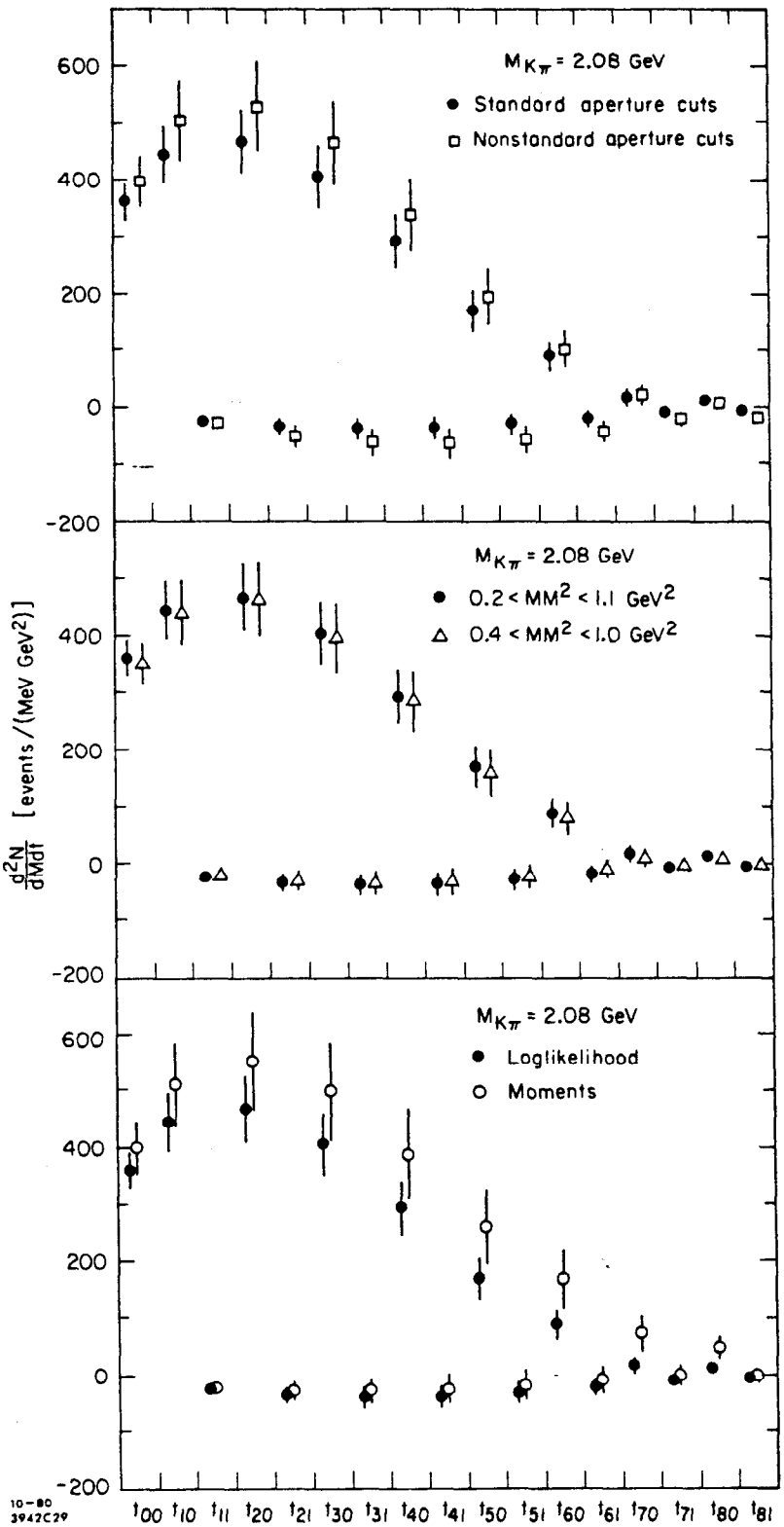

Figure 58 -- Three comparisons of the standard angular moments with moments obtained under differing conditions. The agreement indicates the stability of the standard set of moments. The moments in these three plots are for the Kπ mass bin 2.04-2.12 GeV.

Appendix D

THE STUDY OF THE nπ CUT

It was found in this analysis that the reaction $K^-p \rightarrow K^- + (\pi^+ n)$ contributes a non-negligable background to the strictly $K\pi$ scattering reaction $K^-p \rightarrow (K^-\pi^+) + n$, especially at low $K\pi$ mass. This background problem was also encountered by previous experiments (see ref. [33]) and was often handled by the simple method of cutting away events whose $n\pi$ invariant mass hypothesis was in the high cross section N* mass region. Such a cut was used in this analysis with the value for the cut chosen to be 1.8 GeV (i.e., events with $n\pi$ mass less than 1.8 GeV were removed). However, for the high $K\pi$ mass region, the $n\pi$ cut amounts to a forward $\cos\theta_j$ cut. Since the bulk of the data at high $K\pi$ mass is concentrated in the forward $\cos\theta_j$ region, the $N\pi$ cut drastically reduces the sample. However, very few of the events that are removed by the $n\pi$ cut for high $K\pi$ mass are expected to be due to the N* recoil reaction. This is due to several factors including the small cross section for producing K^-N^{*+} compared to K* n and additional suppression due to the kinematical restrictions imposed in the definition of the $K^+\pi^-n$ sample. Therefore, the $n\pi$ cut was not used in the high $K\pi$ mass regions although events with $n\pi$ masses of less than about 1.4 GeV were nevertheless removed by the geometry of the trigger (the trigger imposes a forward $\cos\theta_j$ cut at high $K\pi$ mass which is, as mentioned above, nearly the same as an $n\pi$ cut).

It was necessary to determine exactly where the $n\pi$ cut should stop being used, so a study was made to find the $K\pi$ mass region where the $n\pi$ cut was no longer useful for removing the N* background. It was known from earlier studies that the $n\pi$ cut was essential in the 0.8 to 1.3 GeV $K\pi$ mass region because without the cut, high order moments (such as t_{30} and t_{40}) were found to be non-zero in regions that were expected to have no high order moments. Therefore, the region from 1.44 GeV to 1.6 GeV was partial wave analysed both with and without the $n\pi$ cut. The results from this analysis is presented in fig. 59, comparing the cut and uncut partial wave amplitudes for the S, P, D, and F waves. It is quite clear from this comparison that the $n\pi$ cut has little or no effect on the amplitudes in this region. The decision was made to stop using the $n\pi$ cut at the $K\pi$ mass of 1.56 GeV since this location would allow both the 1430 and 1780 resonance regions to be free from any change in conditions. It was also found that the basic structure of the partial waves was not greatly changed by continued use of the $n\pi$ cut above a $K\pi$ mass of 1.6 GeV. However, near 1.9 GeV the sample size was effectively reduced to an extent that the errors on the amplitudes became very large and the partial wave fits became unstable.

In summary, an $n\pi$ cut removing events with an $n\pi$ invariant mass of less than 1.8 GeV was imposed for the $K\pi$ mass region from 0.8 to 1.56 GeV. This was effective in removing the N* background from the $K\pi$ scattering amplitudes. For the region above 1.56 GeV, no $n\pi$ cut was applied and thus some N* contribution to the background can be expected although this contribution is known to be small. It should be noted that the $n\pi$ cut was not used at all in any of the angular moments results presented in chapter VII.

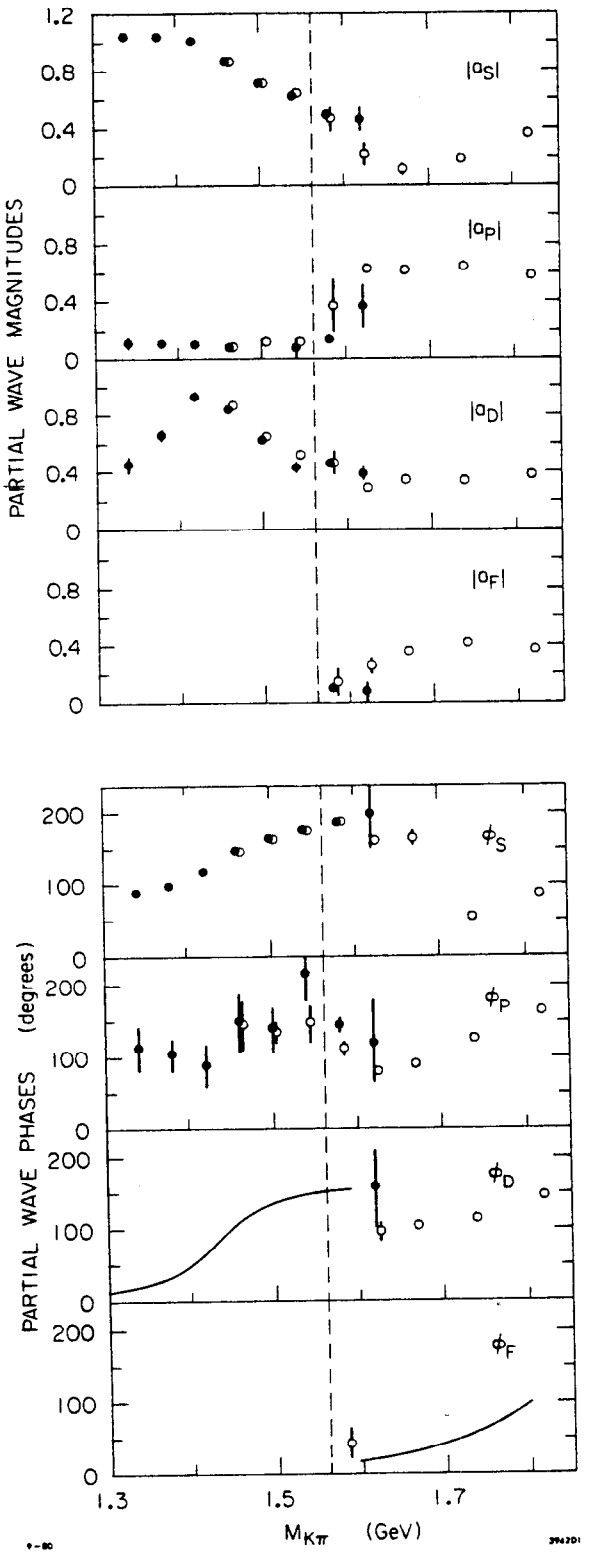

Figure 59 -- The magnitude and phase of the S, P, D, and F wave amplitudes with (•) and without (o) the nπ cut applied to the data sample. Dotted line denotes the point at which the nπ cut was removed in the final PWA (see text for details).

Appendix E

RESONANCE FITTING PARAMETRIZATIONS

Both the resonance fits to the moments and the resonance fits to the partial wave amplitudes were based on a fairly standard relativistic Breit-Wigner resonance form with a Blatt-Weisskopf barrier factor [34]. The exact form is given by eq. E.1:

$$B(M_{K\pi}, M_L, \Gamma_L) = \frac{M_L\Gamma}{(M_L^2 - M_{K\pi}^2) - iM_L\Gamma} \qquad (E.1)$$

where: $\Gamma = \left(\frac{q}{q_L}\right)^{2L+1} \Gamma_L \frac{D_L(q_L R)}{D_L(qR)}$

$$D_0(x) = 1$$

$$D_1(x) = 1 + x^2$$

$$D_2(x) = 9 + 3x^2 + x^4$$

$$D_3(x) = 225 + 45x^2 + 6x^4 + x^6$$

$$D_4(x) = 11025 + 1575x^2 + 135x^4 + 10x^6 + x^8$$

The mass and width with the subscript L were the fit parameters for the L-wave resonance. The mass with the $K\pi$ subscript was the $M(K\pi)$ values for the mass bins used in the fit. The barrier penetration factors $D_L(x)$ were from a square well potential model from ref. [35]. The R factor (the "range" of the potential) was fixed to the equivalent of 1 fm.

1. The resonance fits to the moments

For the case of the fits to the Kπ elastic scattering angular moments, the following assumptions were made:

1) The scattering represented by the moments is completely due to one pion exchange.

2) The $|t'|$ dependence of the scattering amplitude does not vary greatly as a function of Kπ mass.

From the discussion in chapter VIII that lead up to eq. VIII.10, it was shown that the moments, t_{lm}, could be written in terms of the production amplitudes, $L_{\lambda\pm}$, which are defined in eq. VIII.1. Assumption 1) above implies that the production parameters γ_c and γ_a are both zero and assumption 2) implies that the production parameter b is a constant with respect to M(Kπ) hence the production amplitudes can be integrated over $|t'|$ and the relationship between the t_{lm} and the scattering amplitudes, a_L, can be calculated explicitly. For convenience, the partial wave fit amplitude L (where L is the angular momentum of the wave) was created and defined as follows:

$$L \propto \frac{M_{K\pi}\, a_L}{\sqrt{q}} \qquad \text{(E.2)}$$

Now the following parametrization was chosen for the special spin 4 fit

to the t_{60}, t_{70}, and t_{80} moments:

$$D = \frac{M_{K\pi}}{\sqrt{q}}\ e^{i\phi_1}(a_1 + b_1 M_{K\pi})$$

$$F = \frac{M_{K\pi}}{\sqrt{q}}\ \left(e^{i\phi_2}(a_2 + b_2 M_{K\pi} + c_2 M_{K\pi}^2) + N_2 B(M_{K\pi}, M_F, \Gamma_F)\right) \qquad \text{(E.3)}$$

$$G = \begin{cases} \frac{M_{K\pi}}{\sqrt{q}}\ N_3 B(M_{K\pi}, M_G, \Gamma_G) & \text{, for } M_{K\pi} \leq 1.98 \text{ GeV} \\ \frac{M_{K\pi}}{\sqrt{q}}\left(b_3 (M_{K\pi} - 1.98) + N_3 B(M_{K\pi}, M_G, \Gamma_G)\right) & \text{, for } M_{K\pi} > 1.98 \text{ GeV} \end{cases}$$

and the relationship between the moments and the fit amplitudes was given by:

$$t_{60} = \frac{100|F|^2}{33\sqrt{13}} + \frac{20|G|^2}{11\sqrt{13}} + \frac{30\sqrt{5}\,\mathrm{Re}(DG^*)}{11\sqrt{13}}$$

$$t_{70} = \frac{70\sqrt{35}\,\mathrm{Re}(FG^*)}{143\sqrt{3}} \qquad \text{(E.4)}$$

$$t_{80} = \frac{490|G|^2}{143\sqrt{17}}$$

Note that the parametrization in eq. E.3 contains constant and linear background terms in the D wave, up to quadratic background terms in the F wave, and a linear background term for the high mass G wave. The resonance term B in the F wave was fixed by setting the mass and width, M_F and Γ_F, to the result obtained from the fit to the leading t_{60} moment (discussed below). Therefore the fit parameters were:

$$(M_G, \Gamma_G, \phi_1, \phi_2, a_1, a_2, b_1, b_2, b_3, c_2, N_2, N_3) \qquad \text{(E.5)}$$

where only the mass and width were truly important parameters. Next a

chi-squared was defined as follows:

$$\chi^2 = \sum_{M_{K\pi}\text{bins}} \sum_{lm} \frac{(t_{lm}-t_{lm}^{exp})^2}{\sigma_{lm}^{exp\,2}} \qquad (E.6)$$

The FORTRAN program MINUIT was used to minimize the chi-squared for all the resonance fits discussed in this appendix. The resulting mass and width for the spin 4 object are presented in VII.D.

For the fits to the leading moments (t_{20}, t_{40}, t_{60}, t_{80}), the parametrization used for each was the simple no background form:

$$L = \frac{M_{K\pi}}{\sqrt{q}} \; N_L \, B(M_{K\pi}, M_L, \Gamma_L) \qquad (E.7)$$

where the respective moment was equal to $|L|^2$ times the appropriate Clebsch-Gordon coefficient. The chi-squared was again given by eq. E.6 and the minimization lead to the results presented in VII.D.

2. The resonance fits to the PWA amplitudes

The resonance fits to the amplitudes from the PWA results used the following parametrizations. For the P wave, the fit was performed to the P wave phase as given by eq. E.8:

$$\sin\delta_P \, e^{i\delta_P} = \sqrt{3} \; B(M_{K\pi}, M_P, \Gamma_P) \qquad (E.8)$$

For the D, F, and G waves, the fits were performed to the partial wave magnitudes as given by eq. E.9:

$$|a_L| = x \sqrt{2L+1} \; B(M_{K\pi}, M_L, \Gamma_L) \qquad (E.9)$$

where x is the elasticity of the resonance. The chi-squared was therefore a sum over partial wave phase differences or magnitude differences rather than moments differences as in eq. E.6. The minimization resulted in the mass, width, and R for the P wave K*(895) resonance (R was allowed to be a parameter in this fit only). For the D, F, and G wave leading resonances, the mass, width, and elasticities were determined by the minimization fits. Elastic unitarity was assumed for the P wave (below 1.12 GeV) hence the elasticity was not a parameter in the P wave fit (x was fixed to 1). The results for the resonance fits to the leading P, D, F, and G wave amplitudes are presented in VIII.G.6.

REFERENCES

1. Among the many review articles on the subject are:
   a) D. W. G. S. Leith, Proceedings of the Fifth International Conference on Experimental Meson Spectroscopy, 1977, ed. by E. Von Goeler and R. Weinstein (Northeastern University Press, Boston, 1977), p.207.
   b) R. J. Hemingway, Proceedings of Summer Institute on Particle Physics, ed. by M. Zipf (SLAC REPORT-204, Stanford, Ca., 1977), p.401.
   c) T. A. Lasinski, Proceedings of Summer Institute on Particle Physics, ed. by M. Zipf (SLAC REPORT-204, Stanford, Ca., 1977), p. 371.
   d) S. D. Protopopescu and N. P. Samios, Ann. Rev. Nucl. Part. Sci. 29: 339 (1979).
   e) L. Montanet, review talk given at the 20th International Conference on High Energy Physics, Madison, Wis., proceedings to be published (also CERN-EP/80-163).
2. Particle Data Group: R. L. Kelley et al., Rev. Mod. Phys. 52, No. 2, Part II (1980).
3. The MPS is the Multiparticle Spectrometer facility at Brookhaven National Laboratory; OMEGA is a large multiparticle spectrometer facility at CERN; LASS is the Large Aperture Solenoidal Spectrometer facility at SLAC.
4. L. Bird et al., SLAC-PROPOSAL-E-132 (1976).

5. P. Estabrooks et al., Nucl. Phys. B133 (1978) 490.

There are also several other documents associated with the above article that were used in the analysis presented in this paper:

a) G. Brandenburg, SLAC Group B internal memos on Moments Fitting, unpublished (1974).

b) P. Estabrooks, SLAC Group B internal memos and partial wave analysis software documentation, unpublished (1979).

6. F. C. Winkelmann, SLAC REPORT-160 (1973).

7. S. L. Shapiro et al., SLAC-PUB-1713 (1976); also
S. L. Shapiro et al., SLAC-PUB-1714 (1976).

8. B. Bertolucci, SLAC-PUB-1574 (1975).

9. F. G. Oakham, (M.S. thesis, Carleton University, Ottawa, Canada, 1977).

10. Documentation for the various parts of the LASS spectrometer can be found in:

a) S. L. Shapiro et al., LASS documentation to be published.

b) SLAC Group B, LASS Users Handbook, unpublished.

c) H. Jensen et al., SLAC-PUB-1517 (1974).

d) M. G. D. Gilchriese, SLAC-REPORT-202 (1977), Ph.D. thesis.

e) C. L. Woody, (Ph.D. thesis, Johns Hopkins University, Baltimore, Md, 1978).

f) M. Marshall, (Ph.D. thesis, California Institute of Technology, Pasadena, Ca, 1980).

g) D. Blockus, (Ph.D. thesis, Johns Hopkins University, Baltimore, Md, 1980).

11. There are four Real-Time notes:

a) J. Denecke, Real-Time Note 1, SLAC Computing Services.

b) J. Denecke and C. Granieri, Real-Time Note 2, SLAC Computing Services.

c) C. Granieri and J. Wells, Real-Time Note 3, SLAC Computing Services.

d) J. Denecke,L. Hundly, and J. Wells, Real-Time Note 2, SLAC Computing Services

12. For descriptions of the Runge-Kutta method see, for instance:

a) A. Ralston, A First Course in Numerical Analysis (McGraw-Hill, N.Y., 1965), p.191.

b) G. Dahlquist and A. Bjorck, Numerical Methods (Prentice-Hall, N.J., 1974), P.346.

13. The planar solenoid track finding algorithm is first discussed in: G. Luste, SLAC-REPORT-152 (1972).

14. K. Gottfried and J. D. Jackson, CERN-TH-397 (1964).

15. LASS software documentation (GNUCODE), to be published.

16. The estimated correction for the mass cut was based on an average of the results for the mass shapes from experiments at 10, 14.3, and 16 GeV/c incident beam momenta. The results for 10 and 16 GeV/c are from reference a) below; for 14.3 GeV/c from reference b) below:

a) H. Grassler et al., Nucl. Phys. B125 (1977) 189.

b) M. Spiro et al., Nucl. Phys. B125 (1977) 162.

17. High Energy Reactions Analysis Group (V. Flaminio et al.), CERN-HERA 79-02, (1979).

18. P. H. Eberhard and W. O. Koellner, Computer Phys. Commun. 3 (1972) 396.

19. D. Aston et al., (submitted to Phys. Rev. Lett. for publication, 1980).

20. B. R. Martin, D. Morgan, G. Shaw, Pion-Pion Interactions in Particle Physics (Academic Press, N.Y., 1976).

P. Estabrooks and A. D. Martin, Phys. Lett. 60B (1976) 473.

21. A. R. Edmonds, Angular Momentum in Quantum Mechanics, (Princeton University Press, Princeton, N.J., 1957).

22. F. James and M. Roos, Computer Phys. Commun. 10 (1975) 343.

23. E. Barrelet, Nuovo Cimento 8A (1972) 331.

24. For explanation of Wigner condition see, for instance:

M. L. Perl, High Energy Hadron Physics, (Wiley, N.Y., 1974), p.90.

25. M. G. Bowler et al., Nucl. Phys. B126 (1977) 31.

26. C. Nef, talk given at the 6th International Conference on Experimental Meson Spectroscopy, Brookhaven National Laboratory, N.Y., April 25-26, 1980.

27. Evidence for an I=1, spin 5 object in an amplitude analysis of $\pi^- p \to K^+ K^- n$ has been presented in:

B. Alper et al., CERN Preprint, submitted to Phys. Lett., 1980.

28. In addition, the next experiment by SLAC Group B will involve K^+ data and may obtain results on the I=3/2 $K\pi$ scattering amplitudes. This next experiment is discussed in:

D. Aston et al., SLAC-PROPOSAL-E-135 (1979).

29. P. Estabrooks, Proceedings of the 5th International Conference on Experimental Meson Spectroscopy, ed. by E. Von Goeler and R. Weinstein (Northeastern University Press, Boston, 1977), p.185.

30. G. W. Brandenburg et al., Phys. Rev. Lett. 36 (1976) 1239.

31. F. J. Gilman, Proceedings of Summer Institute on Particle Physics, ed. by M. Zipf (SLAC-REPORT-204, Stanford, Ca, 1977), p.307.

32. L. S. Durkin, (Ph.D. thesis, Department of Physics, Stanford University, Stanford, Ca, 1980), to be published as a SLAC REPORT.

33. G. Brandenburg et al., Phys. Rev. Lett. 36 (1976) 703.

34. P. Estabrooks, Phys. Rev. D19 (1979) 2678.

35. R. J. Cashmore, talk given at the 6th International Conference on Experimental Meson Spectroscopy, Brookhaven National Laboratory, N.Y., April 25-26, 1980.

36. Some examples of analyses discussing the N* background in π-π and K-π scattering include ref. [4] above and also:

a) M. J. Corden et al., Nucl. Phys. B157 (1979) 250.

b) G. Grayer et al., Nucl. Phys. B75 (1974) 189.

37. see, for instance: A. Barbaro-Galtieri, Advances in Particle Physics, ed. by R. L. Cool and R. E. Marshak (Wiley, N.Y., 1968), p.175.

38. M. Blatt and V. F. Weisskopf, Theoretical Nuclear Physics, (Wiley, N.Y., 1952), p.361.

39. A. Wicklund et al., ANL-HEP-PR-80-47 (1980).